

PROCESS INTENSIFICATION DURING POWDER PRODUCTION IN PULSATED GAS FLOW

Dissertation

zur Erlangung des akademischen Grades

Doktoringenieur

(Dr.-Ing.)

von **M.Sc. Daniel Pramudita**

geboren am 17. Dezember 1987 in Jakarta, Indonesien

genehmigt durch die Fakultät für Verfahrens- und Systemtechnik
der Otto von Guericke Universität Magdeburg

Promotionskommission:

apl. Prof. Dr.-Ing. habil. Gabor Janiga (Vorsitz)

Prof. Dr.-Ing. habil. Evangelos Tsotsas (Gutachter)

Jun.-Prof. Dr.-Ing. Alba Diéguez Alonso (Gutachter)

Dr.-Ing. Michael Jacob (Gutachter)

Eingereicht am 4. April 2022

Promotionskolloquium am 4. Oktober 2022

Declaration

Hereby I declare that I have prepared this dissertation titled

“Process intensification during powder production in pulsated gas flow”

without inadmissible assistance and without the use of any aids other than those indicated. Facts or ideas taken from other sources, either directly or indirectly have been marked as such.

In particular, I did not use the services of a commercial graduation consultation. Further I have not made payments to third parties either directly or indirectly for any work connected with the contents of the submitted dissertation.

The work has not been submitted as a dissertation either in Germany or abroad in the same or similar form and has also not been published as a whole.

Magdeburg, 2022

Daniel Pramudita

Abstract

This dissertation reports on the investigation of intensified processes occurring during drying of droplets in pulsating gas flow, in a process named pulse combustion drying (PCD). PCD is an advanced drying technique that uses pulsating flue gas flow generated by intermittent combustion. The technique can be used for fine powder production from various materials, including heat sensitive materials such as foods and pharmaceuticals. Gas pulsation increases the overall heat and mass transfer coefficients during the drying process, resulting in process intensification.

Some studies reported that very small particles down to the nanoscale could be produced during PCD. It was claimed that breakup of colloidal droplets is the main enabling mechanism. The process of droplet breakup during PCD is investigated here using the Taylor analogy breakup model, which is coupled to a single droplet drying model previously developed by our group. A liquid droplet may only break before crust is formed on its surface. Simulation results show how the key parameters of pulse combustion drying as well as the colloidal droplet properties influence the droplet breakup. For easier colloidal droplet breakup, a large droplet, small nanoparticles, high surface charge, high gas temperature, strong gas oscillation, and high frequency are favorable. It is shown that while droplet breakup can result from pulse combustion drying conditions, particles below micron-size cannot be produced. This leaves the mechanism that may lead to nanoparticle production unclear.

Further experimental investigation using two metal oxides (SiO_2 and TiO_2) and a sticky organic material (maltodextrin), has been conducted to see how material type and process conditions influence the physical properties of the products. The employed process parameters, namely gas temperature and pulsation frequency, strongly influence final particle shape and size of maltodextrin. Fine metal oxide particles can be obtained with and without pulsation, and no significant differences are observed with the variation of pulsation frequency. The volume fraction of the fine particles is, however, very low. Based on these results, a model of particle production through repetitive crust breakage and drying cycles is proposed. Two possible mechanisms are tested. In the first mechanism crust breaks due to external shear by the surrounding flow. A variable is used as the breakage criterion and an empirical equation is used to determine the number of child particles. In the second mechanism crust breaks when it can no longer withstand the stresses working on it due to pressure and temperature gradients in it. The crust strength is calculated from the interparticle binding forces. It is found that stresses due to temperature and pressure gradients are what may cause the crust to break. It is also shown that formation of debris particles that follows contributes significantly to the number of nano- and submicron-sized particles. The obtained results are in agreement with the experimental data, and the proposed mechanism could explain the production of fine particles regardless of gas pulsation.

To see how the intensified heat and mass transfer could potentially deteriorate heat sensitive material during PCD, a numerical investigation has been carried out for whey protein isolate (WPI). A kinetic model of whey protein denaturation obtained from experiments is used. It is found that small droplets undergo drying and denaturation faster, and stay longer in the drying chamber. The influence of initial solid content is complex and depends on other variables. Gas pulsation has been shown to enhance drying with small reduction in final product activity. It also reduces the discrepancies in product quality and energy consumption in case of different initial droplet size distributions. The influence of frequency and velocity amplitude weakens at higher magnitudes of the same. Average flow velocity has a negligible effect on the properties of dried product, but it determines the droplet residence time. For WPI it is better to dry slowly at moderate temperatures than to dry faster at high temperatures, to prevent excessive denaturation. It is also shown that employing pulsation is a better strategy than increasing temperature to enhance the drying process while preserving product quality.

Zusammenfassung

Diese Dissertation berichtet über die Untersuchung intensivierter Prozesse, die während der Trocknung von Tröpfchen in einem pulsierenden Gasstrom auftreten. Der entsprechende Prozess wird als Pulse Combustion Drying (PCD) bezeichnet. PCD ist eine fortgeschrittene Trocknungstechnik, die den pulsierenden Rauchgasstrom aus einer intermittierenden Verbrennung verwendet. Diese Technik kann für die Feinpulverherstellung aus verschiedenen Materialien verwendet werden, einschließlich wärmeempfindlicher Materialien wie Lebensmittel und Pharmazeutika. Die Gaspulsation erhöht die gesamten Wärme- und Stoffübergangskoeffizienten während der Trocknung, was zu einer Prozessintensivierung führt.

Einige Studien berichteten, dass mittels PCD kleinere Partikel bis hinab in den Nanobereich produziert werden konnten. Das Aufbrechen kolloidalen Tröpfchen sei der Hauptmechanismus, der dies ermöglicht. Der Bruch von Tröpfchen während der PCD wird hier durch Kopplung des als Taylor Analogy Breakup bezeichneten Modells mit einem zuvor von unserer Gruppe entwickelten Einzeltröpfchen-Trocknungsmodell untersucht. Ein Flüssigkeitströpfchen kann nur brechen, bevor sich an seiner Oberfläche eine Kruste bildet. Simulationsergebnisse zeigen, wie die Schlüsselparameter der PCD sowie die kolloidalen Eigenschaften den Tropfenzerfall beeinflussen. Für ein leichteres Aufbrechen sind große Tröpfchen, kleine Nanopartikel, hohe Oberflächenladung, hohe Gastemperatur, starke Gasoszillation und eine hohe Frequenz günstig. Es wird gezeigt, dass Tropfenzerfall zwar aus PCD-Bedingungen resultieren kann, submikrone Partikel können jedoch nicht erzeugt werden. Der Mechanismus, der zur Nanopartikelproduktion führen kann, bleibt somit unklar.

Weitere experimentelle Untersuchungen wurden mit zwei Metalloxiden (SiO_2 und TiO_2) und einem klebrigen organischen Material (Maltodextrin) durchgeführt, um festzustellen, wie Materialtyp und Prozessbedingungen die physikalischen Eigenschaften der Produkte beeinflussen. Die verwendeten Prozessparameter, nämlich Gastemperatur und Pulsationsfrequenz, beeinflussen stark die endgültige Teilchenform und -größe von Maltodextrin. Feine Metalloxidpartikel können mit und ohne Pulsation erhalten werden, und es werden keine signifikanten Unterschiede bei der Variation der Pulsationsfrequenz beobachtet. Der Volumenanteil der feinen Partikel ist jedoch sehr gering. Basierend auf diesen Ergebnissen wird ein Modell der Partikelproduktion durch wiederholte Krustenbrüche und Trocknungszyklen vorgeschlagen. Zwei mögliche Mechanismen werden getestet. Beim ersten Mechanismus bricht die Kruste aufgrund äußerer Scherung durch die umgebende Strömung. Neben einem variablen Bruchkriterium wird eine empirische Gleichung verwendet, um die Anzahl der Tochterpartikel zu bestimmen. Im zweiten Mechanismus bricht die Kruste, wenn sie den auf sie einwirkenden Belastungen aufgrund von Druck- und Temperaturgradienten nicht mehr standhalten kann. Die Krustenfestigkeit wird aus den interpartikulären

Bindungskräften berechnet. Es wurde festgestellt, dass die Kruste in der Regel durch Spannungen aufgrund von Temperatur- und Druckgradienten bricht. Die nachfolgende Bildung von Trümmerpartikeln trägt erheblich zur Anzahl von Partikeln im Nano- und Submikronbereich bei. Die erhaltenen Ergebnisse stimmen mit den experimentellen Daten überein, und der vorgeschlagene Mechanismus kann die Erzeugung feiner Partikel unabhängig von der Gaspulsation erklären.

Um zu sehen, wie die intensivierete Wärme- und Stoffübertragung wärmeempfindliches Material während der PCD zu schädigen vermag, wurde eine numerische Untersuchung für Molkeproteinisolat (WPI) durchgeführt. Ein aus Experimenten erhaltenes kinetisches Modell der Denaturierung von Molkeprotein wird verwendet. Es wurde festgestellt, dass kleine Tröpfchen schneller trocknen und denaturieren, und länger in der Trocknungskammer bleiben. Der Einfluss des anfänglichen Feststoffgehalts ist komplex und hängt von anderen Variablen ab. Es hat sich gezeigt, dass die Gaspulsation das Trocknen bei geringem Aktivitätsverlust des Endprodukts verbessert. Sie reduziert auch die Abweichungen in der Produktqualität und im Energieverbrauch bei unterschiedlichen anfänglichen Tröpfchengrößenverteilungen. Der Einfluss von Frequenz und Geschwindigkeitsamplitude schwächt sich bei höheren Werten dieser Variablen ab. Die durchschnittliche Strömungsgeschwindigkeit hat kaum Einfluss auf die Eigenschaften des getrockneten Produkts, bestimmt jedoch die Tröpfchenverweilzeit. Für WPI ist es besser, langsam bei moderater Temperatur als schneller bei hoher Temperatur zu trocknen, um eine zu starke Denaturierung zu verhindern. Es wird auch gezeigt, dass der Einsatz von Pulsation eine bessere Strategie ist als eine Erhöhung der Temperatur, um den Trocknungsprozess bei Erhaltung der Produktqualität zu beschleunigen.

Contents

Declaration	i
Abstract	ii
Zusammenfassung	iv
Contents	vi
Nomenclature	ix
1. Introduction	1
1.1 Motivation and scope.....	1
1.2 Spray drying.....	2
1.2.1 Droplet atomization	2
1.2.2 Drying process.....	4
1.2.3 Particle collection.....	5
1.3 Advanced spray drying technologies.....	6
1.3.1 Dehumidified air spray drying.....	6
1.3.2 Vacuum spray drying.....	6
1.3.3 Foam spray drying.....	7
1.3.4 Flame spray drying.....	7
1.3.5 Nano spray drying	7
1.4 Pulse combustion drying	7
1.4.1 Pulse combustion.....	8
1.4.2 Applications and researches	12
1.5 Outline of dissertation.....	15
2. Model of single droplet drying in pulsated flow	16
2.1 Previous modeling works in droplet drying	16
2.2 1 st drying stage	21
2.3 Locking point determination	25
2.3.1 Colloidal suspension.....	25
2.3.2 Solution	27
2.4 2 nd drying stage	28
2.4.1 Crust thermal conductivity.....	29
2.4.2 Vapor diffusivity through the crust.....	29
2.5 Droplet movement in pulsed flow	30
2.6 Discretization and computation	31
2.7 Summary.....	32

3. Droplet breakup in pulsed gas flow	33
3.1 Introduction	33
3.2 Secondary atomization	35
3.3 Taylor analogy breakup (TAB) model	37
3.4 Viscosity of colloidal droplet.....	39
3.5 Pressure balance & effective surface tension	39
3.6 Simulation setup	42
3.7 Results & discussions	46
3.7.1 Behavior of DLVO parameters.....	46
3.7.2 Influence of drying process on droplet breakup	49
3.7.3 Influence of operating parameters	51
3.7.4 Assessment of the reference studies: is breakup possible?	53
3.8 Conclusion.....	57
4. Experimental study on powder production using pulsating hot air	58
4.1 Introduction	58
4.2 Materials and methods.....	58
4.2.1 Materials.....	58
4.2.2 PCD-unit.....	59
4.2.3 Drying process	60
4.2.4 Experimental conditions.....	60
4.2.5 Particle size measurement	61
4.3 Results and discussions.....	63
4.3.1 Flow dynamics	63
4.3.2 Maltodextrin.....	64
4.3.3 Metal oxides	66
4.4 Conclusion.....	71
5. Modeling fine particle production via crust breakage.....	72
5.1 pH-dependent charge regulation for droplet breakup calculation	72
5.2 Crust breakage mechanisms	76
5.2.1 Breakage due to external shear	77
5.2.2 Breakage due to internal drying.....	77
5.3 Dry crust strength	82
5.4 Simulation setup	83
5.5 Results and discussions.....	89
5.5.1 Influence of locations in chamber (drying air conditions)	89
5.5.2 Particle size distributions.....	92
5.5.3 Particle morphologies.....	93
5.5.4 Sensitivity upon arbitrarily predefined parameters.....	95

5.5.5	Optimal parameter setting	98
5.6	Conclusion	102
6.	Drying and denaturation of proteins in PCD	103
6.1	Introduction.....	103
6.2	Denaturation model of whey protein	104
6.3	Model validation & simulation parameters	106
6.4	Results and discussions	112
6.4.1	Denaturation model behavior	113
6.4.2	Process time and protein activity of dried particles	115
6.4.3	In specified drying chamber: Residence time and outlet properties	118
6.4.4	Influence of initial droplet size distributions	119
6.4.5	Increased temperature vs gas pulsation.....	123
6.5	Conclusion	125
7.	General conclusion & outlook.....	127
	References	130
	Appendices	147
	Appendix A: Material properties.....	147
	Appendix B: Calculation example for <i>pH</i> -dependent surface charge	148
	Appendix C: Shell thickness measured from SEM images of SiO ₂ and TiO ₂ particles.....	150
	Appendix D: Particle size distribution data from experiments in Chapter 5	152
	Scientific Contributions	156

Nomenclature

A_{cross}	cross-sectional area of droplet (m^2)
A_{H}	Hamaker constant (J)
A_{wh}	normalized protein activity (-)
$A_{\text{wh,avg}}$	A_{wh} obtained by mass averaging the values in crust and in liquid core (-)
$A_{\text{wh,lump}}$	A_{wh} obtained directly from lumped droplet properties (-)
\bar{A}_{cr}	volume-averaged area of crust (m^2)
a_{w}	water activity (-)
B_{T}	Spalding number (-)
B_2	osmotic second virial coefficient (m^3)
C_{drag}	drag coefficient (-)
C_{E}	Einstein viscosity coefficient (= 2.5)
C_{s}	solid mass per droplet (liquid core) volume (kg/m^3)
C_{wh}	protein concentration in solution (g/kg)
$c_{\text{p,d}}$	specific heat capacity of droplet ($\text{J}/(\text{kg}\cdot\text{K})$)
$c_{\text{p,g}}$	specific heat capacity of gas ($\text{J}/(\text{kg}\cdot\text{K})$)
$c_{\text{p,s}}$	specific heat capacity of solid ($\text{J}/(\text{kg}\cdot\text{K})$)
$c_{\text{p,v}}$	specific heat capacity of vapor ($\text{J}/(\text{kg}\cdot\text{K})$)
$c_{\text{p,w}}$	specific heat capacity of water ($\text{J}/(\text{kg}\cdot\text{K})$)
c_{s}	molar concentration of solid (mol/m^3)
c_{w}	molar concentration of water (mol/m^3)
$D_{\text{break,1}}$	droplet diameter at the first breakup event (m)
$D_{\text{child,1}}$	diameter of child droplets resulting from the first breakup event (m)
$D_{\text{child,last}}$	diameter of child droplets resulting from the last breakup event (m)
D_{chamber}	diameter of drying chamber (m)
D_{d}	droplet diameter (m)
$D_{\text{d,end}}$	final droplet diameter (m)
$D_{\text{d,max}}$	maximum droplet diameter (m)
$D_{\text{d,min}}$	minimum droplet diameter (m)
D_{lo}	diameter of liquid orifice in a two-fluid nozzle (m)
D_{max}	maximum value of diameter in a given size range (m)
D_{mid}	middle value of diameter in a given size range (m)
D_{min}	minimum value of diameter in a given size range (m)
D_{p}	dried particle diameter (m)
D_{pp}	primary particle diameter (m)
D_{tail}	tailpipe diameter (m)
$D_{32,\text{d}}$	Sauter mean diameter of sprayed droplets (m)

Nomenclature

$\bar{D}_{p,dbf}$	average diameter of debris particles (m)
\hat{d}	distance between primary particle surfaces (m)
\hat{d}_{\min}	distance between surfaces of two closest primary particles (m)
E_a	reaction activation energy (J/mol)
E_{cr}	Young's modulus of crust (Pa)
e_0	elementary charge ($= 1.60217662 \times 10^{-19}$ C)
f	frequency of gas pulsation (Hz)
f_b	binding force between two particles in contact (N)
f_{dbf}	ratio of h_f to Δ_{cr} at each breakage event (-)
f_{drop}	maximum pressure ratio drop along tailpipe (-)
f_{Ea}	multiplier for reaction activation energy E_a (-)
f_{frg}	ratio of $\bar{D}_{p,dbf}$ to Δ_{cr} at each breakage event (-)
f_{k0}	multiplier for pre-exponential factor k_0 (-)
f_n	multiplier for reaction order n (-)
f_{sint}	binding force component due to sintering (N)
f_{vdw}	van der Waals component of interparticle binding force (N)
$f_{X,k0}$	moisture-dependent multiplier for pre-exponential factor k_0 (-)
H	Hellinger distance (unit depends on the variable)
h_{evap}	latent heat of evaporation per mass (J/kg)
h_f	thickness of breakage surface that turns into debris (m)
h_{lv}	latent heat of evaporation per mass, at 0 °C (J/kg)
h_p	Planck constant ($= 6.62607 \times 10^{-34}$ kg.m ² /s)
j_n	particle coordination number (-)
K^{int}	intrinsic equilibrium constant (-)
K_j	weighting factor for SEM images of j^{th} magnification (-)
Kn	Knudsen number (-)
k	crust permeability (m ²)
k_B	Boltzmann constant ($= 1.380649 \times 10^{-23}$ J/K)
k_h	overall heat transfer coefficient (W/(m ² .K))
k_m	overall mass transfer coefficient (m/s)
k_n	reaction rate constant of an n^{th} order reaction ($g^{1-n}/(kg^{1-n}.s)$)
k_{Wb}	shape parameter of Weibull distribution (-)
k_0	pre-exponential factor for denaturation kinetics ($g^{1-n}/(kg^{1-n}.s)$)
L	length of drying chamber (m)
L_t	tailpipe length (m)
M	molecular mass (kg/mol)
m_a	mass of active (undenatured) protein (kg)
m_d	total mass of droplet (kg)
m_j	number of images obtained with j^{th} magnification (-)
m_s	mass of solid in droplet (kg)
$m_{s,cr}$	mass of solid crust (kg)

x

m_w	mass of water in droplet (kg)
$\dot{m}_{d,in}$	inlet mass flow rate of droplets (kg/s)
$\dot{m}_{d,out}$	outlet mass flow rate of droplets (kg/s)
$\dot{m}_{evap,total}$	total mass flow rate of evaporation (kg/s)
$\dot{m}_{g,dry,in}$	inlet mass flow rate of dry gas (kg/s)
$\dot{m}_{g,dry,out}$	outlet mass flow rate of dry gas (kg/s)
$\dot{m}_{s,in}$	inlet mass flow rate of solid (kg/s)
$\dot{m}_{s,out}$	outlet mass flow rate of solid (kg/s)
$\dot{m}_{v,in}$	inlet mass flow rate of water vapor (kg/s)
$\dot{m}_{v,out}$	outlet mass flow rate of water vapor (kg/s)
$\dot{m}_{w,in}$	inlet mass flow rate of water (kg/s)
$\dot{m}_{w,out}$	outlet mass flow rate of water (kg/s)
N_{Av}	Avogadro number (6.02214×10^{23} / mol)
N_{break}	number of breakage events (-)
N_{DA}	ratio of hydrodynamic drag to interparticle adhesive binding force (-)
N_{Di}	number of particles with diameter $D \leq D_i$ (-)
$N_{d,0}$	number of parent droplets (-)
$N_{d,child}$	number of child droplets after droplet breakup (-)
$N_{d,brkg}$	number of child droplets after crust breakage (-)
N_{dbr}	number of debris particles (-)
N_{el}	number of discretized volume elements (-)
$N_{fr,brkg}$	number of crust fragments after breakage (-)
N_i	number of species i (-)
N_m	number of magnifications (-)
$N_{pp,cr}$	number of primary particles forming a dry crust (-)
$N_{pp,fr}$	average number of primary particles in fragments (-)
N_s	total ionic site densities (mol/m ²)
N_{sint}	number of molecule pairs that form a sinter neck (-)
N_V	number density of particles (1/m ³)
Nu	Nusselt number (-)
n	order of reaction (-)
n_l	refractive index of liquid (-)
n_s	refractive index of solid (-)
Oh	Ohnesorge number (-)
Pr	Prandtl number (-)
p	total pressure (Pa)
p_{amp}	pressure amplitude (Pa)
p_{cap}	capillary pressure (Pa)
$p_{cr,e}$	external pressure experienced by crust (Pa)
$p_{cr,i}$	internal pressure experienced by crust (Pa)
$p_{c,max}$	maximum pressure inside a combustor (Pa)

Nomenclature

p_{Lap}	Laplace pressure (Pa)
p_{osm}	osmotic pressure (Pa)
$p_{\text{s,ref}}$	reference sound pressure ($= 2 \times 10^{-5}$ Pa)
p_{sat}	saturated vapor pressure (Pa)
$p_{\text{sh,e}}$	external pressure experienced by wet shell (Pa)
$p_{\text{sh,i}}$	internal pressure experienced by wet shell (Pa)
p_{st}	pressure due to surface tension (Pa)
pH_{eln}	electroneutrality point (-)
pK	bulk pH at half dissociation (-)
Q_0	number cumulative distribution (-)
Q_3	volume cumulative distribution (-)
$Q_3(D_i)$	volume fraction of particles with diameter lower than D_i (-)
\dot{Q}	total heat flow rate (W)
\dot{Q}_{latent}	total latent heat flow rate (W)
$\dot{Q}_{\text{sensible}}$	total sensible heat flow rate (W)
q	effective surface charge of primary particles (C)
q_A	surface charge density (C/m^2)
$q_{A,\infty}$	surface charge density, without charge regulation (C/m^2)
q_i	charge of species i (C)
q_0	normalized number-based size distribution density (-)
q_3	normalized volume-based size distribution density (-)
R	universal gas constant ($\text{J}/(\text{mol}\cdot\text{K})$)
R_{child}	radius of child droplets (m)
R_{cr}	distance from droplet center to crust surface, equal to R_d (m)
$R_{\text{cr,red}}$	radius of crust after debris formation (m)
R_d	radius of whole droplet (m)
R_h	hydraulic radius of crust pores (m)
R_{lc}	radius of droplet liquid core (m)
R_p	radius of dried particle (m)
R_{pp}	radius of primary particles (m)
R_{sh}	inner radius of wet shell (m)
Re	Reynolds number (-)
RE_{D50}	relative error in log values of median (-)
$RE_{\mu 1}$	relative error in log values of mean (-)
$RRMSE$	relative root mean squared error (-)
r	position in radial direction (m)
r_{sint}	ratio of sinter neck radius to primary particle radius (-)
\hat{r}	distance between centers of two primary particles (m)
Sc	Schmidt number (-)
Sh	Sherwood number (-)
T_{adb}	adiabatic saturation temperature (K)

$T_{cr, avg}$	average crust temperature (K)
$T_{cr, surf}$	temperature of crust surface (K)
T_d	droplet (liquid core) temperature (K)
$T_{d, avg}$	lumped droplet temperature, obtained by enthalpy-averaging (K)
T_g	bulk gas temperature (K)
$T_{g, in}$	inlet gas temperature (K)
$T_{g, out}$	outlet gas temperature (K)
T_{glass}	glass transition temperature (K)
$T_{g, pore}$	temperature of gas in crust pores (K)
$T_{m, s}$	melting temperature of solid (K)
T_0	reference temperature (= 0 °C)
t	time (s)
t_{dry}	drying time (s)
t_{res}	droplet residence time (s)
u_d	droplet velocity (m/s)
u_g	gas velocity (m/s)
$u_{g, amp}$	velocity amplitude of gas (m/s)
\bar{u}_g	average velocity of gas (m/s)
$u_{n, g}$	velocity of atomizing gas (m/s)
$u_{n, l}$	velocity of liquid feed in nozzle (m/s)
u_{rel}	relative velocity between droplet and gas (m/s)
u_{sound}	sound velocity (m/s)
V_{cr}	crust volume (m ³)
$V_{cr, red}$	volume of crust after debris formation (m ³)
V_d	droplet volume (m ³)
V_{dbr}	total volume of debris particles (m ³)
V_{mol}	molecular volume (m ³ /mol)
$V_{tot, j}$	total volume of particles measured in m_j images under j^{th} magnification (m ³)
$\bar{V}_{p, dbr}$	(average) volume of a debris particle (m ³)
$\dot{V}_{n, g}$	volume flow rate of atomizing gas (m ³ /s)
$\dot{V}_{n, l}$	volume flow rate of liquid feed in nozzle (m ³ /s)
\dot{V}_{spray}	volume flow rate of sprayed droplets (m ³ /s)
\dot{V}_{vap}	volume flow rate of water vapor from evaporation (m ³ /s)
w	potential of mean force (J)
w_{es}	electrostatic potential (J)
w_{hyd}	hydration potential (J)
w_{vdW}	van der Waals potential (J)
w_0	steric contact potential (J)
We	Weber number (-)
X	moisture content (d.b.) (-)

Nomenclature

X_{cr}	critical moisture content (d.b.) (-)
X_{dry}	targeted moisture content (d.b.) of product (-)
X_{eq}	equilibrium moisture content (d.b.) (-)
x	surface displacement of distorted droplet (m)
x_s	mass fraction of solid in liquid droplet (-)
x_w	mass fraction of water in liquid droplet (-)
$x_{c,wh}$	mass fraction of whey protein component (-)
$x_{V,w,0}$	initial volume fraction of water in droplets (-)
$Y_{d,surf}$	absolute humidity (d.b.) on droplet surface (-)
$Y_{g,in}$	absolute humidity (d.b.) of gas at chamber inlet (-)
$Y_{g,out}$	absolute humidity (d.b.) of gas at chamber outlet (-)
$Y_{g,s}$	absolute humidity (d.b.) of gas at droplet surface (-)
$Y_{g,sat}$	absolute humidity (d.b.) of gas at saturation (-)
$Y_{g,\infty}$	absolute humidity (d.b.) of bulk gas (-)
y	non-dimensional distortion (-)
$\mathcal{Y}_{V,air,in}$	volume fraction of dry air in inlet gas (-)
z	minimal intermolecular distance (m)
z_{GB}	thickness of sintering grain boundary (m)

Greek symbols

α	heat transfer coefficient in gas (W/(m ² .K))
$\alpha_{T,cr}$	thermal expansion coefficient (-)
β	mass transfer coefficient in gas (m/s)
Γ_s	number site density of surface groups (1/m ²)
γ	accommodation coefficient (-)
γ_s	surface energy of solid (N/m)
$\dot{\gamma}$	shear rate (1/s)
Δ_{cr}	crust thickness (m)
δ_{GB}	grain boundary diffusion coefficient (m ² /s)
δ_{SE}	mass diffusion coefficient of solid in water from Stokes-Einstein equation (m ² /s)
$\delta_{v,cr}$	effective mass diffusion coefficient of vapor in crust (m ² /s)
$\delta_{v,g}$	mass diffusion coefficient of vapor in gas (m ² /s)
$\delta_{v,pore}$	mass diffusion coefficient of vapor in crust pores (m ² /s)
$\delta_{w,s}$	mass diffusion coefficient of solid in water (m ² /s)
ε_{cr}	crust porosity (-)
$\varepsilon_{r,l}$	relative permittivity of solvent (-)
$\varepsilon_{r,s}$	relative permittivity of solid (-)
ε_{sh}	wet shell porosity (-)
ε_0	vacuum permittivity (= 8.854187817 × 10 ⁻¹² F/m)

θ_d	degree of deprotonation (-)
κ	inverse of Debye length (1/m)
Λ	mean free path of gas molecules (m)
$\lambda_{cr,eff}$	effective thermal conductivity of crust (W/(m.K))
λ_g	thermal conductivity of gas (W/(m.K))
λ_{pore}	thermal conductivity in crust pores (W/(m.K))
λ_{sound}	acoustic resonance wavelength (m)
λ_{Wb}	scale parameter of Weibull distribution (-)
λ_0	steric decay length (m)
μ_d	dynamic viscosity of droplet (Pa.s)
$\mu_{k,3}$	k^{th} normalized moment of volume-based size distribution
μ_{lgn}	parameter of log-normal distribution (-)
μ_w	dynamic viscosity of water (Pa.s)
u_e	main electronic absorption frequency in UV (1/s)
u_g	kinematic viscosity of gas (m ² /s)
ν_{cr}	Poisson's ratio of crust (-)
ξ	normalized drying rate (-)
ρ_{air}	mass density of dry air (kg/m ³)
ρ_d	mass density of droplet (kg/m ³)
ρ_g	mass density of gas (kg/m ³)
$\rho_{n,g}$	mass density of atomizing gas (kg/m ³)
$\rho_{n,l}$	mass density of liquid feed (kg/m ³)
ρ_s	mass density of solid (kg/m ³)
ρ_v	mass density of water vapor (kg/m ³)
ρ_w	mass density of liquid water (kg/m ³)
σ_d	surface tension of droplet (N/m)
σ_{lgn}	parameter of log-normal distribution (-)
$\sigma_{M,r}$	mechanical stresses in radial direction in crust (Pa)
$\sigma_{M,t}$	mechanical stresses in tangential direction in crust (Pa)
σ_r	radial stress experienced by crust (Pa)
$\sigma_{T,r}$	thermal stresses in radial direction in crust (Pa)
$\sigma_{T,t}$	thermal stresses in tangential direction in crust (Pa)
σ_t	tangential stress experienced by crust (Pa)
σ_w	surface tension of water (N/m)
σ_3	standard deviation of volume-based particle size distribution (m)
$[\sigma_r]$	radial stress experienced by wet shell (Pa)
$[\sigma_{sh}]$	strength of wet shell (Pa)
$[\sigma_t]$	tangential stress experienced by wet shell
$\bar{\sigma}_g$	gas molecule diameter (m)
$\bar{\sigma}_s$	solid molecule diameter (m)
Φ	characteristic moisture content (-)

Nomenclature

ϕ_{\max}	maximum volume fraction of packed spherical particles (≈ 0.6)
ϕ_s	volume fraction of solid (-)
ϕ_V	volume fraction of particles in droplet (-)
ϕ_V^*	effective volume fraction of particles in droplet (-)
ϕ_w	volume fraction of water (-)
φ	oscillation phase (rad)
ψ_0	surface potential (V)
ω	frequency of distortion oscillation (1/s)

1. Introduction

1.1 Motivation and scope

Drying is the removal of liquid, particularly water, by evaporation or sublimation from a moist solid material or liquid mixture of solid and liquid. What differentiates drying from other mechanisms of liquid removal such as filtration is the involvement of heat transfer along with mass and momentum transfer. The purposes of drying include material conservation and preservation, easier handling, lower cost and energy for transportation & storage, product formulation, removal of toxins, and process safety. The most important product quality parameter is moisture content. Other parameters include composition, appearance and other sensory properties, processability, and special properties that are product specific.

Spray drying is probably the most prominent technique for producing solid particles and fine powder from liquids. It has been widely applied in specialty chemical, food, and pharmaceutical industries. The products range from pure chemicals to encapsulated food ingredients. More details on applications have been covered in many publications [1–9]. The process is very fast and has low operational costs (less than one-fourth of those required by freeze drying and vacuum drying [6]), despite having lower thermal efficiency. The total heat consumption per kg of evaporated water can be more than double the latent heat of evaporation [5]. The inefficiency is mainly due to the large volume of drying medium that flows through the chamber without contact with the droplets [7].

The process can be further intensified by various modifications, one of them being utilization of pulsating gas flow as the drying medium. The gas flow is flue gas supplied by a pulse combustion unit (i.e., the flue gas), so that in the process called "pulse combustion drying" (PCD) the drying gas velocity is fluctuating regularly. Combustion occurs in intermittent (pulsed) way, instead of the more common continuous combustion. The pulsation generates oscillation of velocity, pressure, and, to some extent, temperature, which intensifies the heat and mass transfer; see the reviews by Meng et al. and Kudra [10,11].

While the technology of pulse combustion has been known for long time, its utilization for drying is relatively new. PCD has been applied for production of powders from solution (or suspension) of different types of materials, from ceramics and polymers to food ingredients and pharmaceuticals. While use of combustion flue gas for drying hygienic products might seem counterintuitive, this is made possible by cleaner flue gas that results from more intensive combustion compared to that found in the more orthodox method [11]. Examples of PCD applications and products are given later in this chapter.

Although the intensifying effect has been known for quite long time, industrial implementations are still limited compared to conventional spray dryer due to a lack of understanding of process dynamics. The whole process is very complex and is a function of

many interacting variables. Of interest is the influence of amplitude and frequency of the pulsating flow on the interaction between the droplets and the flow, as well as on the powder properties. Turbulence created by the pulsation of gas flow makes the use of a simple nozzle for the liquid feed possible. The chaotic gas flow will cause the liquid jet from the nozzle to disintegrate to droplets, and these droplets might further break up to smaller ones [12].

There have not been many studies on PCD and the phenomena occurring during the process. Okuyama and co. reported that pulse combustion drying can result in finer particles with narrower size distribution [13–15]. However, the reason for this is still unclear. It has been hypothesized that breakup of liquid droplets is the reason for the production of fine particles, even down to nanoscale [13,16]. The influence of gas pulsation on liquid atomization was considered by Xiao et al. [12]. Aspects of pulse combustion processes have been modelled in some studies [17–19], which investigated how pulsation affects the movement of spherical solid particles inside a chamber. The effects of water evaporation and the subsequent reduction of droplet size were taken into account in a study by Zbiciński et al. [20]. Further details on researches and applications of PCD for product formulation will be discussed later.

The main objective of this study is to investigate how process intensification due to pulsating gas flow in PCD may result in better product properties than those obtained using spray drying. Focus is given to finer particle production and heat-induced degradation. Analyses are carried out to see the influence of process parameters on the process dynamics and product properties.

1.2 Spray drying

A spray dryer generally consists of a feed line, an atomizing unit, a drying gas channel, a drying chamber, a particle collector, and a fan (or a vacuum pump), which is used to ensure flow integrity of the whole process. Steps of spray drying are atomization (droplet generation), spray-air contact (the drying process), and particle collection.

1.2.1 Droplet atomization

Atomization is the process during which droplets are generated and released into the drying chamber. It is also referred to as “primary atomization” and is differentiated from “secondary atomization” discussed later in Chapter 3. The process can be continuous or intermittent. The feed material is a liquid mixture of solvent and solute. The key material properties here are viscosity, surface tension, and solid content. Lower surface tension or viscosity result in smaller droplet sizes, regardless of the type of atomizer used [21]. Higher feed viscosity, on the other hand, gives narrower spray pattern and angle. Too viscous feed, however, can cause clogging [22]. Lower initial solid contents give narrower size distributions. Viscosity and surface tension are influenced by the feed components and mixture composition. When the solid content is too high, the feed material becomes too viscous. The spray might then collapse and the feed dries quickly and blocks the nozzle [22].

There are many types of atomizers that can be used in spray drying. The most commonly found in industrial spray dryers are pressure nozzles. For single-fluid pressure nozzles, the fluid is atomized by pressurizing it to flow through an orifice. Droplet size is determined by the nozzle diameter (typically 1 mm or larger) and spraying pressure (and, consequently, the feed rate). It is usually in a range of 20-200 μm . Higher pressure leads to smaller droplet sizes, but with wider size distributions [23]. Using smaller nozzle diameter, while resulting in smaller droplets, increases the risk of clogging [24].

Two-fluid nozzles also belong to the pressure nozzle group. The difference is, as the name suggests, in the use of two fluids, namely liquid feed and spraying gas. Taking a cross-sectional view of the nozzles, the channel for the liquid is located in the center and surrounded by the gas channel. High pressure is not needed for the feed, as it only has to come out steadily from the channel hole. High pressure is applied to the gas to create high velocity flow that will break liquid ligaments. Mixing of liquid feed and atomizing gas can occur externally or internally, depending on the nozzle design. Two-fluid nozzles are able to generate narrower spray angles and smaller droplets with more uniform sizes [25]. Lower spraying gas density results in smaller size and higher velocity of droplets [26]. Droplet sizes obtained using two fluid nozzles are less affected by feed composition when the solid mass concentration is $>5\%$, compared to when single pressure nozzles are used [27,28]. The downside is that they need more energy [23]. Additionally, there is a higher risk of backflow and clogging due to the Venturi effect resulting from high velocity of atomizing gas [27].

Rotary atomizers use the centrifugal force resulting from high-speed rotation to break liquid ligaments from feed holes into droplets. The feed holes are usually arranged in an angle to form a conical spray pattern, so that droplet deposition on the chamber wall can be minimized. Rotary atomizers do not need high pressure, unlike single and two-fluid nozzles. However, being mechanical in nature makes them prone to friction-induced wear. One way to deal with this is by using non-contact magnetic bearings in so-called magnetic rotary atomizers.

Ultrasonic atomizers can generate smaller droplets with narrower size distributions and better control [29,30], making them suitable for producing nanoparticles [30]. In an ultrasonic nozzle, a piezoelectric crystal vibrates at high frequency and generates ultrasound. The ultrasound energy is transmitted to the liquid. The vibrational energy overcomes the surface tension, breaking the liquid layer into droplets [4]. Problems related to mechanical stress of the feed, which is often found in other types of nozzles [7], are thus eliminated. This helps to better preserve probiotics [4] and active compounds in biological materials [29,31]. Ultrasonic nozzles are less space-taking and more flexible in positioning inside the chamber. However, they can only deal with low-viscosity liquids due to their working mechanism. Their lower spraying capacity, while helping reduce deposition on the chamber wall, also means that they are not feasible for most industrial operations [4].

Mesh nebulizers also utilize ultrasounds. The difference is that the ultrasonic energy is transferred to a vibrating mesh instead of directly to the liquid feed. The feed is passed through the vibrating mesh and droplets are generated. Adjustment of droplet size can be

done by choosing the right size of (replaceable) mesh [30]. Mesh nebulizers have the same advantages as ultrasonic nozzles, but with an upper hand in dealing with suspensions.

1.2.2 Drying process

Water evaporation from the feed material ideally happens only in the drying chamber. Air and inert gases such as nitrogen and carbon dioxide are commonly used as the drying medium. Use of an inert gas is usually aimed at oxidation and explosion prevention [32]. High area-to-volume ratio of the material and high temperature difference make evaporation happen quickly as soon as droplets come in contact with drying gas. The gas becomes more humid and its temperature decreases due to evaporative cooling effect, which reduces the drying rate. Additional heating can be provided through the chamber wall to slow down the decrease in gas temperature, if necessary [13]. Typical temperature range of inlet gas is 150-220 °C, whereas at the chamber outlet it is 50-80 °C [7]. Choice of temperature depends on the material to be dried. Foods and pharmaceuticals are in general thermolabile and easily degraded by heat, thus requiring mild temperature. Gas temperature must also be kept not too high when drying materials with low glass transition temperature, in order to prevent sticking, caking, or lumping [7].

Drying chamber can be positioned vertically or horizontally, although the former is more common. Gas flow can be in co-current, counter-current, or mixed configuration with respect to the feed flow (see Fig. 1.1). Co-current means that the gas and the droplets flow in the same direction. The temperatures of gas and droplet at the chamber outlet will be between the initial droplet temperature and the inlet gas temperature. This configuration can be easily applied for both vertical and horizontal chambers. In counter-current configuration, droplets and gas flow in opposite direction. As a result, the sprayed droplets come in contact with cooler gas, whereas the particles are exposed to hotter gas. The overall energy consumption can thus be lower than in co-current flow. However, final particle temperature can possibly be higher than the outlet gas temperature. Additionally, the residence time is longer due to decelerating effect on the droplets. Thus, counter-current flow is less suitable for materials that are prone to thermal degradation. In a mixed flow configuration, droplets will initially flow against the gas before being dragged by the gas to the opposite direction. This leads to longer travel path and residence time. This configuration is suitable for materials that are harder to dry or need complete water removal [33]. Longer residence time found in counter-current and mixed configurations makes the application in horizontal chamber difficult, as the risk of particle deposition on chamber wall is higher.

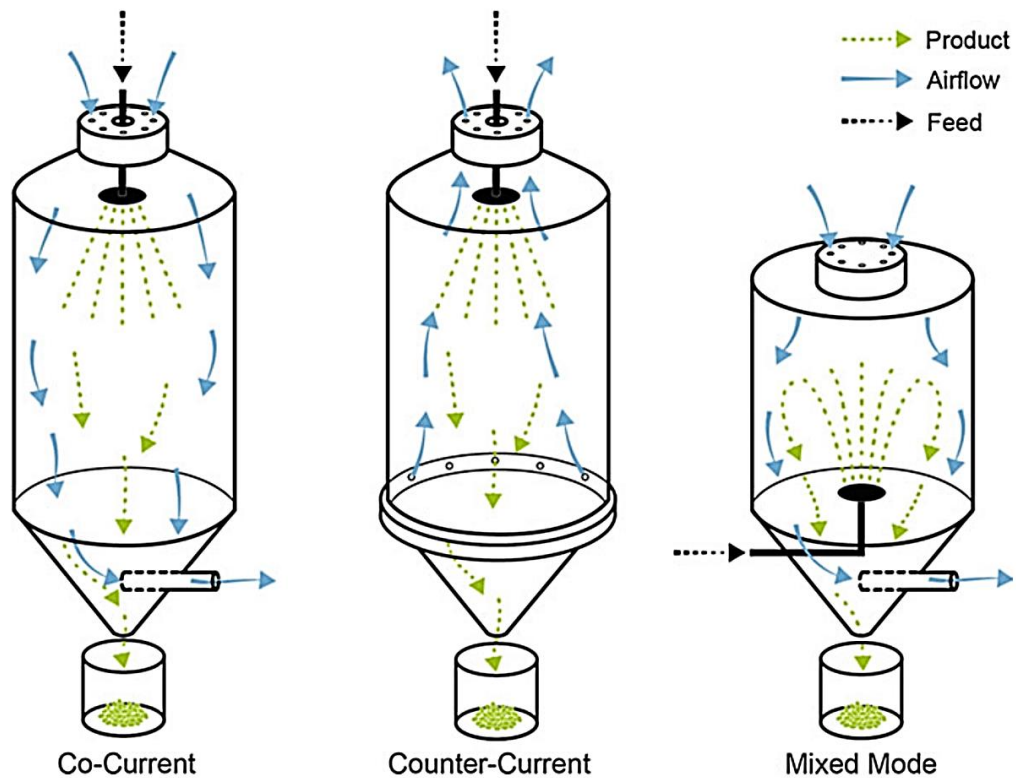


Fig. 1.1. Flow configurations in a vertical spray dryer (from [33], with permission).

1.2.3 Particle collection

The simplest particle collection method is based on filtration. The most common filtration-based particle collector is bag filters, which are filtration surfaces arranged in a housing in a way that total collecting surface can be greatly increased in a given space volume. Depending on the filter material used, fine particles down to submicron or even nano-scale can be collected. The main disadvantage of filtration-based particle collection is saturation of filtration surface by the collected product, which may lead to efficiency drop. As a result, the process must be stopped and the filtration unit must be replaced or cleaned regularly. Additionally, wear of filter material due to gas flow reduces the filtration efficiency over time.

Continuous particle collection can be done by using cyclones. A cyclone consists of a cylindrical part at the top (i.e., the barrel) and conical part at the bottom (the cone). Vortices are created inside the cyclone from the flow due to the cyclone shape. Gas (and particle) flow enters the cyclone from the top, tangentially to the barrel. The flow moves downwards in a helical path, creating the first (outer) vortex. Separation of entrained particles takes place due to centrifugal force, which causes the particles to strike the wall and fall to the bottom of the cyclone. When the flow reaches the cone, it moves upwards, creating the inner vortex. Cyclones are usually not efficient for particles smaller than 15 μm , as those are easily entrained by the inner vortex instead of falling to the collection outlet [2]. A combination of cyclone and filters is usually used to deal with this problem and improve the overall collection

performance [34]. A cyclone able to sample the particles based on their size class was developed by [35]. The mechanism takes advantage from the tendency of larger particles to stay further away from the vortex core in a cyclone. Bins are arranged coaxially at variant radial distances. Particles will fall to the bins according to their size: the large ones into the outer bins while the small ones into the central bins.

For collecting nano-sized particles more effectively, electrostatic particle collectors can be used [5]. The working principle is based on attractive electrostatic force between the particles and an electrode that acts as the collecting surface. On the opposite side of the collecting surface is a discharge electrode. Potential difference between the two electrodes generates an electric field between them. The nanoparticles are charged by negative ions generated in the gas. Very small particle size makes it easy for the electrostatic force to overcome gravity and pull the nanoparticles to the collecting surface. Influence of drag is limited by using laminar flow. Similar to bag filters, the collection capacity is limited by the area of the collecting surface. Furthermore, capacity may be too low for industrial-scale operations.

1.3 Advanced spray drying technologies

Combination of conventional spray drying with other techniques can be done to address the limitations and improve the process performance. Some modified spray drying technologies are briefly introduced here. Another advanced spray drying technique is PCD, which is the main focus of this dissertation and is discussed more specifically in the next section.

1.3.1 Dehumidified air spray drying

Drying can be made faster by using dehumidified air as the drying medium. As the drying capacity is higher, lower outlet temperature can be achieved. It helps deal with sticky materials [7] and reduces or totally eliminates the need for carrier substances [5]. Product recovery is reportedly higher than in conventional spray drying [36]. Products with smoother surface, better physicochemical properties and flowability can be obtained [5,36]. However, more energy is required due to the presence of the dehumidification system [37].

1.3.2 Vacuum spray drying

Creating vacuum in the drying chamber also makes the process faster and enables to use low temperatures. Superheated steam may be supplied using another nozzle to provide the latent heat [26]. A study reported higher retention of heat-sensitive compounds and encapsulation efficiency than in conventional spray drying for the production of essential oil microparticles [38]. The drawbacks of this technology are that it gives lower powder yield than conventional spray drying [39] and is relatively expensive [38]. Use of ultrasonic nozzle for vacuum spray drying has been reported to improve the particle yield of bovine serum albumin and the survival of probiotic cells [40].

1.3.3 Foam spray drying

In foam spray drying, the feed is foamed by injecting gas into the high-pressure feed line. Products with better solubility and dispersibility can be obtained in one step [41], without normally required additional steps such as agglomeration. The improved properties are attributed to many small, instead of single big, internal voids in the particles, which result from foaming [42]. The amount of voids and final particle size are positively influenced by the gas solubility in the liquid [43]. Foaming feed makes drying process more efficient. More regularly shaped particles can also be obtained [5].

1.3.4 Flame spray drying

In flame spray drying, liquid fuel is combusted directly in the droplet zone, providing the process energy. The fuel is in fact mixed and sprayed together with the feed solution into the chamber, before being ignited [5]. The modification required on a conventional spray dryer is relatively simple, mainly only the ignition unit. Typical fuels are ethanol, vegetable oils, and biofuels. Flame length and temperature vary with the fuel used [5,44]. Particle residence time is strongly influenced by the flame length. The challenges are keeping the flame stable and better controlling the process and final product quality [45]. This technology requires lower energy supply than conventional spray drying, as there are no heat losses in the supply line of drying gas [46]. A possible improvement in energy efficiency can be done by periodically supplying fuel in the spray mixture, resulting in intermittent combustion [5].

1.3.5 Nano spray drying

Nano spray drying differs from other spray drying technologies in the use of laminar gas flow and different nozzle and electrostatic particle collection technology [30]. Very fine droplets (submicron or smaller) are generated from a mesh nebulizer. The dried particles are charged by an electric field between two electrodes, and deposit on the surface of collecting electrode. Use of laminar flow eliminates the risk of wall deposition. The gentle nature of this technology makes it suitable for heat sensitive biological materials. For example, [47] studied production of protein powder from β -Galactosidase (with trehalose as stabilizer) using nano spray dryer. The disadvantages of nano spray drying include the low product throughput and the batch nature of the particle collection system [5].

1.4 Pulse combustion drying

As mentioned earlier, PCD utilizes flue gas flow produced by intermittent combustion in a pulse combustor. Periodic burning of fuel-air mixture and exhausting of flue gas generate acoustic waves inside the chamber. The resulting pulsed flow atomizes the feed and dries the material. When a lower drying gas temperature is required, adjustment can be done by introducing cooling air into the chamber [14].

The process is illustrated in Fig. 1.2. The steps are similar to those in a conventional spray dryer. Feed atomization is supported by the pulsating gas. This allows the use of a simple tube, instead of the more sophisticated atomizers presented earlier. It is fairly safe to say that in fact the feed tube plays little role in atomization, as most work is done by the flow. Tube diameter of about 6 mm, far bigger than in other spray nozzles, makes it possible to use highly viscous products and even granulates as the feed material [5,10]. The process hygiene is ensured by the clean combustion gas and very short contact time with the material [5]. Table 1.1 shows typical energy consumptions in various dryers. PCD has better energy efficiency than conventional spray drying and other drying techniques [48,49].

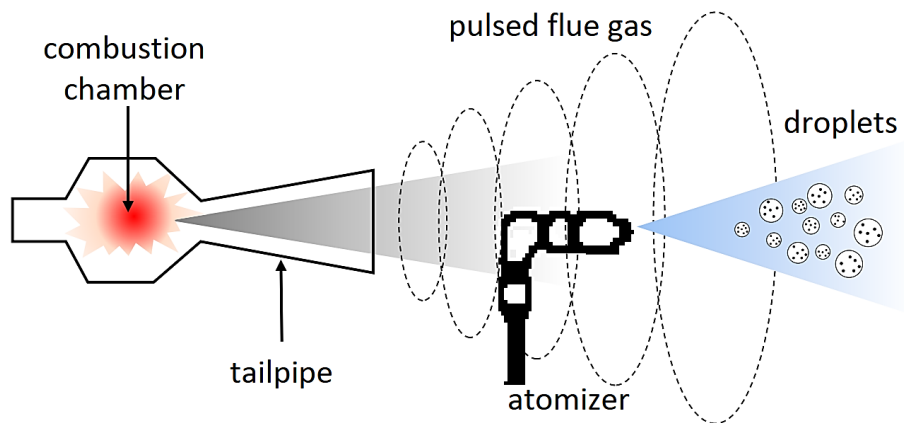


Fig. 1.2. An Illustration of use of flue gas from pulse combustion unit for drying of droplets.

Table 1.1. Typical energy consumption by various types of dryer (adapted from [49], with permission).

Dryer	Energy consumption (in kJ) per kg H ₂ O evaporated
Tunnel dryer	5500-6000
Band dryer	4000-6000
Impingement dryer	5000-7000
Rotary dryer	4600-9200
Fluidized bed dryer	4000-6000
Flash dryer	4500-9000
Spray dryer	4500-11500
Pulse combustion dryer	3000-3500

1.4.1 Pulse combustion

The main components of pulse combustor are fuel and air inlets, a combustion chamber, and a tailpipe. Based on chamber geometry and working mechanism, pulse combustors are classified into Helmholtz, Schmidt, and Rijke types [10]. The first is the most widely used in

industry. It is based on the principle of Helmholtz acoustic resonator. Fuel-air intake system can be either valved or valveless [10,15,49]. Types of valves used are flapper, reed and rotary. The valves open and close automatically due to pressure oscillation inside the combustion chamber. A valveless pulse combustor on the other hand utilizes fluid mechanics effects to prevent combustion products from going out through the air-fuel inlets. Schematics of valve types and valveless combustor are presented in Fig. 1.3.

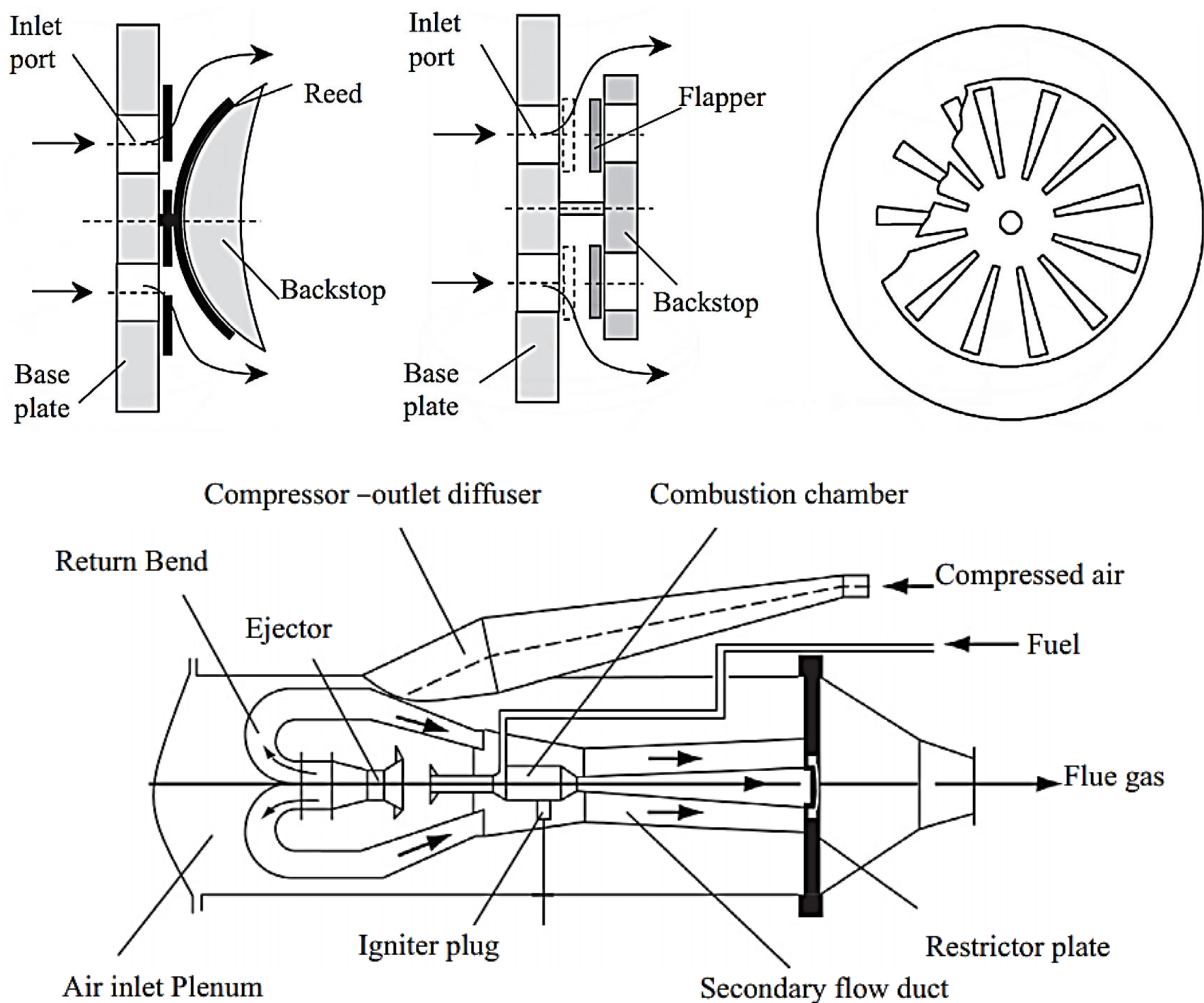


Fig. 1.3. Schematics of valves used in a pulse combustor, from left to right: reed, flapper, and rotary (*top*), and a valveless pulse combustor (*bottom*) (from [10,49], with permissions).

Figure 1.4 shows the cycle of pulse combustion, which is as follows:

- A. Air and fuel enter the combustion chamber.
- B. Fresh charge ignited, pressure rises as combustion gases heat up, air and fuel valves are pushed back.
- C. Combustion is completed, flue gases are vented (to the drying chamber).
- D. Momentum of exhausting gases creates negative pressure in combustion chamber; valves are open again.

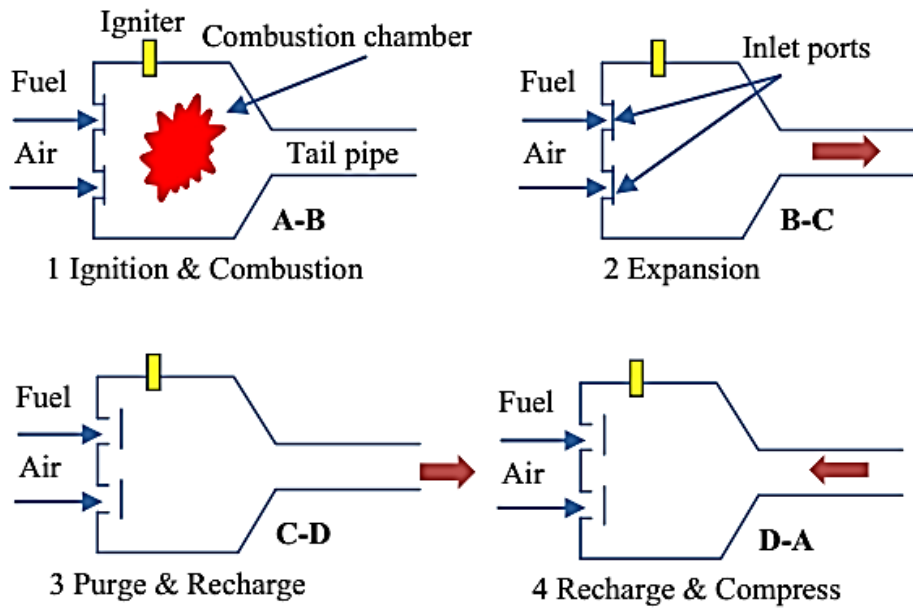


Fig. 1.4. A cycle of pulse combustion in a Helmholtz-type combustor (from [10], with permission).

High efficiency of combustion, which lowers the oxygen level in the hot reactor zone, is achieved at higher pressure amplitude and frequency [50]. However, it potentially also lowers the temperature inside the combustor, which is not desired. The goal is thus to have as high as possible reactor temperature while keeping the oxygen level inside the reactor as low as possible. Surplus of fuel is usually required to drive gas oscillation [51]. When the temperature of combustion chamber is too high (e.g., 1200 K), reactions are too fast and there is not enough surplus. As the result, the oscillation dies out. Timing of returning flow is critical to reaction acceleration. At low flow time (fast fuel input), combustion rate is low compared to mixing time and as a result the flame dimes out. At longer flow time, combustion time is longer due to lower fuel input rate. Mixing thus becomes a limiting factor. The most stable and efficient condition is achieved when the frequencies in the combustor and in the pipe are in resonance [50].

Concentrations of species emitted from the combustion chamber are heavily influenced by the temperature and velocity of the exhaust gas mixture [52]. Nusselt number in tailpipe is a strong function of pulsation frequency [53]. Dec and Keller found from their experiments that pressure oscillation is related to velocity oscillation, with linear acoustic behavior assumed [54]. The ratio of velocity amplitude to average velocity is more important than the average velocity in enhancing heat transfer [53]. Intensification of heat transfer is positively correlated with the ratio of velocity amplitude to mean velocity. Numerical modeling and simulation of turbulent flow in pulse combustor tailpipe has been carried out using computational fluid dynamics (CFD) by [55] and the results were experimentally validated. Length of tailpipe was varied to change the natural resonance frequency of pulsation and see its effect on heat transfer. Frequency, however, could not be separated from pressure oscillation due to natural resonance of the tailpipe. Increasing frequency can either reduce or increase pressure

oscillation. Thus, to isolate the effect of frequency is practically impossible. For a given frequency heat transfer increases with amplitude, while for a given amplitude an increase in frequency enhances heat transfer (i.e., both have a positive effect). In their experiments, an increase in pressure oscillation in the combustion chamber led to an increase in gas velocity amplitude. A decrease in pressure oscillation, however, caused the average velocity to increase.

Table 1.2 presents some characteristics of pulse combustion compared to steady continuous combustion. Pulse combustion offers higher combustion efficiency and intensity, leading to more efficient fuel consumption, higher transfer coefficients, cleaner flue gases produced [49]. Lower production of CO and NO_x has been mainly attributed to shorter exposure time to high temperature caused by the intermittent combustion and the mixing of hot combustion gases with backflow from the tailpipe and new reactants coming into the combustion chamber. Production of the pollutants can be decreased by increasing pulsation frequency, using a bigger combustion chamber and a longer tailpipe, and by optimizing air-fuel ratio [10]. Another advantage of pulse combustion is that it usually requires relatively small space compared to a steady state combustion [49].

Table 1.2. Comparison between steady-state combustion and pulse combustion (adapted from [49], with permission).

Parameters	Steady-state combustion	Pulse combustion
Combustion intensity (kW/m ³)	100-1,000	10,000-50,000
Burning efficiency (%)	80-96	90-96
Concentration in exhaust		
CO (%)	0-2	0-1
NO _x (mg/m ³)	100-7000	20-70
Convective heat transfer coefficient (W/(m ² .K))	50-100	100-500
Noise (dB)	85-100	110-180

The main problem associated with pulse combustion is the noise it generates, which mainly comes from the detonating nature of pulse combustion and the vibration of the equipment resulting from the oscillating flow and pressure. Fluctuating gas velocity difference inside and outside the chamber also contributes to the noise to some extent. Since operating conditions are less compromisable as they are related to process requirements, noise reduction strategies are usually carried out by optimizing the design of unit components. Some examples are by applying acoustic insulation, increasing the tailpipe length, using acoustic decouplers, shielding the space between ejector, inlet and outlet, and using sound-adsorptive materials [10,49]. Types of fuel used on the other hand have been shown to have a negligible effect on

the noise production [56]. Another problem that might occur is entrapment of dried products inside the chamber due to the pulsated flow. Deposition of powder near the air inlet was reported in some studies [10,49]. Positioning of nozzle and gas inlet as well as the drying chamber design must be optimized to avoid dead zones.

1.4.2 Applications and researches

Table 1.3 lists some publicly available patents on industrial application of PCD and their respective processed materials. Other patents on equipment design for universal use are not presented here. More than the listed companies have been active in this field. Application of PCD in industrial scale began about 40 years ago [49]. Ocean Proteins Inc. developed in 1980 a PCD for fish meal using valveless pulsed combustor and horizontal drying chamber. One year later Tektronix Inc. used a similar design for electro-chemical wastes. Sonodyne Industries Inc. built a mobile PCD device for various materials covering foodstuffs and industrial wastes in 1984. In 1985 Nuclear Metals Inc. used PCD for dealing with nuclear waste in form of radioactive-depleted uranium oxide. Novodyne Ltd. in Canada concentrates on the application for wood materials [57]. Berghausen Corporation (Cincinnati, USA) began developing a PCD technology for food additives and flavorings in 2003. Few years later Canaan Fertilizers in South Africa used PCD for producing fertilizer powder from chemical plant byproducts, and Altair Nanotechnology (Nevada, USA) used the technology for producing nano-sized fine chemicals [11]. More recently, EKONEK from Spain developed their own PCD that is specialized for high dry matter and viscosity pastes of various materials. Most companies reported better product quality, process efficiency, and versatility than obtained by conventional spray dryers.

Table 1.3. Some patents of industrial applications of PCD.

Assignee	Patent No.	Year	Materials
Jetsonic Processors, Ltd.	US 4,395,830	1983	food materials
Pulse Drying Systems, Inc.	US 4,637,794	1987	particulates
National Starch & Chemical Company, Plainfield, NJ	US 4,859,248	1989	starches
Hosokawa Bepex Corporation	US 5,252,061 A	1993	ceramics, food seasonings & additives, pharmaceutical, dairy products, polymers, agrochemicals, pigments
Osaka Fuji Kogyo	US 5,881,475 A	1997	human wastes
Manufacturing and Technology Conversion International, Inc.	US 2005/0050759 A1	2005	biomass
Pulse Holdings LLC	US 2018/0127458	2018	heat-sensitive protein-based products
Hart Associates SARL	EP 3 109 546 B1	2018	wet feedstocks

Applications with various materials are also investigated in some studies. Buchkowski & Kitchen used PCD for wet wood waste [58]. The moisture mass fraction was successfully reduced from 60% to 10%. They argued that drying enhancement is due to reduced boundary layer thickness. Kudra et al. conducted research by using white pine as the feed material [59]. Patterson et al. applied PCD for thick-grade paper [60]. The enhancement effects were found to depend on combustor configuration, nozzle geometry, supporting material, and chamber pressure. Wang et al. reported higher dissolution rate of nitrendipine powder obtained from PCD [61], which is attributed to improved hydrophilicity and dispersibility. Similar observations were made by Xu et al. when producing ibuprofen with Kollidon carriers of different grades [62]. Wu et al. used Helmholtz-type pulse combustor to dry pasty sewage sludge [63]. The tailpipe also served as the drying chamber, and the material was simply fed through an orifice plate. A better performance compared to convective and microwave drying was obtained. They also studied the production of white egg powder using a pilot-scale PCD [14]. The product particles were smaller with more uniform size distributions compared to those obtained using spray drying. Moreover, they had better color, foaming and gelling properties. San Martin et al. recently employed PCD in the production of animal feed from food waste [64].

Some researches were focused on getting a better understanding of the phenomena happening during PCD. Jayadev in 1984 conducted performance and cost analyses on PCD, reporting extremely high fuel efficiency, clean gas, and lower operational cost [65]. Olzer performed numerical simulations of the flow in the vicinity of a sphere [66]. He found that boundary layer become thinner when the flow is oscillating. CFD simulations conducted by Strumillo et al. showed that oscillations of velocity, pressure and temperature become weaker along the distance from the chamber inlet, with temperature being the fastest to decline [67]. Kuts and co. conducted a series of numerical studies on the interaction between the oscillating flow and the discrete phase, and the mechanisms of process intensification. They first investigated the gas dynamics in the combustion chamber [18]. They followed by studying the movement of spherical solid particles in pulsed gas flow and the resulting improvement of heat and mass transfer [19]. A twofold increase in heat transfer coefficient was found, and this was attributed to the high relative velocity between the two phases.

Okuyama and co. produced nano- and submicron-sized metal oxide particles via drying and pyrolysis in PCD [13,16]. The pulse combustor generated flow in the temperature range of 300-350 °C using propane as the fuel. Additional heating through the chamber wall was possible, with a variation of wall temperature from 300 to 600 °C. Normal spray drying operation at 500 °C could only yield submicron-sized zinc oxide particles, whereas with PCD highly crystalline spherical nanoparticles were always obtained regardless of the temperature used [13]. Higher temperatures in PCD contributed positively to crystal growth and final particle size. Some experiments were also carried out for Gadolinium(III) oxide, but with a higher maximum temperature of 800 °C. At this temperature, nanoparticles were not detected, and the obtained particles were nonspherical. The particles obtained with spray drying, while having larger sizes, are in polycrystalline form with smaller crystal size compared to those

produced using PCD. Investigations on the influence of feed rate on the obtained particle size were also performed [16]. A two-fluid nozzle was used. Lower feed flow rates resulted in larger particles that are partially agglomerated. This is interesting, as sprayed droplets are normally smaller when the feed rate is low. Higher flow rate gives smaller ZnO particles with lower crystallinity. They argued that when droplets enter the higher region of the heated zone evaporation is more rapid, which leads to better crystal growth followed by further droplet fragmentation and drying into finer particles.

An experimental study on the influence of atomizing and flow parameters on droplet size was conducted by Xiao et al. [12]. A simple feed tube with a diameter of 14 mm and length of 40 mm was used and placed near the tailpipe of a pulse combustor. Droplet atomization is thus governed by how the liquid stream interacts with the pulsating gas flow from the tailpipe. In the range of pulsation frequency employed (61-100 Hz), an increase in pulsation frequency led to narrower droplet size distributions and smaller average sizes. The influence on the lower limit of droplet size, however, was limited. Pressure at the end of the tailpipe (1 m in length) was reported to oscillate between 93.7 and 114.8 kPa. Amplitude and mean velocity were reported at ± 100 and 26.8 m/s, respectively. No explanation is given on whether and how these values were affected when the pulsation frequency was altered.

Teiwes et al. numerically investigated solid particle dynamics in hot pulsating gas [68]. A vertical chamber with upward flow was simulated. Pulsation frequency, velocity amplitude, and particle size were varied. It was found that when the inlet flow frequency is in resonance with the chamber volume (at 160 Hz), the response amplitudes of pressure oscillation will go beyond the excitation amplitudes. Otherwise, the response amplitudes are always lower. An increase in pulsation frequency also makes the particle spout narrower. The spout is also narrower when the average particle size is smaller. Pulsation thus leads to less wall deposition and higher particle yield. Grouping of particles was also observed when the flow is pulsed. The number of groups over the chamber length increases with pulsation frequency and particle size, but decreases when the pulsation amplitude is increased. Interestingly, although they found that heat transfer can be enhanced by pulsation, the difference in the enhancement effects obtained at the lowest (40 Hz) and the highest (160 Hz) frequencies is negligible. Frequency also has a negligible influence on the mean particle residence time. However, the shape of the density distribution for particle residence time is influenced by gas pulsation. The distribution becomes more bimodal with higher velocity amplitude and lower pulsation frequency. It was found that, when the velocity amplitude is lower than average flow velocity, mean residence times are longer than in stationary flow. The opposite happens when the velocity amplitude is higher than the average velocity. The distribution also becomes wider and the average residence time becomes longer with larger particle size.

1.5 Outline of dissertation

This dissertation consists of five main chapters. It is organized as follows.

Chapter 2: A single droplet drying model is presented. Due to small droplet size and low Biot number, uniform temperature in the liquid droplet is assumed. The model captures the dynamic change in solute concentration profile in a droplet, with two stages of drying resulting from formation of dry crust at droplet surface. Ranz-Marshall correlations with Spalding correction are used to calculate the heat and mass transfer coefficients between the droplet and the surrounding gas. Interaction between the droplets and the surrounding gas also results in the dynamic movement of the droplet, which is calculated from the drag force. The model acts as the basis and departing point for the models introduced in the following chapters.

Chapter 3: Breakup of droplets into smaller ones in pulsating flow is discussed. Taylor analogy breakup (TAB) model is used. A new variable named modified surface tension is defined from the difference between Laplace pressure and osmotic pressure of a colloidal droplet. The osmotic pressure is calculated by considering interparticle forces governed by the DLVO theory. Influence of operating conditions and process phenomena on droplet movement and breakup time is investigated. The model is used to evaluate published experimental data, to elucidate whether and to which extent droplet breakup plays a role in finer particle formation.

Chapter 4: An experimental study using a pilot scale dryer is reported. Three different materials are used. Air temperature and pulsation frequency have been varied to investigate the influence of operating conditions on particle morphology and size distributions, which are obtained by analyzing scanning electron microscopy (SEM) images.

Chapter 5: Based on the experimental results in Chapter 4, a mechanism of fine particle production by means of repetitive breakage of solid crust is proposed. A model is developed by assuming two possible crust breakage mechanisms. Taking into account possible debris particle formation, some predetermined variables are introduced. The simulation results are evaluated by analyzing the statistical differences with the experimental data.

Chapter 6: Drying intensification in pulsating gas flow and possible product deterioration that goes along with it are investigated. Whey protein isolate (WPI) is selected as the material. An experimentally-derived kinetic model of whey protein inactivation (denaturation) is used with the drying model. Influence of process parameters on process dynamic, final product quality, and energy use is discussed. Lastly, an evaluation is made on how gas pulsation could be a good strategy for intensifying the drying process in respect to product quality.

Chapter 7: The conclusions are summarized and an outlook for future research is given.

2. Model of single droplet drying in pulsated flow

This chapter discusses an in-house single droplet drying model, which serves as the basis for the models discussed in Chapters 4, 6, and 7. Within the framework of this dissertation, the model has also been presented in following publications:

1. *“A model of pulse combustion drying and breakup of colloidal suspension droplets”, published in Powder Technology [69].*
2. *“Crust breakage in production of fine particles using pulse combustion drying: Experimental and numerical investigations”, published in Powder Technology [70].*
3. *“Droplet drying and whey protein denaturation in pulsed gas flow - A modeling study”, published in Journal of Food Engineering [71].*

In this chapter, a single droplet drying model that has been developed previously by our group is presented. It serves as the core with which the models introduced later in this dissertation are coupled. The drying model has been validated for colloidal suspensions [72,73] and solutions [74]. Sub-models depicting phenomena such as agglomeration of primary particles in a colloidal droplet [72] and inflation-deflation [74] have been used in combination with the droplet drying model.

2.1 Previous modeling works in droplet drying

The efforts to model the drying of single solid-containing droplets dates back to 1960, when Charlesworth and Marshall developed a model based on their experiment using a droplet suspended on a glass wire [75]. Droplet diameter was taken as constant throughout the time. The droplet then virtually received solute through the surface to match the phenomena observed in the experiment, and the rate of solute penetration was fitted to experimental data. Heat and mass transfer between the droplet and the drying gas, however, was not considered.

The first model that considered solid concentration profile was that of Sano and Keey [76]. Fickian diffusion was used to predict the change in spatial moisture content. Temperature distribution in the droplet was neglected for the 1st (constant rate) and the 2nd (falling rate) drying stages, but the change in average temperature in time was accounted for. Since the model was developed to explain experimental data of milk drying, single inflation-deflation events were taken into account. Two possibilities were proposed. In the 1st scheme, the droplet inflates to a maximum radius (determined from experiment) and stays there (i.e., no following deflation). A void volume is created by inflation and becomes larger due to further

water evaporation. In the 2nd, the outer skin shrinks after reaching the maximum radius, while the void volume radius remains the same.

Drying of a slurry droplet was modeled by Cheong et al. in 1986 [77]. The process is divided into two stages separated by crust formation at the surface. Evaporation occurs only at the receding interface between the crust and the liquid core. Heat transfer from the gas is convective, while through the crust it is solely by conduction. Concentration and temperature gradients in the liquid core were neglected, whereas in the crust linear profiles were assumed. A significant inaccuracy when validated with experimental data was found, which was attributed to the assumptions taken.

Abuaf and Stauf (1985) considered the influence of Stefan-flow through the crust in their model [78]. Evaporation rate was obtained by multiplying vapor flux with crust porosity. Temperature distribution is totally neglected. Borde and Zlotnitsky (1991) [79] in their model assumed a droplet with insoluble solids as a pseudo porous body. There was no separation between constant rate and falling rate drying. Similar calculation method to [78] was used for evaporation rate. However, temperature profile in the crust and the respective dependences of heat capacity and vapor diffusion coefficient were considered. Levi-Hevroni et al. (1995) [80] improved the model and used it to simulate the situation in a drying chamber, in which temperature changes along the length. Modification was made to the thermal conductivity determination, as crust morphology was taken into account. An uncommon approach was proposed by Elperin and Krasovtsov (1995) [81], who used solid-to-liquid volume ratio to express solid concentration. Temperature profile in liquid core was neglected, whereas for heat and mass transfer in the crust and surrounding drying medium a set of partial differential equations were formulated. Evaporation rate was calculated using the equation from [78]. These four models [78–81] were not validated with experiments.

Nešić and Vodnik developed in 1991 a model for a droplet containing soluble or insoluble solids [73]. Temperature profiles were neglected, whereas Fickian diffusion was considered for the solids. The diffusion coefficient was given as a function of concentration only. The influence of Stefan flow in the crust was neglected. Validation was carried out using experimental data for colloidal silica, sodium sulphate, and skim milk. Good agreement was found, except for milk droplet temperature. Farid also made in 2003 an effort to develop a general model [82]. However, in contrast to Nešić and Vodnik, while temperature distribution inside the droplet was taken into account, solid concentration gradient was not. Energy balance on droplet surface was used to calculate the time required to form a thin crust (layer) of particles that start the 2nd drying stage. A similar assumption as in [83] was made for the temperature at the liquid core-crust interface. Furthermore, the resistance on heat and mass transfer due to crust was neglected, which led to a significant inaccuracy during the 2nd drying stage.

Furuta et al. (1994) developed a semi empirical model for drying of food liquid [84]. Concentration profiles during constant and falling rate drying stages were calculated. Evaporation rate was determined from experimental data. A similar approach was used by

Kuts et al. (1996) [83]. They argued that moisture content can be either linearly or exponentially dependent on time, and proposed two equations for drying time. While in the 1st drying stage temperature profile is neglected, moisture and temperature profiles in both liquid core and crust after locking point were calculated. However, adiabatic saturation temperature was taken as the liquid-crust interface temperature; something that is usually valid only during constant rate drying stage.

As mentioned earlier when discussing the model by Sano and Keey [76], in the drying of organic sticky material inflation-deflation phenomena might occur during the falling-rate drying stage. Most efforts to model this process have been empirical. In a one-dimensional plug-flow model of a counter-current spray drying tower developed by Ali et al. [85], it was assumed that the droplets inflate to their initial diameters after the locking point. Surface drying time and drying rate were calculated using empirical equations. Tran et al. [74] observed inflation-deflation phenomena during the drying of a skim milk droplet when the drying gas temperature was above the boiling point. They used an error function to calculate inflated/deflated particle diameter as a post processing variable. During the inflation-deflation stage, it was assumed that the influence of crust on heat and mass transfer can be eliminated.

Handscomb [86–88] combined population balance model with single droplet drying model to investigate the influence of solute and suspended solids on final particle morphology. Mixture of solute and solvent is treated as the continuous phase, with evolving composition due to crystallization (into suspended solid, i.e., discrete phase) and evaporation. Consequently, solute concentration gradient leads not only to back-diffusion, but also advection due to concentration gradient of the continuous phase. Repetitive buckling of the saturated layer happens as long as it is not strong enough to withstand the pressure working on it. Unlike in [89], the strength is a critical buckling pressure, which is a function of Young's modulus and Poisson's ratio, whereas capillary pressure is the only disturbing pressure. Two models were used for the second drying stage: dry skin and wet skin. In the first model, the drying front recedes from droplet surface towards the center, thus creating a dry crust through which evaporated water diffuses to the surrounding air. In the wet shell scheme, a bubble of saturated air is formed in droplet center after the surface has been saturated. The interface between the bubble and the liquid serves as the drying front. Evaporation makes the bubble grow and the interface moves outwards. Colloidal primary particles are pushed towards the droplet surface, which leads to thickening of the saturated layer. After the layer (wet skin) has been totally saturated and the primary particles cannot be pushed further, evaporation front moves to the surface and the process continues as in the first scheme.

Sadafi et al. observed the drying phenomena of a NaCl solution droplet suspended on a wire, and developed a model for it [90]. They found that crust forms gradually from the bottom to the top of droplet surface, instead of enveloping the whole droplet surface, after a critical point has been reached. The critical point here is the mass fraction of solid at which crust formation starts, which was determined visually. The stage during which crust forms at the bottom until it fully envelops the surface is regarded as the transition period. Thus,

computationally critical surface concentration is the concentration at which the transition stage ends, as opposed to its start that is usually defined in other studies [89,91–93].

Wang and Langrish developed a distributed-parameter model for drying of droplets containing more than one solute species [94]. Precipitation of solutes is considered, although its effect on the process is not elaborated. While there is more than one solute species, diffusivity of one species is not influenced by the others. The approach was adopted by Parienta et al. to model exhaled respiratory droplets of mixed composition [95]. Further improvement to the distributed-parameter model was done by Gac and Gradon [96] by taking into account solute solubility and crystallization kinetics in crust formation. Abdullahi et al. [97] similarly modelled drying of a droplet containing two solute species with different primary particle size distributions. Determination of locking point is based on a critical porosity, which is an empirical function of the width of the size distribution of the solute particles. Effective diffusivity of individual species is correlated to binary diffusivity of the dominant solute in the solvent.

The previously mentioned models put emphasis on accurate theoretical depiction of physical phenomena occurring during drying. Another possibility is to use semi-empirical models, in which the main transport equations are combined with empirical equations that are obtained by fitting to drying kinetics data. The empirical equations here are directly connected to and describe the process kinetics, instead of merely used for transfer coefficients and material properties. Typical semi-empirical drying models are the characteristic drying curve (CDC) model and the reaction engineering approach (REA) model.

The concept of characteristic drying curve was introduced by van Meel in 1958 in his study on batch convective drying [98]. He argued that a single characteristic drying curve can be obtained for one material undergoing convective drying. The curve is depicted in Fig. 2.1. The key parameters here are characteristic moisture content,

$$\Phi = \frac{X - X_{eq}}{X_{cr} - X_{eq}}, \quad (2.1)$$

where X_{cr} is the critical moisture content at which the drying rate starts to fall and X_{eq} the equilibrium moisture content (from sorption isotherm); and normalized drying rate,

$$\xi = \frac{\text{instantaneous drying rate}}{\text{drying rate in the 1}^{st} \text{ stage}}. \quad (2.2)$$

As seen in Fig. 2.1, ξ is a function of Φ in the 2nd drying stage, which depends on the nature of the material. The function is empirically determined by fitting to available experimental data. The type of function can be chosen arbitrarily. ξ thus serves as a factor in calculation of drying rate during the 2nd stage from that in the 1st stage (e.g., Eq. 2.9).

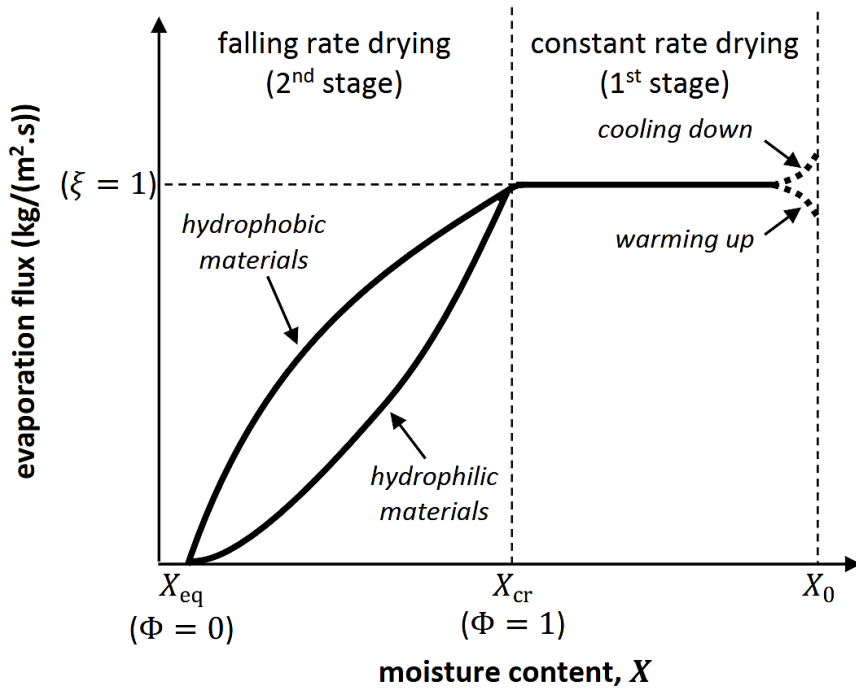


Fig. 2.1. Characteristic drying curve (adapted from [99], with permission).

The reaction engineering approach (REA) for drying was proposed by Chen [99,100]. In this approach, droplet temperature distribution is neglected. The model is based on the idea that surface relative humidity, average moisture content, and temperature of droplet (or any other drying object) are uniquely related. Furthermore, evaporation is considered analogous to an activation process during which an energy barrier must be overcome. Surface relative humidity is related to object temperature in an Arrhenius type equation, which is often found in chemical reaction kinetics; giving the name to the model:

$$RH_{\text{surf}} = \exp\left(-\frac{E_{a,v}}{R T_d}\right). \quad (2.3)$$

The activation energy $E_{a,v}$ is taken as a function of moisture content. When the surface is fully covered by liquid ($RH_{\text{surf}} \rightarrow 1$), $E_{a,v}$ goes to zero, indicating that there is less resistance to evaporation. As moisture content decreases due to evaporation, relative humidity at the surface decreases as it becomes more dominated by solid. The activation energy thus increases, and there is more resistance to the evaporation process. Similarly, saturation vapor concentration is expressed as

$$Y_{\text{sat}} = K_v \exp\left(-\frac{h_{\text{evap}}}{R T_d}\right), \quad (2.4)$$

with h_{evap} denoting the latent heat of evaporation and K_v being a constant termed as apparent reaction frequency. Substituting the equations into a drying rate equation, direct fitting to experimental data can be done to obtain $E_{a,v}$. This approach eliminates the need to

determine critical moisture content and gives a smooth transition between the 1st and the 2nd drying stages [99].

Recent advances in computational fluid dynamics (CFD) show that flow dynamics and heat and mass transfer between droplets and the flow can be satisfactorily calculated. However, studies on energy optimization and control of final product quality are still limited [5]. The semi-empirical models mentioned above are simpler and less computationally demanding than mechanistic models. This makes them easier to incorporate into robust CFD simulations. For example, Tran et al. used CDC model in CFD simulations of skim milk drying [101]. Woo et al. compared the performances of REA and CDC models when incorporated into CFD [102]. Although similar flow and product properties at the outlet were obtained, different responses to initial solid concentration were found.

The simplicity of semi-empirical models also gives room for additional processes to be calculated simultaneously in CFD. For example, REA and lysine degradation kinetics were used in CFD simulations to predict drying and loss of lysine by Schmitz-Schug et al. [103]. The kinetics of lysine loss was modeled using pseudo-second order reactions [104]. Validation was carried out by comparing the moisture content and lysine loss of the product as well as the outlet gas properties. Jaskulski et al. [105], on the other hand, used CDC model along with a protein denaturation model [106] for CFD simulations and validated the results with experiments. Higher whey protein activity is observed at higher feed rates, which is attributed to lower temperature fields in the drying chamber. Habtegebriel et al. [107] used a more simplified approach by totally neglecting the reduction of drying rate due to surface saturation and crust formation. A boiling rate equation is used instead, once the boiling point has been reached. The model overestimated the final particle temperature at high drying temperatures. Interestingly, they found that loss in camel milk casein is more drying temperature-dependent than loss of whey proteins.

2.2 1st drying stage

When a droplet is released from a spray nozzle and comes in contact with the drying gas, heat is transferred from the gas to the droplet due to their temperature difference. The droplet temperature starts to increase and water will evaporate due to the difference in vapor pressure at droplet surface and in the bulk gas. Although the temperature difference between the droplet surface and bulk hot air is high, for the small spherical droplets of a spray the temperature gradient in the droplet during the 1st drying period is negligible due to the low Biot number; this has been shown numerically and experimentally [108]. Neglecting heat loss, the droplet energy balance is given by

$$\dot{Q} = \dot{Q}_{\text{latent}} + \dot{Q}_{\text{sensible}}, \quad (2.5)$$

$$k_h 4\pi R_{1c}^2 (T_g - T_d) = h_{\text{evap}} \frac{dm_w}{dt} + (m_s c_{p,s} + m_w c_{p,w}) \frac{dT_d}{dt}. \quad (2.6)$$

2 Model of single droplet drying in pulsated flow

In the above equation k_h is the overall heat transfer coefficient, R_{lc} the liquid core radius (equal to the droplet radius R_d during the first drying stage), T_g the gas temperature, and $c_{p,s}$ and $c_{p,w}$ the specific heat capacities of solid and water, respectively. Rearranging the equation, the change in droplet core temperature can be obtained:

$$\frac{dT_d}{dt} = \frac{k_h 4\pi R_{lc}^2 (T_g - T_d) - h_{\text{evap}} \frac{dm_w}{dt}}{m_s c_{p,s} + m_w c_{p,w}}. \quad (2.7)$$

The evaporation enthalpy h_{evap} can be calculated with 0 °C as the benchmark,

$$h_{\text{evap}} = -c_{p,w}(T_d - 273.15) + h_{lv} + c_{p,v}(T_g - 273.15), \quad (2.8)$$

with $c_{p,v}$ specific heat capacity of water vapor and h_{lv} latent heat of water evaporation at 0 °C. In this sense, water is first cooled down to 0 °C (273.15 K), evaporates at the reference temperature, and the vapor is then heated to the gas temperature.

It is assumed that the droplet maintains its spherical shape during the whole drying process. In the first drying stage, the droplet shrinks due to water evaporation. The rate at which water evaporates from the droplet is given by

$$\frac{dm_w}{dt} = k_m \rho_g 4\pi R_{lc}^2 (Y_{g,s} - Y_{g,\infty}), \quad (2.9)$$

with k_m the mass transfer coefficient of water vapor in gas, $Y_{g,s}$ the moisture content of air at droplet surface, $Y_{g,\infty}$ the moisture content in the bulk of gas phase, and ρ_g the density of gas phase in the bulk.

For solutions containing molecules instead of the colloidal particles in suspensions, the concentration of solid at the droplet surface can influence the evaporation rate via surface water activity a_w ,

$$\frac{dm_w}{dt} = k_m \rho_g a_w 4\pi R_{lc}^2 (Y_{g,s} - Y_{g,\infty}). \quad (2.10)$$

Evaporation rate is set to zero when an equilibrium moisture content is reached. The latter can be calculated using a modified SPS sorption isotherm model [109] to

$$X_{\text{eq}} = A \exp\left(-B (T_d - 273.15) \ln\left(\frac{Y_{g,\text{sat}}}{Y_{g,\infty}}\right)\right), \quad (2.11)$$

with A and B solid material-dependent constants. For a solution of water and small solute molecules such as salts, water activity can be taken as the molar fraction of water in the solution. For solutions containing large molecules such as proteins, it can be estimated using Flory-Huggins theory [110],

$$a_w = \exp(\phi_s + \ln \phi_w). \quad (2.12)$$

In the above equation ϕ_s and ϕ_w are the volume fractions of solute and water, respectively.

From Eq. 2.9, the rate of droplet shrinkage is thus

$$\frac{dR_{lc}}{dt} = -k_m \frac{\rho_g}{\rho_w} (Y_{g,s} - Y_{g,\infty}). \quad (2.13)$$

During the first drying stage after the preheating period, the droplet temperature will stay at the adiabatic saturation temperature and the moisture content at the droplet surface is the adiabatic saturation moisture content ($Y_{g,s} = Y_{g,sat}$). The saturation moisture content is

$$Y_{g,sat} = 0.622 \frac{p_{sat}}{p - p_{sat}}. \quad (2.14)$$

The saturation pressure p_{sat} can be calculated from the Antoine equation for water:

$$p_{sat} = \exp\left(A - \frac{B}{C + (T_g - 273.15)}\right), \quad (2.15)$$

with $A = 23.4588$, $B = 3977.3782 \text{ K}^{-1}$, and $C = 233.3172 \text{ K}$.

Evaporation of water not only reduces the droplet size, but also results in solid concentration profiles. On the surface, evaporation causes an increase in local solid concentration. The gradient of concentration then causes the so-called back-diffusion, where the solid particles diffuse to the center of the droplet. Assuming diffusion to occur only in radial direction r , the change in concentration profile can be described as

$$\frac{\partial C_s}{\partial t} = \frac{1}{r^2} \frac{\partial}{\partial r} \left(r^2 \delta_{w,s} \frac{\partial C_s}{\partial r} \right), \quad (2.16)$$

in which $\delta_{w,s}$ is the binary diffusion coefficient of nanoparticles or solute molecules and water, and C_s is the mass of solid per suspension volume. The initial and boundary conditions for the diffusion equation are derived by considering the symmetry in radial direction and solid mass conservation:

$$r = 0: \quad \frac{\partial C_s}{\partial r} = 0, \quad (2.17)$$

$$r = R_{lc}: \quad C_s \frac{\partial R_{lc}}{\partial t} - \delta_{w,s} \frac{\partial C_s}{\partial r} = \rho_s (1 - \varepsilon_{cr}) \frac{\partial R_{lc}}{\partial t}, \quad (2.18)$$

$$t = 0: \quad C_s = C_0. \quad (2.19)$$

The right-hand side of Eq. 2.18 expresses the solid mass that is given away from the liquid core to the dry crust formed after the process has continued to the second drying stage. ε_{cr} denotes the porosity of the crust. Before the second drying stage, there is no crust and $\varepsilon_{cr} = 1$.

2 Model of single droplet drying in pulsated flow

The diffusion coefficient of nanoparticles in water is calculated using the Stokes-Einstein equation,

$$\delta_{w,s} = \frac{k_B T_d}{3\pi \mu_d D_{pp}}. \quad (2.20)$$

k_B denotes the Boltzmann constant, μ_d the dynamic viscosity of colloidal droplet, and D_{pp} the diameter of primary particles. The term “primary particle” here refers to the colloidal particles in the droplet and is differentiated from only “particle”, which is used for the final dried product.

For the case of large molecular substances (e.g. proteins) in water, the diffusion coefficient $\delta_{w,s}$ is related to Stokes-Einstein diffusion coefficient δ_{SE} according to [111],

$$\delta_{w,s} = \delta_{SE} \frac{1 - 9\phi_s/32}{1 + H_V + (\phi_s/\phi_{mx})/(1 - \phi_s/\phi_{mx})^2}; \quad (2.21)$$

ϕ_{mx} is the maximum possible solid volume fraction, which for large molecular substances can be taken at 0.5718 [111]. H_V is a function of solid volume fraction ϕ_s defined as

$$H_V = \frac{2b^2}{(1-b)} - \frac{c}{(1+2c)} - \frac{bc(2+c)}{(1+c)(1-b+c)}, \quad (2.22)$$

with $b = \sqrt{9\phi_s/8}$ and $c = 11\phi_s/16$.

The overall heat and mass transfer coefficients are calculated by considering the formation of crust:

$$k_h = \frac{1}{\frac{1}{\alpha} + \frac{R_d^2}{\lambda_{cr,eff}} \left(\frac{1}{R_{lc}} - \frac{1}{R_{cr}} \right)}, \quad (2.23)$$

$$k_m = \frac{1}{\frac{1}{\beta} + \frac{R_d^2}{\delta_{v,cr}} \left(\frac{1}{R_{lc}} - \frac{1}{R_{cr}} \right)}. \quad (2.24)$$

R_{lc} and R_{cr} are, respectively, liquid core radius and crust radius. Before crust formation there is no distinction between the two variables and they have the same value, i.e., $R_{lc} = R_{cr} = R_d$. Thus, the second term of resistance caused by the crust disappears. Radiation heat transfer is neglected Eq. 2.23 because its contribution will be very small compared to that of convection. A preliminary calculation shows that due to the small droplet sizes the convective heat transfer coefficient will be by at least one order of magnitude higher than that of radiation.

The coefficients of heat transfer (α) and mass transfer (β) at the gas side can be obtained from Nusselt and Sherwood numbers using the modified Ranz-Marshall correlations for evaporating spherical droplet [112]:

$$Nu = \frac{\alpha 2R_d}{\lambda_g} = \left(2 + 0.6 Re^{1/2} Pr^{1/2}\right) (1 + B_T)^{-0.7}, \quad (2.25)$$

$$Sh = \frac{\beta 2R_d}{\delta_{v,g}} = \left(2 + 0.6 Re^{1/2} Sc^{1/2}\right) (1 + B_T)^{-0.7}. \quad (2.26)$$

Here, $B_T = c_{p,v}(T_g - T_d)/h_{\text{evap}}$ is the Spalding number, which accounts for the effect of Stefan flow from the droplet surface. Reynolds, Prandtl, and Schmidt numbers are defined as

$$Re = \frac{\rho_g |u_{\text{rel}}| D_d}{\mu_g} = \frac{|u_{\text{rel}}| D_d}{\nu_g}, \quad (2.27)$$

$$Pr = \frac{\mu_g/\rho_g}{\lambda_g/(c_{p,g} \rho_g)} = \frac{\nu_g c_{p,g} \rho_g}{\lambda_g}, \quad (2.28)$$

$$Sc = \frac{\mu_g}{\rho_g \delta_{v,g}} = \frac{\nu_g}{\delta_{v,g}}. \quad (2.29)$$

The Reynolds number is defined by the relative velocity of the droplet in the gas u_{rel} , and it is thus directly affected by the pulsation of the hot gas.

2.3 Locking point determination

Locking point marks the transition from the first stage (constant drying rate) to the second stage (falling rate) of drying.

2.3.1 Colloidal suspension

Locking point during drying of colloidal suspension is determined following the method explained by Mezhericher et al. [89,92]. In this method, a transition period before the second drying stage is considered. When the volume fraction of solid particles at droplet surface has reached a critical value (0.6 for a random packing of spheres), a shell of nanoparticles is formed and as the drying process continues its thickness increases. In the layer of particles liquid menisci are formed (see Fig. 2.2.). Surface tension and capillary effects create compressive internal and external forces, which result in tangential and radial stresses:

$$[\sigma_r](r) = \frac{p_{\text{sh},e} R_d^3 (r^3 - R_{\text{sh}}^3)}{r^3 (R_{\text{sh}}^3 - R_d^3)} - \frac{p_{\text{sh},i} R_{\text{sh}}^3 (r^3 - R_d^3)}{r^3 (R_{\text{sh}}^3 - R_d^3)}, \quad (2.30)$$

$$[\sigma_t](r) = \frac{p_{\text{sh},e} R_d^3 (2r^3 + R_{\text{sh}}^3)}{2r^3 (R_{\text{sh}}^3 - R_d^3)} - \frac{p_{\text{sh},i} R_{\text{sh}}^3 (2r^3 + R_d^3)}{2r^3 (R_{\text{sh}}^3 - R_d^3)}. \quad (2.31)$$

Here, R_{sh} and R_d denote the internal and external radii of the shell, while r indicates positions along the shell thickness ($R_{\text{sh}} < r < R_d$).

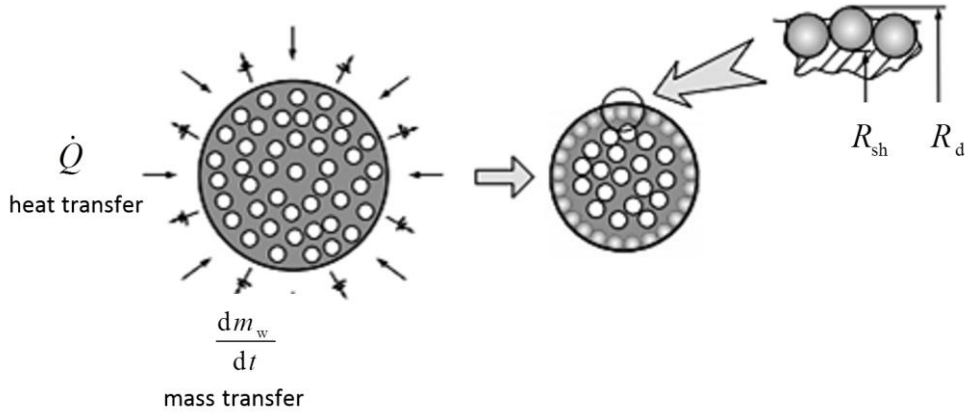


Fig. 2.2. Shell formation after the droplet surface has been saturated with nanoparticles (from [89], with permission).

The internal pressure is caused by the liquid interface and is given by the Laplace-Young equation,

$$p_{sh,i} = \frac{2\sigma_w}{R_d}. \quad (2.32)$$

Capillary force and surface tension contribute to the external pressure,

$$p_{sh,e} = p_{cap} + p_{st} = \frac{6\sigma_w}{D_{pp}} \left(\frac{1 - \epsilon_{sh}}{\epsilon_{sh}} \right) \cos \theta + \frac{2\sigma_w}{R_d}. \quad (2.33)$$

At the surface, an additional compressive stress in tangential direction is created by capillary effects [113,114]. Considering the capillary force created by a liquid bridge between two spherical particles (see Fig. 2.3) the stress can be calculated as follows:

$$[\sigma_{t,c}]_{r=R_d} = -\frac{2\sigma_w \cos(\alpha + \theta)}{R_{pp} \sin \alpha} + \sigma_w \left(\frac{1}{L} - \frac{1}{\rho} \right). \quad (2.34)$$

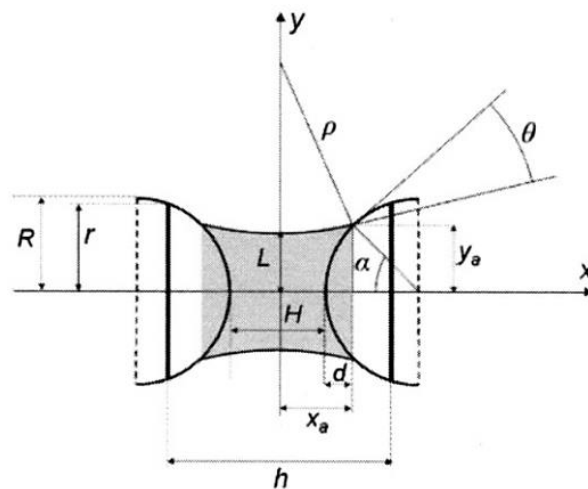


Fig. 2.3. Liquid bridge between two spherical particles (from [114], with permission).

It is important to note that stresses due to other causes such as heat are neglected in this model. Forces from the surrounding gas flow are also assumed to have no impact directly on the shell.

The total tangential stress at the surface is therefore the sum of the stress due to pressure difference and the stress due to the capillary effects,

$$[\sigma_t]_{r=R_d} = \frac{p_{sh,e} R_d^3 (2r^3 + R_{sh}^3)}{2r^3 (R_{sh}^3 - R_d^3)} - \frac{p_{sh,i} R_{sh}^3 (2r^3 + R_d^3)}{2r^3 (R_{sh}^3 - R_d^3)} - \frac{2\sigma_w \cos(\alpha + \theta)}{R_{pp} \sin \alpha} + \sigma_w \left(\frac{1}{L} - \frac{1}{\rho} \right). \quad (2.35)$$

If the compressive forces can overcome the strength of the created shell, the structure of the shell will be disturbed, and the shell will be dragged away from the surface until it becomes fully submerged into the liquid. The strength of the wet shell is expected to be proportional to the strength of a packing of mono-sized particles, which can be calculated using the Rumpf equation [115]. It is a function of primary particle size (D_{pp}), binding force between two particles in contact (f_b), particle coordination number (j_n), and shell porosity (ε_{sh}), which can be assumed equal to the porosity of randomly packed mono-sized spheres (≈ 0.4):

$$[\sigma_{sh}] \sim j_n \frac{1 - \varepsilon_{sh}}{\pi} \frac{f_b}{D_{pp}^2}. \quad (2.36)$$

It is important to note that here the presence of water between the primary particles and below the wet shell means that the apparent strength would be greater. In previous studies using this model [89,92,93], the strength was only approximated and then evaluated with experimental data. Before the shell is strong enough to withstand the compressive stresses, it will undergo a sequence of submergences and resurgences. The process of shell shrinkage and thickening has been explained in detail by Mezhericher et al. [89] and will not be discussed here. It was shown that the timescale of this process is negligible compared to that of water evaporation from the surface [89]. Therefore, during this stage liquid always exists at the surface and the drying rate of the droplet is thus the same as the rate during the first drying stage.

When the stresses are lower than the shell strength, the shell layer will not submerge below the liquid surface but hold its position. From this point onward the droplet size will remain constant, provided that no other phenomena such as inflation-deflation will occur. The liquid evaporation front will go below the outer surface of the shell and a dry layer of agglomerated nanoparticles, i.e., crust, will be formed.

2.3.2 Solution

For solution, the previous method cannot be used due to the more dispersed nature of the solid material. The easiest way is then to use a critical solid concentration at the surface. This method, however, is very prone of numerical errors as it depends on the size of the discretized volume element in which the critical concentration of solids shall be reached. While in most cases smaller discretization elements intuitively give more accurate calculation results, for

small (micron-sized or less) droplets containing solids it is not the case. The lower size limit of discretization elements should arguably be the size of primary particles or solute molecules. Preliminary simulations showed that the calculation discrepancies do not diminish when the thickness of discretization elements is decreased to the lower limit. They increase with smaller droplet size and higher drying temperature, i.e., when drying is faster. To overcome this problem, Tran et al. [74] used empirical equations obtained from experimental data to determine the critical moisture content from process parameters. However, those are only valid within narrow ranges of variable values and the materials being used. Another possibility is using the difference between glass transition temperature and droplet temperature at the surface as the critical variable [116]. The glass transition temperature has the advantage of being dependent on less variables and directly related to material composition. However, this method still suffers from the problem of numerical determination of surface layer thickness [116]. In this study, a method based on saturated layer strength and thickness ratio is proposed and will be discussed later in Chapter 6.

2.4 2nd drying stage

During the 2nd stage droplet liquid core is covered by a solid crust. Assuming quasi steady state condition in the crust, change in average crust temperature $T_{cr,avg}$ can be calculated as

$$\frac{dT_{cr,avg}}{dt} = \frac{\alpha 4\pi R_{cr}^2 (T_g - T_{cr,surf}) - k_h 4\pi R_{lc}^2 (T_g - T_{lc})}{m_{s,cr} c_{p,s}} \quad (2.37)$$

R_{cr} and $m_{s,cr}$ are respectively the outer radius and mass of the crust. The first term on the right-hand side of the equation is the heat received at the crust surface from the surrounding gas, whereas the second term indicates the heat that is further transferred from the crust to the liquid core. The difference is thus taken as sensible heat kept in the crust.

The temperature at any position r in the crust can be calculated as

$$T_{cr}(r) = T_{cr,surf} - (T_{cr,surf} - T_{lc}) \left(\frac{R_{lc}}{r} \right) \left(\frac{R_{cr} - r}{R_{cr} - R_{lc}} \right) \quad (2.38)$$

$T_{cr,surf}$ is the temperature at crust surface. Assuming that $c_{p,s}$ does not change much in the investigated temperature range, at a point $r = \bar{r}$ at which the crust is divided into two layers of same mass, the temperature would be equal to $T_{cr,avg}$. Using this and rearranging Eq. 2.38, we obtain

$$T_{cr,surf} = \frac{T_{cr,avg} - T_{lc} \left(\frac{R_{lc}}{\bar{r}} \right) \left(\frac{R_{cr} - \bar{r}}{R_{cr} - R_{lc}} \right)}{\left(1 - \left(\frac{R_{lc}}{\bar{r}} \right) \left(\frac{R_{cr} - \bar{r}}{R_{cr} - R_{lc}} \right) \right)} \quad (2.39)$$

2.4.1 Crust thermal conductivity

The effective thermal conductivity in the crust can be determined using Krischer's model [117], which is based on series and parallel combinations of resistances,

$$\lambda_{\text{cr,eff}} = \frac{\lambda_{\text{pore}}}{\frac{\alpha_{\lambda}}{\lambda_{\text{series}}/\lambda_{\text{pore}}} + \frac{1 - \alpha_{\lambda}}{\lambda_{\text{parallel}}/\lambda_{\text{pore}}}}. \quad (2.40)$$

Here, α_{λ} is a factor taken as 0.2, and the series and parallel combinations are given by

$$\lambda_{\text{series}} = \frac{1}{\frac{\varepsilon_{\text{cr}}}{\lambda_{\text{pore}}} + \frac{1 - \varepsilon_{\text{cr}}}{\lambda_{\text{s}}}}, \quad (2.41)$$

$$\lambda_{\text{parallel}} = \varepsilon_{\text{cr}}\lambda_{\text{pore}} + (1 - \varepsilon_{\text{cr}})\lambda_{\text{s}}. \quad (2.42)$$

λ_{s} denotes the thermal conductivity of the solid phase, whereas λ_{pore} is that of the pore.

If the crust is formed by nanoparticles, the effective pore size is very small and thus Knudsen effect should be considered when calculating the transport coefficients. λ_{pore} is thus calculated from the thermal conductivity of gas considering the Knudsen effect,

$$\lambda_{\text{pore}} = \frac{\lambda_{\text{g}}}{1 + Kn} = \frac{\lambda_{\text{g}}}{1 + \frac{2\Lambda(2/\gamma - 1)}{D_{\text{pp}}}}. \quad (2.43)$$

Λ is the mean free path of gas molecules defined as

$$\Lambda = \frac{1}{\sqrt{2}} \frac{R(T_{\text{g,pore}} + 273.15)}{\pi p \bar{\sigma}_{\text{g}}^2 N_{\text{Av}}}, \quad (2.44)$$

with $T_{\text{g,pore}}$ the gas temperature in the pores, $\bar{\sigma}_{\text{g}}$ the gas molecule diameter, and N_{Av} the Avogadro number.

The accommodation coefficient for collisions of gas molecules with the solid phase is calculated as

$$\gamma = \frac{1}{1 + 10^{\left(0.6 - \left(\frac{1000}{T_{\text{g,pore}} + 273.15} + 1\right)/C\right)}}, \quad (2.45)$$

with $C = 3.6$ for H_2O (approximately used also for wet air).

2.4.2 Vapor diffusivity through the crust

Effective diffusivity through the crust, on the other hand, can be determined by assuming a bundle of tortuous cylindrical paths created by the nanoparticles. It is given by

$$\delta_{\text{v,cr}} = \delta_{\text{v,pore}} \left(1 - \sqrt{1 - \varepsilon_{\text{cr}}}\right). \quad (2.46)$$

The vapor diffusivity in the crust pores is taken as the molecular diffusivity of water vapor in air given by [118]

$$\delta_{v,pore} = \delta_{vg} = \begin{cases} 1.87 \times 10^{-10} T^{2.072}/p, & 280K < T \leq 450K, \\ 2.75 \times 10^{-9} T^{1.632}/p, & 450K < T < 1070K. \end{cases} \quad (2.47)$$

For the case of crust of nanoparticles forming nanocylindrical pathways in which the Knudsen effect cannot be neglected, the diffusion coefficient is according to [119]

$$\delta_{v,pore} = \frac{4R_h}{3} \sqrt{\frac{2R(T_{g,pore} + 273.15)}{\pi M}} \left(\frac{2}{\gamma} - 1\right) \quad (2.48)$$

in the assumed cylindrical tubes with hydraulic radius

$$R_h = \frac{D_{pp}}{3} \left(\frac{\varepsilon_{cr}}{1 - \varepsilon_{cr}}\right). \quad (2.49)$$

2.5 Droplet movement in pulsed flow

Intermittent combustion in the pulse combustion unit produces flue gas with fluctuating velocity. The oscillation of drying gas velocity can be expressed as a sine function,

$$u_g = \bar{u}_g + u_{g,amp} \sin(2\pi ft + \varphi), \quad (2.50)$$

with \bar{u}_g the average velocity of gas, $u_{g,amp}$ the velocity amplitude, φ the oscillation phase, and f the pulsation frequency. The velocity amplitude is correlated to pressure oscillation inside the chamber as [68]

$$u_{amp} = \frac{p_{amp}}{\sqrt{2} \rho_g u_{sound}}, \quad (2.51)$$

with u_{sound} the sound velocity calculated by assuming ideal gas mixture,

$$u_{sound} = \sqrt{\left(\frac{c_{p,g}}{c_{p,g} - R}\right) \frac{R T_g}{M_g}}. \quad (2.52)$$

In the above equation, R is the universal gas constant, $c_{p,g}$ the specific heat capacity of gas at constant pressure, M_g the molar mass of gas mixture.

Soon after a droplet has been injected into the drying chamber, it will be dragged away by the pulsating gas flow. Therefore, the droplet will have its own pulsating velocity due to inertia and the forces working on it. Because the droplet size generated by the nozzle is relatively small (below 50 μm), the surrounding gas flow is still in laminar regime in respect to the droplet, although the flow in drying chamber is turbulent [120]. Additionally, the surrounding gas density is very low, gravity force and buoyancy force can be neglected. Considering only

the drag force due to gas flow, the equation for change in droplet velocity inside the drying chamber is

$$m_d \frac{du_d}{dt} = C_{\text{drag}} A_{\text{cross}} \rho_g |u_g - u_d| (u_g - u_d). \quad (2.53)$$

A_{cross} is the cross-sectional area of droplet, and C_{drag} the drag coefficient of a sphere, which is given by

$$C_{\text{drag}} = \frac{24}{Re} + 0.5. \quad (2.54)$$

2.6 Discretization and computation

The drying model is coupled and solved simultaneously with the models presented in the next chapters using ode15s solver in MATLAB. For this purpose, the partial differential equations used to calculate spatial distributions must first be transformed to ordinary differential equations. It is done by discretizing the spatial derivatives, resulting in a set of time derivatives for all discretization positions. The discretization method presented in [72] is used, in which the droplet is discretized in radial direction (1D) into N volume elements of same thickness Δr (see Fig. 2.4). The number of volume elements is predetermined and remains constant during calculation. Droplet shrinkage due to evaporation leads to uniform decrease in the element thickness.

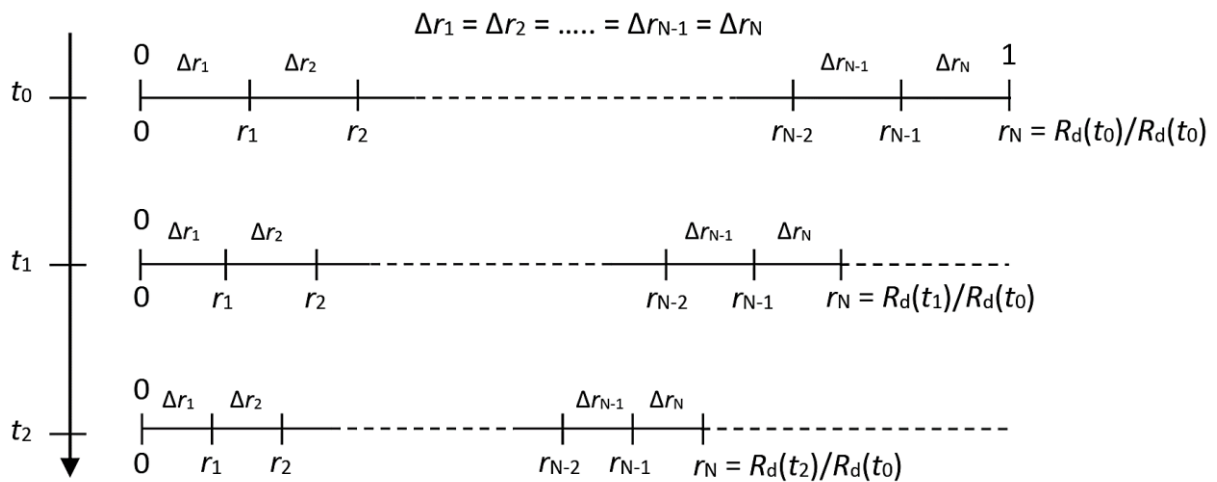


Fig. 2.4. Illustration of the discretization scheme, adapted from [72]. The discretization grid moves as the droplet undergoes drying.

2.7 Summary

The droplet drying model that serves as the basis with which the models discussed later in Chapters 3, 5, and 6 are coupled has been presented in this chapter. The drying model has been used and validated previously [72,74,92], and thus further validation is not necessary. In the model, change in solute concentration profile in the droplet due to water evaporation and consequently back-diffusion to the droplet center are considered. Temperature profile in the liquid core is, however, neglected due to the small droplet size and low Biot number. Ranz-Marshall correlations are used to calculate the heat and mass transfer coefficients between the droplet and the surrounding gas. Influence of Stefan flow from the droplet surface is taken into account by using Spalding correction. During drying droplet velocity changes due to the drag force exerted by the pulsating flow, leading to dynamic changes in relative velocity between the droplet and its surrounding gas and in transfer coefficients. When a critical concentration has been reached at the surface, solid crust is formed and acts as a resistance to heat and mass transfer. Inflation-deflation phenomenon is not considered in the current study, and thus droplet diameter stays constant from the point of crust formation on (i.e., from the locking point). Consequently, the locking diameter is the final particle size. The crust-liquid core interface recedes to the center as water continues to evaporate.

The transition from the 1st to the 2nd drying period starts when solid concentration in the droplet surface region reaches a critical value. In the here considered application of PCD, locking point determination is based on whether a layer of wet primary particles at droplet surface can withstand the stresses due to evaporation and shrinkage [69,89]. The still wet particle layer is termed as “shell”, whereas “crust” is the dry layer of primary particles that forms after the locking point. The shell starts to form from colloidal primary particles in the computation when the porosity of a bed of spheres (≈ 0.4) has been achieved for a surface layer thickness equal to the diameter of the primary particle. The wet shell will undergo a repeated process of submergences and resurgences until it has enough strength to overcome the stresses due to droplet shrinkage. If it is not resilient enough, the submergence-resurgence process will be prolonged and as a result the final powder particles will be more compact and smaller. During the transition period the droplet is still treated as a liquid droplet and phenomena such as droplet breakup may occur. The shift from resurgence to submergence is assumed to occur instantaneously. The droplet surface thus remains fully wet and the wet shell has no influence on the drying rate. During this thickening period the wet shell porosity remains constant. When the wet shell is thick and strong enough to overcome the stresses, the primary particles will become “locked” in their positions and the 2nd drying stage starts.

3. Droplet breakup in pulsed gas flow

This chapter contains an extended part of the publication “A model of pulse combustion drying and breakup of colloidal suspension droplets”, which was published in Powder Technology [69].

3.1 Introduction

In a recent work carried out by Widiyastuti et al. [13], a comparison between conventional spray drying (SD) and spray drying combined with pulse combustion (PCD) for production of ZnO particles was carried out. The cases considered were SD combined with furnace heating at 500 °C, PCD without furnace heating, and PCD with furnace heating at 300, 400, and 600 °C. The results showed that while the SD process could produce only submicron particles, the PCD process could provide ZnO nanoparticles irrespectively of whether furnace heating was employed or not. Oscillation of velocity created by PCD was thus sufficient for the formation of nanoparticles. The additional heat supplied by the heated furnace wall was found to contribute positively to crystal growth. Conventional spray drying, on the other hand, gave small crystal size compared to PCD, but the final particles were in polycrystalline form with submicron size. The authors of [13] hypothesized that nano-sized particles could be produced because after primary nanoparticles had been formed from the precursors inside a droplet, the droplet broke up in the PCD, but not in the SD. The study was continued by Joni et al. [16], who investigated the use of two-fluid atomizers for nanoparticle production using PCD. Highly crystalline nanoparticles with average size of 15.6 nm were produced with PCD. An interesting finding is that higher feed flow rate resulted in larger initial droplets, but gave smaller particles. They argued that when droplets entered the heated zone, evaporation and crystal growth became faster, followed by fragmentation to finer final particles.

The hypothesis of breakup in both studies was based on investigations by Lyonnard et al. [121] on the drying of TiO₂ (anatase) nanoparticle sols in presence and absence of salts. It is argued that a droplet will break when the osmotic pressure of the sol exceeds the Laplace pressure of the droplet. This was based on stability criterion of colloids containing trapped species that has been theoretically derived by Webster and Cates [122]. The osmotic pressure was calculated from the interaction potential between colloidal particles, which was based on the extended version of Derjaguin-Landau-Verwey-Overbeek (DLVO) theory [123–125]. Based on the model proposed, the salt-free sol droplet was predicted to fragment, while the one containing salt would not. The presence of salt creates a double layer effect near particle surfaces (screening) and decreases the overall electrostatic component of DLVO forces. Thus, attractive force becomes more dominant and agglomeration occurs.

The model proposed by Lyonnard et al. [121] only considers the role of internal factors of the droplet in the determination of breakup: the droplet undergoes evaporation and its solute concentration increases, and at some point osmotic pressure exceeds Laplace pressure, causing the droplet to break. The way the droplet is heated and how fast the evaporation of solvent takes place do not have any effect on whether the droplet will break up or not. The process investigated by Lyonnard et al. [121] was actually just normal spray drying. This is inconsistent with the hypothesis by Widiyastuti et al. and Joni et al. [13,16], which says that droplet breakup may occur in case of PCD but not in conventional SD. In the more classical theory, breakup of a droplet is determined from whether the droplet can withstand the disturbance created by the surrounding flow. In PCD, there is an oscillation of fluid flow velocity which, combined with its high frequency, could potentially create more disturbances on droplet surface. The mechanism proposed in the more classical theory is therefore sounder, although the role of pressure inside the droplet cannot be overlooked.

Fine particle generation by breakup of droplet/particle agglomerates in wet flue gas desulfurization system has been previously modelled by [126]. In their drying model, the balance between the velocity of primary particles movement to the center and that of receding liquid surface due to evaporation is used to determine whether the primary particles will stay in a droplet or escape to the environment. The particle movement to the center is, however, not caused by concentration gradient (i.e., diffusion is not considered), but rather by attraction force from the water molecules. Particles at the surface experience lower pulling force, whereas in the liquid bulk, attractive forces from water molecules are balanced from all directions. Accordingly, three results are possible: a single solid sphere, scattered particles (when all particles “escape” due to very fast evaporation), and a hollow sphere that may undergo further breakage into smaller particles. The presented model is quite questionable for following reasons. First, there is a rather unclear or inconsistent definition on what actually breaks: a wet droplet (before crust formation) or the dried particle agglomerate formed after crust formation. It was assumed that breakup occurs simply when the rate of water evaporation is larger than the rate of vapor diffusion to environment. Additionally, the calculation of water evaporation is also unclear.

It is interesting to see, whether droplet breakup is the main mechanism that leads to nanoparticle production, as hypothesized in the previous studies [13,16,121]. The proposed mechanism can be modelled mathematically and compared to the experimental results. In this chapter, the breakup of a colloidal droplet during pulse combustion drying is investigated by modeling the integrated process of evaporation and breakup of the droplet. In the model a droplet that already contains primary nanoparticles is considered. Formation of the primary nanoparticles from precursors by means of precipitation is out of the scope of this study. Important process parameters are investigated to elucidate their role in determining droplet breakup and to find the process criteria for breakup. The model is expected to show, whether the conditions created in PCD can result in nanoparticle production, or not.

3.2 Secondary atomization

The breakup of a droplet due to surrounding fluid flow, which occurs after the droplet has been fully released from a nozzle, is referred to as secondary atomization. It is differentiated from primary atomization, which refers to droplet formation from a liquid ligament in the course of spraying. After a droplet has been fully released from a liquid ligament, aerodynamic forces from the surrounding gas distort the droplet surface. Mass is removed from the droplet after it has been exposed to the moving fluid. Impurities and particulates may serve as initiation points for breakup [127]. Fragmentation continues until aerodynamic drag has reduced the drop-flow relative velocity to a level where the disruptive forces are no longer large enough to overcome the restorative forces. Duration of the disruptive flow must be sufficient to lead to breakup [128]. Equations of characteristic breakup time have been given by many authors, most notably by Ranger & Nichols [129]. However, they are not always accurate and very much case-dependent [130].

Droplet breakup is usually characterized by two dimensionless numbers, the Weber number and the Ohnesorge number. Weber number is the ratio of the inertial force of the surrounding gas to the surface tension force of the droplet, given as

$$We = \frac{\rho_g u_{rel}^2 D_d}{\sigma_d} \quad (3.1)$$

Ohnesorge number is the ratio of viscous forces of the droplet to the geometric mean of surface tension force and inertial force, given as

$$Oh = \frac{\mu_d}{\sqrt{\rho_d \sigma_d D_d}} \quad (3.2)$$

At low Oh (< 0.1), the breakup regime can be determined only from We . The breakup regimes and their respective We ranges at $Oh < 0.1$ are

1. Vibrational breakup ($We < 11$)
2. Bag breakup ($We = 11 - 35$)
3. Multimode (also known as bag-and-stamen) breakup ($We = 35 - 80$)
4. Sheet-thinning breakup ($We = 80 - 350$)
5. Catastrophic breakup ($We > 350$)

Breakup process for each regime is illustrated in Fig. 3.1, from top to bottom.

For higher Oh , at which the role of viscosity cannot be neglected, there is no commonly accepted We range as breakup criterion, as different researches gave different results [130]. At higher Oh , breakup becomes more difficult and takes longer time. Critical value of We (at which a droplet starts to break up) increases with Oh and fluid viscosity. Combination of viscosity, surface tension, densities, and relative velocity thus plays an important role [131]. For droplets smaller than $100 \mu\text{m}$, the influence of surface tension becomes more important [132].

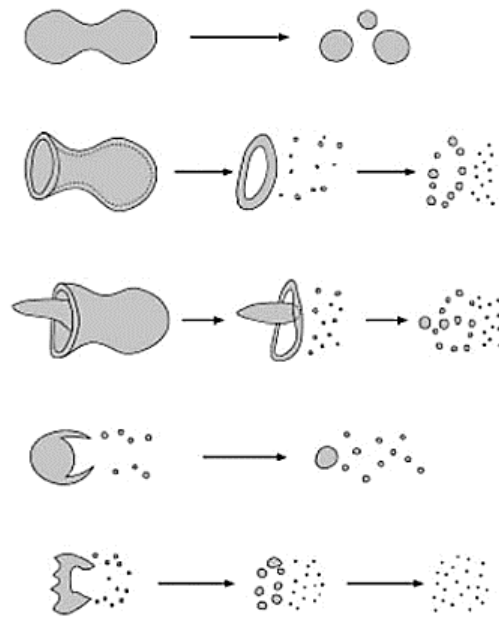


Fig. 3.1. Modes of secondary droplet breakup (from [130], with permission).

The term secondary (and primary) breakup does not only apply to the case of liquid droplet in gas, but also to other cases of gas bubble or liquid droplet in another liquid continuum. For such cases, different criteria apply. As an example, an empirical correlation of $We \sim Oh^{0.4}$ can be applied for nanoemulsions [133].

Conditions of droplet breakup can be calculated using some mathematical models: Taylor analogy breakup (TAB) model [134], drop deformation breakup (DDB) model [135], wave breakup model, Kelvin-Helmholtz-Rayleigh-Taylor (KHRT) model [136], stochastic secondary droplet (SSD) model, volume of fluid (VOF) method, and double-mass model [137]. Among those, VOF is considered as most accurate [130], but at the same time less practical and computationally very expensive. So far there is no single model that works at any We and Oh and captures all phenomena occurring during breakup.

While there have been studies on droplet breakup [134,138,139], most dealt with droplets of constant average size and properties. None has considered how the drying process and the presence of solute inside the droplet could affect the secondary atomization process. For the case of spray drying processes (including PCD), the droplets are relatively small in size and thus the Weber number is most likely small too, i.e., the breakup mode is vibrational (oscillatory) breakup. One of the models that characterize oscillatory breakup is the TAB model [134], which is based on the analogy to an oscillating and distorting spring-mass system. There are shortcomings of this model [130], however they are less likely to be crucial in the case of PCD as the process is rapid and the droplet size is small. The model is also considered superior than the other models for oscillation breakup, such as the DDB model [130,139], and has been validated in many studies [137,139–142]. There have been some modifications to the TAB

model [137,143,144]. However, the results obtained are in general still inconsistent and did not result in satisfactory improvements [130], despite the fact that the model complexity has been far increased. Thus, the original version of the TAB model is used here.

3.3 Taylor analogy breakup (TAB) model

For the case of colloidal droplet, it is assumed that breakup can only occur before crust formation. Breakup after the first drying stage is not considered in this chapter. Figure 3.2 shows the stages of drying and breakup of a suspension droplet. Before crust formation, the droplet may break due to the reasons to be explained in the following. The breakup process can occur more than once, and results in smaller child droplets. After crust formation, breakup will not occur and the particle size remains the same until drying ends. The study will focus on drying until the final droplet size has been reached or a stable crust has been formed.

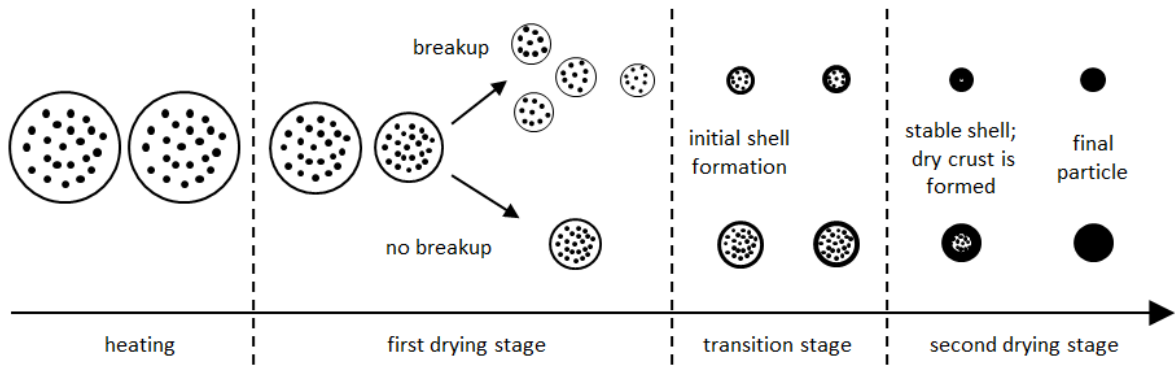


Fig. 3.2. Stages of drying and breakup of a suspension droplet.

As aforementioned, the TAB model is built based on the analogy between oscillating droplet and oscillating spring-mass system (Fig. 3.3). There are three forces considered in the spring-mass system: external force working on the spring, damping force, and restoring force of the spring. In the TAB model, those forces are analogous to the drag force hitting the droplet, droplet viscous force, and surface tension force, respectively. The external force will cause droplet shape to be distorted, with displacement from the original radius denoted by x (see Fig. 3.3).

Taking the non-dimensional distortion $y = x/(C_b R_d)$, the governing equation is

$$\frac{d^2y}{dt^2} = \frac{C_F \rho_g u_{rel}^2}{C_b \rho_d R_d^2} - \frac{C_k \sigma_d}{\rho_d R_d^3} y - \frac{C_d \mu_d}{\rho_d R_d^2} \frac{dy}{dt}, \quad (3.3)$$

with R_d the undisturbed droplet radius, x the displacement from R_d due to oscillation, and C_b , C_F , C_k , and C_d coefficients with default values 0.5, 1/3, 8, and 5, respectively. The analytical solution of the governing equation is

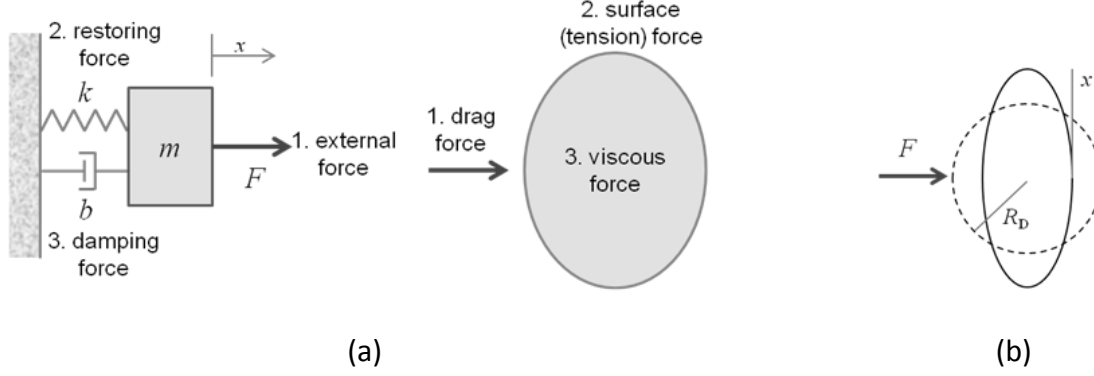


Fig. 3.3. (a) An analogy between spring-mass-damper system and droplet being distorted in fluid flow; (b) the distortion of droplet due to external forces.

$$y(t) = We^* + \left[\frac{1}{\omega} \left(\frac{dy_0}{dt} + \frac{y_0 - We^*}{t_d} \right) \sin(\omega t) + (y_0 - We^*) \cos(\omega t) \right] \exp(-t/t_d), \quad (3.4)$$

$$\frac{dy(t)}{dt} = \frac{We^* - y(t)}{t_d} + \left[\frac{1}{\omega} \left(\frac{dy_0}{dt} + \frac{y_0 - We^*}{t_d} \right) \cos(\omega t) - (y_0 - We^*) \sin(\omega t) \right] \omega \exp(-t/t_d). \quad (3.5)$$

with $t_d = 2 \rho_d R_d^2 / (C_d \mu_d)$ and $We^* = C_F We / (C_k C_B)$. The initial droplet distortion y_0 and its rate dy_0/dt are usually taken as zero. ω denotes the frequency of oscillation, given by

$$\omega = \sqrt{\frac{C_k \sigma_d}{\rho_d R_d^3} - \left(\frac{C_d \mu_d}{2 \rho_d R_d^2} \right)^2}. \quad (3.6)$$

The droplet breaks up if $y \geq 1$, i.e., when the distortion exceeds a certain critical ratio of droplet radius determined by C_b . Droplet will breakup into several child droplets. The Sauter mean radius of child droplet size distribution is derived from energy balance between parent and child droplets. It is given by

$$R_{\text{child}} = R_{32} = \frac{R_d}{1 + \frac{8K}{20} \frac{y^2}{\sigma_d} + \frac{\rho_d R_d^3 (dy/dt)^2 (6K - 5)}{120}}. \quad (3.7)$$

K denotes the ratio of total energy in distortion and oscillation to the energy in the fundamental mode. The value $K = 10/3$ has been derived from energy balance by O'Rourke & Amsden [134]. By mass conservation, the number of child droplets after breakup is

$$N_{d,\text{child}} = N_{d,0} \left(\frac{R_d}{R_{\text{child}}} \right)^3, \quad (3.8)$$

with $N_{d,0}$ the number of parent droplets before the breakup event.

In colloidal droplet, the solid mass does not dissolve into water and exists as very small particles. With the knowledge of average particle size and the assumption of perfect spherical

shape, the initial number of primary particles, $N_{pp,0}$, can be calculated from the initial solid mass fraction, $x_{s,0}$:

$$N_{pp,0} = \frac{x_{s,0} m_{d,0}}{\rho_s \left(\frac{4}{3} \pi R_{pp}^3 \right)}. \quad (3.9)$$

For application of the TAB model in CFD, the drag force is an outer force given by the fluid flow, whereas inner forces are determined by the droplet properties. Two intrinsic properties are important for this model: viscosity and surface tension. Droplet distortion γ is treated as an intrinsic property and does not have any impact on either droplet shape or size. Therefore, the assumption of spherical droplet remains and droplet distortion does not affect heat and mass transfer between the droplet and the surrounding gas.

3.4 Viscosity of colloidal droplet

One of the most frequently used equations for determining the dynamic viscosity of colloids at high concentration of solid particles is that of Krieger & Dougherty [145], which considers the hard sphere model of particles; resulting in

$$\frac{\mu_d}{\mu_w} = \left(1 - \frac{\phi_V^*}{\phi_{max}} \right)^{-C_E \phi_{max}} \quad (3.10)$$

with μ_d dynamic viscosity of colloid (the droplet), μ_w dynamic viscosity of water (solvent), C_E Einstein viscosity coefficient equal to 2.5, and ϕ_{max} the maximum packing fraction of spherical particles (≈ 0.6); ϕ_V^* is the effective volume fraction of particles in the droplet given by

$$\phi_V^* = \frac{\tan \alpha}{C_E} \phi_V, \quad (3.11)$$

in which ϕ_V is the volume fraction of particles in the droplet and $\tan \alpha$ is the slope of the real viscosity ratio vs volume fraction ϕ_V plot, which shows the material-dependent deviation from Einstein's viscosity equation. In the simulation, the deviation is neglected because of lack of available data.

3.5 Pressure balance & effective surface tension

In the theory of colloids, it is known that the balance of two pressures in a droplet containing solid particles, namely osmotic pressure (p_{osm}) and Laplace pressure (p_{Lap}), determines the stability of the colloidal droplet [121,122]. When the Laplace pressure is higher than the osmotic pressure, the droplet is in thermodynamically stable condition.

Laplace pressure is the difference between the pressure of liquid inside the droplet and the pressure of fluid surrounding the droplet. It is given as

$$p_{\text{Lap}} = \frac{2 \sigma_w}{R_d}. \quad (3.12)$$

Osmotic pressure in this case is the difference between the pressure of a droplet of pure liquid and the pressure of droplet containing solutes. It can be determined by utilizing the McMillan-Mayer theory of solution [146]. In this theory, the statistical thermodynamic virial equation for pressure is used, in a way that the solute particles are analogous to gas molecules and the solvent is considered as continuum. The virial equation for dilute mixture is given as

$$p_{\text{osm}} = N_V k_B T_d [1 + B_2 N_V + \dots] \quad (3.13)$$

with N_V the number density of particles. The term in the bracket accounts for the non-ideality of the mixture. The first virial term in the equation is the van't Hoff factor, which considers the solutes but not the interaction among them, i.e., the ideal condition. Interactions of pairs of solute particles are considered by the osmotic second virial coefficient B_2 . The contribution of the interactions among three or more particles, which is represented by the 3rd and higher order virial coefficients, is usually small and thus neglected for practical purposes. When the mixture is ideal, second virial coefficient is equal to zero and the equation reduces to the famous van't Hoff equation.

The van't Hoff equation was originally derived with the assumption of dilute mixture. For a non-dilute mixture, the following equation should be used [147]

$$p_{\text{osm}} = - \frac{\ln\left(\frac{c_w}{c_w + c_s}\right)}{\tilde{V}_w} N_{\text{Av}} k_B T_d, \quad (3.14)$$

where c_s and c_w are molar concentrations of solute and solvent (water), respectively. By comparing the equation for a dilute mixture with that for a non-dilute mixture, a new variable

$$N_V^* = \frac{\ln(1 + c_s/c_w)}{\tilde{V}_w} N_{\text{Av}} \quad (3.15)$$

can be introduced and used in the place of number density N_V . The osmotic second virial coefficient is given by

$$B_2 = \frac{1}{2} \int_0^\infty (1 - \exp[-w(\hat{r})/(k_B T_d)]) dV \quad (3.16)$$

which in radial coordinate can be expressed as

$$B_2 = 2\pi \int_0^\infty (1 - \exp[-w(\hat{r})/(k_B T_d)]) \hat{r}^2 d\hat{r}. \quad (3.17)$$

Here \hat{r} is the distance between centers of two particles in the droplet and $w(\hat{r})$ is the potential of mean force for the pair of particles.

For colloids and proteins, the potential mean force can be calculated using the Derjaguin-Landau-Verwey-Overbeek (DLVO) theory. It combines the effect of hydration force, van der Waals force, and electrostatic force [121,125]:

$$w(\hat{r}) = w_{\text{hyd}}(\hat{r}) + w_{\text{vdW}}(\hat{r}) + w_{\text{es}}(\hat{r}), \quad (3.18)$$

$$w_{\text{hyd}}(\hat{r}) = w_0 \exp((2R_{\text{pp}} - \hat{r})/\lambda_0), \quad (3.19)$$

$$w_{\text{vdW}}(\hat{r}) = -\frac{A_{\text{H}}}{6} \left(\frac{2R_{\text{pp}}^2}{4R_{\text{pp}}\hat{d} + \hat{d}^2} + \frac{2R_{\text{pp}}^2}{(2R_{\text{pp}} + \hat{d})^2} + \ln \frac{4R_{\text{pp}}\hat{d} + \hat{d}^2}{(2R_{\text{pp}} + \hat{d})^2} \right), \quad (3.20)$$

$$w_{\text{es}}(\hat{r}) = \frac{1}{4\pi \varepsilon_{\text{r}} \varepsilon_0 \hat{r} (1 + \kappa D_{\text{pp}})} \exp(\kappa(D_{\text{pp}} - \hat{r})), \quad (3.21)$$

in which q effective surface charge of primary particles, λ_0 is steric decay length, w_0 steric contact potential, D_{pp} diameter of primary particles, and \hat{d} distance between primary particle surfaces, which is equal to $(\hat{r} - D_{\text{pp}})$. κ is the inverse of Debye screening length λ_{D} ,

$$\kappa^{-1} = \lambda_{\text{D}} = \sqrt{\frac{\varepsilon_{\text{r,l}} \varepsilon_0 k_{\text{B}} T_{\text{d}}}{\sum (N_i q_i^2 / V_{\text{w}})}}, \quad (3.22)$$

with ε_0 vacuum permittivity, $\varepsilon_{\text{r,l}}$ relative permittivity of the solvent, N_i number of species i , and q_i charge of species i , respectively. The Hamaker constant A_{H} is calculated as [125]

$$A_{\text{H}} = \frac{3}{4} k_{\text{B}} T_{\text{d}} \left(\frac{\varepsilon_{\text{r,s}} - \varepsilon_{\text{r,l}}}{\varepsilon_{\text{r,s}} + \varepsilon_{\text{r,l}}} \right)^2 + \frac{3 h_{\text{p}} v_{\text{e}} (n_{\text{s}}^2 - n_{\text{l}}^2)^2}{16\sqrt{2} (n_{\text{s}}^2 + n_{\text{l}}^2)^{1.5}} \quad (3.23)$$

with h_{p} Planck constant, v_{e} main electronic absorption frequency in UV, and n_{s} and n_{l} refractive indices of solid and liquid, respectively.

For numerical calculation special attention should be paid to the integration limits in Eq. 3.17. At the lower limit of $\hat{r} \rightarrow 0$ the van der Waals force will go to minus infinity due to the form of Eq. 3.20, and as a result the second virial coefficient will go to infinity. Cameretti [148] suggested that the minimum distance between two particles should be the minimal intermolecular distance instead of zero. The value is approximated by 0.2 nm [125]. On the other hand, the upper integration limit is an even more obvious problem, which is commonly faced in molecular dynamics simulations. A cut-off distance, above which the interparticle interaction is considered negligible, is usually used to overcome this problem [149,150]. The cut-off distance (r_{cut}) can be given as in the unit of particle size. It was found that not much variation of molecular dynamics simulation results was observed for $r_{\text{cut}} > 6 D_{\text{pp}}$. Vanishing interaction potential from the distance above $5 D_{\text{pp}}$ was also observed in colloid-semipermeable membrane systems [151]. With consideration of larger particle size and minimum screening due to no-salt electrolytes, $r_{\text{cut}} = 10 D_{\text{pp}}$ is used. This distance is

comparable to the distance of long range forces at molecular level, which is usually up to 100 nm [125].

During drying, the droplet decreases in volume due to evaporation of solvent, so that the concentration of solid particles in the droplet increases. Thus, the osmotic pressure may become higher than the Laplace pressure. Beyond this point, the droplet is expected to break into smaller droplets to reach a thermodynamically more favorable condition. The thermodynamic droplet breakup criterion is thus

$$p_{\text{Lap}} < p_{\text{osm}}. \quad (3.24)$$

After breaking up, the droplets may once again reach the condition of larger Laplace pressure than osmotic pressure in each droplet.

From the droplet stability criterion, one can see that the Laplace pressure opposes, whereas the osmotic pressure encourages the breakup. Thus, the net pressure that keeps the droplet together is the difference between the two pressures. From this fact, one can derive an effective (or modified) surface tension of the droplet containing particles as

$$\sigma_{\text{eff}} = \sigma_{\text{d}} = \frac{(p_{\text{Lap}} - p_{\text{osm}})R_{\text{d}}}{2}. \quad (3.25)$$

From this equation, it can be seen that the effective surface tension of a colloidal droplet is smaller than the surface tension of a pure liquid droplet. Smaller surface tension will though give larger Weber number at the same droplet size and flow condition. Unlike in the case of particle containing droplets in emulsions, in spray drying droplet breakup is not only encouraged by the thermodynamics of the droplet, but also by the external shearing forces working on the droplet. Thus, the osmotic pressure does not necessarily have to overcome the Laplace pressure for the droplet to breakup.

3.6 Simulation setup

To understand the influence of process parameters on breakup of a droplet, some key droplet properties and process conditions are selected and varied. Those are sizes of the droplet and the particles contained in it, initial concentration (given as mass fraction) of the solid particles, surface charge of the particles, drying gas temperature, and the flow pulsation parameters of Eq. 2.50. The selected values of these variables are presented in Table 3.1.

The developed model is also used to investigate whether the mechanism of droplet breakup proposed in the reference studies [13,16] can really explain why nanoparticles can be produced by pulse combustion drying. As explained earlier, a key feature of PCD is the fluctuation of velocity. The PCD unit used by Joni et al. [16] is depicted in Fig. 3.4. It is in general the same as that used by Widiyastuti et al. [13] with the only difference in the droplet generation unit, which is a two fluid nozzle instead of an ultrasonic nebulizer.

Table 3.1. Variations of process parameters used for PCD simulations.

Variables	Unit	Variation
Initial droplet size	μm	4, 10, 40*, 100
Nanoparticle size	nm	5, 10*, 15
Initial solid mass fraction	-	0.05, 0.1*, 0.15
Gas temperature	$^{\circ}\text{C}$	300, 400, 500*, 600, 700
Surface charge density	mC/m^2	-5, -10*, -15
Average flow velocity	m/s	15*, 30, 45, 60
Velocity amplitude	m/s	0, 15, 30*, 45
Pulse frequency	Hz	100, 200, 300, 400*, 500, 600, 700
Oscillation phase	rad	0*, $\pi/4$, $\pi/2$, $-\pi/4$, $-\pi/2$

* the main value

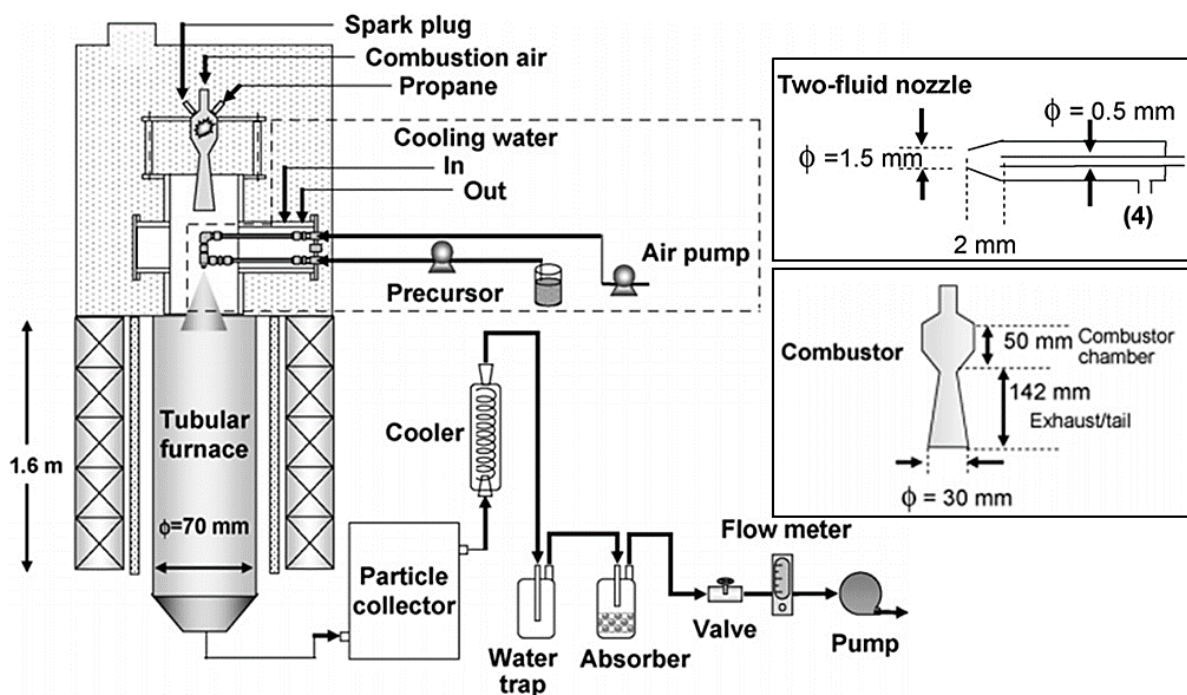
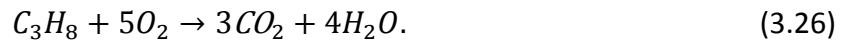


Fig. 3.4. Scheme of the PCD system used in the reference studies (adapted from [16], with permission).

In the experiments conducted in both studies, the flow velocity inside the drying chamber was not measured directly. The only given information are the feed rate of fuel and air for combustion, and the volumetric flow rate of the gas mix just before it is exhausted to the surrounding with a vacuum pump, which was located at the end of the process line (see Fig. 3.4).

One method to calculate the flow velocity is from fuel and air feed rate data. By assuming perfect mixing of flue gas components and considering the increase in specific volume due to heating from ambient temperature (assumed 20 °C) to the drying gas temperature, one can calculate the average flue gas velocity \bar{u}_g at given drying chamber dimension. The composition of combustion product can be calculated from the reaction mass balance, assuming perfect combustion. In the experiments propane was used as the fuel, and the combustion reaction is



For the simulation, dry air consisting (in mass fraction) of 78.1% N₂, 21% O₂, and 0.9% Ar is assumed as the input air for combustion. The properties of flue gas are calculated based on each component's mass fraction. The properties of individual gas component are given as empirical functions of temperature (Table A.1. in Appendix A) based on published data. Calculation using chamber diameter of 7 cm for gas temperature of 330 °C results in the average flue gas velocity of 0.16 m/s.

Another way to calculate the drying gas average velocity is from the volumetric flow rate of the cooled exhaust gas mixture. The gas mix had been cooled down with a condenser and the water vapor had been removed using a water trap and an absorber. Assuming that the water trap and absorber remove only the water vapor resulting from drying, composition and mass flow rate of the exhaust gas will be the same as the composition and mass flow rate of the flue gas. Here the important information needed is the temperature of the gas mixture at the point of measurement (before entering the vacuum pump). From the specification sheet of the vacuum pump used for the experiments (GCD-136X, Ulvac Kiko Inc., Kanagawa, Japan) it is known that the safe temperature range for operation is from 7 to 40 °C. Thus, it can safely be assumed that the exhaust gas temperature was between 30 to 40 °C. From the calculation it is found that the average gas velocity does not vary too much in that temperature range, with an average value of 0.3 m/s.

From the two calculation methods it is found that the value calculated directly from the feed rates is significantly lower. The main reason for this is because calculation is based on the whole drying chamber diameter. This is far from the real situation where the velocity at the center area (along the axis) is the highest, especially if we consider the design of the drying chamber (with narrowing exit) and how the diameter of the burner tailpipe (30 mm) is smaller than the chamber diameter. On the other hand, using the tailpipe diameter for the calculation cannot be justified due to the expanding design of the tailpipe. A more reasonable diameter of the flue gas jet thus lies between the two diameters. Calculation using a linear average $((D_{\text{tail}} + D_{\text{chamber}}) / 2)$ gives an average gas velocity of 0.305 m/s, which is really close to the value calculated from the second method.

The actual values of flow pulsation frequency and the amplitude of velocity oscillation in the experiments were not explicitly given. It was only stated that the pulse combustion unit generated 155 dB at 700 Hz [13] and 115 dB at 1000 Hz [16]. Those frequencies are considerably high, compared to the common range from 20 to 200 Hz [11]. The frequency of velocity pulsation can be assumed to be most likely the same with the frequency of pulse combustor or other unit that produces the pulsed flow.

The amplitude of velocity is a function of the maximum pressure generated inside the combustor, which itself can be calculated from the maximum sound power level,

$$p_{c,\max} = (1 - f_{\text{drop}}) \sqrt{2} p_{s,\text{ref}} 10^{L_t/20}, \quad (3.27)$$

with $p_{s,\text{ref}}$ reference sound pressure ($= 2 \times 10^{-5}$ Pa), L_t the tailpipe length, and f_{drop} the maximum pressure ratio drop along tailpipe, estimated at 10% [152]. The velocity amplitude can be calculated as [54]

$$u_{g,\text{amp}} = \frac{p_{c,\max} \lambda_{\text{sound}}}{2\pi \rho_g u_{\text{sound}} L_t} \sin\left(\frac{2\pi L_t}{\lambda_{\text{sound}}}\right). \quad (3.28)$$

Here λ_{sound} and u_{sound} are the acoustic resonance wavelength and the sound velocity in the gas at the respective temperature. From the Eqs. 3.27 & 3.28, the obtained velocity amplitude is 5.43 m/s for $p_{\max} = 155$ dB.

Release velocity of a droplet from a two-fluid nozzle can be calculated from the nozzle size specification (given in Fig. 3.4) and the volumetric flow rates of liquid feed and atomizing gas, which are 250 mL/hour and 8.3 L/minute, respectively. The velocity of the droplet is somewhere between the average velocity of the liquid going out continuously from the nozzle tip, $u_{n,l}$, and the velocity of the atomizing gas, $u_{n,g}$; both can be calculated from the volumetric flow rates and nozzle dimensions. For simplicity it is assumed that

$$u_{d,0} = \frac{1}{2}(u_{n,l} + u_{n,g}). \quad (3.29)$$

The droplet release velocity calculated with Eq. 3.29 is used in all variations. The obtained value is 39.3 m/s, which is of the same magnitude of the typical droplet release velocity of 40.8 m/s found in other studies [138,153].

The values of parameters common to all simulations are given in Table 3.2. The droplet considered in the simulations is a colloidal droplet with water and Zinc oxide particles. For 16 nm particles good matches were previously obtained with $[\sigma_{\text{sh}}] = 100$ MPa [89,92,93]. The value is adjusted to the particle size used in this study (10 nm) according to Eq. 2.36, resulting in 256 MPa. The material properties are given in Table 3.3.

Table 3.2. Input variables for simulations.

Variables		Values
No. of discretization volume elements	N_{el}	100
Gas pressure (Pa)	p	101325
Initial droplet temperature (°C)	$T_{d,0}$	20
Volumetric flow rate of combustion air (L/minute)	\dot{V}_a	20
Volumetric flow rate of fuel (L/minute)	\dot{V}_f	0.67
Droplet release velocity (m/s)	$u_{d,0}$	39.3

Table 3.3. Properties of the materials.

Variables		Values	References
Specific heat capacity of ZnO (J/kg.K)	$c_{p,s}$	545	[154]
Specific heat capacity of liquid water (J/kg.K)	$c_{p,w}$	4187	-
Latent heat of evaporation (J/kg)	h_{lv}	2.3×10^6	-
Thermal conductivity of ZnO (W/m.K)	λ_s	0.8	[155]
Molar mass of fuel (kg/kmol)	M_f	44	-
Molar mass of solid (kg/kmol)	M_s	81.38	-
Molar mass of liquid (kg/kmol)	M_w	18	-
Mass density of liquid water (kg/m ³)	ρ_w	998	-
Mass density of ZnO (kg/m ³)	ρ_s	5606	-
Dielectric constant of ZnO	$\epsilon_{r,s}$	8.66	[156]
Refractive index of water	n_l	1.333	[125]
Refractive index of ZnO	n_p	1.9597	[157]
Steric decay length (nm)	λ_0	0.6	[125]
Steric contact potential (J/m ²)	w_0	10^{-3}	[125]
Main electronic absorption frequency in UV (Hz)	ν_e	3×10^{15}	[125]

3.7 Results & discussions

3.7.1 Behavior of DLVO parameters

The DLVO forces play an important role in determining osmotic pressure, which in turn determines the effective surface tension. It is therefore interesting to see how the droplet and particle properties affect the behavior of DLVO forces. Since osmotic pressure is an entropic property and a function of the number of particles, higher concentration of solute at a given nanoparticle size will give higher osmotic pressure and thus lower effective surface tension.

Similarly, at a given solute concentration, smaller nanoparticle size is also expected to result in higher osmotic pressure because of the more particles present.

Figure 3.5 shows the values of the DLVO forces as a function of the distance between the surfaces of two particles. Each component of DLVO force has its own characteristic of working range: electrostatic force is a long-range force, while the van der Waals and hydration forces are short ranged. At far distance electrostatic force dominates and for same charged particles the overall force is repulsive. At shorter distances, hydration forces contribute to repulsion. As the particles get closer, the influence of van der Waals force becomes stronger and the total interaction force decreases. Whether or not interaction force will fall to the attractive region (i.e., become negative) depends on the values of Hamaker constant, which determines the magnitude of van der Waals force, and steric decay length, which determines the effective working distance of the hydration force.

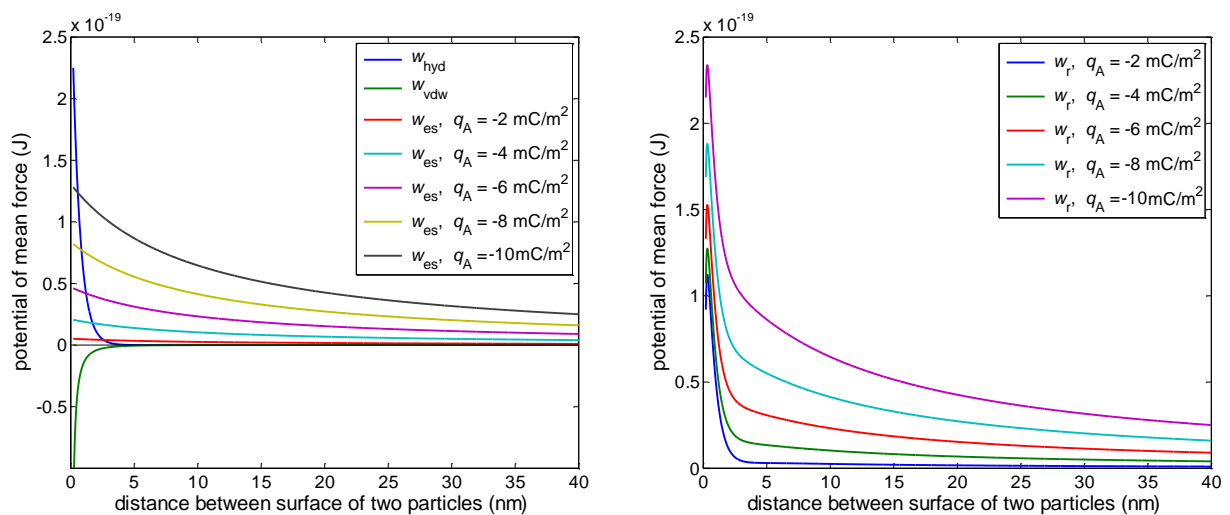


Fig. 3.5. Potential of mean forces as a function of the distance between two particles: each component (*left*), and total potential mean force (*right*).

Aside of their size, which is related to the total particle mass and number concentration, interaction forces between two particles are influenced by the properties of the surface. Higher surface charge density gives higher electrostatic force, which means higher repulsion. Although at a short distance the repulsion due to hydration force overcomes the contribution of electrostatic force, at far distance the effect of surface charge density is more pronounced. Since droplet breakup is likely to occur when the particles are still not close to each other, the influence of surface charge cannot be overlooked. Surface charge can be regulated by adjusting the pH of the mixture; pH will influence how many surface groups are ionized [125]. The degree of ionization, and subsequently the change in surface charge, depends strongly on the nature of the surface groups, which differs for different materials. This will not be further discussed in this study.

3 Droplet breakup in pulsed gas flow

Figure 3.6 shows how the non-ideality parameter, which is the product of second osmotic virial coefficient B_2 and particle number density, i.e., $B_2 N_V^*$ (Eq. 3.13), and Laplace and osmotic pressures change as a droplet is dried and its size decreases. The non-ideality parameter describes interactions between particles, and thus is referred as interaction coefficient. As water evaporates, the droplet size decreases and the solute particles come closer to each other. Higher surface charge thus results in faster increase in osmotic pressure, making it easier to overcome the Laplace pressure. The interaction coefficient decreases again as the potential mean forces go to the direction of attraction.

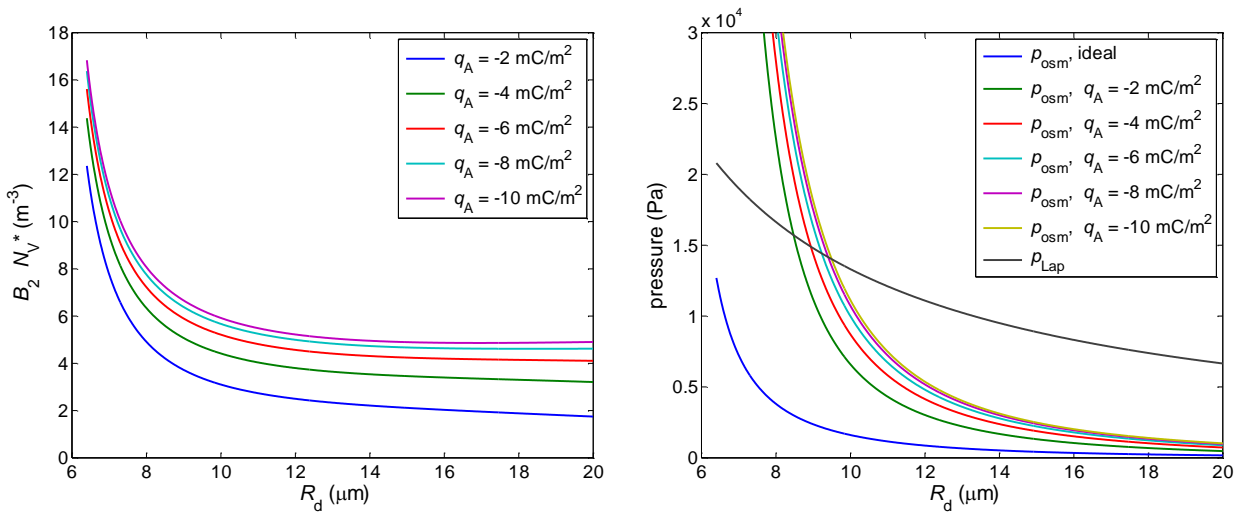


Fig. 3.6. Evolution of the non-ideal deviation term, $B N_V^*$ (left) and the Laplace and osmotic pressures (right) with decreasing droplet size.

For colloidal suspensions with additional salts, the excluded salt volume should theoretically not be neglected. The presence of salt ions between two particles will create more screening and reduce the long-range electrostatic forces. Thus, the total interaction is expected to move towards attraction [158]. However, its osmotic contribution has very little effects on the second virial coefficient and phase equilibria, as shown in numerical investigations [148]. In this study, no salts are considered and screening is thus only contributed by ionized water molecules [125].

In a solution, as opposed to a colloidal suspension, the size of a solute particle (molecule) is way smaller and more comparable to the size of a water molecule. In this regard, hydration force becomes really small and can even be neglected. For a solute species that is ionized in water, the electrostatic force becomes more complicated as there is not only interaction between like charge molecules but also between those of opposite charge. The total electrostatic force will be lower compared to that of mono-charged colloidal suspension due to the attractive contribution by opposite charged molecules. Van der Waals force will thus be dominant, and the overall particle interaction will be attractive. In this regard, particle interaction will lower the osmotic pressure.

3.7.2 Influence of drying process on droplet breakup

In most breakup cases that have been modelled previously, a droplet of constant properties has been considered [130,139]. In the situation considered here, drying causes droplet properties to change. Most notably, droplet size decreases due to water evaporation. It is interesting to see how the drying process influences the droplet breakup. Figure 3.7 presents the changes in velocities of the drying gas and the droplet, as well as the relative velocity between them, for cases with and without drying. In the first case, the size and mass of droplet decrease due to water evaporation. During the evaporation of a pure liquid droplet, reduction in size (diameter) will reduce the droplet mass faster than the cross-sectional area. According to Eq. 2.53, droplet acceleration due to drag force will thus become higher and the droplet will be carried away more easily by the flow. Droplet velocity in the chamber will consequently increase, whereas its relative velocity to the gas will decrease. For a colloidal droplet, the decrease of relative velocity is expected to be slower. This is because the overall droplet density increases due to the solid having much higher mass density than water. Therefore, given same initial droplet size, relative decrease in mass will be higher for a colloidal droplet than for a pure liquid droplet. In the case of no water evaporation, the droplet maintains its size and mass. Total mass of the droplet as well as the working area of the drag force remain the same, and the droplet does not accelerate as quickly as when evaporation takes place. The relative velocity then decreases at much lower pace compared to the case of evaporating colloidal droplet, as can be seen from Fig. 3.7. No drying also means that there was no change in solute concentration profile. The changes in osmotic and Laplace pressure were only due to the increase in droplet temperature.

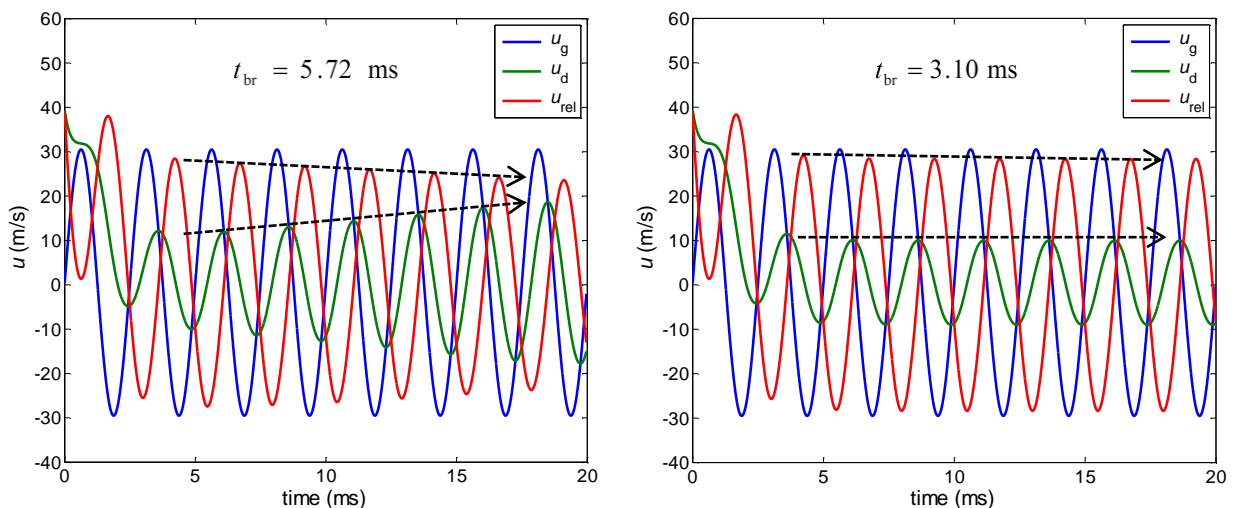


Fig. 3.7. Changes in gas velocity, droplet velocity, and droplet-gas relative velocity for the case of drying (*left*) and without drying (*right*).

From the definition of Weber number, decreasing droplet size also means that it becomes harder for the droplet to break. For the non-evaporating droplet, the criterion $\gamma \geq 1$ was reached after 3.10 ms, whereas for the evaporating droplet it was reached after 5.72 ms. Solvent evaporation causes not only a decrease in droplet size, but also an increase in droplet viscosity. To see which one of the two hampering factors plays a bigger role in preventing droplet breakup, another simulation with constant concentration for viscosity calculation was performed. In this case, the concentration of solute was assumed constant even when the droplet size decreased. The change in viscosity was thus only influenced by droplet temperature. The simulation gave breakup time of 5.71 ms. This means that viscosity plays a much smaller role in preventing droplet breakup compared to the reduction in droplet size.

Figure 3.8 shows the changes in droplet oscillation and relative velocity for two cases: when heat and mass transfer between droplet and gas is not considered; and when it is considered, i.e. for the normal PCD process. In the first case, the properties of the droplet do not change because its temperature and composition remain the same. It is dragged by the pulsating flow and the oscillation of relative velocity becomes steady-state after some time. When heat and mass transfer is present, droplet temperature and solute concentration increase, which makes the effective surface tension decrease. Increasing solute concentration leads to an increase in viscosity. However, increasing droplet temperature causes a reduction in solvent viscosity. The effect of increasing temperature is greater than that of increasing concentration, because viscosity of the solvent (water) is a strong function of temperature. Consequently, the overall droplet viscosity decreases. For example, viscosity decreases from 1.052 mPa.s to 0.576 mPa.s when the droplet temperature is increased from 20 °C to 50 °C. When the solid mass fraction of 0.1 is doubled at 50 °C, the viscosity only increases to 0.612 mPa.s. A lower viscosity means that the droplet has less resistance to distortion, and thus the distortion oscillation is enhanced.

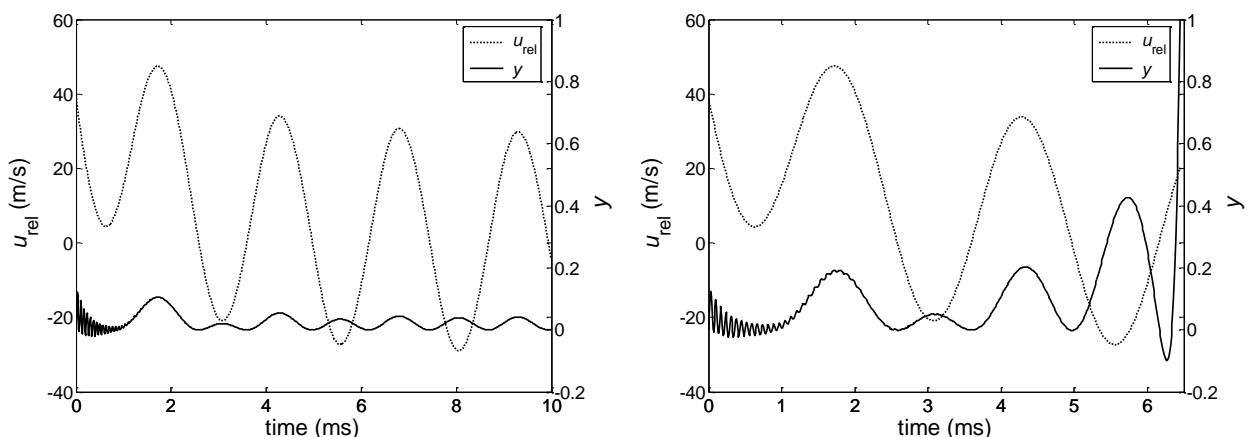


Fig. 3.8. Droplet oscillation and relative velocity: without heat and mass transfer (*left*) and with heat and mass transfer (*right*).

3.7.3 Influence of operating parameters

Droplet size, as well as concentration, surface charge and size of particles are important properties of a colloidal droplet that determine how hard it is for the droplet to break. Figure 3.9 shows how the properties affect droplet breakup. It can be seen that the breakup criterion is achieved faster when the droplet size is large. As the droplet size decreases, it becomes harder for the droplet to break, and at even smaller initial sizes (4 and 10 μm) the droplet fails to break before the locking point is reached. As aforementioned, particle number density, influenced by solute concentration or colloid particle size, determines effective surface tension and viscosity. For same initial concentration of solute, it is easier for a droplet with smaller colloidal particles to break because the effective surface tension is smaller. Similarly, given the same particle size, it is easier for a droplet containing more solute to break. It has been discussed earlier how surface charge affects the behavior of DLVO force and osmotic pressure. As expected, the droplet breaks up earlier when its surface charge density is increased to -15 mC/m^2 , and later when it is lowered to -5 mC/m^2 .

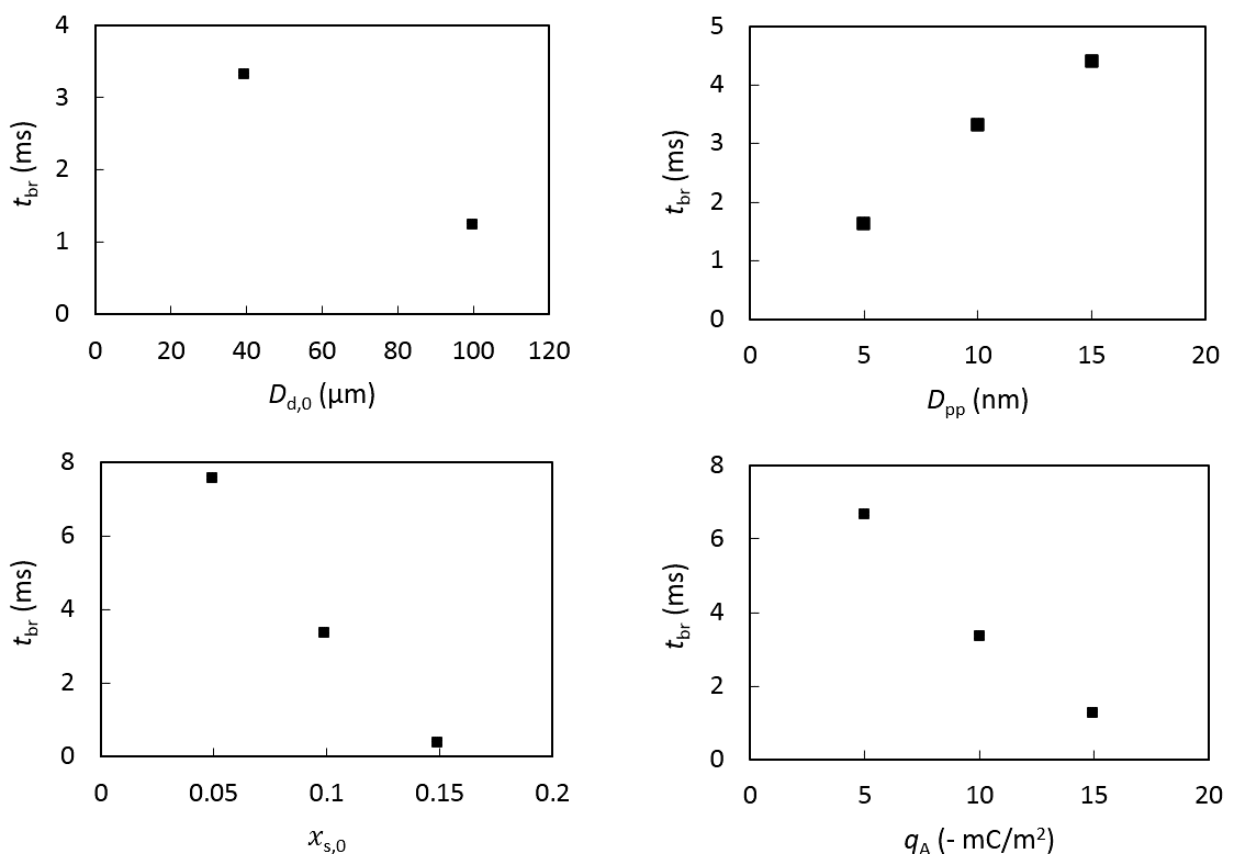


Fig. 3.9. Influence of droplet properties on breakup times.

Figure 3.10 shows how the conditions inside the drying chamber affect the breakup times. Temperature regulates not only how much heat can be transferred to the droplet for water evaporation, but also how fast droplet properties change. As mentioned earlier, the droplet

3 Droplet breakup in pulsed gas flow

will be heated up until its temperature reaches the adiabatic saturation temperature. Although higher gas temperatures also mean higher adiabatic saturation temperatures, the increase of the later is comparably smaller to that of droplet-gas temperature difference. Thus, the increase in diffusion coefficient because of higher droplet temperature (Eq. 2.20), and the increase in diffusion rate cannot match the increase in evaporation rate, and thus locking point will be achieved faster. The increase in gas temperature causes breakup to occur earlier because faster evaporation makes the solute concentration in the droplet increase faster. However, at some point the evaporation rate (i.e., decrease in droplet size) might become too fast compared to diffusion and locking point might be reached before the droplet can achieve the required distortion for breakup.

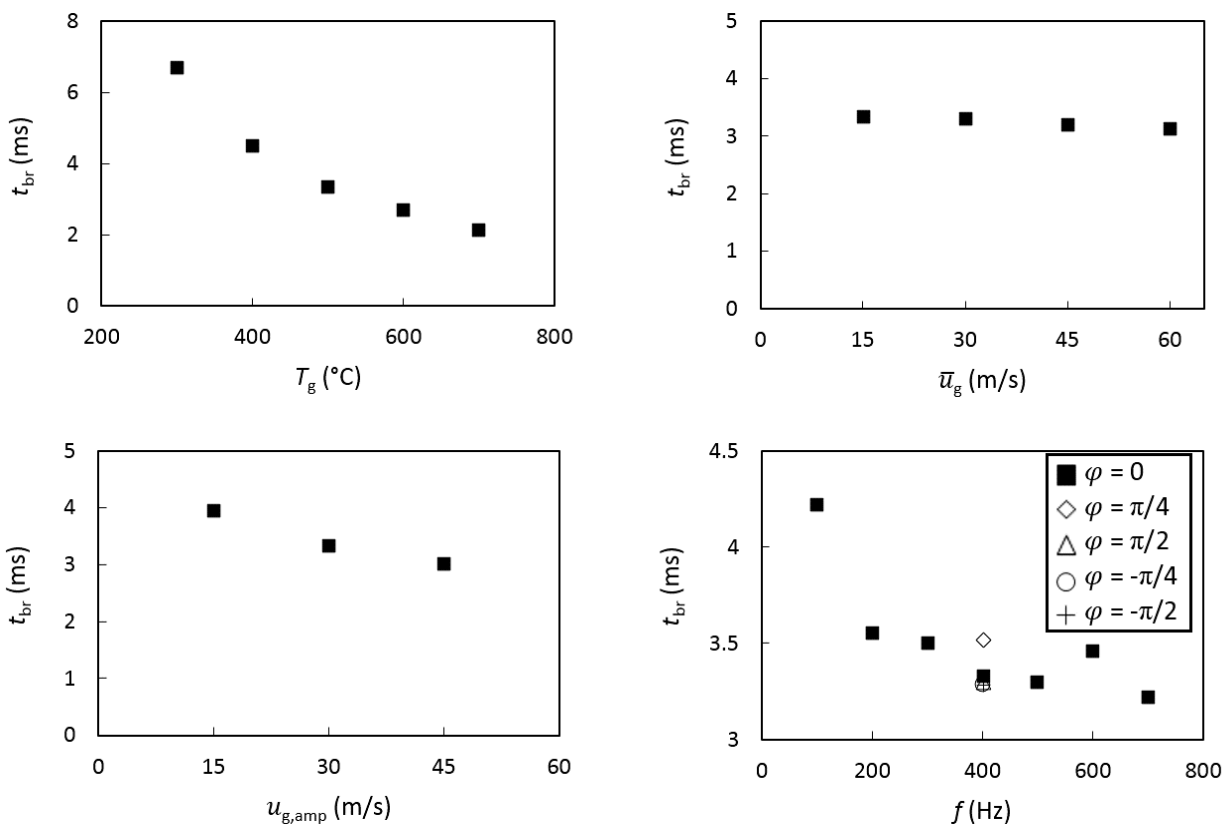


Fig. 3.10. Influence of process conditions on breakup time.

Gas pulsation parameters also affect the droplet breakup. Frequency plays a role in determining how intense the droplet aerodynamically interacts with the surrounding gas. It can be deduced from Fig. 3.8 that droplet distortion oscillation is very much related to the oscillation of the relative velocity. For most of the time, the frequency of droplet distortion is twice the frequency of relative velocity fluctuation. According to the TAB model, the droplet will still oscillate when there is no pulsation. From Fig. 3.10, it can be seen that when the frequency is increased, the droplet breaks earlier. However, after some certain point the effect of frequency becomes ambiguous. When the frequency is too low, the droplet has less

distortion inertia and enough time to recover its shape. When the frequency is too high, the relative velocity falls too early and the droplet cannot reach its maximum possible distortion. It is important to keep in mind that the external force that causes droplet distortion is a complex function of relative velocity and pulsation frequency. Thus, the optimum frequency for breakup will also be determined by the average and amplitude velocities as well. In real pulse combustion dryers, droplets are injected continuously into the chamber. The breakup time can be shorter if the initial relative velocity is already high. This is influenced by the average gas velocity and the phase of pulsation at the time the droplet is introduced into the chamber. The effect, however, is not so big. It is also shown in Fig. 3.10 that compared to the average velocity the amplitude of gas velocity has a noticeably stronger influence on droplet breakup. Higher velocity amplitudes result in shorter breakup times.

In Fig. 3.11, changes in gas velocity, droplet velocity, and droplet distortion for two contrasting cases are presented. In the first case the gas flow is pulsed, with average velocity of 0.5 m/s and amplitude of 30 m/s. The second is the case of steady and non-pulsating gas flow with an average velocity of 100 m/s. The trend obtained here is similar to that shown by Kuts and coworkers [18,19], who also simulated the case of spherical objects in a pulsed gas flow. From the comparison, it can be seen that the gas average velocity only affects the relative velocity at the beginning. As the process continues, it is the amplitude of velocity oscillation that determines how the relative velocity is kept oscillating. This oscillation of gas velocity, and consequently of droplet relative velocity, influences the oscillation of droplet distortion and lets the critical droplet distortion be reached faster. When there is no pulsation, the droplet will be carried away by the gas and its relative velocity quickly goes asymptotically to zero. Consequently, the transfer coefficients decrease and the droplet will require more time to reach the locking point. Even though it has more time to break, it is not stressed strongly enough by the flow because of the low relative velocity. As the result the distortion oscillation is not maintained and the droplet cannot break.

3.7.4 Assessment of the reference studies: is breakup possible?

In the previous section it has been seen how the process parameters affect droplet breakup. The key parameters are droplet diameter, particle size and concentration, surface charge density, velocity amplitude, temperature, and frequency. To evaluate whether the processes in [13,16] can result in droplet breakup as claimed, zones in which a combination of parameters will lead to droplet breakup, or not, will be defined. To visualize the zones in a 3D plot, the number of key parameters will be reduced to three.

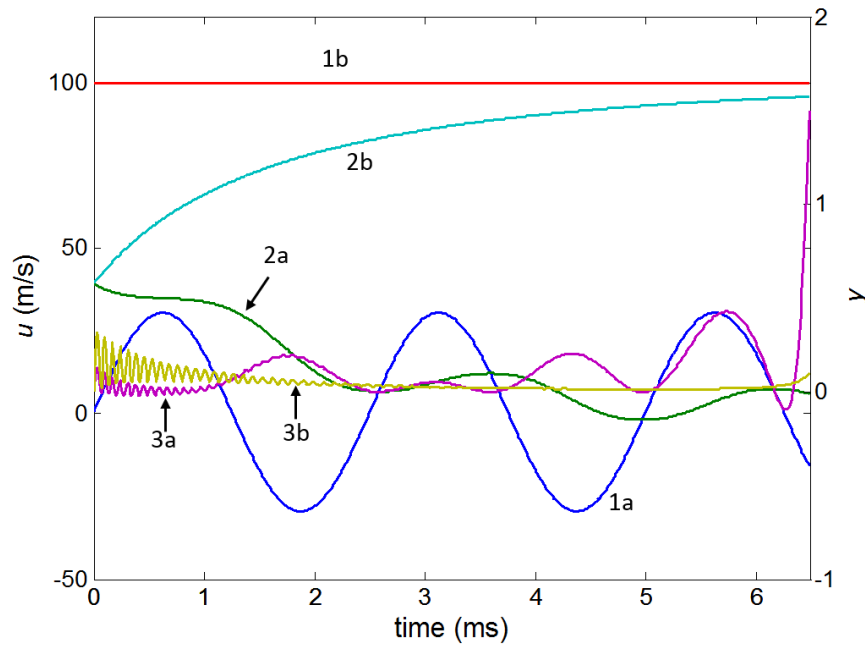


Fig. 3.11. Changes in gas velocity (1), droplet velocity (2), and droplet distortion (3) for the case of: (a) drying with pulsation ($\bar{u}_g = 0.5$ m/s & $u_{g,amp} = 30$ m/s); and (b) without pulsation ($\bar{u}_g = 100$ m/s).

Both studies used the same pulse combustion unit, with optional application of a heating element surrounding the chamber (Fig. 3.4). It can be assumed that the average temperatures generated inside the drying chamber without additional heating would be the same, which is 330 °C. Both studies used frequencies higher than 300 Hz for the process. As has been seen in Fig. 3.10, if the frequency is increased to more than 300 Hz its influence on breakup time is less pronounced. Therefore, it is safe to assume the same high value for both cases. According to Eq. 3.28, given same apparatus and temperature employed, the amplitude of velocity is only a function of sound power level. The values for the two studies are 155 and 115 dB, which result in velocity amplitudes of 5.4308 and 0.0556 m/s. These values are very low compared to the values used for simulation variation here. Initial solid molar concentrations were 0.1 M [13] and 0.6 M [16], which correspond to solid mass fractions of 0.81% and 4.7%, respectively. There was no information on surface charge density of the colloidal particles. Here a uniform value of 10 mC/m² is assumed. Primary particle diameters were regulated by the reactions of the precursors and obtained to 24.8 and 15.3 nm, which are higher than the assigned values for the simulation study.

Figure 3.12 gives a 3D plot of three selected key parameters, with defined breakup and no-breakup zones. The selected parameters are droplet size, initial solid concentration, and velocity amplitude. For simulation a common particle size of 10 nm was used, which is lower than the particle sizes in the experiments [13,16]. This means that the simulations have been slightly in favor of droplet breakup compared to the experimental studies. From Fig. 3.12 it can be seen that with the process conditions in the experiments droplets would not break. For

the given droplet sizes (4.22 and 20.9 μm), in order to make a droplet break the solid concentration and the velocity amplitude must be seriously increased. It is important to note that the surface separating breakup zone and no-breakup zone in Fig. 3.12 is only valid for the ranges of variables defined here.

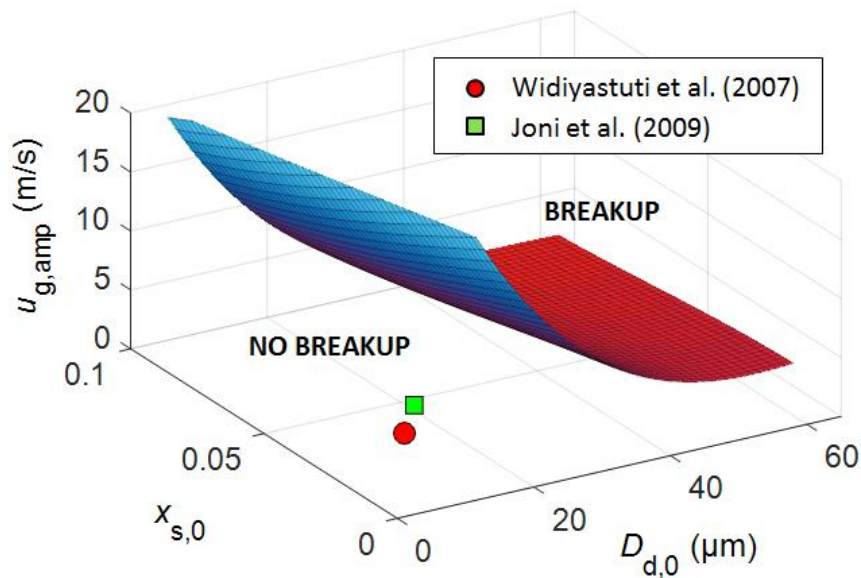


Fig. 3.12. 3D plot of the 3 key parameters for colloidal droplet breakup: combination of parameters above the surface will lead to droplet breakup, while combination below the surface will not.

The result indicates that with the processes described in literature it is unlikely that the droplets will undergo secondary atomization (breakup) due to the pulsating gas flow. In Table 3.4 the number of breakup events (N_{break}), sizes of parent droplet and child droplets at the first breakup ($D_{break,1}$ and $D_{child,1}$, respectively), as well as the final droplet diameter ($D_{d,end}$) for all simulation variations are presented. For the same initial droplet size, earlier breakup obviously results in bigger child droplets. However, a droplet may break more than once depending on the conditions, and this leads to a smaller final droplet size. The final droplet sizes are still in microscale, ranging from 2 to 32 μm depending on the droplet properties at breakup point and the number of subsequent breakups. This means that even if a droplet is predicted to break up, the final particle size would still be far from nanoscale. Nanoparticles are thus unlikely to be produced by droplet breakup, as contrary to the explanations given in the mentioned studies.

Table 3.4. Droplet sizes and numbers of breakup events for all simulation variations.

Parameter	Variation	N_{break}	$D_{\text{break},1}$ (μm)	$D_{\text{child},1}$ (μm)	$D_{\text{child},\text{last}}$ (μm)	$D_{\text{d,end}}$ (μm)
	Main	2	34.59	14.09	4.85	3.98
T_g ($^{\circ}\text{C}$)	300	2	34.52	13.24	4.58	3.70
	400	2	34.58	12.29	4.06	3.38
	600	1	34.55	12.84	12.84	9.87
	700	1	34.59	12.49	12.49	9.56
$D_{\text{d},0}$ (μm)	4	0	-	-	-	2.11
	10	0	-	-	-	6.20
	100	3	100.00	41.48	4.57	3.77
D_{pp} (nm)	5	2	38.02	15.59	4.74	3.77
	15	1	32.38	10.56	10.56	7.95
$x_{\text{s},0}$	0.05	1	25.46	10.32	10.32	8.17
	0.15	2	39.99	17.04	5.94	4.78
q_{A} (mC/m ²)	-5	1	27.36	9.22	9.22	7.04
	-15	1	38.97	14.28	14.28	10.93
\bar{u}_g (m/s)	30	2	34.61	14.10	4.87	4.00
	45	2	34.64	14.04	4.59	3.76
	60	1	34.65	12.06	12.06	9.12
$u_{\text{g,amp}}$ (m/s)	0	0	-	-	-	32.01
	15	1	34.04	14.29	14.29	11.39
	45	2	34.74	12.96	4.24	3.53
f (Hz)	100	1	34.26	14.08	14.08	11.10
	200	1	34.62	12.95	12.95	9.94
	300	1	34.55	13.14	13.14	10.13
	500	1	34.65	11.46	11.46	8.58
	600	1	34.27	12.80	12.80	9.92
	700	2	34.66	12.74	3.71	2.97
φ	$\pi/4$	1	34.30	12.62	12.62	9.74
	$\pi/2$	1	34.57	12.04	12.04	9.13
	$-\pi/4$	1	34.64	11.50	11.50	8.63
	$-\pi/2$	1	34.54	13.65	13.65	10.60

The model presented here considers a classic single droplet drying in which the dried droplet (an agglomerate of colloid particles) will remain as a unity and its size will not change after the locking point has been reached. High temperature and gas pulsation could possibly affect the dried agglomerate further, and this is not considered in the model. Breakup of dried

agglomerated particles has been observed in a previous study [121]. It would be interesting to study how pulsation might possibly break the dried droplet. In the real pulse combustion drying velocity fluctuation is not uniform, and it is thus possible to get a mixture of large sized particles and of nanoparticles resulting from crust breakage. During the second drying stage, breakage of crust can also lead to the formation of a secondary crust below the first crust, resulting in a layered hollow particle or a hollow particle with one or more agglomerates inside [91,159]. The breakage of crust can result from thermal and mechanical stresses due to high temperature and pressure buildup inside the droplet [160]. The wet core will then undergo gas-side controlled drying once more, until a second locking point has been reached.

3.8 Conclusion

A model that considers drying, diffusion and breakup processes of a colloidal droplet during PCD has been developed. The idea of using TAB breakup model combined with a modified surface tension could predict and explain the physical mechanism of colloidal droplet breakup. It has been shown how the situation created in PCD facilitates droplet breakup. The presence of solid particles inside a droplet makes the droplet more vulnerable to the surrounding fluid flow and easier to break. The interactions among solid particles are important here. Electrostatic repulsion, especially, plays a big role in determining osmotic pressure and effective surface tension of a colloidal droplet. For easier colloidal droplet breakup, a large droplet, small nanoparticles, high surface charge, high gas temperature, strong gas oscillation, and relatively high frequency are favorable.

It has been shown that for the processes presented in previous studies [13,16] droplets are unlikely to break. Moreover, even if large droplets can break, there is still a minimum droplet size for breakup. Therefore, droplet breakup cannot be considered as the main reason for the reported production of nanoparticles by PCD. Another explanation for the production of nanoparticles is required. In this context, it would be interesting to investigate how the dried droplet is further affected by the surrounding environment.

4. Experimental study on powder production using pulsating hot air

This chapter contains an extended part of the publication “Crust breakage in production of fine particles using pulse combustion drying: Experimental and numerical investigations”, which was published in Powder Technology [70].

4.1 Introduction

In the previous chapter it has been shown that while droplet breakup can happen during drying, there is a limit of how small the droplets can be until they can no longer break before locking point is reached. Without any inflation-deflation, the locking diameter is the minimum diameter that a particle resulting from a droplet can have. An experimental study has been performed to see whether fine particles smaller than anticipated (down to nanoscale) can be obtained. Three materials, namely silica (SiO_2), titania (TiO_2), and maltodextrin, were used for the experiments to investigate the influence of material types and properties. The first two are water-insoluble metal oxides with quantitatively different properties. The last one is a potentially sticky and water-soluble material of totally different nature. Two main process parameters in PCD, namely gas temperature and pulsation frequency were varied to see how they influence the morphology and size distribution of the produced particles. Atmospheric air is used as the drying gas instead of combustion flue gas for technical and safety reasons. Possible influences of types of drying media and the humidity of drying gas on product properties are outside of the scope of this study.

4.2 Materials and methods

4.2.1 Materials

Commercially available colloidal silica LUDOX® HS-40 (Sigma-Aldrich, USA) with pH of 9.7 and SiO_2 content of 40%-m, and average primary particle diameter of 12 nm is used. Silica suspension with concentration of 10%-m ($\approx 4.49\%$ -v) was prepared by diluting the colloid with water, resulting in pH of 8.92. The suspension of TiO_2 was prepared by dispersing TiO_2 nanoparticles (NanoArc™, anatase, Alfa Aesar, ThermoFisher GmbH, Germany, $D_{pp} = 32$ nm) in water to achieve a 5%-m ($\approx 1.23\%$ -v) mixture. The nanoparticle suspensions were homogenized (sonicated) using Sonopuls Ultrasonic Homogenizer HD 3200, probe MS 72 (BANDELIN electronic, Germany) at 50% power for 2 minutes, according to the requirements

set in [161,162]. Maltodextrin solution of 10%-m was made by dissolving maltodextrin powder (DE20) in water.

4.2.2 PCD-unit

A smaller version of the Glatt Powdersynthesis® pulse spray dryer by Glatt Ingenieurtechnik GmbH is used for the experiments. Schematic of the lab-scale unit is given in Fig. 4.1. The main chamber for the drying process has a height of 1.5 m and diameter of 0.1 m. The chamber is insulated with 3 cm of glass wool. Air flow is created by a vacuum pump with absolute pressure of 500 Pa, which gives an air flow rate of 60 m³/h at 20 °C. The stationary air flow is converted into a pulsed flow with a pulsation generator, which has a rotating unit that will create an intermittent opening for the gas flow. The maximum opening cross sectional area can be adjusted with a valve mechanism. The rotation frequency is set by an electric motor with controllable frequency. It will be the same as the pulsation frequency once the flow pulsation becomes steady.

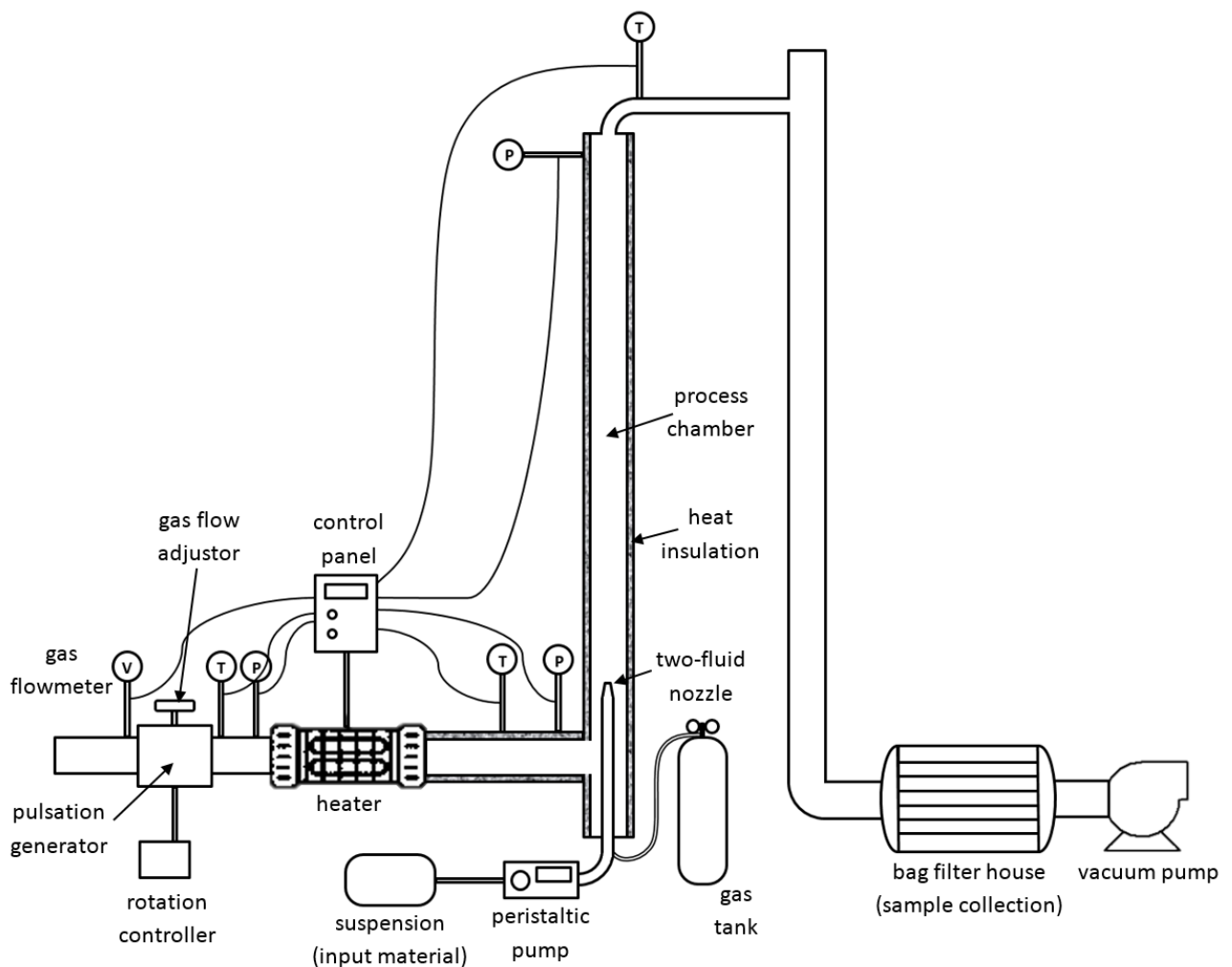


Fig. 4.1. Schematic of the lab-scale pulse combustion drying unit.

4.2.3 Drying process

The suspensions were fed into the drying chamber using a peristaltic pump operated at 17 rpm, giving flow rate of 25 mL/min. They were atomized using two-fluid nozzles (Schlick 970/0-S04, Germany) with nozzle diameter of 1 mm for the metal oxide suspensions and 2 mm for maltodextrin, gauge pressure of 1 bar and atomizing gas flow at 2.2 Normal m³/h (1.18 m³/h at 20 °C). The initial velocity of droplets released from the two-fluid nozzle is estimated at 40 m/s, which is in the range of values calculated or measured in other studies [69,138]. Dried powders were collected in a filter house equipped with Polyphenylensulfid filter cartridges (class H13). The obtained samples were analyzed with a scanning electron microscope.

4.2.4 Experimental conditions

Inlet gas temperature is varied at 400, 500, and 600 °C for the metal oxide colloids. For maltodextrin, the temperatures are set lower at 200, 250, 300, and 400 °C to avoid the possibility of dust explosion. Pulsation frequency is varied at 0, 40, 80 and 120 Hz. The sets of operating conditions are given in Table 4.1.

Table 4.1. Sets of operating conditions used for the experiments.

Material	$T_{g,in}$ (°C)	f (Hz)	$T_{g,out}$ (°C)	ΔT_g (°C)	p_{amp} (Pa)	\bar{u}_g (m/s)	$u_{g,amp}$ (m/s)
SiO ₂	500	0	347	153	6	5.60	0.02
	500	40	335	165	55	5.60	0.15
	500	80	341	159	1656	5.60	4.63
	500	120	373	167	194	5.60	0.54
	400	120	259	141	1222	4.87	3.19
	600	120	369	231	194	6.32	0.58
TiO ₂	500	0	296	204	30	5.60	0.08
	500	40	291	209	210	5.60	0.59
	500	120	319	181	200	5.60	0.56
	500	80	349	151	790	5.60	2.21
	400	80	225	175	1247	4.87	3.26
	600	80	370	230	615	6.32	1.83
Maltodextrin	300	0	167	133	32	4.15	0.08
	300	120	188	112	120	4.15	0.29
	300	80	176	134	1420	4.15	3.42
	200	80	102	98	1295	3.43	2.84
	250	80	139	111	1210	3.79	2.79
	400	80	242	158	1247	4.87	3.26

The variables obtained from measurement during the experiments are gas temperature at the end of the drying chamber $T_{g,out}$ and pressure amplitude p_{amp} . The latter is measured at the chamber entrance and can be used to obtain the amplitude of gas velocity surrounding the droplets (Eq. 2.51).

4.2.5 Particle size measurement

The morphology and size distribution of the produced particles were investigated using scanning electron microscopy (FEI/Philips XL30 ESEM FEG). Characteristic size (diameter) of each particle D_i was obtained by drawing a center line on each particle in the image, and filtering the image so that only the marking lines are left (see Fig. 4.2). The pixel length of each line was converted to physical length units to obtain the diameter of each particle. In the images, some particles are located at the image border. From these particles, only those with more than 50% shown area of projection were considered and marked. This center line marking method has some advantages over other image analysis methods such as projection area measurement, in which the pixel number of the projected area of a particle is used to calculate its diameter. A similar method has been used to analyze the size distribution of ground ferronickel slag [163] and pulverized peat particles [164]. Projection area methods, usually require conversion into a binary image with a certain threshold value to determine whether a pixel is considered as black or white [165]. This may lead to reduction of border area of the particles, omission of small particles, and inclusion of non-existent particles. Such undesired effects will not happen with the center line marking method. Another obvious advantage of this method is that it is possible to measure overlapping particles, as can be seen in Fig. 4.2. The main disadvantage is that this method is more manual and relies on the subjective judgment for determining the center line and the objects to be included.

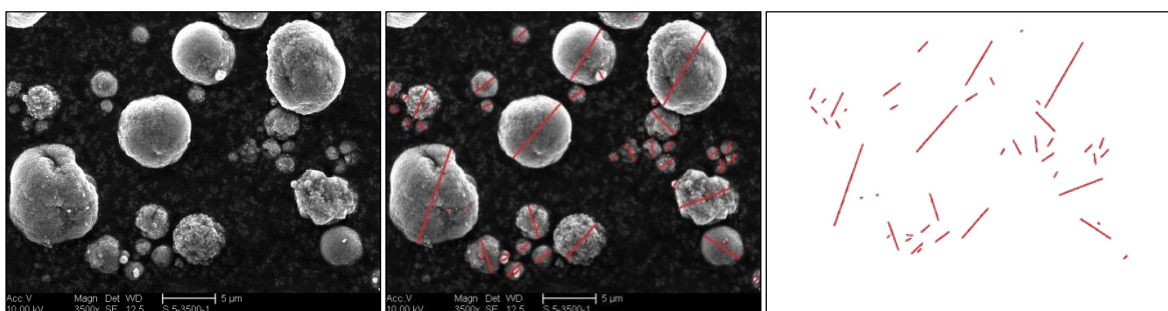


Fig. 4.2. SEM images of TiO_2 particles before marking (*left*), after marking (*middle*), and after filtering (*right*).

An SEM image of a certain magnification can show clearly only particles of a certain size range. Larger particles can be captured better with low magnification, whereas the smaller ones require large magnification. Thus, to get the distribution of the wide range of particle sizes expected here (from nano- to microscale) SEM images of different magnifications must be

obtained. Four magnifications, namely 1200x, 3500x, 8000x, and 35000x were used for all samples. Additional magnifications of 800x and 15000x were also used for SiO₂ particles.

Volume and number distributions of particles over the whole size range could be obtained using a method proposed by Mazumdar and Irdi [166]. While the method has been introduced for particle diameter, in principle it is also applicable for other types of particle size measures (number, volume, etc.). The volume and number distributions of particles were calculated from the measured SEM data using the method by Mazumdar and Irdi [166]. Particle data obtained from each SEM image are weighted based on the image area, which is determined by the magnification. The weighting factor for SEM images of j^{th} magnification, K_j , is calculated as the ratio of the image area of a reference magnification to the image area of j^{th} magnification. In this study the magnification 1200x is used as the reference. For every range of particle size, the estimated total volume of particles in an image of the reference magnification is given by

$$V_{\text{eq}} = \sum_{j=1}^{N_m} \frac{K_j V_{\text{tot},j}}{m_j}. \quad (4.1)$$

Here, m_j is the number of images obtained with j^{th} magnification, and N_m is the number of magnifications. $V_{\text{tot},j}$ denotes the total volume of particles measured in m_j images under j^{th} magnification.

Volume-based normalized particle size distribution (cumulative) is defined as

$$Q_3(D_i) = \frac{\sum_{i=1}^{N_{D_i}} V_i}{\sum_{i=1}^N V_i}, \quad (4.2)$$

with N_{D_i} as the number of particles with diameter $D \leq D_i$ and N as the total number of particles. $Q_3(D_i)$ quantifies to the volume fraction of particles with diameter lower than D_i . Particle volume V_i is calculated directly from D_i , by assuming a perfect spherical shape and neglecting the void volume. For the current case with multiple image magnifications, V_{eq} is used in the place of V_i in Eq. 4.2.

The normalized distribution density is the first derivative of the cumulative distribution, which in logarithmic plots (as presented in this manuscript) is calculated as

$$q_3(\log D_i) = \frac{dQ_3(D_i)}{d \log D_i}. \quad (4.3)$$

The k^{th} normalized moment of the distribution is defined as:

$$\mu_{k,3} = \int_{D_{\min}}^{D_{\max}} D^k dQ_3(D) \approx \sum_{i=1}^N D_{\text{mid},i}^k (Q_3(D_{\text{mid},i}) - Q_3(D_{\text{mid},i-1})), \quad (4.4)$$

where N is the number of bins and $D_{\text{mid},i}$ indicates the middle value of particle size range i , defined as $D_{\text{mid},i} = (D_i + D_{i-1})/2$. For $k = 1$, the equation yields the mean particle diameter $\mu_{1,3}$.

The standard deviation of the particle size distribution is calculated as

$$\sigma_3 = \sqrt{\mu_{2,3} - (\mu_{1,3})^2}. \quad (4.5)$$

The index 3 in above equations indicates that the distribution is calculated on the basis of volume. Similar equations hold when the other types of particle size measures are used as the basis.

4.3 Results and discussions

4.3.1 Flow dynamics

It has previously been reported that with a higher inlet gas temperature the difference between inlet and outlet temperature of a spray dryer increases [22]. In the experiments, this trend is also observed for all materials (Table 4.1). It indicates a better thermal efficiency of the dryer, which is defined as the ratio between the energy used for evaporation to the energy supplied [2]. The evaporative efficiency, which is the ratio of evaporated water to the moisture uptake capacity of the drying air, can, however, be lower. The effect of pulsation frequency is, on the other hand, unclear. Oscillation of gas velocity has been shown to result in higher heat and mass transfer between the gas and solid spherical objects [19], as the relative velocity between the object and the gas could be prevented from going to zero quickly.

It can also be seen from Table 4.1 that at a given temperature, varying pulsation frequency results in different velocity amplitude. The two parameters are always related in a real situation, as different frequencies would give different pressure fluctuation in the pulse combustion dryer and subsequently change the amplitude of velocity fluctuation. The data show that at 500 °C the frequency that gives the highest velocity amplitude is 80 Hz. Measurement of pressure fluctuation has shown that in the drying chamber resonances could be obtained in the ranges of 55-65 Hz and 80-90 Hz. When the frequency is closer to the resonant frequencies, higher pressure and velocity amplitude can be expected. In general, the gas velocity amplitude is still smaller than the average velocity, due to the relatively minor pressure fluctuation.

A previous simulation study shows that when the pulsation is intensified droplets tend to stay more in the center region of the chamber [68], and thus wall deposition can be decreased. This tendency becomes stronger with smaller droplet size. Simulations in [68] were conducted with the same drying chamber as used here, but with much larger droplets of 125-500 μm . It can thus be safely assumed that in our study the droplets will stay in the center region.

Therefore, even though with the two-fluid nozzle the droplets were sprayed with a spray angle, wall deposition could be minimized.

4.3.2 Maltodextrin

In drying practice, maltodextrin can be used as an additive for sugar-rich and sticky food materials. It results in a harder droplet crust and lowers the diffusivity of vapor through the crust [167]. This, in addition to the low heat capacity of maltodextrin, increases the droplet temperature quickly as drying proceeds and maltodextrin concentration increases. Addition of maltodextrin, however, also results in visible surface wrinkles and droplet deformation from the spherical shape, which to some extent may increase the evaporation rate. During the second drying stage of a solid crust with liquid core, the temperature of surface solid increases to surrounding gas temperature. For materials like maltodextrin, glass transition temperature (T_{glass}) determines whether the material is sticky or glassy in nature. The material is sticky when T_{glass} of the surface layer is lower than droplet temperature, and is non-sticky when T_{glass} is higher than droplet temperature by 10 °C [168]. With the high gas temperatures employed in this study, the droplet surface temperature will increase above the glass transition temperature after the transition to the 2nd drying stage, and as a result the crust becomes sticky.

Figure 4.3a shows SEM images of maltodextrin powder produced at different temperatures and pulsation frequencies. Mostly hollow particles with high porosity were produced. At gas temperatures of 200, 250 and 300 °C most particles are non-spherical with surface wrinkles (shriveled particles), while at 400 °C most of the particles are spherical with relatively smooth surface. At frequency of 80 Hz and inlet gas temperature of 200 °C the spherical particles made up around 11.2% of the total volume (Fig. 4.3b). This share increased to 53.0% at 250 °C. When the temperature is further increased to 300 °C, the fraction of spherical particles decreases again. Instead, torn (split-broken) particles appear. Interestingly, these torn particles were not found at 200, 250 and 400 °C, but were always there at 300 °C, no matter whether there was gas pulsation or not. From Fig. 4.3 it can be inferred that the torn particles were originally spherical, smooth-surfaced, and relatively large compared to the remaining population. The higher tendency of spherical particles to break, compared to the shriveled ones, has also been reported for the case of protein powder production from β -Galactosidase using nano spray dryer [47]. At 400 °C and 80 Hz most particles (94.7% by volume) are spherical and fine particles can be found on their surface. Some cracks on the surface as well as some cracked particles were observed (but not considered in the measurement).

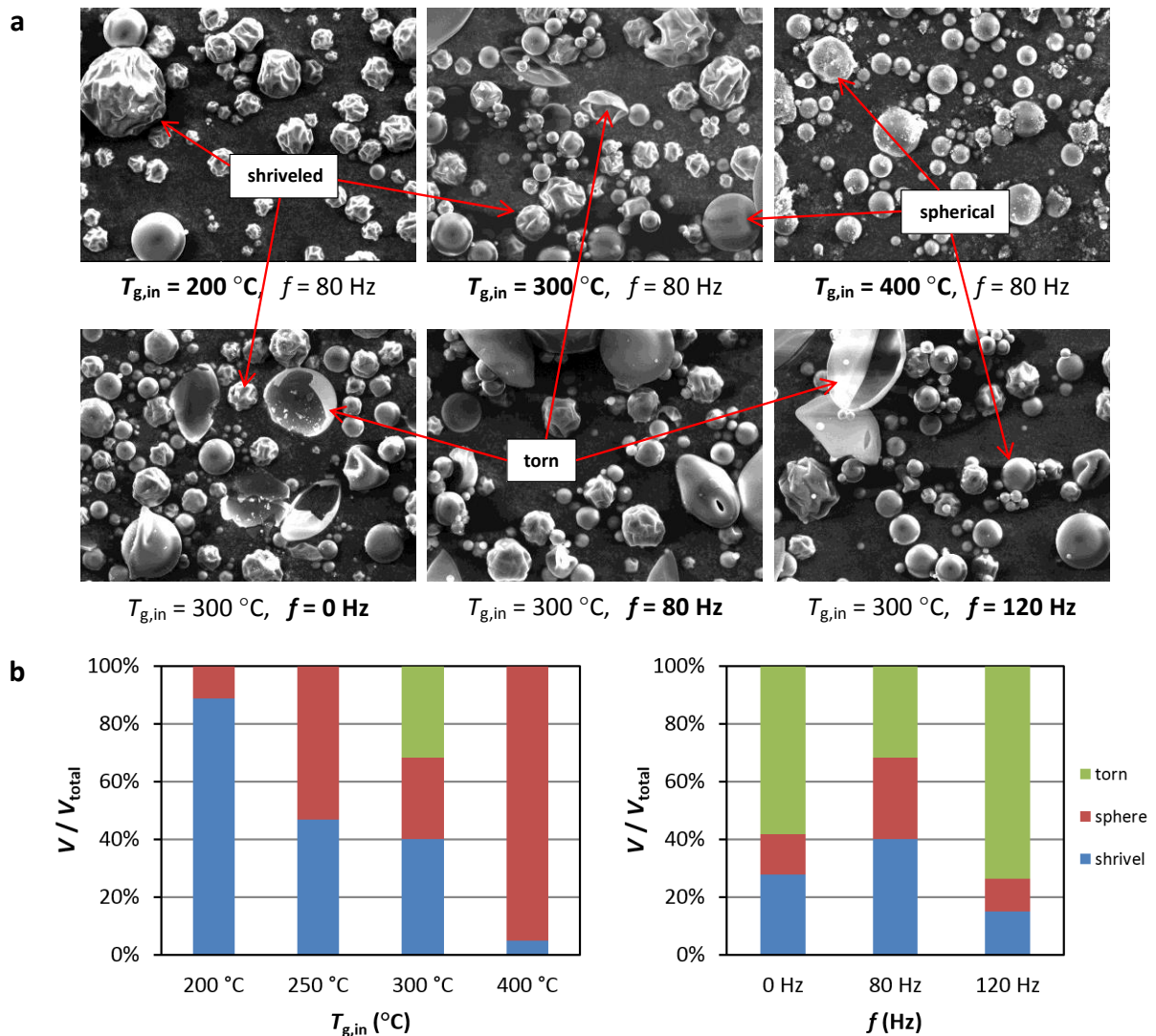


Fig. 4.3. (a) SEM images and (b) fractions of shriveled, spherical, and torn maltodextrin particles obtained with $f = 80\text{ Hz}$ at different inlet gas temperatures (*left*) and with $T_{g,in} = 300\text{ }^{\circ}\text{C}$ at different pulsation frequencies (*right*).

The change in the morphology of the maltodextrin particles with temperature can be explained as follows. During crust formation, the surface temperature increases above the glass transition temperature and the crust becomes sticky. The moisture diffusivity through the crust is greatly reduced, while the droplet temperature quickly increases. Pressure builds up inside the droplet as water evaporates and the droplet may undergo an inflation-deflation process, resulting in the formation of shriveled particles. Shriveled and irregularly-shaped particles could also be produced when there are inhomogeneities of concentration distribution in surface layer [32]. With higher surrounding gas temperature, the crust surface hardens and becomes less elastic quicker, so that inflation-deflation may not happen, resulting in more spherical particles. The pressure buildup inside the droplet is more rapid as the gas temperature is increased to $300\text{ }^{\circ}\text{C}$. The hardened crust cannot withstand the pressure and thus breaks. When the gas temperature is further increased to $400\text{ }^{\circ}\text{C}$, the crust hardens

even quicker and mostly spherical particles are produced. Additionally, thermal degradation of the maltodextrin, which usually happens when heated above 250 °C [169], starts. With inlet gas temperature of 400 °C, the outlet temperature was recorded at 242 °C. In the central region of the tube, where most of the process occurs, the probability of the droplet temperature going beyond 250 °C is high. Thermal degradation results in particles with different surface appearance compared to those found at lower temperatures.

4.3.3 Metal oxides

Figure 4.4a shows two SEM images of SiO₂ and TiO₂ particles obtained at $T_{g,in} = 500$ °C and $f = 120$ Hz, as examples. Unlike found for maltodextrin, there are no striking differences in morphology observed with different operating conditions (images not shown). If one compares between the materials, the most apparent difference is that the TiO₂ particles are more compact yet look more like agglomerates from the outside, while SiO₂ particles are slightly hollower with thinner yet solid crust. When the magnification was increased, fine particles down to nano-size were detected, as shown in Fig. 4.4b. Fine particles of submicron and nanometer sizes were found mostly on the surface of larger particles. Nanoparticles were always present in case of SiO₂, whereas hard to detect for TiO₂. This is due to the surface structure of the TiO₂ particles, which makes it hard to distinguish separate particles from surface primary particles.

Number and volume fractions of the obtained SiO₂ and TiO₂ particles at different combinations of inlet gas temperature and pulsation frequency are presented in Fig. 4.5. There are no particular trends with the variation of operating conditions. However, between the materials the differences are clear. Volume-wise the SiO₂ particles are mostly above 10 μm in diameter, and particles with diameter below 5 μm are practically negligible. However, this negligible volume constitutes a large fraction, number-wise. The distributions of TiO₂ particles are more polydisperse compared to those of SiO₂. Moreover, they are shifted to the left. The largest TiO₂ particles are smaller than the largest SiO₂ particles, which could be due to the fact the TiO₂ colloid had a lower initial solid content. The volume- and number-based statistics of SiO₂ and TiO₂ particles are presented in Table 4.2. For both materials, the fractions of nano- ($D_p \leq 100$ nm) and submicron-sized particles are negligible volume-wise. They, however, represent large parts of the whole population number-wise. The nano-sized SiO₂ particles dominate the number population, whereas for TiO₂ it is dominated by submicron particles. The influences of gas temperature and pulsation frequency on the produced fine particles are not clear.

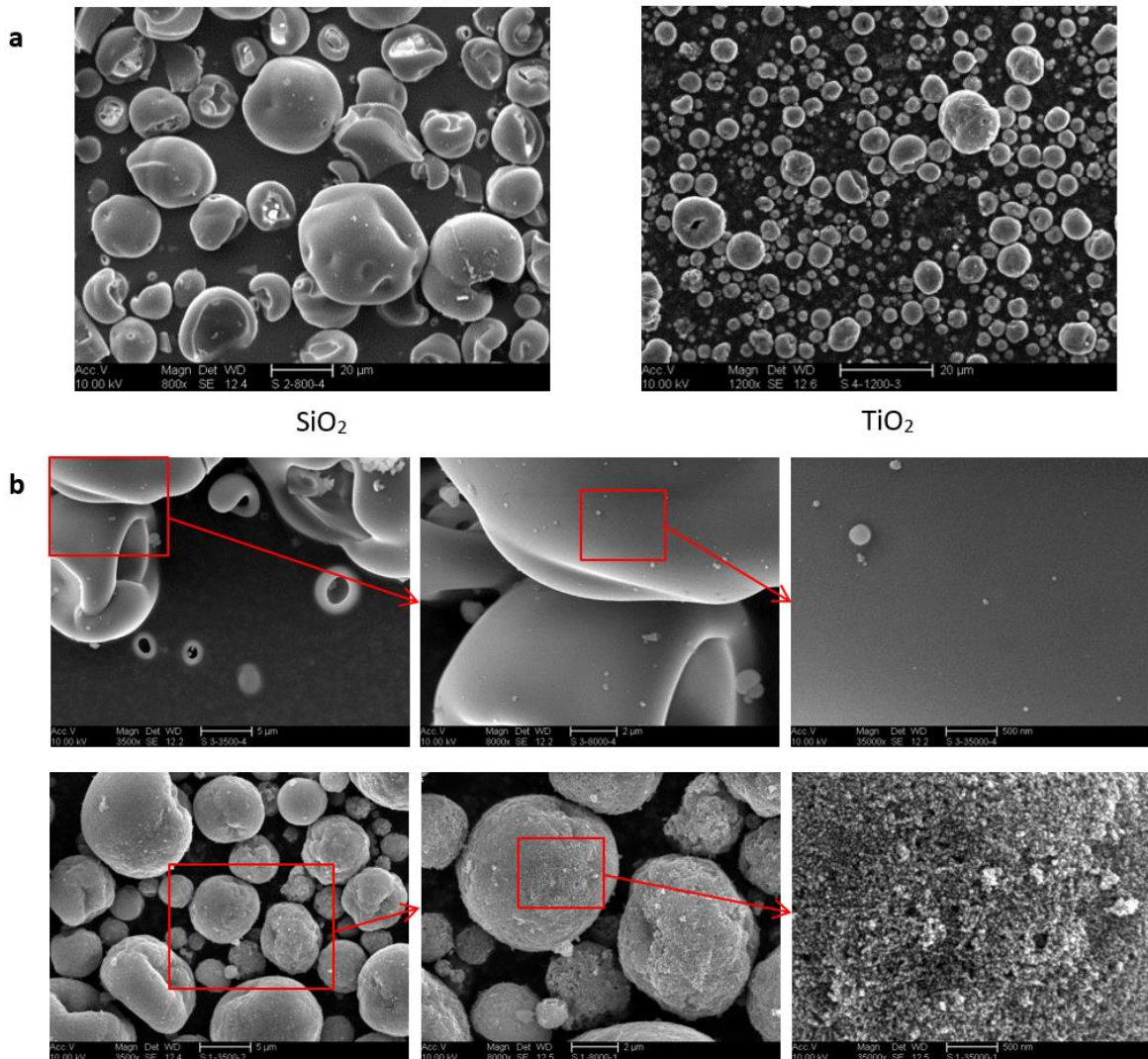


Fig. 4.4. (a) SEM images of SiO₂ and TiO₂ particles produced at $T_{g,in} = 500$ °C and $f = 120$ Hz; and (b) zoomed in SEM images (from left to right, respectively 3500x, 8000x, and 35000x magnifications) showing fine particles of SiO₂ (upper) produced at $T_{g,in} = 500$ °C and $f = 40$ Hz and TiO₂ (lower) produced at $T_{g,in} = 500$ °C and $f = 80$ Hz. Nano- and submicron particles were found mostly on the surface of larger particles.

Regarding the volume-based size distribution, it is found that in general the TiO₂ particle populations have bigger distribution spans than the SiO₂ populations. This can be explained with the fact that the SiO₂ particle size distributions have a better-defined peak, whereas for the TiO₂ particles polydispersity is observed. The span of volume-based distribution decreases in Table 4.2 with inlet gas temperature for SiO₂ and increases for TiO₂. At 400 °C both the average particle size and the distribution span are the largest for SiO₂, but for TiO₂ the particle size and the span are the smallest. The results obtained at gas temperatures of 500 °C and 600 °C are not so different. Gas pulsation results in narrower volume-based size distribution of TiO₂ particles. For the SiO₂ particles the influence on the distribution span is not clear, even though at 80 Hz its value is lower. 80 Hz is the closest frequency to one of the resonance

frequency ranges of the apparatus (80-90 Hz), and at this frequency the pulsation intensity is strongest. A difference in the average size of the oxide particles is also notable at this frequency compared to the others. At that frequency, noticeably smaller SiO_2 particles and larger TiO_2 particles were obtained.

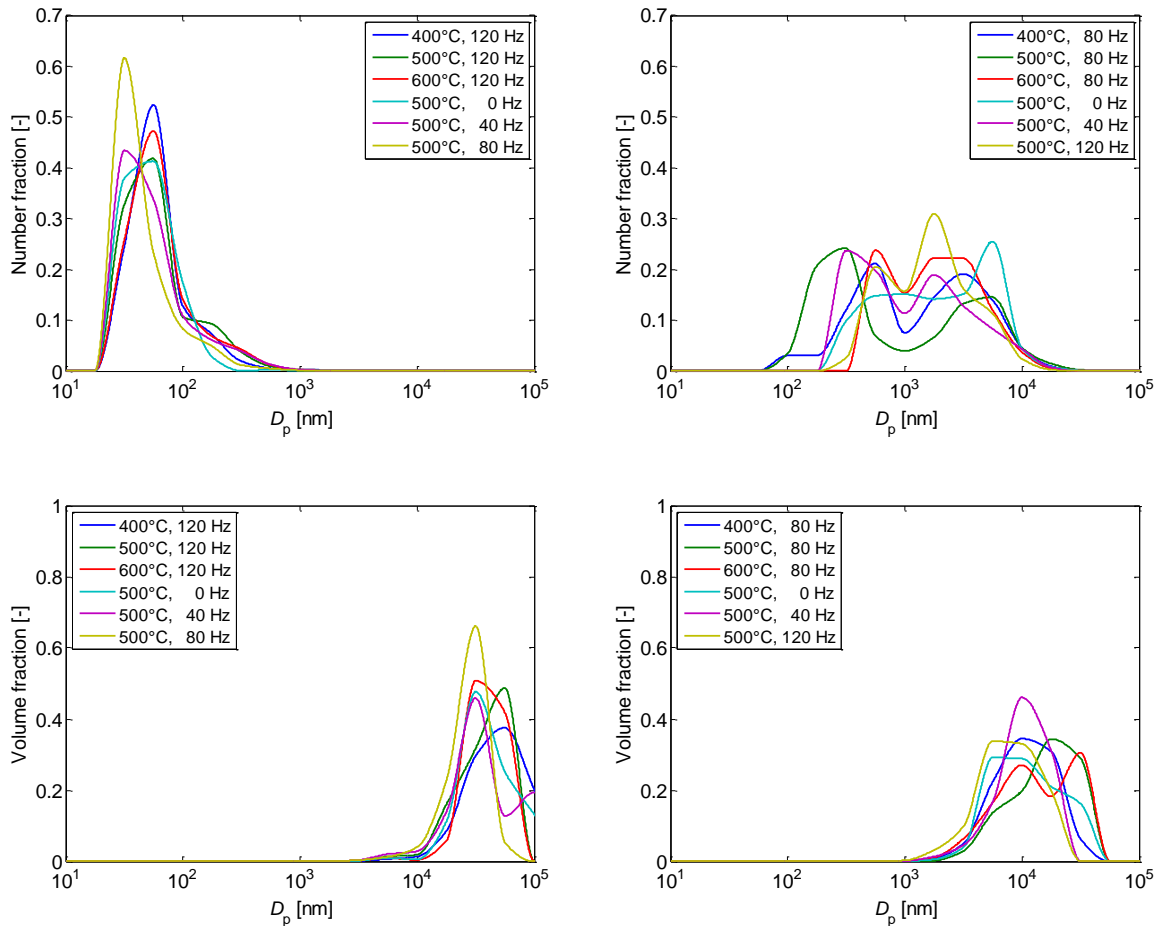


Fig. 4.5. Number (*top*) and volume (*bottom*) fractions of SiO_2 (*left*) and TiO_2 (*right*) particles obtained at different combinations of inlet gas temperature and pulsation frequency.

Aside of the diameter, for some particles it is also possible to measure the thickness of the dry crust. Figure 4.6 shows SEM images of SiO_2 and TiO_2 particles with markings for diameter and crust thickness. Only well-positioned particles with visually perceivable crust thickness could be measured. Given the difference in the morphologies of the particles, the number of TiO_2 particles of which the crust can be identified and measured is noticeably lower than that of SiO_2 particles, but still large enough for evaluation. The measurable particles are mostly in micron size. Finer particles were not measured because the crust thickness could not be seen and at smaller scale the accuracy would be very low.

Table 4.2. Number and volume-based statistics of nano- and submicron-sized particles of SiO₂ and TiO₂ obtained at various gas inlet temperatures and pulsation frequencies (span = $(D_{90} - D_{10})/D_{50}$).

Parameter	Inlet gas temperature			Pulsation frequency			
	400 °C	500 °C	600 °C	0 Hz	40 Hz	80 Hz	120 Hz
SiO₂	(at $f = 120$ Hz)			(at $T_{g,in} = 500$ °C)			
<i>Number-based</i>							
nano (%)	89.710	85.286	87.152	96.570	87.942	93.039	85.286
submicron (%)	9.965	14.267	12.580	3.321	11.632	6.755	14.267
D_{mean} (μm)	0.068	0.084	0.077	0.056	0.078	0.054	0.084
D_{10} (μm)	0.024	0.023	0.024	0.022	0.022	0.021	0.023
D_{50} (μm)	0.041	0.039	0.042	0.037	0.035	0.028	0.039
D_{90} (μm)	0.102	0.130	0.122	0.074	0.117	0.077	0.130
span	1.87	2.71	2.35	1.39	2.74	2.01	2.71
<i>Volume-based</i>							
nano (%)	0.002	0.002	0.002	0.002	0.002	0.003	0.002
submicron (%)	0.038	0.033	0.037	0.021	0.058	0.053	0.033
D_{mean} (μm)	39.92	30.42	30.52	33.69	33.84	21.34	30.42
D_{10} (μm)	16.98	13.65	19.16	16.03	13.03	12.02	13.65
D_{50} (μm)	36.10	31.08	28.84	27.38	25.26	21.50	31.08
D_{90} (μm)	69.98	46.24	44.93	62.37	71.61	29.01	46.24
span	1.47	1.05	0.89	1.69	2.32	0.79	1.05
TiO₂	(at $f = 80$ Hz)			(at $T_{g,in} = 500$ °C)			
<i>Number-based</i>							
nano (%)	3.027	3.457	<0.001	<0.001	<0.001	<0.001	<0.001
submicron (%)	43.856	55.820	39.163	39.789	54.804	55.820	38.822
D_{mean} (μm)	1.90	1.76	1.93	2.30	1.56	1.76	1.70
D_{10} (μm)	0.23	0.13	0.42	0.32	0.24	0.13	0.41
D_{50} (μm)	1.17	0.35	1.34	1.51	0.79	0.35	1.24
D_{90} (μm)	4.47	4.65	4.07	4.81	3.87	4.65	3.74
span	3.63	13.04	2.72	2.97	4.62	13.04	2.67
<i>Volume-based</i>							
nano (%)	<0.001	<0.001	<0.001	<0.001	<0.001	<0.001	<0.001
submicron (%)	0.159	0.059	0.178	0.128	0.222	0.059	0.479
D_{mean} (μm)	9.28	13.60	12.57	10.17	8.44	13.60	6.82
D_{10} (μm)	3.74	4.44	3.57	3.76	3.89	4.44	2.75
D_{50} (μm)	8.13	12.73	9.72	7.67	7.99	12.73	5.92
D_{90} (μm)	15.76	23.99	24.55	21.13	13.49	23.99	12.37
span	1.48	1.53	2.16	2.26	1.20	1.53	1.62

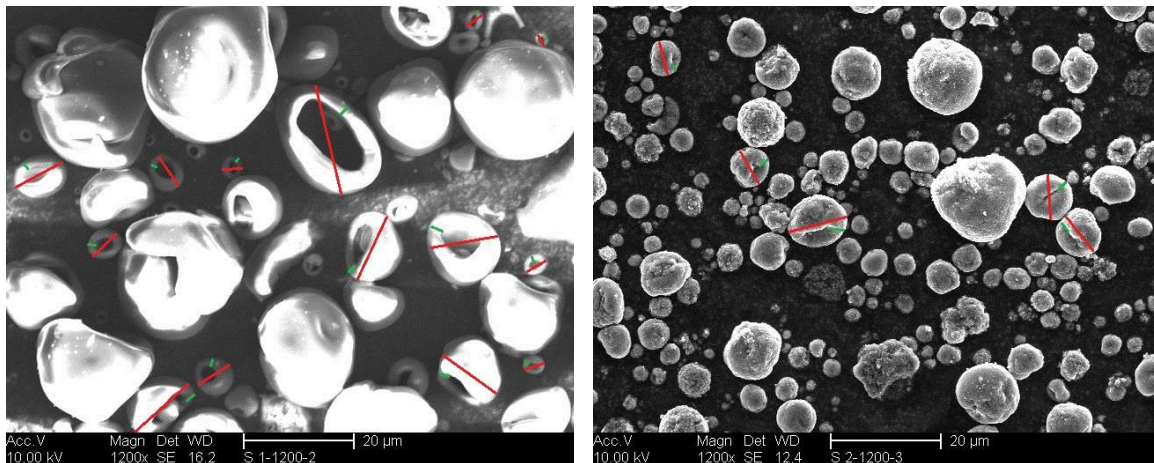


Fig. 4.6. SEM images of SiO₂ (left) and TiO₂ (right) particles with the markings of diameter (red lines) and crust thickness (green lines).

Average particle crust thickness Δ_{cr} normalized to the particle radius R_p is plotted in Fig. 4.7 for different inlet gas temperatures and frequencies. The plots indicate roughly linear correlations. The crust thickness is found to decrease with the increase in gas temperature, although the differences are small. The effect of the frequency magnitude is also small, especially for TiO₂, but it is apparent that particles produced with gas pulsation have in general thinner dry crusts. At higher temperatures evaporation is faster and the locking point, which marks the transition to the 2nd drying stage, is reached earlier, resulting in a larger particle with thinner crust and larger total porosity. Gas pulsation enhances the heat and mass transfer, so that higher evaporation rates also result in earlier locking point and thinner dry crusts.

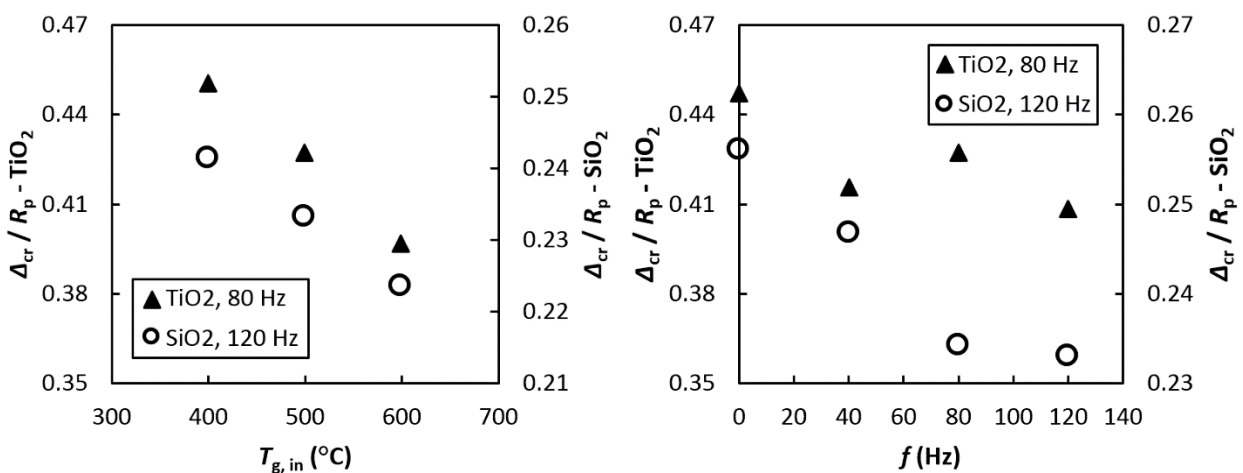


Fig. 4.7. Influence of inlet gas temperature and pulsation frequency on the measured crust thickness of the oxide particles produced.

The experimental results show that the influences of gas pulsation and its intensity on the morphologies and size distributions of the particles are still not clear. Very fine particles of nano- and submicron-size were found regardless of whether there was gas flow pulsation or not. The fine particles are too small if they are compared to the smallest possible particles that can be obtained directly from droplets sprayed from the nozzle. Taking 10 μm as the size of the smallest sprayed droplet, theoretically the smallest particle sizes that can be obtained by drying the droplet are 4.22 μm for SiO_2 and 2.78 μm for TiO_2 . Even if the droplet is made 10 times smaller, the obtained particles are still not small enough. And, particle morphologies give a hint that the dry crusts broke during the 2nd drying period.

4.4 Conclusion

Production of fine particles using pulse combustion drying has been investigated experimentally. Experiments with three different materials have been conducted to see how the material types and process conditions influence the physical properties of the final products. For a sticky organic material like maltodextrin, the final particle shapes and sizes are strongly dependent on the employed process parameters. For the metal oxides it has been shown that there are neither apparent differences nor trends in the fractions of fine particles produced with and without drying gas pulsation, within the investigated temperature range.

It must be noted that only the final products collected in the bag filter house are used as the samples here. To better validate the mechanism, more samples taken from various positions along the drying chamber would be highly desirable. However, they are still difficult to obtain and thus the data are not available yet. Further investigations on sampling methods suitable for PCD are thus required.

Based on the obtained particle morphology, it is hypothesized that further deformation and size reduction happen after the crust has been formed, and this leads to production of finer particles. In the following chapter, we propose a model that considers repetitive crust breakage events during drying as a possible mechanism that can explain the production of fine particles. The model is developed for the two colloidal oxides used in the experiments. Due to its polymeric nature, maltodextrin behaves differently and is not yet modelled.

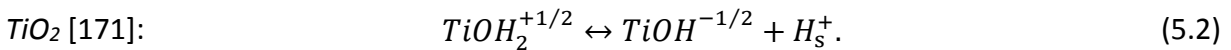
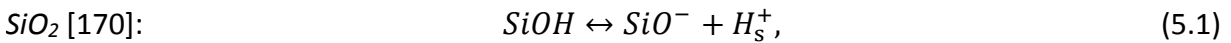
5. Modeling fine particle production via crust breakage

This chapter contains an extended part of the publication “Crust breakage in production of fine particles using pulse combustion drying: Experimental and numerical investigations”, which was published in *Powder Technology* [70].

5.1 pH-dependent charge regulation for droplet breakup calculation

The breakup model explained in Chapter 3 is used to investigate whether the colloidal droplets in the experiments might have broken up. The only difference, aside of the materials, is that the surface charge of primary particles changes dynamically with the change in the pH of the colloid, instead of previously assumed constant values. pH-dependent surface charge is calculated using 1- pK model [170,171] taking into account charge regulation [172] without overcharging [173,174].

The model is improved here by taking into account influences of colloid pH and charge regulation on the surface charge. The pH-dependence of surface charge can be calculated with the classical 1- pK model, which is quite simple yet still valid and gives accurate results for a wide range of metal oxides [170,171,175,176]. It has an advantage over the 2- pK model, in terms of being less dependent on data fitting for obtaining its input variables [177], while being similarly accurate [178]. In this study it is assumed that the surface of the metal oxides does not have any structural charge. The surface charge thus comes from deprotonation of surface groups, which follows



The respective intrinsic equilibrium constants K^{int} are given by

$$SiO_2 : \quad K^{\text{int}} = \frac{[SiO^-][H_s^+]}{[SiOH]} = \frac{[SiO^-][H^+]}{[SiOH]} \exp\left(-\frac{e_0 \psi_0}{k_B T}\right), \quad (5.3)$$

$$TiO_2 : \quad K^{\text{int}} = \frac{[TiOH^{-1/2}][H_s^+]}{[TiOH_2^{+1/2}]} = \frac{[TiOH^{-1/2}][H^+]}{[TiOH_2^{+1/2}]} \exp\left(-\frac{e_0 \psi_0}{k_B T}\right). \quad (5.4)$$

In the above equations, ψ_0 , e_0 , and T are the surface potential, the elementary charge, and the temperature of the colloid system, respectively. The exponential term correlates the activity of the removed proton on the surface, $[H_s^+]$, to that in the bulk liquid, $[H^+]$, which can be obtained from the pH of the colloid.

The total ionic site densities (as concentration per area) on the surface are

$$\text{SiO}_2 : \quad N_s = [\text{SiOH}]_0 = [\text{SiOH}] + [\text{SiO}^-], \quad (5.5)$$

$$\text{TiO}_2 : \quad N_s = [\text{TiOH}_2^{+1/2}]_0 = [\text{TiOH}_2^{+1/2}] + [\text{TiOH}^{-1/2}]. \quad (5.6)$$

Index “0” indicates the state prior to deprotonation. Defining θ_d as the fraction of surface group that deprotonates (i.e. degree of deprotonation), we get for each respective material $[\text{SiOH}]$ and $[\text{TiOH}_2^{+1/2}]$ equal to $(1 - \theta_d)N_s$, whereas $[\text{SiO}^-]$ and $[\text{TiOH}^{-1/2}]$ are equal to $\theta_d N_s$. The site density has been reported as number density ($\Gamma_s = N_{\text{AV}} N_s$) at 4.6 and 3.9 nm⁻² for SiO₂ and TiO₂ surfaces, respectively [179]. Taking into account the curvature effect due to particle shape, as well as the dense arrangement of the nanoparticles in a droplet, the effective site densities would actually be less than that in cases of two flat surfaces found in studies. In this study a single value of 3 nm⁻² is assumed.

For both cases intrinsic equilibrium constant can also be expressed as

$$K^{\text{int}} = \frac{\theta_d}{1 - \theta_d} [H^+] \exp\left(-\frac{e_0 \psi_0}{k_B T}\right), \quad (5.7)$$

which gives the correlation between bulk H^+ ion concentration, the equilibrium constant, and the degree of protonation. Rearranging the equation, we get

$$\theta_d = \frac{K^{\text{int}}}{K^{\text{int}} + [H^+] \exp\left(-\frac{e_0 \psi_0}{k_B T}\right)}. \quad (5.8)$$

By using pK , which is the bulk pH at half dissociation ($\theta_d = 1/2$), and substituting Eq. 5.7 into Eq. 5.8 gives

$$\theta_d = \frac{[H^+]_{pK} \exp\left(-\frac{e_0 \psi_{0,pK}}{k_B T}\right)}{[H^+]_{pK} \exp\left(-\frac{e_0 \psi_{0,pK}}{k_B T}\right) + [H^+] \exp\left(-\frac{e_0 \psi_0}{k_B T}\right)}, \quad (5.9)$$

with $[H^+]_{pK}$ and $\psi_{0,pK}$ the bulk H^+ ion concentration and the surface potential at $pH = pK$. Since for TiO₂ $\theta_d = 1/2$ is the condition of electroneutrality (see Eq. 5.12), $pK^{\text{int}} = pK = pK_{\text{eln}}$ [175]. For SiO₂, $pK = 7.5$ [179].

The dependence of surface potential ψ_0 on pH is calculated using the modified Nernst equation [180]

$$\psi_0 = \alpha_N k_B T \frac{\ln 10}{e_0} (pH_{\text{eln}} - pH). \quad (5.10)$$

pH_{eln} is electroneutrality point or pristine point of zero charge [181], which is taken at 2.0 for SiO₂ [182] and 5.5 for TiO₂ [183].

The variable α_N denotes the deviation from Nernstian behavior, which is the case for most metal oxides. The values for bulk SiO_2 and TiO_2 are 0.68 [184] and 0.69 [177], respectively. For nanoparticles it is expected that the values get closer to ideality and the charge density is reduced [185].

The surface charge densities are thus

$$\text{SiO}_2 : \quad q_A = e_0 N_A (-[\text{SiO}^-]) = -e_0 \Gamma_s \theta_d, \quad (5.11)$$

$$\text{TiO}_2 : \quad q_A = e_0 N_A \left(\frac{1}{2} [\text{TiOH}_2^{+1/2}] - \frac{1}{2} [\text{TiOH}^{-1/2}] \right) = e_0 \Gamma_s \left(\frac{1}{2} - \theta_d \right). \quad (5.12)$$

Surface charge density can thus be calculated as a function of pH by using Eqs. 5.9-5.12. However, it is in this way derived for dilute suspension, which is not the case of the current study. As in the present study the droplet shrinks due to evaporation, the primary particles approach each other and will come into contact at some point. Change in the distance between particle surfaces will though affect the system equilibrium and alter the surface charge density and potential [178,186,187]. This is known as charge regulation, and is illustrated in Fig. 5.1. At a certain distance between two surfaces in a polar solvent, some ions are dispersed in the solvent between the surfaces and some attach to the surface. When the two surfaces get closer to each other (the distance is decreased), the equilibrium is changed and some of the dispersed ions will attach to the surface, and thus the surface charge density decreases.

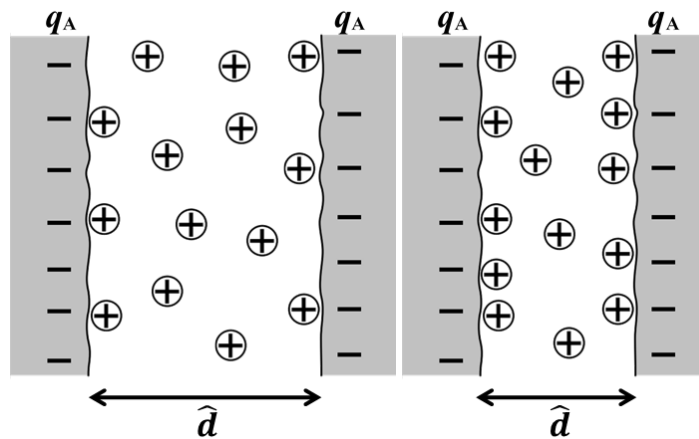


Fig. 5.1. Charge regulation due to changes in surface separation distance and ion concentration.

The average separation distance \hat{d}_{\min} between two closest primary particles in a droplet can be calculated from the droplet size, the size and number of primary particles, and by assuming that the primary particles are evenly distributed in the droplet, i.e., by neglecting concentration profiles. First, imagine that the droplet volume is fully packed with N_{pp} spheres. One sphere represents a primary particle and an imaginary space surrounding it. Taking two

closest spheres, the diameter is equal to $R_{pp} + \hat{d}$, as illustrated in Fig. 5.2. Volume of each sphere, and consequently the diameter, can be calculated from the droplet volume V_d , N_{pp} , and ϕ_{max} .

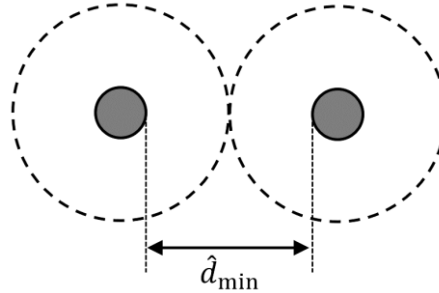


Fig. 5.2. An illustration of two imaginary spheres in contact. Each sphere represents a primary particle (*inner, solid*) and the imaginary spherical volume (*outer, dashed*) surrounding it.

The effective surface charge under this condition can be calculated from the dilute value $q_{A,\infty}$ (obtained from Eqs. 5.11 & 5.12) as a function of surface separation [172],

$$q_A(\hat{d}_{min}) = \frac{q_{A,\infty}}{p + (1 - p) \coth(\kappa \hat{d}_{min}/2)}, \quad (5.13)$$

with p a regulation parameter [186]. The value of $p = 0$, which indicates constant potential condition, is taken here. This assumption, while not the most realistic, has been shown effective and accurate enough [172], especially for oxides [186]. Primary particle density thus plays a role in charge regulation by determining the interparticle surface distance and the Debye screening length. An example of calculation is given in Appendix B.

Water evaporation increases solid concentration and pushes the pH further away from the electroneutral point. However, the dispersed ions will gradually return to the surface of colloidal particles when the interparticle distance decreases. As a result, the absolute charge density decreases, as shown in Fig. 5.3. Without charge regulation, the surface charge will continue to increase even when the primary particles are very close to each other. This is physically unrealistic, as a strong and increasing surface charge will create a strong repulsive force and not even allow a primary particle to approach another. The model explained here thus allows the determination of dynamic surface charge as a function of pH and primary particle concentration. The surface charge density then determines the DLVO forces, osmotic pressure, and effective surface tension of the colloid.

To see how surface charge and breakup of a colloidal droplet is influenced by the initial pH of the suspension, additional simulations have been performed for ZnO (the investigated material in Chapter 3). Just like TiO_2 , ZnO has the same surface charging behavior as most metal oxides [188], with pH_{eln} taken at 8.5 [189] and $\alpha_N = 0.9$ [185,190]. The results are shown in Table 5.1. Other than stated, the operating parameters are according to the main condition given in Table 3.1. At all given initial pH_0 values, droplet could break at least once.

Interestingly, droplet breakup could occur even when the colloid is initially electroneutral. As the suspension is initially basic, water evaporation increases the pH . For initially electroneutral colloidal droplet, it leads to surface charging as the pH moves away from the electroneutrality point. At $pH_0 = 8.0$, evaporation moves the droplet pH closer to the electroneutrality point. Thus, although the initial charge magnitude is the same as at $pH_0 = 9.0$ ($|q_{A,0}| = 10.9 \text{ mC/m}^2$), it takes longer for the droplet to break and the number of breakup events is less.

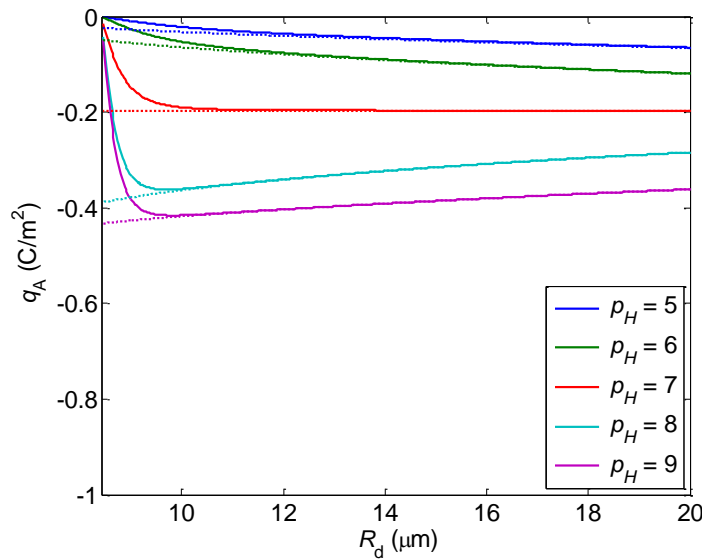


Fig. 5.3. The influence of initial pH of a colloidal silica droplet ($D_{d,0} = 40$, $x_{s,0} = 0.1$, $D_{pp} = 12$ nm), on dynamic change in surface charge during drying, with (solid lines) and without (dotted lines) regulation.

Table 5.1. Influence of initial pH on surface charge and breakup of a ZnO droplet.

pH_0	$q_{A,0}$ (mC/m ²)	N_{break}	$t_{br,1}$ (ms)	$D_{break,1}$ (μm)	$D_{child,1}$ (μm)	$D_{child,last}$ (μm)	$D_{d,end}$ (μm)
8.0	+10.9	1	9.10	23.89	7.93	7.93	5.93
8.5	0.0	2	5.78	30.16	10.84	3.48	2.59
9.0	-10.9	2	3.09	35.19	12.00	3.71	2.49
9.5	-25.0	2	1.58	38.16	13.68	4.37	2.81

5.2 Crust breakage mechanisms

It is hypothesized that the phenomenon that explains the existence of ultrafine particles in the product is breakage of the dry crust during the second drying period. In the current model two mechanisms are considered. First, the crust might break due to external force exerted by

the surrounding gas flow on the surface. Second, breakage could occur due to thermal and mechanical stresses created by the drying process inside the droplet.

5.2.1 Breakage due to external shear

Breakage of agglomerates due to external shear force is governed by the ratio of hydrodynamic drag on the compound particle to the adhesive binding force that keeps primary particles together [191],

$$N_{DA} = \frac{6 \pi \mu_g R_p^2 \dot{\gamma}}{f_b}. \quad (5.14)$$

In the above equation, μ_g is gas viscosity, f_b the binding force (defined later), and $\dot{\gamma}$ the shear rate, which is calculated [192] as

$$\dot{\gamma} = \sqrt{6} \frac{u_{rel}}{D_d}. \quad (5.15)$$

It has been observed that breakage of agglomerates into smaller fragments starts to occur when the force ratio N_{DA} is at least 5 [193], which serves as the breakage criterion in this study. The average number of primary particles in fragments resulting from agglomerate breakage due to shear flow given by [191] is

$$N_{pp,fr} = 27.9 N_{DA}^{-0.872}. \quad (5.16)$$

The number of crust fragments ($N_{fr,brkg}$) is calculated as

$$N_{fr,brkg} = N_{d,brkg} = \frac{N_{pp,cr}}{N_{pp,fr}}, \quad (5.17)$$

with $N_{pp,cr}$ the number of primary particles forming the dry crust. The number of child droplets ($N_{d,brkg}$) is assumed equal to that of crust fragments. This is a rough estimate based on the hypothesis that each crust fragment will separate a corresponding volume of liquid core. DEM simulations conducted for micron sized-agglomerates showed that the breakage timescale is 10^{-4} s [191]. Thus, it can be assumed that the crust breakage happens almost instantaneously.

5.2.2 Breakage due to internal drying

Mezhericher et al. [194] suggested that the crust will break when its strength is overcome by stresses, namely (i) thermal stresses due to the temperature profile in the dry crust and (ii) mechanical stresses due to the internal pressure of evaporating liquid.

During the second drying stage temperature of crust surface $T_{cr,surf}$ quickly increases to that of the surrounding gas, while the temperature of the liquid core T_{lc} increases at slower rate and reaches a maximum at the boiling point. As a result, there is a temperature gradient across the crust. The gradient causes thermal stresses in radial and tangential directions [195]:

$$\sigma_{T,r}(r) = \frac{2\alpha_{T,cr}E_{cr}}{1-\nu_{cr}} \left[\frac{r^3 - R_{lc}^3}{r^3(R_{cr}^3 - R_{lc}^3)} \int_{R_{cr}}^{R_{lc}} (T_{cr}(r) - 273.15) r^2 dr - \frac{1}{r^3} \int_{R_{lc}}^r (T_{cr}(r) - 273.15) r^2 dr \right], \quad (5.18)$$

$$\sigma_{T,t}(r) = \frac{2\alpha_{T,cr}E_{cr}}{1-\nu_{cr}} \left[\frac{2r^3 + R_{lc}^3}{2r^3(R_{cr}^3 - R_{lc}^3)} \int_{R_{cr}}^{R_{lc}} (T_{cr}(r) - 273.15) r^2 dr + \frac{1}{2r^3} \int_{R_{lc}}^r (T_{cr}(r) - 273.15) r^2 dr - \frac{T(r)}{2} \right]. \quad (5.19)$$

In the equations, r denotes positions along the radial direction in the crust, with $R_{lc} < r < R_{cr}$. $\alpha_{T,cr}$, E_{cr} , and ν_{cr} are, respectively, thermal expansion coefficient, Young's modulus, and Poisson's ratio of the crust. They are calculated from the solid material properties by considering the temperature and porosity of the crust [196],

$$\frac{\alpha_{T,cr} E_{cr}}{1-\nu_{cr}}(r) = \frac{\alpha_{T,s} E_s}{1-\nu_s} \left(1 - 0.35 \frac{T_{cr}(r) - 273.15}{T_{m,s} - 273.15} \right) (1 - \varepsilon)^2, \quad (5.20)$$

with $T_{m,s}$ the melting temperature of the solid.

Assuming a quasi-steady state condition, the temperature at position r in the crust is

$$T_{cr}(r) = T_{cr,surf} - (T_{cr,surf} - T_{lc}) \left(\frac{R_{lc}}{r} \right) \left(\frac{R_{cr} - r}{R_{cr} - R_{lc}} \right). \quad (5.21)$$

Substituting in Eqs. 5.18 and 5.19, it follows:

$$\sigma_{T,r}(r) = \frac{\alpha_{T,cr} E_{cr} (T_{cr,surf} - T_{lc}) R_{lc} R_{cr}}{1-\nu_{cr} (R_{cr}^3 - R_{lc}^3)} \left[R_{lc} + R_{cr} - \frac{1}{r} (R_{cr}^2 + R_{lc}R_{cr} + R_{lc}^2) + \frac{R_{lc}^2 R_{cr}^2}{r^3} \right], \quad (5.22)$$

$$\sigma_{T,t}(r) = \frac{\alpha_{T,cr} E_{cr} (T_{cr,surf} - T_{lc}) R_{lc} R_{cr}}{1-\nu_{cr} (R_{cr}^3 - R_{lc}^3)} \left[R_{lc} + R_{cr} - \frac{1}{2r} (R_{cr}^2 + R_{lc}R_{cr} + R_{lc}^2) - \frac{R_{lc}^2 R_{cr}^2}{2r^3} \right]. \quad (5.23)$$

Mechanical stresses experienced by the crust in radial and tangential directions are given by [195]

$$\sigma_{M,r}(r) = \frac{p_{cr,e} R_{cr}^3 (r^3 - R_{lc}^3)}{r^3 (R_{lc}^3 - R_{cr}^3)} - \frac{p_{cr,i} R_{lc}^3 (r^3 - R_{cr}^3)}{r^3 (R_{lc}^3 - R_{cr}^3)}, \quad (5.24)$$

$$\sigma_{M,t}(r) = \frac{p_{cr,e} R_{cr}^3 (2r^3 + R_{lc}^3)}{2r^3 (R_{lc}^3 - R_{cr}^3)} - \frac{p_{cr,i} R_{lc}^3 (2r^3 + R_{cr}^3)}{2r^3 (R_{lc}^3 - R_{cr}^3)}. \quad (5.25)$$

The difference between external gauge pressure $p_{cr,e}$ and internal gauge pressure at the liquid core-crust interface $p_{cr,i}$ is calculated from the pressure drop that corresponds to the evaporation volume flow rate \dot{V}_{vap} in the crust of thickness Δ_{cr} and volume-averaged area \bar{A}_{cr} . By analogy to a bed of primary particles [197], it is

$$\Delta p = \frac{\Delta_{cr} \mu_g \dot{V}_{vap}}{k \bar{A}_{cr}}, \quad (5.26)$$

with permeability

$$k = \frac{(1 - \sqrt{1 - \varepsilon}) R_h^2}{8} f_{Kn}. \quad (5.27)$$

Hydraulic radius is from Eq. 2.49, with

$$f_{Kn} = \left(1 + a \frac{\Lambda}{R_h}\right) \left(1 + \frac{4\Lambda}{R_h - b\Lambda}\right), \quad (5.28)$$

as a function of flow regime defined [197], slip coefficient $b = -1$ for the present case [197] and

$$a = \frac{a_0}{1 + A \left(\frac{R_h}{\Lambda}\right)^B} \quad (5.29)$$

with $a_0 = 1.205$, $A = 0.199$, and $B = 0.365$ for water vapor [198,199].

Total stresses in radial and tangential directions are calculated by superposition of the thermal and mechanical stress:

$$\sigma_r(r) = \sigma_{T,r}(r) + \sigma_{M,r}(r), \quad (5.30)$$

$$\sigma_t(r) = \sigma_{T,t}(r) + \sigma_{M,t}(r). \quad (5.31)$$

Breakage is assumed to happen when either the total radial stress or the total tangential stress exceeds the mechanical strength of the dry crust (explained later) at more than half of the crust thickness.

Figure 5.4 illustrates successive breakage events of dry crust due to stress buildup. It is hypothesized that the crust will break into two parts (binary breakage), resulting in the half-spherical shells that can be observed in the SEM images. During the breakage it can be expected that a small fraction of the crust at the breakage line (i.e., crack surface) will be shattered into small debris particles. The liquid core containing water and solid primary particles will be splashed due to the breakage into smaller droplets, which will undergo further drying process. Just like in the case of droplet breakup during the first drying stage, the breakage and splashing will create a mixing effect, so that solids inside the child droplets will be redistributed and the concentration gradient will vanish. For simplicity it is assumed that child droplets have the same size. Their diameter thus depends on how many child droplets are created. It is initially assumed that the number of child droplets from one liquid core will be the same as the number of broken crust pieces.

As mentioned earlier, a small fraction at the crack surface may get fragmented into small particles. If the thickness of the shattered part is known, the volume of debris and the diameter of debris particles can be calculated from the dimensions of the crust at the point of breakage, which is depicted in Fig. 5.5.

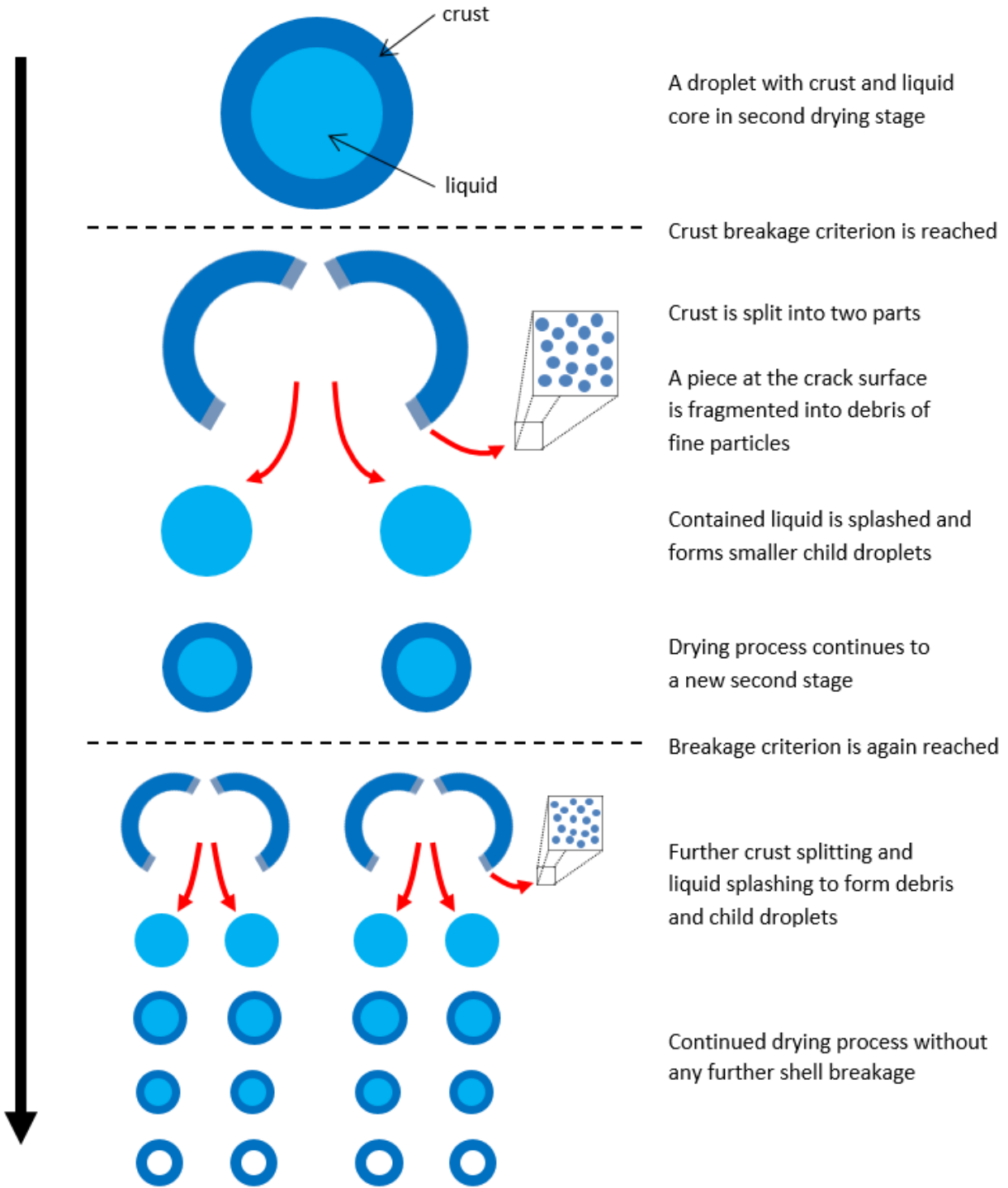


Fig. 5.4. An illustration of the hypothesized processes of binary crust breakage and smaller droplet formation from the liquid core right after the crust breakage. The number of resulting child droplets may vary.

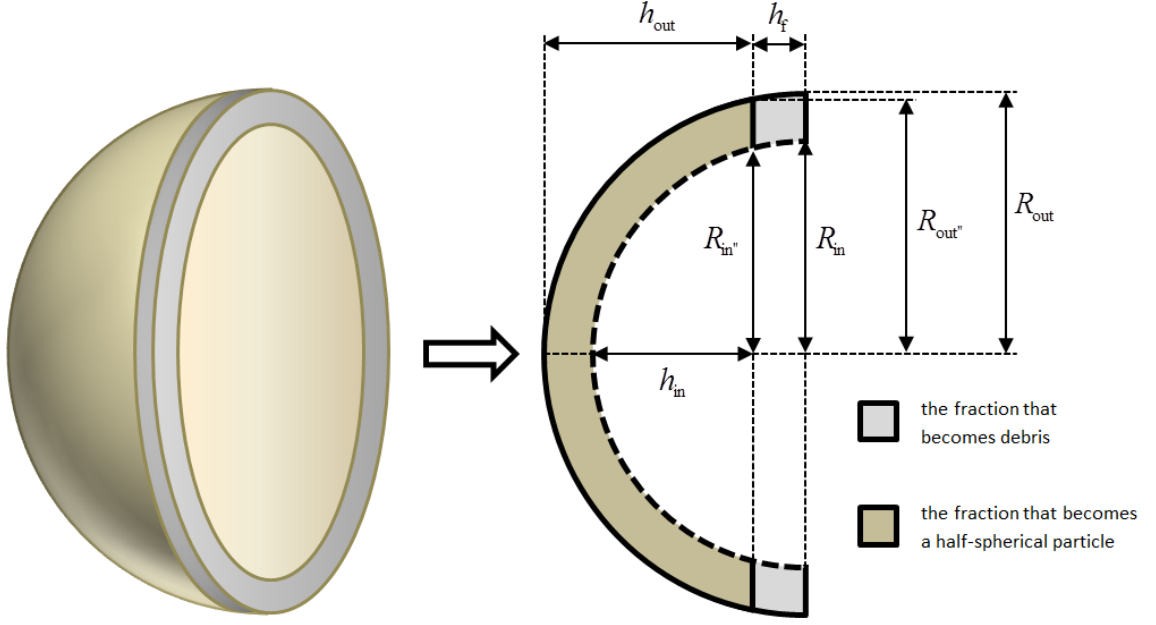


Fig. 5.5. An illustration of a half-split broken crust and its dimensions.

Volume of crust right before breakage can be calculated from the outer radius $R_{\text{out}} = R_{\text{cr}}$ and inner radius (i.e., the liquid core radius) $R_{\text{in}} = R_{\text{lc}}$ as follows,

$$V_{\text{cr}} = \frac{4}{3}\pi(R_{\text{out}}^3 - R_{\text{in}}^3). \quad (5.32)$$

The thickness of the piece that turns into debris h_f is assumed to be equal or smaller than crust thickness at the point of breakage

$$h_f = f_{\text{dbr}}(R_{\text{out}} - R_{\text{in}}), \quad (5.33)$$

by an adjustable factor $f_{\text{dbr}} (\leq 1)$. From Fig. 5.5 it can also be seen that

$$h_f = R_{\text{out}} - h_{\text{out}} = R_{\text{in}} - h_{\text{in}}. \quad (5.34)$$

The volume of crust after debris formation is

$$V_{\text{cr,red}} = \frac{2\pi}{3} \left(h_{\text{out}}^2 (3R_{\text{out}} - h_{\text{out}}) - h_{\text{in}}^2 (3R_{\text{in}} - h_{\text{in}}) \right), \quad (5.35)$$

whereas the new outer radius, i.e., the radius of the obtained hollow particles, is calculated as

$$R_{\text{cr,red}} = R_{\text{out}'} = \sqrt{2R_{\text{out}}h_{\text{out}} - h_{\text{out}}^2}. \quad (5.36)$$

Similarly, the new inner radius is

$$R_{in''} = \sqrt{2 R_{in} h_{in} - h_{in}^2}. \quad (5.37)$$

The volume of debris is thus given by

$$V_{dbr} = V_{cr} - V_{cr,red}. \quad (5.38)$$

Although it can be expected that there will be a size distribution for the debris, it is assumed that the distribution will be narrow enough so that it can be neglected without later affecting the final particle size distribution. The number of debris particles can thus be calculated from the average size $\bar{D}_{p,dbr}$ as

$$N_{dbr} = \frac{V_{dbr}}{V_{p,dbr}} = \frac{6}{\pi} \frac{V_{dbr}}{\bar{D}_{p,dbr}^3}. \quad (5.39)$$

The average debris particle size is also calculated as a fraction of the crust thickness,

$$\bar{D}_{p,dbr} = f_{frg} (R_{out} - R_{in}). \quad (5.40)$$

The number of debris particles calculated using Eq. 5.39 does not necessarily have to be an integer, as in the end it will be summed up to obtain the size distribution. The minimum limit of debris particle size is ideally the primary particle size, however in the measurements no particles as small as the primary particles were found. Therefore, the lower size limit is set to the minimum particle sizes found, which are approximately equal to $2 D_{pp}$ (24 nm) for SiO₂ and $3 D_{pp}$ (96 nm) for TiO₂. The two key parameters, which are f_{dbr} and f_{frg} , will be varied in the simulation to see how they influence the final particle size distributions.

5.3 Dry crust strength

The strength of the dry crust is directly calculated as the strength of particle agglomerate using Rumpf equation [115]:

$$\sigma_{cr} = j_n \frac{1 - \varepsilon_{cr}}{\pi} \frac{f_b}{D_{pp}^2}. \quad (5.41)$$

The adhesive force f_b may in general have a van der Waals and a sintering component

$$f_b = f_{vdw} + f_{sint} = \frac{A}{12} \frac{R_{pp}}{z^2} \left(1 + N_{sint} \frac{\bar{\sigma}_s}{2R_{pp}} \right), \quad (5.42)$$

with z the minimal intermolecular distance. Assuming that a primary particle is composed of spherical molecules, z is taken equal to the effective molecular diameter and can be calculated from solid density ρ_s and molar mass M_s ,

$$z = \sqrt[3]{\frac{6M_s(1 - \varepsilon_{\text{bed}})}{\pi \rho_s N_{\text{Av}}}} \quad (5.43)$$

The adhesive force due to sintering f_{sint} is defined as the attractive force between two solid molecules times the number of molecule pairs N_{sint} that form a sinter neck. For metal oxides, sintering is dominated by grain boundary diffusion, which does not lead to compaction (i.e., distance between particle centers remains the same). The increase in the ratio of sinter neck radius to the primary particle radius $r_{\text{sint}} = R_{\text{neck}}/R_{\text{pp}}$ can be calculated as [200]

$$\frac{dr_{\text{sint}}}{dt} = \frac{32 z_{\text{GB}} \delta_{\text{GB}} \gamma_s V_{\text{mol}} r_{\text{sint}}^{-5}}{R T R_{\text{pp}}^4}; \quad (5.44)$$

with z_{GB} the thickness of grain boundary (taken as 0.5 nm), δ_{GB} grain boundary diffusion coefficient, γ_s surface energy of the material, and V_{mol} the molecular volume (in m³/mol). The grain boundary diffusion coefficient and the surface energy can be calculated for TiO₂ [201] and SiO₂ [202] using the following equations, respectively:

$$D_{\text{GB}}\gamma_s = \frac{1.064 \times 10^{-19}R}{\delta V_{\text{mol}}} \exp\left(-\frac{258000}{RT}\right), \quad (5.45)$$

$$D_{\text{GB}}\gamma_s = \frac{2.703 \times 10^6 RT}{\delta V_{\text{mol}}} \exp\left(-\frac{61000}{T}\right). \quad (5.46)$$

Preliminary simulations show that the sintering effect is very small and negligible. This is because the process happens in a much smaller timescale compared to that of sintering.

5.4 Simulation setup

A flow chart of the whole simulation incorporating droplet drying, droplet breakup, crust formation, and crust breakage is presented in Fig. 5.6. The simulation starts with the 1st drying stage. During this period droplet breakup may occur several times, as long as the locking point has not been reached. When the droplet surface has been saturated with solid, a shell of primary particles is formed. As drying continues and the evaporation front recedes, primary particles are pulled to the center by the receding liquid surface; the shell undergoes cycles of submergence-resurgence and gets thicker. When the shell is thick and strong enough to withstand the compressive stresses, it will keep its position (locking point) and the second drying stage starts. When the breakage criterion is fulfilled, the crust breaks and the liquid core splits into smaller droplets. The child droplets will again undergo the drying process from the 1st stage and the process keeps on repeating until the droplets exit the chamber.

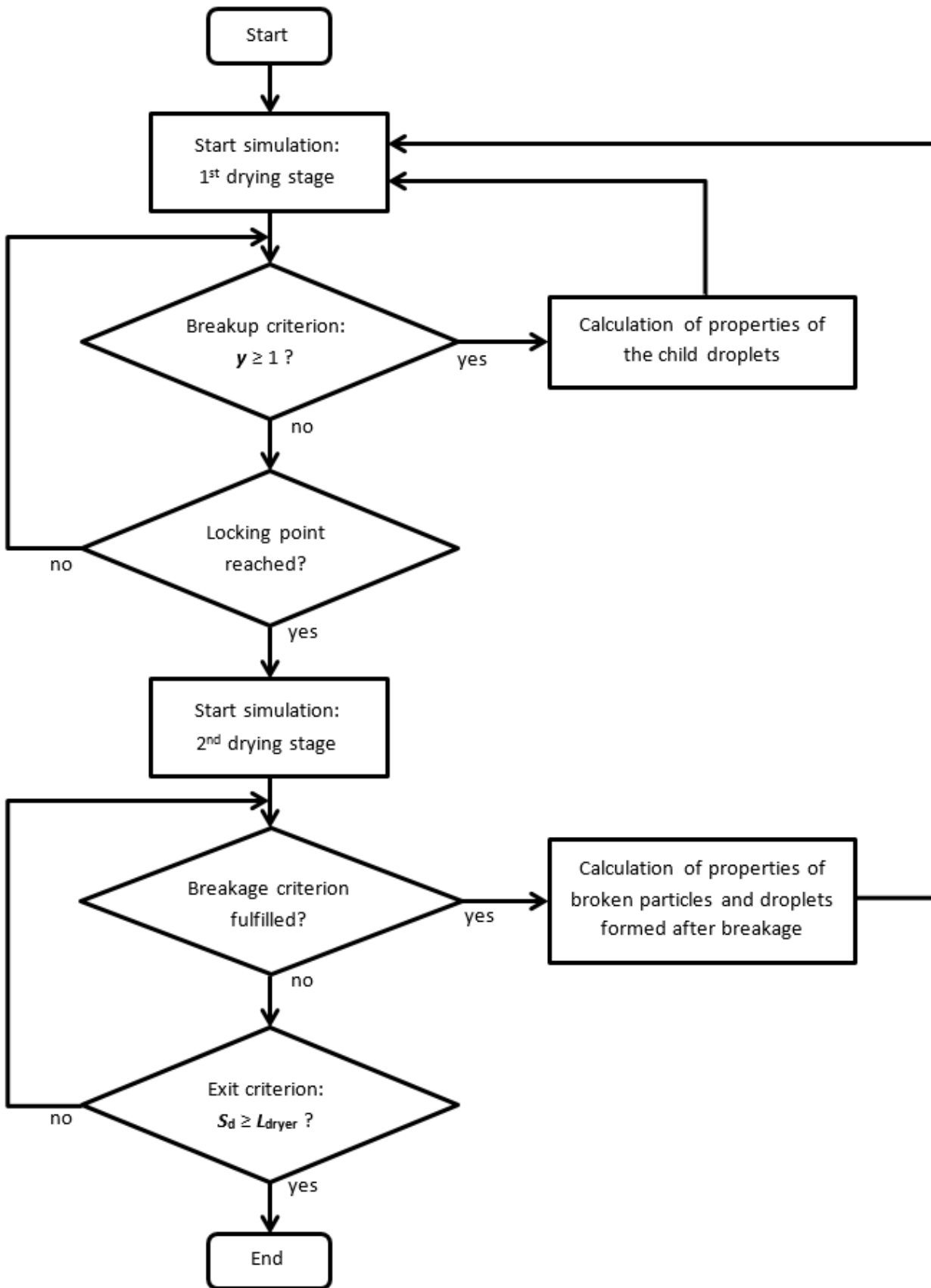


Fig. 5.6. Flow diagram of the simulation.

When a two-fluid nozzle is used, atomization is mainly influenced by the nozzle spraying properties and not by the surrounding flow. According to the specification datasheet, at the atomizing pressure the nozzle gives water droplet sizes in the range of 25-70 μm , with most droplets below the middle value. The Sauter mean diameter (SMD) of droplets produced using a two-fluid nozzle can be calculated with good accuracy using the equation by Mansour & Chigier [203],

$$D_{32,d} = D_{1o} \left(1 + \frac{\dot{V}_{n,l}}{\dot{V}_{n,g}} \right) k_2 \left(\frac{\mu_1 \sqrt{\sigma_1}}{\rho_{n,g} u_{n,g}^2 D_{1o}^{1.5} \sqrt{\rho_{n,l}}} \right)^{k_1}. \quad (5.47)$$

In this equation D_{1o} is the diameter of liquid orifice, $\dot{V}_{n,l}$ and $\dot{V}_{n,g}$ the flow rates of atomizing gas and liquid, respectively, $\rho_{n,l}$ and $\rho_{n,g}$ the mass densities of the liquid and gas, and $u_{n,g}$ the atomizing gas velocity. The effective dynamic viscosity μ_1 and the surface tension σ_1 of the metal oxide colloids are calculated as 1.394 mPa.s and 68.46 mN/m for SiO_2 , and 1.329 mPa.s and 69.49 mN/m for TiO_2 . The quantities k_1 and k_2 in are two fitting parameters, with default values of 0.496 and 3.414 [203]. These are upper limits considered suitable for liquids with low solid concentration, as used here. The calculated SMDs for SiO_2 , and TiO_2 droplets are 37.0, and 36.4 μm , respectively. Since the SMDs are not so different, the average value (36.7 μm) is taken as the mean droplet size, $D_{d,0}$. As a comparison, the value obtained for water is 34.23 μm , which is quite close to those obtained for the materials used. Therefore, the same range of droplet sizes can also be expected.

To represent the droplet size distribution two commonly used functions, the log-normal distribution and the Weibull distribution (mathematically equal to the Rosin-Rammler distribution [204]) are compared. The two parameters of the log-normal distribution, σ_{ign} and μ_{ign} , are related to the mean value $D_{32,d}$ and standard deviation SD as follows:

$$\sigma_{\text{ign}} = \sqrt{\ln \left(\frac{SD^2}{D_{32,d}^2} + 1 \right)}, \quad (5.48)$$

$$\mu_{\text{ign}} = \ln \left(\frac{D_{32,d}^2}{\sqrt{SD^2 + D_{32,d}^2}} \right). \quad (5.49)$$

The two parameters for Weibull distribution, namely the scale parameter λ_{wb} and the shape parameter k_{wb} , are related to the mean value and standard deviation as follows:

$$D_{32,d} = \lambda_{\text{wb}} \Gamma \left(1 + \frac{1}{k_{\text{wb}}} \right), \quad (5.50)$$

$$SD^2 = \lambda_{\text{wb}}^2 \left[\Gamma \left(1 + \frac{2}{k_{\text{wb}}} \right) - \left(\Gamma \left(1 + \frac{1}{k_{\text{wb}}} \right) \right)^2 \right], \quad (5.51)$$

with Γ indicating a gamma function.

Rearranging Eq. 5.50 and substituting λ_{Wb} to Eq. 5.51,

$$\left(\frac{SD}{D_{32,d}}\right)^2 = \frac{\Gamma\left(1 + \frac{2}{k_{Wb}}\right)}{\left(\Gamma\left(1 + \frac{1}{k_{Wb}}\right)\right)^2} - 1 \quad (5.52)$$

is obtained. This way, the required parameters are reduced to only one, which can be calculated from the average size and the standard deviation. For large sample data, which is the case with the droplet size distribution, the standard deviation can be estimated as $SD = (D_{d,max} - D_{d,min})/6$ [205].

The probability densities (i.e., the normalized number distribution) of droplet size obtained using log-normal distribution and Weibull distribution are shown in Fig. 5.7. The main differences are in the range of droplet size and the droplet size with the highest probability density (the peak of the curves). With the aforementioned information on droplet size range ($D_{d,min} = 25 \mu\text{m}$, $D_{d,max} = 70 \mu\text{m}$) and distribution (skew to the left) from the datasheet, the log-normal distribution can be considered to better represent of the droplet size distribution.

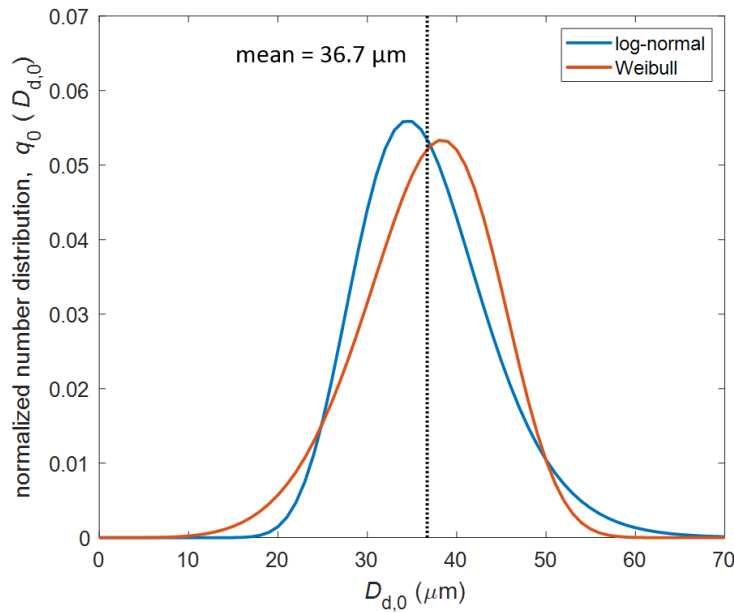


Fig. 5.7. Droplet size distribution obtained with log-normal and Weibull distribution equations.

It can be recalled from Chapter 2, that the locking point is identified by a strength of the wet shell. Figure 5.8 shows shell thickness (normalized to the droplet radius) as a function of shell strength obtained from simulation at $T_{g,in} = 500 \text{ }^\circ\text{C}$ and $f = 80 \text{ Hz}$. Previously crust thickness has been measured for micron-sized droplets (see Fig. 4.7). Simulation results show that for micron-sized droplets the crust breaks quickly after the locking point. Dry crust thickness

would thus be approximately equal to the wet shell thickness at the locking point. To obtain thickness-radius ratios in the ranges observed in experiment, the required shell strengths for SiO_2 and TiO_2 particles are in the ranges of 130-140 MPa and 33-36 MPa, respectively. Here the values of 135 and 35 MPa are taken.

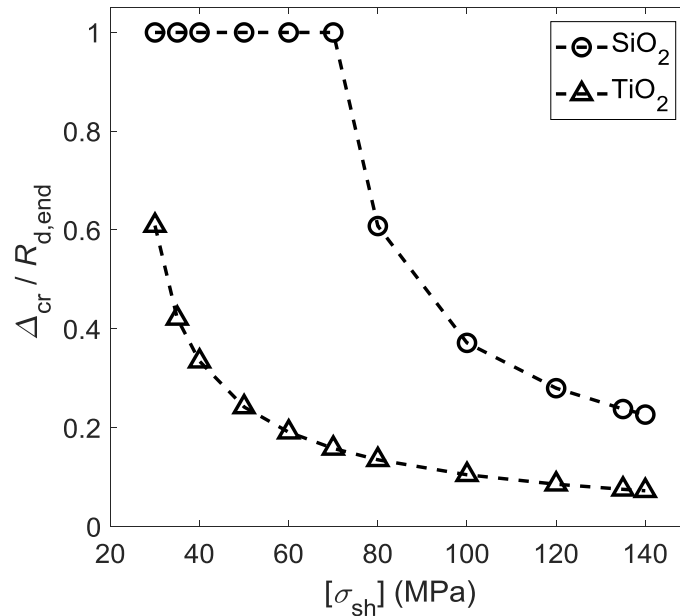


Fig. 5.8. Thickness (normalized to the droplet radius at the locking point) of wet shell at the droplet surface as a function of shell strength obtained from simulation at $T_{g,in} = 500$ °C and $f = 80$ Hz.

It has already been mentioned that with the process conditions used here droplets tend to stay in the central region of the chamber and wall deposition is less likely. Uniform velocity around the droplets and minimum wall deposition are in favor of the situation considered in the numerical simulations, and consequently the validity of the particle size distributions to be obtained. However, in the real drying chamber air humidity increases as the drying proceeds, accompanied by a decrease in gas temperature.

To see how much the change in gas properties in the axial direction can influence the result, simulations are also performed with the properties of gas at the dryer outlet. If it is assumed that the residence time of the droplets allows water to be completely removed, the air humidity at the outlet can be calculated to

$$Y_{g,out} = Y_{g,in} + \frac{\dot{m}_{evap,total}}{\dot{m}_{g,dry,in}} = Y_{g,in} + \frac{x_{V,w,0} \dot{V}_{spray} \rho_w}{y_{V,air,in} \dot{V}_{g,in} \rho_{air}}, \quad (5.53)$$

with $x_{V,w,0}$ the initial volume fraction of water in droplets and $y_{V,air,in}$ the volume fraction of dry air in the inlet gas calculated as

$$x_{V,w,0} = \frac{(1 - x_{s,0})/\rho_w}{\frac{1 - x_{s,0}}{\rho_w} + \frac{x_{s,0}}{\rho_s}} \quad (5.54)$$

$$y_{V,air,in} = \frac{1/\rho_{air}}{\frac{1}{\rho_{air}} + \frac{Y_{g,in}}{\rho_v}} \quad (5.55)$$

Assuming, furthermore, that dried particles are at gas temperature, the reduced gas temperature at the outlet can be calculated from the energy balance $\dot{Q}_{in} = \dot{Q}_{out}$, with $T_0 = 0^\circ\text{C}$ as a reference temperature:

$$\dot{Q}_{in} = (\dot{m}_{g,dry,in} c_{p,g} + \dot{m}_{v,in} c_{p,v})(T_{g,in} - T_0) + \dot{m}_{d,in} c_{p,d}(T_{d,0} - T_0), \quad (5.56)$$

$$\dot{Q}_{out} = (\dot{m}_{g,dry,out} c_{p,g} + \dot{m}_{v,out} c_{p,v} + \dot{m}_{d,out} c_{p,d})(T_{g,out} - T_0). \quad (5.57)$$

The inlet mass flow rate of droplets is $\dot{m}_{d,in} = \dot{m}_{w,in} + \dot{m}_{s,in}$, and thus $\dot{m}_{d,in} c_{p,d} = \dot{m}_{w,in} c_{p,w} + \dot{m}_{s,in} c_{p,s}$. With the assumption of complete drying, we get $\dot{m}_{vap,out} = \dot{m}_{vap,in} + \dot{m}_{w,in}$ and $\dot{m}_{d,out} = \dot{m}_{s,out} = \dot{m}_{s,in}$. The equations can thus be simplified and rearranged to obtain the gas temperature at the outlet:

$$T_{g,out} = \frac{(\dot{m}_{g,dry,in} c_{p,g} + \dot{m}_{v,in} c_{p,v}) T_{g,in} + (\dot{m}_{w,in} c_{p,w} + \dot{m}_{s,in} c_{p,s}) T_{d,0}}{\dot{m}_{g,dry,out} c_{p,g} + (\dot{m}_{v,out} + \dot{m}_{w,in}) c_{p,v} + \dot{m}_{s,in} c_{p,s}} \quad (5.58)$$

For simplicity it is assumed that the decrease in temperature does not affect the fluctuating gas flow velocity. Instead, it reduces the pressure, which is calculated based on the assumption of quasi-steady state and ideal gas behavior.

The material properties and simulation parameters are compiled in Table 5.2. The inlet gas temperature and the pulsation frequency are varied, with $T_{g,in} = 500^\circ\text{C}$ and $f = 80\text{ Hz}$ used as the main values. The chamber length is taken at 1 m, which is the distance from the tip of the spray nozzle to the chamber outlet. Properties of water and temperature-dependent properties of gas are given in Appendix A. Unlike in the experiments, average velocity and velocity amplitude are set constant in order to better compare the influences of gas temperature and pulsation frequency.

Table 5.2. Process parameters and solid material properties used in the simulations.

Variables		Values	
<i>General simulation parameters</i>			
No. of discretization elements	N_{el}	50	
Initial droplet size (μm)	$D_{d,0}$	10; 15; 20; 25; 30; 35; 40; 45; 50; 55; 60; 70	
Length of drying chamber (m)	L	1	
Average pressure (Pa)	p	100,825	
Average velocity (m/s)	\bar{u}_g	6	
Velocity amplitude (m/s)	$u_{g,amp}$	6	
<i>Varied parameters</i>			
Inlet gas temperature ($^{\circ}\text{C}$)	$T_{g,in}$	200; 300; 400; 500 $^{\phi}$; 600	
Pulsation frequency (Hz)	f	0; 40; 80 $^{\phi}$; 120; 200; 300; 400	
<i>Material properties</i>		<i>SiO₂</i>	<i>TiO₂</i>
Solid density (kg/m^3)	ρ_s	2,600	4,000
Molar mass of solid (g/mol)	M_s	60.08	79.87
Specific heat capacity ($\text{J}/(\text{kg}\cdot\text{K})$)	$c_{p,s}$	705 [206]	690 [207]
Thermal conductivity ($\text{W}/(\text{m}\cdot\text{K})$)	λ_s	1.4 [206]	8.3 [207]
Electroneutral point	pH_{eln}	2.0 [183]	5.5 [182]
Hamaker constant of primary particles in crust (J)	A_H	1.7×10^{-20} [208]	1.97×10^{-19} [209]
Thermal expansion coefficient (1/K)	$\alpha_{T,s}$	7.5×10^{-7} [206]	2.2×10^{-6} [210]
Young's modulus (GPa)	E_s	100 [211]	80 [212,213]
Poisson's ratio	ν_s	0.2 [214]	0.28 [207]
Wet shell strength (MPa)	$[\sigma_{sh}]$	135	35

$^{\phi}$ the main value

5.5 Results and discussions

5.5.1 Influence of locations in chamber (drying air conditions)

The simulations show that droplet breakup does not occur. This is to be expected since the pulsation intensities achieved with the drying unit are weaker compared to the threshold calculated in Chapter 3. Similarly, pulsations are not strong enough to break the particles. All particle breakage events have been found to be caused by stress buildup instead of flow shear force.

Figure 5.9 shows number and volume distributions of SiO₂ and TiO₂ particles obtained with inlet and outlet gas conditions. Although negligible volume-wise, differences in number distributions are apparent. Changing gas conditions along the drying chamber thus have some

5 Modeling fine particle production via crust breakage

influence on the whole process in the here investigated range. The results shown from this point onward are obtained with mixed gas properties of inlet and outlet conditions, to take the effect into account.

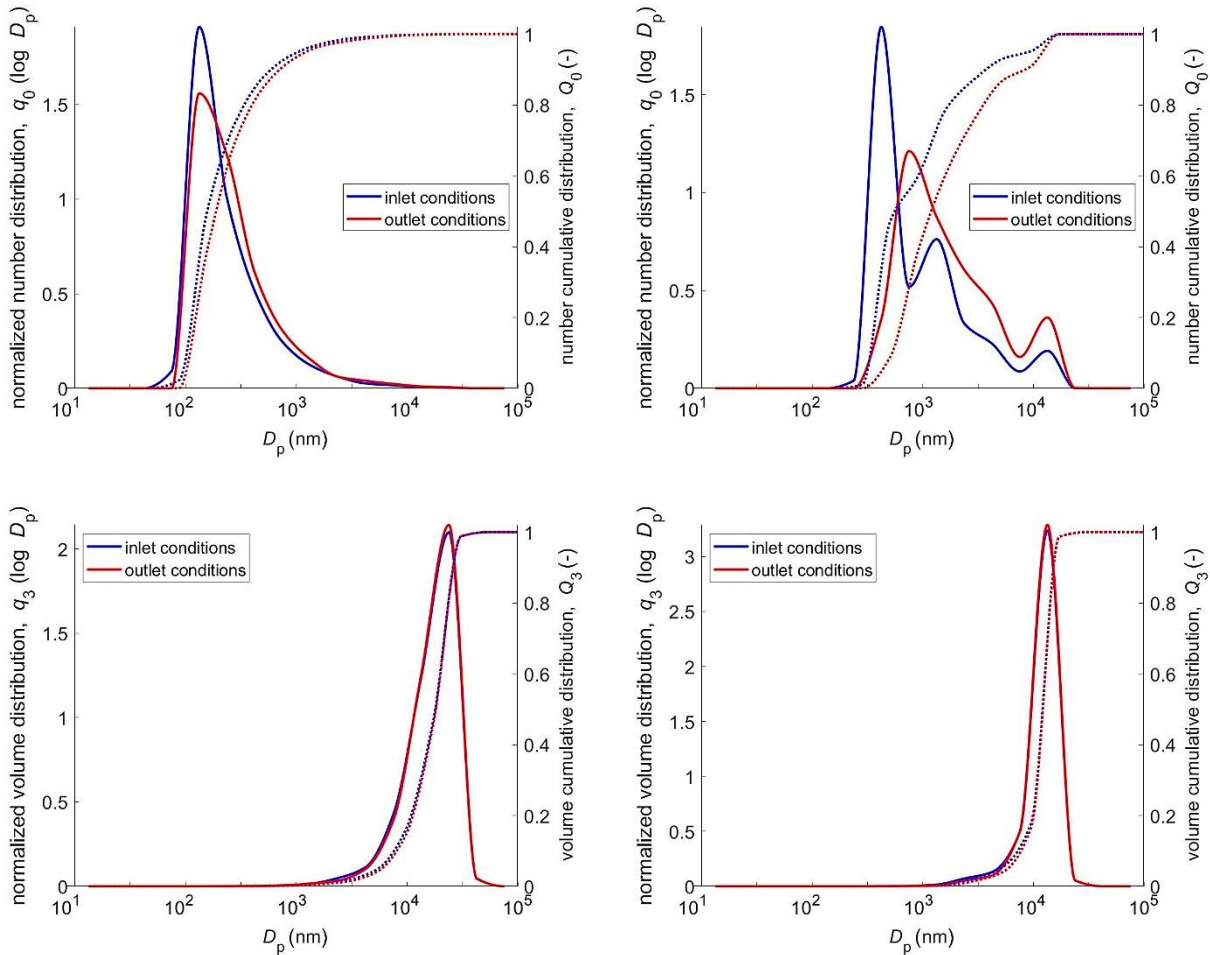


Fig. 5.9. Number (*top*) and volume (*bottom*) distributions of SiO₂ (*left*) and TiO₂ (*right*) particles obtained at $f = 80$ Hz, with inlet ($T_{g,in} = 500$ °C) and outlet (see Table 5.3) gas conditions, without debris formation.

When crust breakage is not considered, according to the drying model the final particle sizes will be equal to the droplet sizes at the locking point. Figure 5.10 shows size distributions and the times required to reach the locking point of SiO₂ and TiO₂ particles obtained at different temperatures. Locking points are achieved earlier at higher gas temperatures. Although gas pulsation leads to earlier locking point, the influence of pulsation frequency is, however, very small and thus the results are not plotted. The pulsation frequency plays role in maintaining relative velocity between the droplet and the surrounding gas, thus keeping the overall transfer coefficients from decreasing quickly over time. Compared to the ones in Chapter 3 (15-45 m/s), the velocity amplitude is low here (up to 6 m/s). As a result, the differences in pulsation frequency do not result in significant differences in overall heat and mass transfer.

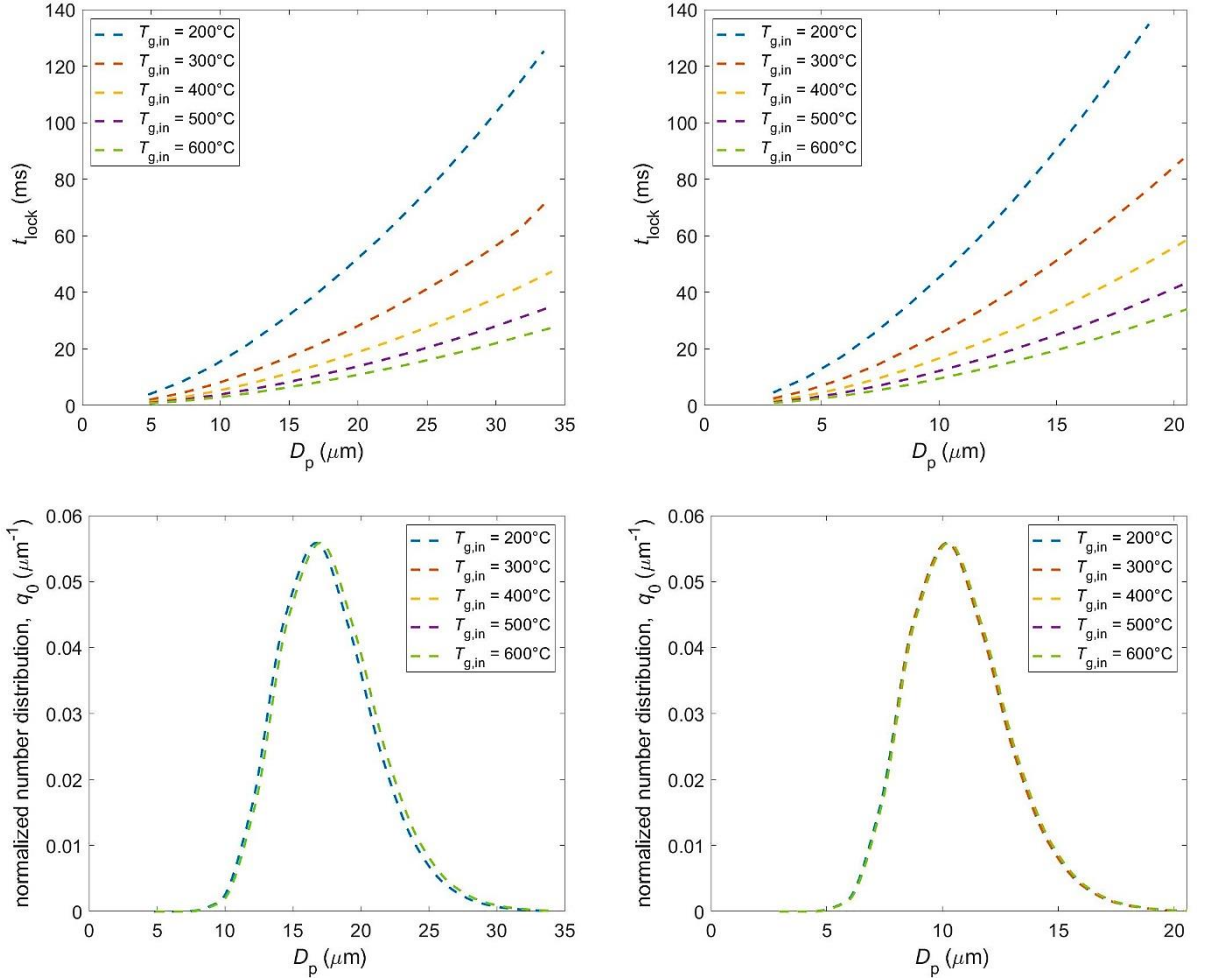


Fig. 5.10. Times required to reach the locking point (*top*) and the respective number distributions (*bottom*) of SiO_2 (*left*) and TiO_2 (*right*) particles at different gas temperatures and $f = 80$ Hz.

Despite the difference in locking times, the influence of gas temperature on the locking diameter is too small and almost negligible. At same initial diameter and higher gas temperatures, droplet surface gets saturated with primary particles faster. However, locking point will not be reached until the wet shell is strong enough to withstand the stresses acting on it. At high temperatures the transition period can be longer than the time required for initial surface saturation. The stresses acting on the wet shell are a function of water surface tension and thus droplet temperature (Eqs. 2.30-2.35), which is during the transition period equal to the adiabatic saturation temperature. The values of adiabatic saturation temperature (T_{adb}) and their respective surface tension (σ_w) and surface vapor concentration ($Y_{\text{d,surf}}$) at various inlet gas temperatures ($T_{\text{g,in}}$) are given in Table 5.3, along with the outlet gas temperatures ($T_{\text{g,out}}$) and vapor contents ($Y_{\text{g,out}}$). Despite the big differences in gas temperature, the differences in adiabatic saturation and surface tension are small, and as a result the differences in stresses would also be small.

Table 5.3. Adiabatic saturation temperature, surface tension, surface vapor content, and outlet gas properties at various inlet gas temperatures and $y_{g,in} = 8 \text{ g}_{\text{H}_2\text{O}}/\text{kg}_{\text{air}}$.

$T_{g,in}$ (°C)	$T_d = T_{adb}$ (°C)	$Y_{d,surf}$ at T_{adb} ($\text{g}_{\text{H}_2\text{O}}/\text{kg}_{\text{air}}$)	σ_w at T_{adb} (mN/m)	$T_{g,in}$ (°C)		$Y_{g,out}$ ($\text{g}_{\text{H}_2\text{O}}/\text{kg}_{\text{air}}$)	
				SiO ₂	TiO ₂	SiO ₂	TiO ₂
200	48.53	79.8	68.26	187.80	187.72	51.4	52.7
300	56.68	126.5	66.90	276.92	276.77	58.0	59.5
400	62.51	177.0	65.90	363.64	363.37	64.8	66.5
500	66.94	230.3	65.13	447.83	447.40	71.8	73.7
600	70.45	285.7	64.51	529.67	529.03	78.6	80.8

5.5.2 Particle size distributions

Number- and volume-based particle size distributions calculated at different gas temperatures and frequencies in case of no debris formation are plotted in Fig. 5.11 and Fig. 5.12. It is found that by increasing the inlet temperature the distributions are in general shifted towards smaller particle sizes. The influence of frequency magnitude is, however, still unclear as the distributions tend to coincide with one another. In a previous study [68] a simple drying process in pulsated gas flow has been simulated using computational fluid dynamics (CFD). It has been reported that while the presence of gas pulsation gives a significant difference compared to the stationary gas flow, the frequency magnitude itself has a weak influence in case of small droplet size range as considered here.

Some qualitative similarities with the experimental results are observed here. While the volume fractions of fine particles are almost negligible, number-wise the fine particles constitute significant fractions of the population. However, for both materials the minimum particle sizes are still bigger than the ones observed in the SEM images. When the child droplets become too small, at some point the crust will not break anymore. Fine particle formation is shown not possible only with binary breakage without debris formation.

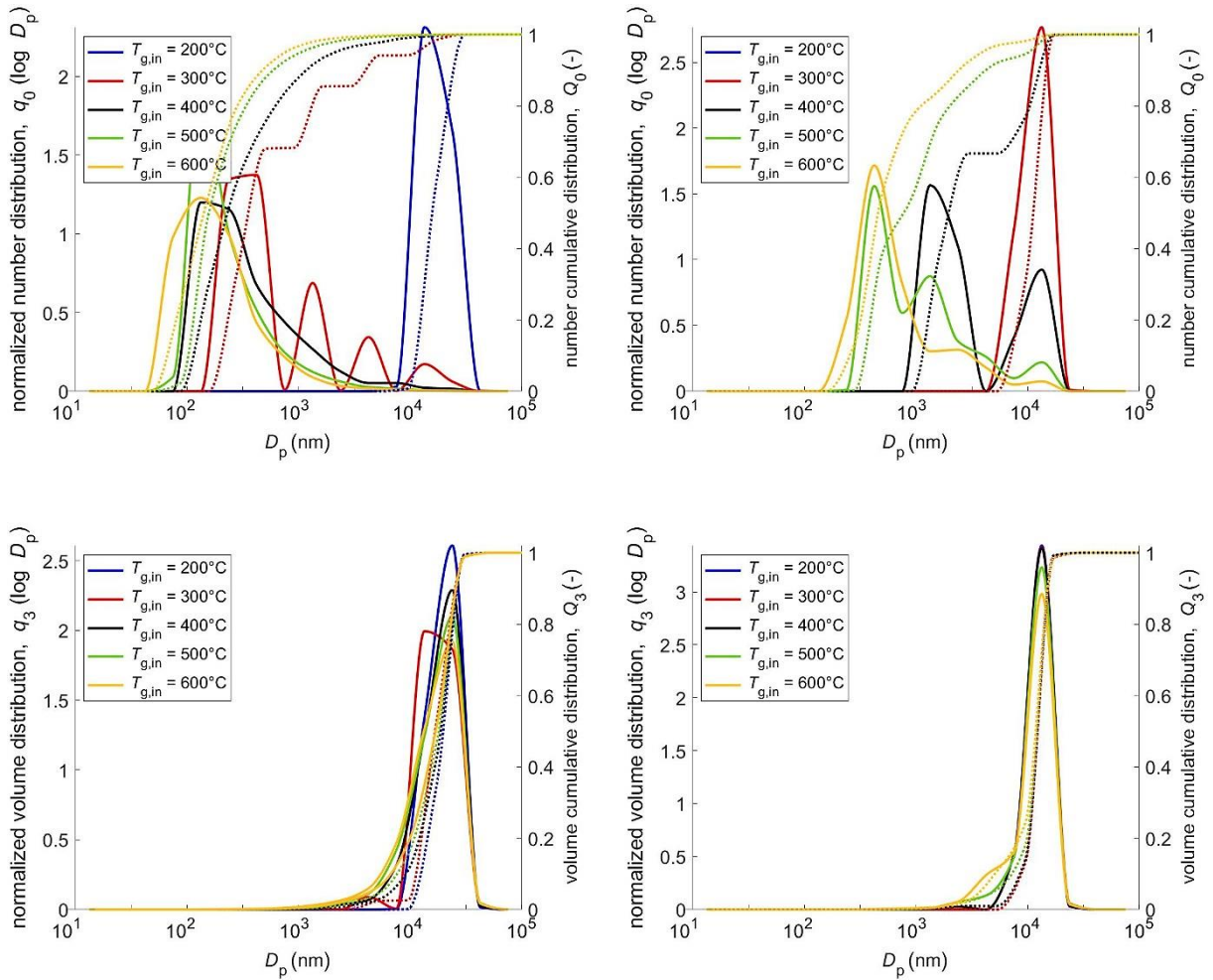


Fig. 5.11. Number and volume distributions of SiO₂ (left) and TiO₂ (right) particles obtained without debris formation at different gas temperatures and $f = 80$ Hz.

5.5.3 Particle morphologies

Initially after its formation the dry crust has a porosity equal to ε_{bed} . As the 2nd drying stage continues, the liquid core shrinks and the crust gets thicker due to the primary particles from the outermost liquid core layer attaching to the dry crust. The porosity of newly-formed inner layer of the crust thus depends on the solid concentration in the surface of the liquid core. Solid concentration in the liquid core gradually decreases towards the center and with time due to crust formation. The innermost crust layer will be composed of less and less dense primary particles, and as a result the total crust porosity starts to decrease as well.

5 Modeling fine particle production via crust breakage

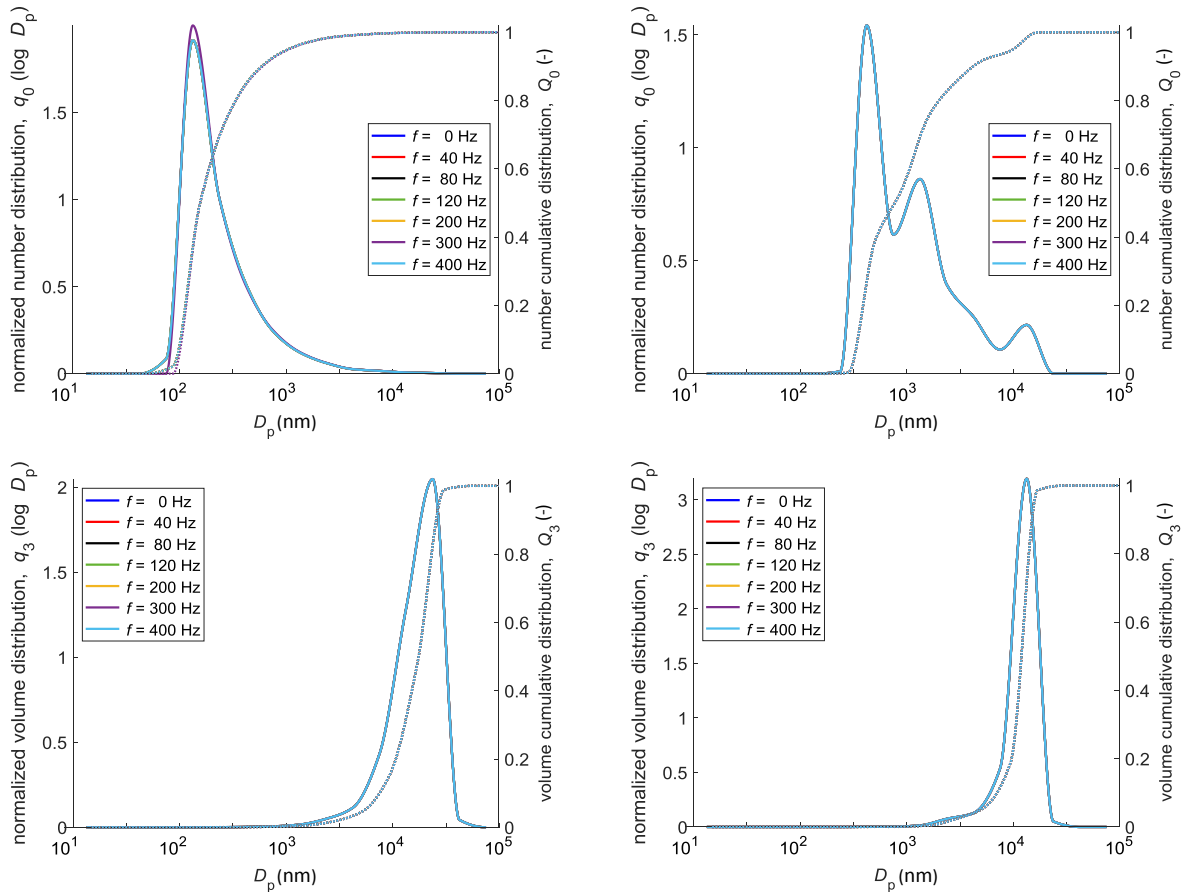


Fig. 5.12. Number and volume distributions of SiO_2 (left) and TiO_2 (right) particles obtained without debris formation at different pulsation frequencies and $T_{g,in} = 500^\circ\text{C}$.

Figure 5.13 shows how gas temperature influences the particle morphology, which is represented by the crust thickness (normalized to particle radius) and porosity. At 200 and 300 °C totally compact particles can even be obtained when the particles are small enough. At higher temperatures of 400-600 °C, the obtained particles are mostly hollow. For these particles the normalized thickness is mostly a function of only gas temperature and not the particle size, until the particles are very small (<300 nm). At higher gas temperatures the crust is thinner as breakage happens earlier, since the temperature gradient in the crust is higher and the evaporation rate is faster, leading to higher thermal and mechanical stresses. The simulation results agree with the experimental results in Fig. 4.7. The normalized crust thickness is in the range of 0.34-0.55 for TiO_2 , with an average of 0.43. For SiO_2 , they are respectively 0.19-0.29 and 0.23. The ranges are wider than the ones obtained from experiments (0.40-0.45 for TiO_2 and 0.22-0.25 for SiO_2), showing that the influence of temperature on the crust thickness is overestimated. Despite this, the average values are close and the same trends with the experiment are still obtained.

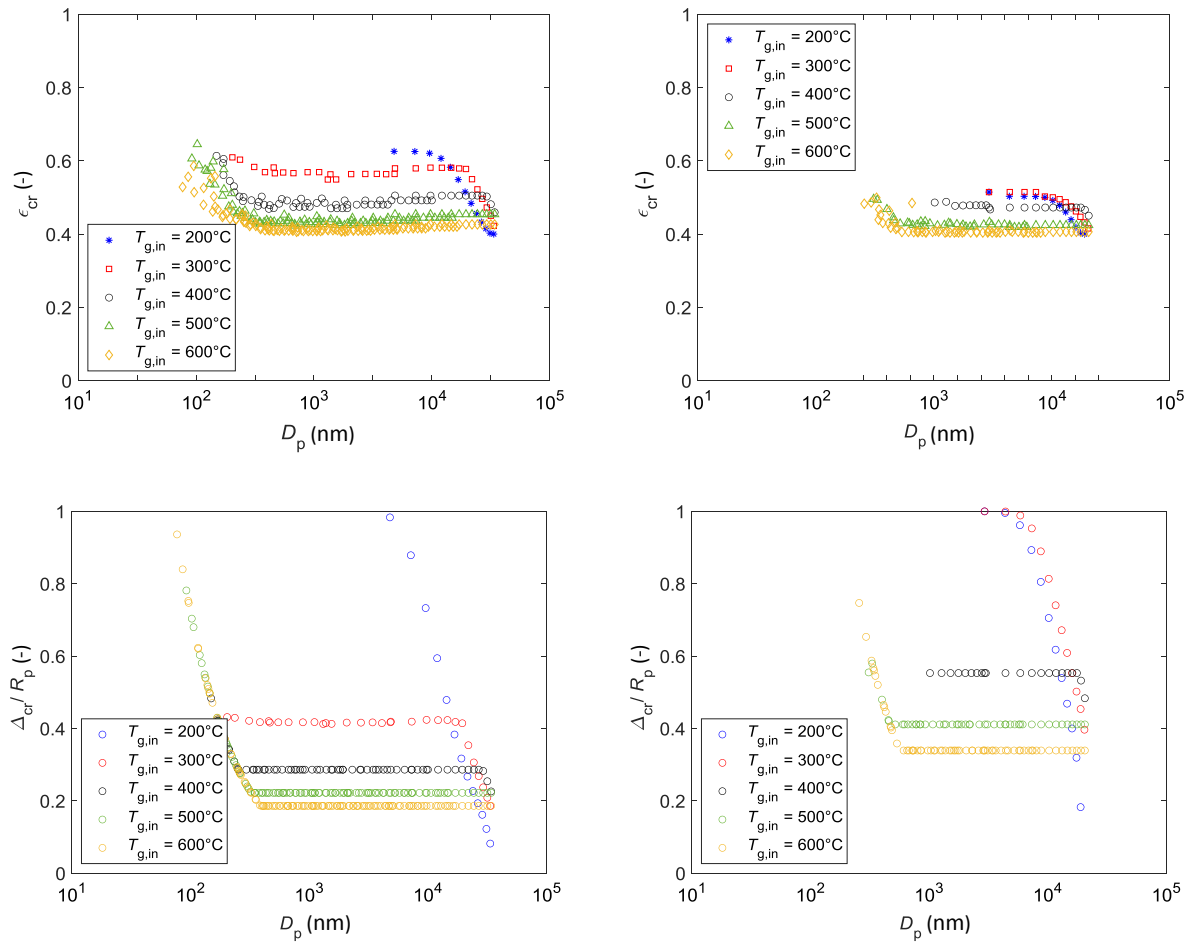


Fig. 5.13. Crust porosity (*top*) and thickness (*bottom*; normalized to particle radius) of SiO₂ (*left*) and TiO₂ (*right*) particles obtained at different gas temperatures and $f = 80$ Hz, without debris formation.

While the crust is thinner at higher temperatures, it is more packed. At lower temperature, it is thicker but more porous. Initially after its formation the dry crust has a porosity equal to ε_{bed} . As drying continues the crust gets thicker due to the primary particles from the outermost liquid core layer attaching to the dry crust. The porosity of newly-formed inner layer of the crust thus depends on the solid concentration in the interface of the liquid core. Solid concentration decreases towards the center and the total solid mass in the liquid core decreases over time due to crust formation. When the 2nd drying stage is longer, as found at lower gas temperature, the innermost crust layer will be composed of less and less dense primary particles, and as a result the crust becomes more porous.

5.5.4 Sensitivity upon arbitrarily predefined parameters

Important arbitrarily set parameters of the model are the number of child droplets created after each breakage event, $N_{\text{d,brkg}}$, as well as the parameters f_{dbr} and f_{frg} , which determine the size and amount of debris particles. In the following we try to check how strongly the

results change when these parameters are varied. Tested values are 1, 2, 4, 6, 8, and 10 for $N_{d,brkg}$; 0.2, 0.4, 0.6, 0.8 and 1 for f_{dbr} ; and 0.05, 0.01, 0.15, 0.2, 0.4, 0.6, 0.8 and 1 for f_{frg} .

Figure 5.14 shows how the number of breakage events experienced by droplets and the final number and volume distributions change in respect to $N_{d,brkg}$. The number of breakage events is less for smaller droplets. However, if the droplets are too big the stresses may not be strong enough to break the crust before they exit the chamber, as shown for SiO_2 . More breakage events are experienced by SiO_2 droplets than by TiO_2 droplets. This explains why smaller particles could be produced from SiO_2 droplets, although the initial solid content is higher. The solid concentration in the child droplets decreases with each breakage event. With lower initial solid content, it then takes more time to reach the next locking point. Moreover, the crust is thicker for TiO_2 compared to SiO_2 , meaning that for the same locking diameter more time is required from the locking point until the crust breaks. The time interval between two consecutive breakage events will therefore be even longer and the number of breakage events decreases.

When $N_{d,brkg}$ is increased, the number of breakage events decreases. This is because with more child droplets produced in each breakage event, the initial size of these droplets will obviously be smaller. As can also be seen in the plots, smaller droplets tend to have less breakage events. With more child droplets produced the minimum of obtainable product particle diameter is approached faster. This minimum is influenced by the dynamics of the process, including crust temperature, evaporation rate, and vapor pressure, and thus cannot be assessed in advance.

Normalized number distributions seem to be more influenced by $N_{d,brkg}$ compared to the normalized volume distributions. Even though with more child droplets the number of breakage events is less, more small particles can still be produced. When number of child droplets is increased, the distributions are shifted to smaller sizes. However, as the number of breakage events decreases as well, the lower limit of obtainable particle size will increase; as a result the distributions become narrower, with middle peaks at submicron scale.

The volume and number distributions can also be shifted towards smaller particle sizes by the formation of debris particles when the crust breaks. Fig. 5.15 and Fig. 5.16 show the influence of f_{dbr} and f_{frg} on the calculated number and volume distributions of the oxide particles. The difference made by debris formation is clear. Decreasing f_{frg} shifts the distribution to smaller particles. The same applies to f_{dbr} , but the effect is less pronounced. f_{dbr} plays more role in affecting the distributions in vertical direction.

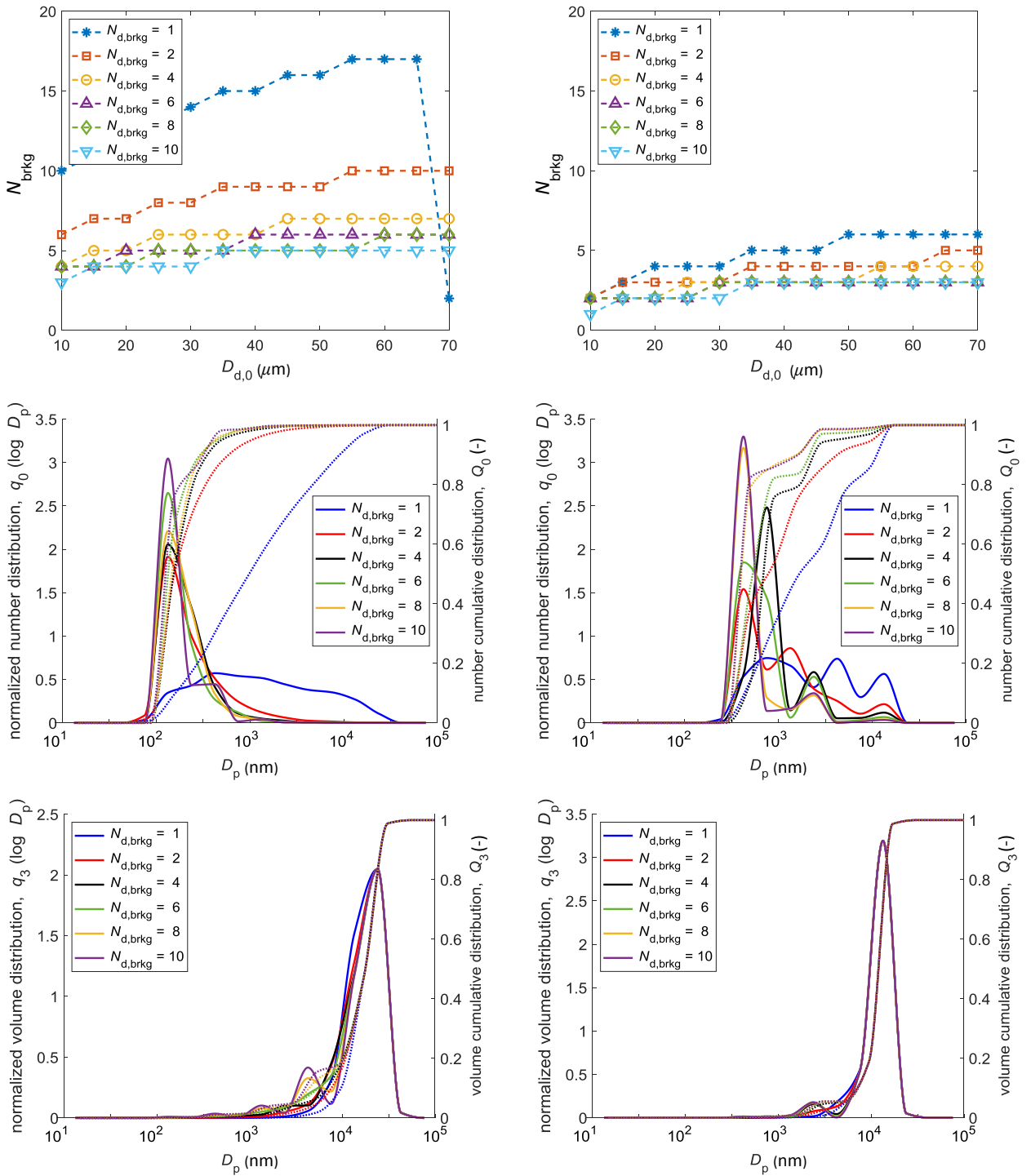


Fig. 5.14. Influence of the number of child droplets produced after crust breakage on (*from top to bottom*) number of breakage events, and number and volume distributions of SiO_2 (*left*) and TiO_2 (*right*) particles obtained at $T_{\text{g,in}} = 500 \text{ }^\circ\text{C}$ and $f = 80 \text{ Hz}$, without debris formation.

5 Modeling fine particle production via crust breakage

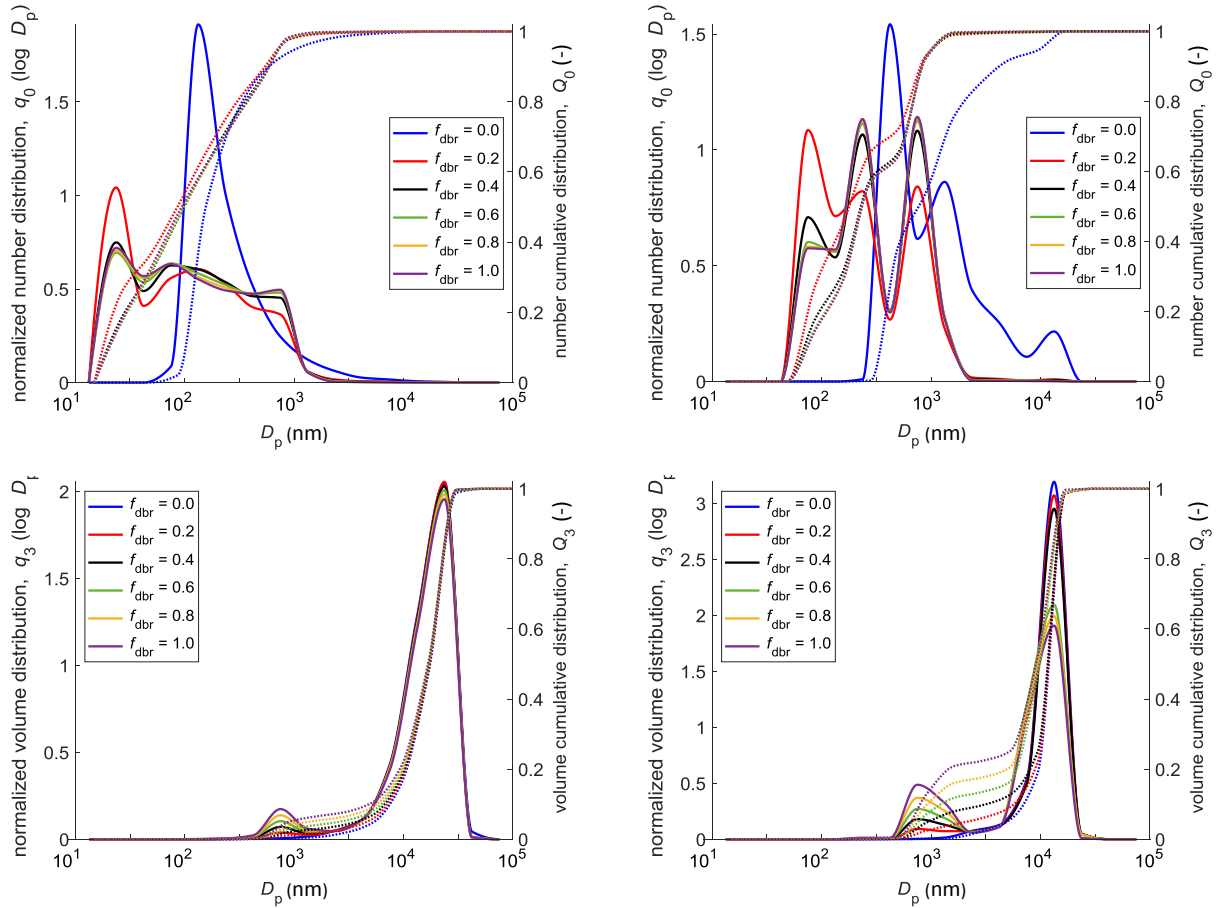


Fig. 5.15. Number and volume distributions of SiO_2 (left) and TiO_2 (right) particles obtained with different ratio of chipped layer thickness to crust thickness, f_{dbr} , at $T_{\text{g,in}} = 500$ °C, $f = 80$ Hz, $N_{\text{d,brkg}} = 2$, and $f_{\text{irg}} = 0.4$. Data for smaller f_{dbr} values are not shown for practical reasons.

5.5.5 Optimal parameter setting

In order to find the optimal combinations of said parameters, the simulated size distributions must be quantitatively compared to those obtained from experiment. The combination must be optimized for all operating conditions, but can be different for SiO_2 and for TiO_2 . The closeness (accuracy) of two distribution curves in a plot can be evaluated in vertical (ordinate, y -axis) and horizontal (abscissa, x -axis) directions. In vertical direction fractions at different particle sizes can be compared, whereas in horizontal direction key properties of the population such as mode, median, and mean can be used. Several statistical parameters have been used for comparing size distribution data [215,216]. In the current study relative root mean squared error ($RRMSE$) and Hellinger distance (H) are used in vertical direction, whereas for the accuracy in horizontal direction the relative errors in log values of median (RE_{D50}) and mean diameter ($RE_{\mu 1}$) are evaluated:

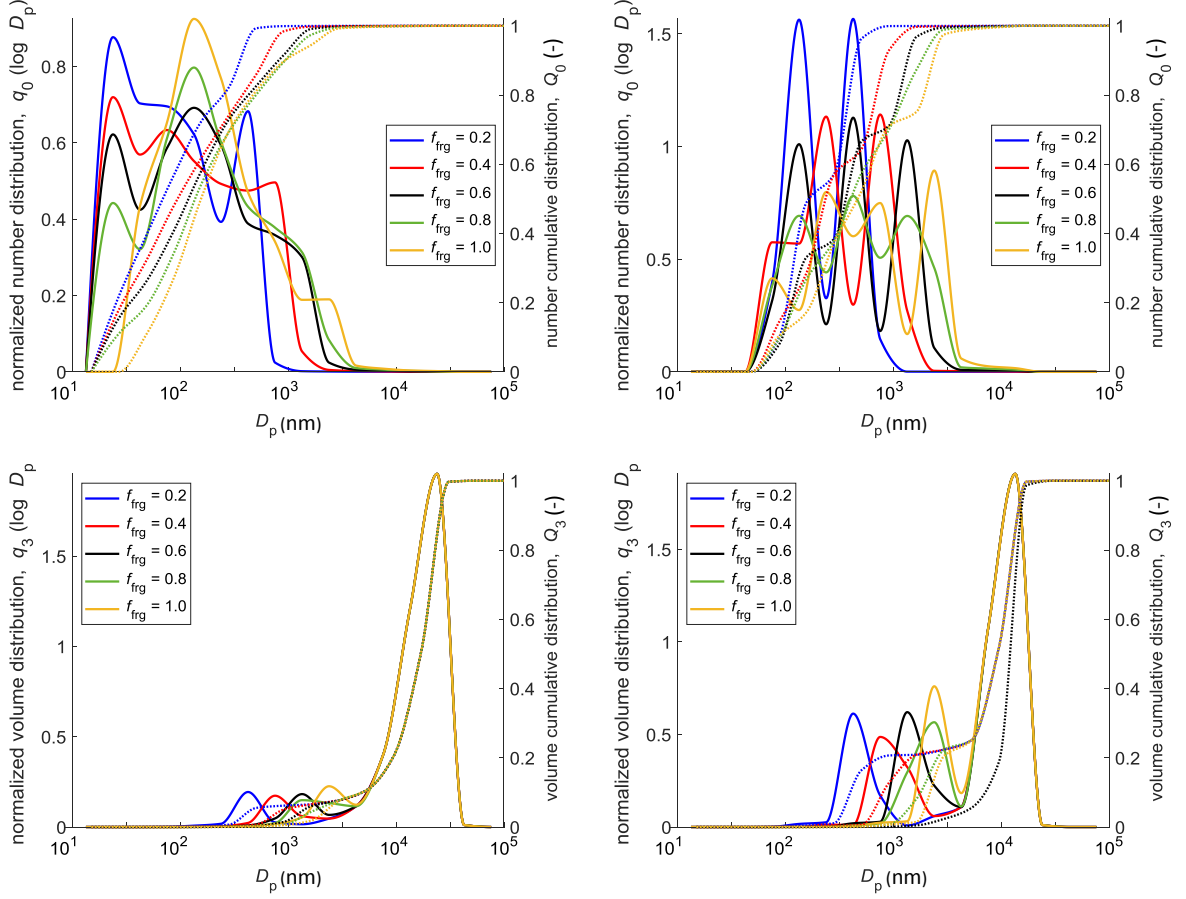


Fig. 5.16. Number and volume distributions of SiO₂ (left) and TiO₂ (right) particles obtained with different ratio of debris particle diameter to crust thickness, f_{frg} , at $T_{\text{g,in}} = 500$ °C, $f = 80$ Hz, $N_{\text{d,brkg}} = 2$, and $f_{\text{dbr}} = 1$. Data for smaller f_{frg} values are not shown for practical reasons.

$$RRMSE = \frac{\sqrt{\sum_{i=1}^n (\hat{q}_i - \bar{q}_i)^2 / n}}{\bar{q}_i}, \quad (5.59)$$

$$H = \sqrt{\frac{1}{2} \sum_{i=1}^n (\sqrt{\hat{q}_i} - \sqrt{\bar{q}_i})^2}, \quad (5.60)$$

$$RE_{D50} = \frac{|\log \hat{D}_{50} - \log \dot{D}_{50}|}{\log \dot{D}_{50}}, \quad (5.61)$$

$$RE_{\mu_1} = \frac{|\log \hat{\mu}_1 - \log \dot{\mu}_1|}{\log \dot{\mu}_1}. \quad (5.62)$$

The equations are used for volume- and number-based size distributions. For any variable y in the equations, \dot{y} denotes the values obtained from the experiment, which serve as the validation data; and \hat{y} the predicted values obtained from simulation.

For all statistical parameters, smaller values indicate closer resemblance between the two distribution curves. Since direct averaging is not possible, due to the statistical parameters having completely different ranges of value, rank values have been considered and averaged. For each statistical parameter, the ranking is based on an average value obtained for all operating conditions. Each of in total 270 combinations from the 3 parameters will thus have 8 rank values, which come from 2 types of distribution (number and volume) and 4 statistical parameters. The optimum combination is therefore the one with the lowest average rank value for the operating conditions overall.

Table 5.4 shows five combinations with the lowest rank values for each metal oxide. The simulations have been conducted with the operating conditions used in the experiment, shown in Table 4.1. It can be seen that the two materials require totally opposite combinations of the presumed variables. The closest match is obtained with $N_{d,brkg} = 2$, $f_{dbr} = 0.8$, and $f_{frg} = 1$ for TiO_2 , whereas for SiO_2 it is $N_{d,brkg} = 1$, $f_{dbr} = 0.05$, and $f_{frg} = 0.4$. Relatively high values of f_{dbr} and f_{frg} required for TiO_2 mean that the debris particles are quite large in comparison to the crust thickness. The opposite is required for SiO_2 , as both f_{dbr} and f_{frg} are much smaller. Thus, although in each breakage event the fraction of crust that turns into debris is quite small, more debris particles can be produced since their size is smaller. Moreover, as shown in Fig. 5.14, the number of breakage events for SiO_2 is higher than for TiO_2 at same $N_{d,brkg}$.

Table 5.4. Top 5 and bottom 2 combinations of $N_{d,brkg}$, f_{dbr} , and f_{frg} that give simulation results closest to the experiment results. The scores are based on the average ranking of number- and volume-based distributions obtained with each combination for each statistical parameter.

No.	$N_{d,brkg}$	f_{dbr}	f_{frg}	<i>RRMSE</i>	<i>H</i>	<i>RE_{D50}</i>	<i>RE_{μ1}</i>	average
<i>SiO₂</i>								
1	1	0.05	0.4	134.5	5.0	8.0	6.0	38.4
2	1	0.05	0.6	134.0	5.0	7.5	13.0	39.9
3	1	0.05	0.2	138.5	7.5	9.0	5.5	40.1
4	1	0.1	0.4	132.5	13.0	8.0	12.5	41.5
5	1	0.1	0.6	132.5	9.0	7.5	20.5	42.4
:	:	:	:	:	:	:	:	:
269	4	1	0.8	137.0	172.5	258.0	231.5	199.8
270	4	1	1	144.5	184.0	261.0	231.5	205.3
<i>TiO₂</i>								
1	2	0.8	1	1.5	4.5	26.5	24.5	14.3
2	4	0.8	1	11.0	21.5	5.0	22.0	14.9
3	2	0.6	1	11.0	6.0	63.5	10.5	22.8
4	4	0.6	1	27.5	25.5	36.0	7.5	24.1
5	1	0.8	1	11.0	11.5	49.0	31.5	25.8
:	:	:	:	:	:	:	:	:
269	8	0.05	0.2	253.0	256.5	250.0	235.0	248.6
270	10	0.05	0.2	254.5	261.0	250.5	233.0	249.8

The simulation results obtained with the optimum combinations are compared with experimental results in Fig. 5.17. In general, the simulation results are qualitatively in agreement with the experiment data. The assumption of minimum possible debris particle sizes, which were $2 D_{pp}$ (24 nm) for SiO_2 and $3 D_{pp}$ (96 nm) for TiO_2 , could give a quite good agreement with the experiment data in terms of the lower limit of particle size distribution. However, the number of particles of respective size is still overestimated. The predicted size and amount of the biggest particles, on the other hand, cannot really match the experiment. In the volume-based size distributions, the largest particles obtained from the simulation are always smaller than the ones from experiment.

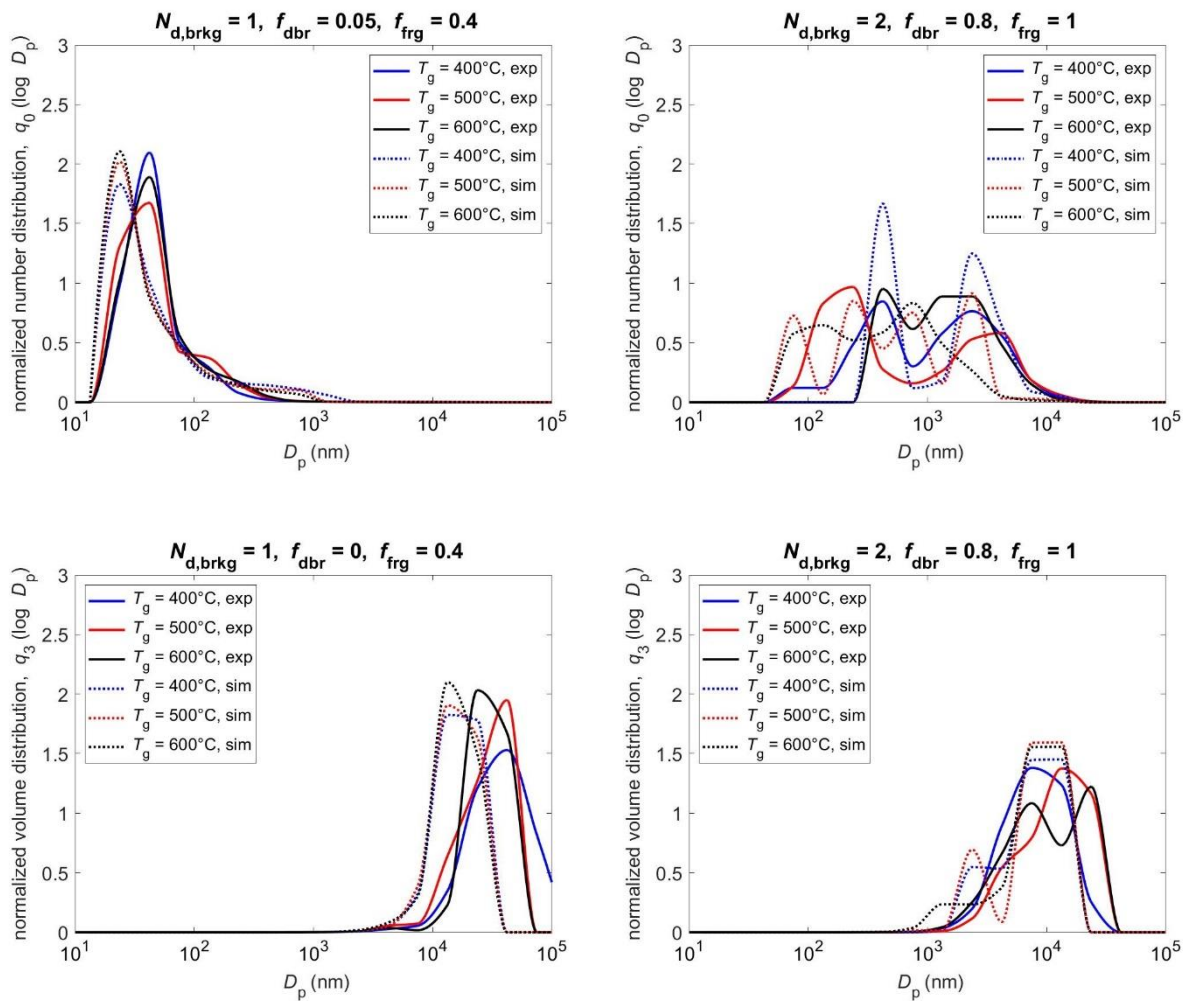


Fig. 5.17. Normalized number (*top*) and volume (*bottom*) distributions of SiO_2 (*left*) and TiO_2 (*right*) particles obtained from experiment compared to those obtained from simulation with the optimum combination of $N_{d,brkg}$, f_{dbr} , and f_{frg} values. The pulsation frequencies are 120 Hz for SiO_2 and 80 Hz for TiO_2 .

The difficulty in fitting is mainly due to the fact that the largest particle size is limited by the maximum initial droplet size. For the simulation it has been assumed that the maximum initial droplet size is 70 μm . Table 4.2 though indicates that particles which are very close or even larger than the largest calculated droplet size exist, particularly for SiO_2 . One possible reason may be that evaporation could have already started in the nozzle, given the high temperature of the surrounding gas. This would increase the solid content and the viscosity and could lead to formation of larger droplets than assumed. Another possibility is rearrangement of the primary particles, which could happen after crust breakage and make the particles smaller. The particle shapes in SEM images (Fig. 4.4) hinted that this could have happened, particularly for TiO_2 . Suh et al. argued that rearrangement and deformation could be due to the hydration force that reduces the strength of assembly of primary particles with hydrophilic surfaces like SiO_2 and TiO_2 [217].

5.6 Conclusion

Based on the observed particle morphology in the previous chapter, a model of fine particle production through repetitive crust breakage and drying cycles has been developed. Two possible mechanisms, namely shear-induced breakage and internal stresses-induced breakage, have been investigated. It is found that shear stress from the flow is not strong enough to break the crust, due to small particle size and low fluid density. The possible cause for breakage is thus stresses in the crust due to temperature and pressure gradients. This explains why fine particles can be produced even when gas pulsation is not present. Debris particle formation at breakage has been taken into account, with some predetermined variables optimized according to the simulated materials. This was done by statistically testing how close the particle size distributions obtained from simulation are in relation to those from the experiments in Chapter 4. It is shown that debris formation contributes significantly to the number based-size distribution. In addition to the size distributions, calculated crust thickness at breakage has also been compared to the measured value. The results obtained with the model are qualitatively in agreement with the experimental data.

6. Drying and denaturation of proteins in PCD

This chapter contains an extended part of the manuscript “Droplet drying and whey protein denaturation in pulsed gas flow: A modeling study”, which is published in Journal of Food Engineering [71].

6.1 Introduction

One classic question in thermal processing of foods and pharmaceuticals is how much useful compounds deteriorate due to heat. Vitamins, enzymes, and active compounds in foods and pharmaceuticals are heat-sensitive and get inactivated quickly. Inactivation or destruction of bioactive compounds can occur due to heat or presence of agents such as acid, alkali, or organic polar solvents.

There are two mechanisms of inactivation: degradation and denaturation. Through degradation reactions, new compounds with different properties are formed from the original substances (i.e., the reactants). Some examples are cracking of hydrocarbons and degradation of vitamins. Denaturation is an inactivation mechanism that happens in proteins and enzymes. There is no chemical transformation and only the compound structure changes. This causes the proteins or enzymes to lose their biological activity. It starts with reversible unfolding and ends with irreversible denaturation [218], without breakage of peptide bonds. Proteins mostly undergo denaturation when heated above 60 °C. While this does not really change the nutritional value in foods, it reduces the flowability and solubility of the powders, which is not desired. Moreover, it may cause fouling and nozzle blocking [106].

Depending on the materials and the purposes, one can employ low temperature long time (LTLT), high temperature short time (HTST), or ultra-high temperature (UHT) process. Alternatively, thermal processing can also be combined with or even replaced by non-thermal processing, such as applications of pressure, ultrasound, light, or electric field in preservation processes [219]. Combinations of thermal and non-thermal techniques are usually aimed at faster processing, less deterioration, and more efficient energy use. Pulse combustor is known for being more energy efficient and clean compared to conventional combustors, whereas PCD provides intensified heat and mass transfer which promises faster process. However, it is still unknown how much this influences end product quality. Wu et al. conducted an experimental study of egg white powder production using PCD [14]. While they showed that compared to normal spray drying PCD could give better overall product properties, very less has been said on the influence of process parameters.

This chapter presents an investigation on how much intensified heat and mass transfer due to pulsating flow influences protein inactivation (denaturation). Previously, the semi-empirical characteristic drying curve (CDC) model and a whey protein inactivation model have been combined and applied in computational fluid dynamics (CFD) simulation for the case of spray drying of skim milk [105]. Protein fraction in skim milk is composed mainly of casein and whey proteins. It is mostly whey proteins that undergo denaturation, whereas casein is more heat-stable, although its size can change by bonding with whey protein compounds [220]. Interaction between casein and whey proteins is limited during fast heating, which makes the influence of casein on whey protein denaturation negligible [221]. Here, a more complex single droplet drying model, in which solute transport inside the droplet is considered, is used and combined with a denaturation kinetic model obtained from an experimental study. Firstly, the model is described and validated. A parametric study on process variables is then conducted to understand their influence on the process dynamics and final product quality, which is evaluated from moisture content and protein activity. Lastly, a comparison of two process intensification strategies, namely increasing temperature and employing gas pulsation, is presented.

6.2 Denaturation model of whey protein

Modelling of whey protein inactivation (denaturation) during spray drying of skim milk solution has been performed by Jaskulski et al. [105], by combining the CDC drying model with a whey protein inactivation model developed by Atuonwu et al. [106]. The denaturation rate is given as a function of solution composition and temperature. The model worked well when combined with characteristic drying curve model and applied in CFD simulation [105]. However, its performance when coupled with drying models that consider non-uniform distribution of solid and liquid has been found less satisfactory [222], especially when the moisture content is too low. During the 2nd drying period, it is expected that solid materials in the crust inactivate faster than those in the liquid core due to very low moisture content and quickly increasing temperature.

The kinetic model by Oldfield et al. [223] is used here to simulate denaturation of whey protein isolate (WPI). This model features different reaction orders and reaction constants for different whey protein components, namely β -lactoglobulin A, β -lactoglobulin B, α -lactalbumin, and bovine serum albumin (BSA); more complete than those in other kinetic models [106,224–226]. Additionally, influence of concentration was taken into account explicitly both in the experiments and in the kinetic analyses. These two features make Oldfield's model relatively more versatile and thus selected.

Protein denaturation is calculated separately for the liquid core and the crust. The following derivation applies for both locations. For simplicity, the symbols are given without location specific indices. The general equation for reaction rate is

$$\frac{dC_{wh}}{dt} = -k_n C_{wh}^n, \quad (6.1)$$

where C_{wh} is protein concentration in g/kg solution and k_n is reaction rate constant of an n^{th} order reaction with unit of $\text{g}^{1-n} \text{kg}^{n-1} \text{s}^{-1}$. The latter is temperature-dependent following an Arrhenius-type equation,

$$k_n = k_0 \exp\left(-\frac{E_a}{RT}\right), \quad (6.2)$$

with E_a reaction activation energy, R universal gas constant, and T temperature in K.

C_{wh} in Eq. 6.1 is converted to activity A_{wh} , which indicates the ratio of actual to initial mass fraction of undenatured protein. Using the definition of C_{wh} and converting the unit to kg protein/kg solution, C_{wh} is related to the activity and solution composition by

$$C_{wh} = 1000 \frac{m_a}{m_w + m_s}, \quad (6.3)$$

with m_s and m_w obtained from the drying model as functions of time. Here, m_a is the active portion of solid compound given by

$$m_a = A_{wh} m_s. \quad (6.4)$$

Since separate calculations are performed for the liquid core and the crust, solid mass is a function of time and its derivative is not zero. Substituting Eqs. 6.2 & 6.3 into Eq. 6.1,

$$-\frac{dC_{wh}}{dt} = -1000 \frac{d}{dt} \left(\frac{m_a}{m_w + m_s} \right) = k_n \left(1000 \frac{A_{wh} m_s}{m_w + m_s} \right)^n \quad (6.5)$$

is obtained. Derivation results in

$$1000 \left(\frac{m_a \left(\frac{dm_s}{dt} + \frac{dm_w}{dt} \right) - (m_w + m_s) \frac{dm_a}{dt}}{(m_w + m_s)^2} \right) = 1000^n k_n \left(\frac{A_{wh} m_s}{m_w + m_s} \right)^n. \quad (6.6)$$

Substituting

$$\frac{dm_a}{dt} = A_{wh} \frac{dm_s}{dt} + m_s \frac{dA_{wh}}{dt} \quad (6.7)$$

from Eq. 6.4 into Eq. 6.6 and rearranging results in

$$\frac{dA_{wh}}{dt} = \frac{A_{wh} m_s \left(\frac{dm_s}{dt} + \frac{dm_w}{dt} \right) - 1000^{(n-1)} k_n \left(\frac{A_{wh} m_s}{m_w + m_s} \right)^n (m_w + m_s)^2 - A_{wh} (m_w + m_s) \frac{dm_s}{dt}}{m_s (m_w + m_s)}. \quad (6.8)$$

Possible reverse reactions are not considered explicitly and instead the kinetics of some components are given as non-1st order reactions. The reaction orders, kinetic parameters, and mass fractions of the whey protein components are given in Table 6.1. The overall whey

protein activity is taken as the total of the contributions from these components, which are calculated according to their mass fractions. After the activity has been calculated for each location, the overall droplet activity is obtained by averaging on solid mass basis.

During drying of dairy solutions protein molecules near the droplet surface adsorb at the water-air interface. This phenomenon has been shown to play a competing role with back diffusion in determining the concentration distribution [108]. It is enhanced by the presence of fat at droplet surface [108,227]. As fat is non-existent here, surface protein adsorption is assumed insignificant compared to back-diffusion and thus neglected.

Table 6.1. Mass fractions ($x_{c,wh}$), reaction orders (n) and parameters for reaction constant equation (k_0 and E_a) for each whey protein component [223].

Component	$x_{c,wh}$ (%)	n	k_0^\dagger	E_a/R^\dagger
β -lactoglobulin A	38.35	1.4	2.1453×10^{13}	12998.1
β -lactoglobulin B	46.45	1.5	3.5363×10^{12}	12231.7
α -lactalbumin	15.88	1.0	3.0255×10^6	7705.9
BSA	3.92	1.3	1.9275×10^{10}	9957.5

† obtained by plotting and regressing the data from Table 2 in [223].

6.3 Model validation & simulation parameters

Experimental data by Haque et al. [228] are used to validate the model. A 10 %-w/v (≈ 10.01 %-w) solution of whey protein isolate (WPI) 895 was used. In the experimental setup, a droplet suspended on a glass filament was dried with a hot air flow. The experimental operating conditions are given in Table 6.2. Changes in temperature, moisture content, and residual protein contents were measured. A characteristic drying curve (Fig. 6.1) has been obtained from the moisture content history and is used to estimate a critical average moisture content which marks the shift from the 1st (constant rate) to the 2nd (falling rate) drying stage. Since the data of the particle diameter is not available, the droplet surface area is calculated from the initial droplet volume and the change in moisture content by assuming uniform shrinkage of the droplet. While this is correct for the 1st drying stage, it leads to inaccuracy for the 2nd drying stage. Nevertheless, the point at which drying rate begins to decline still indicates the shift in drying stage. From the curve, the critical average moisture content is estimated at 3.5 kg solid/kg water.

Table 6.2. Operating conditions in the experiment by Haque *et al.* [228].

Variables		Values
Initial droplet diameter (mm)	$D_{d,0}$	1.6
Drying air velocity (m/s)	\bar{u}_g	0.5
Drying air temperature (°C)	T_g	80
Initial droplet temperature (°C)	$T_{d,0}$	24
Initial solid mass fraction (%)	$x_{s,0}$	10.01
Relative humidity of the drying air (%)	RH	3.0
Critical moisture content (kg/kg)	X_{cr}	3.5

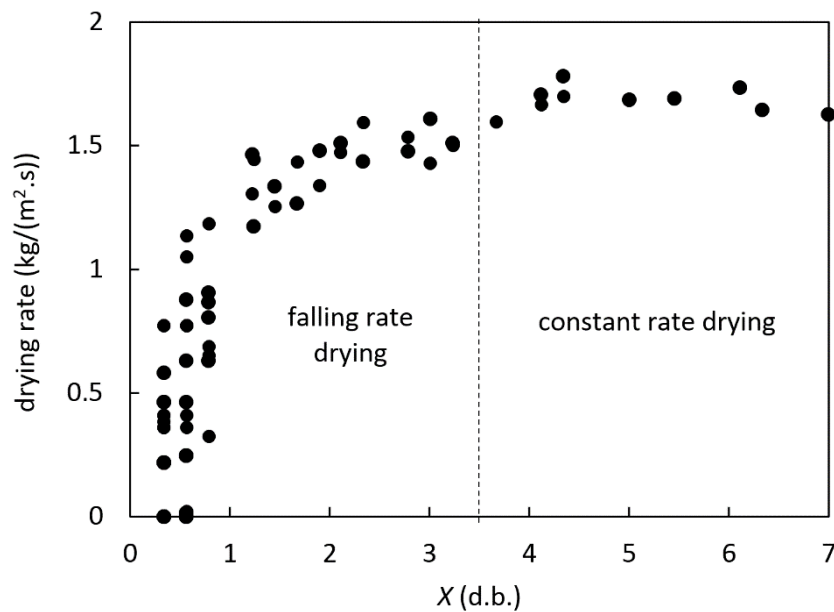


Fig. 6.1. A characteristic drying curve obtained from the experimental data [228]. The shift from the 1st to the 2nd drying stage is estimated to occur at the average moisture content of 3.5 kg/kg.

Comparison between the calculation results and the measured values are given in Fig. 6.2. The average moisture content can be predicted accurately by the drying model. After locking point, the decrease in overall moisture content is slower due to more resistance from the formed crust, while in the liquid core the moisture content increases again as the more solid forms the crust. The model also predicts accurately the droplet temperature during the 1st drying stage. The temperature does not stay at the adiabatic saturation temperature due to reduced water activity at droplet surface. After locking point, the calculated crust surface and average temperatures ($T_{cr,surf}$ and $T_{cr,avg}$, respectively) quickly rise to the drying air temperature. Temperature in the liquid (T_{lc}) also increases but at a much slower rate. The calculated temperatures during the 2nd drying stage appear to deviate from the measured temperature, except at the beginning and at the end. In the experiment droplet temperature measurement

was carried out in parallel [229], by suspending another droplet at the tip of a T-type thermocouple. Initially after the locking point the thermocouple still measured the temperature of the liquid core. During this period, the measured temperature still coincides with the predicted liquid core temperature. As drying continued and the liquid volume was reduced further, some part of the thermocouple tip might have become more exposed and no more in contact with liquid. Thus, the measured temperature could have been a combined temperature of liquid, crust, and drying air. It kept on increasing until it finally reached the drying air temperature.

Two calculation schemes are used for the whey protein denaturation. In the first scheme it is calculated separately for liquid core and for crust using their respective temperatures. Overall droplet activity ($A_{wh,avg}$) is then obtained by mass-averaging. In the second one a lumped droplet temperature $T_{d,avg}$ (obtained by enthalpy-averaging) is used to calculate directly the change in overall activity ($A_{wh,lump}$). Figure 6.2 shows that the first scheme gives more accurate results than the second. Denaturation of whey proteins starts at around 65 °C [228,230], and from the figure it can be seen that lumped droplet temperature reaches the denaturation temperature later than the crust temperature. As a result, the onset of protein denaturation in the second scheme occurs later compared to the one observed in the experiment.

So, in general, the ability of the drying model to predict changes in droplet temperature, moisture content, and protein activity is confirmed. Although this validation refers to experimental data without pulsation, good performance can be expected also for the PCD, as long as the changes in temperature and moisture content are realistically captured, as it has been shown in Chapter 3, see also [69]. Good prediction capability can be expected as long as the individual processes are modelled accurately. As aforementioned, the drying model has been validated for various types of material including foods ingredients [74], and good levels of accuracy could also be obtained when combined with other models [69,70,72]. The denaturation models used here, on the other hand, have been developed directly from experiments using pure materials [223], and thus the accuracy should be high to begin with.

It should though be noted that there are some limitations in the here used approach. In the model, heat and mass transfer influences protein denaturation but not the other way round. Heat source terms by reaction are assumed to play a small role compared to the heat supplied by the drying medium and thus neglected. Chemical changes might alter physical properties of organic materials that have an influence to the heat and mass transfer process. Here, such influences are also neglected. Additionally, the water content in droplet drying is higher than in the measurements of protein activity in pure WPI, which served as the basis of the denaturation model. Possible influence of moisture content on the denaturation reaction constant is addressed later in this chapter. Nevertheless, in spite of all the limitations in the models, it has been shown that acceptable results could be obtained. Consequently, the model is used in the following sections to elucidate how the process and the final product properties are influenced by input material properties and operating conditions.

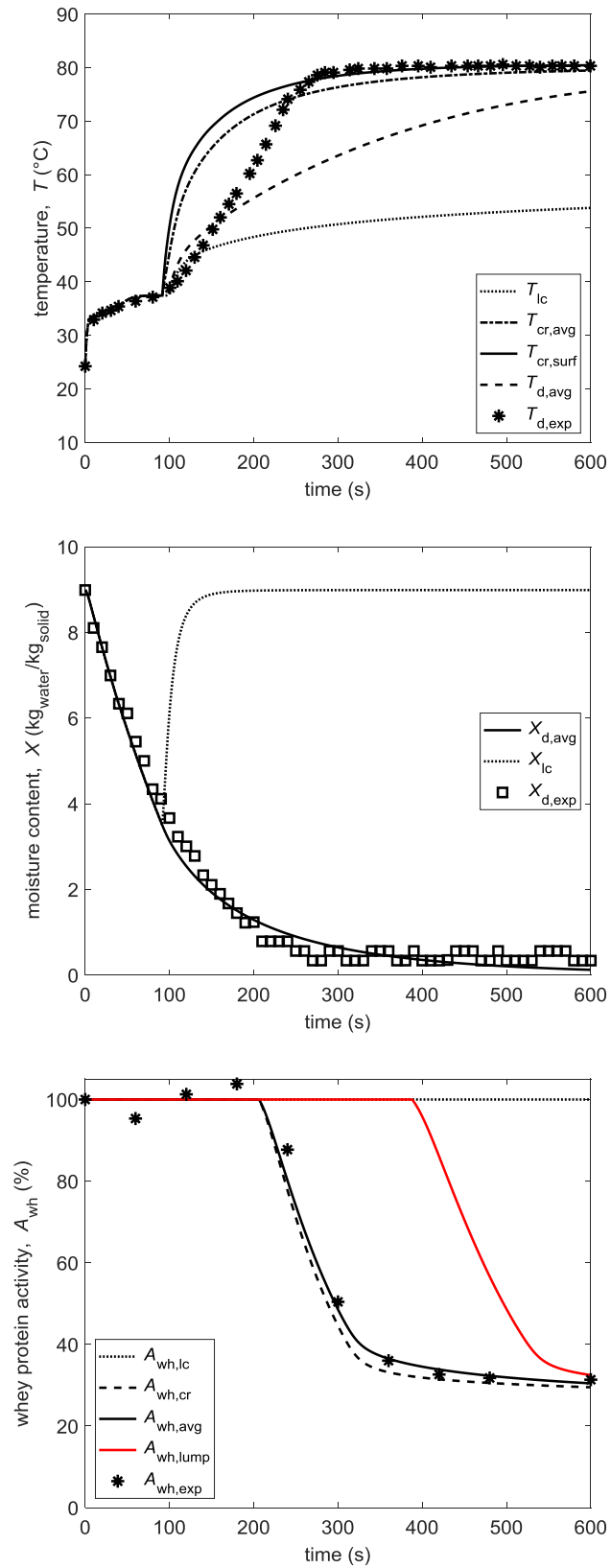


Fig. 6.2. Calculated changes in (from top to bottom) droplet temperatures, moisture contents, and whey protein activities compared to the experimental data [228].

Inactivation kinetic parameters are in general solid material-dependent. Different sources of protein or totally different materials result in different kinetic parameters. To understand how sensitive the denaturation kinetics and final product quality are to changes in these parameters, three variable multipliers namely f_n , f_{E_a} , and f_{k_0} are used for n , E_a , and k_0 , respectively. With a default value of unity, if not otherwise mentioned, they have been varied in some simulations.

In addition to solid properties, moisture content may also play a role in denaturation kinetics and affect the reaction constant. One way to include this influence is by making the pre-exponential factor in Eq. 6.2 a function of moisture content. This approach has been used successfully in some studies [104,106,231], with various functional forms. Here an additional multiplier f_{X,k_0} that is moisture content-dependent is applied to the prefactor k_0 , as previously done by Sloth et al. [231]. It is thus

$$k_0 = f_{X,k_0} f_{k_0} k_{0,\infty}. \quad (6.9)$$

$k_{0,\infty}$ is the default value of pre-exponential factor, which is independent of moisture content and given for each protein component in Table 6.1. Three cases of moisture content dependence are considered: *Case 1*: Denaturation rate is independent of moisture content; *Case 2*: Denaturation rate is large at high moisture content, then decreases as the moisture content becomes lower; and *Case 3*: Denaturation becomes more severe as the droplet dries out. To obtain the desired behaviors, a sigmoid dependence of f_{X,k_0} on moisture content

$$f_{X,k_0} = \frac{1}{1 + \exp(-10(x_w - 0.5)/q)} \quad (6.10)$$

has been used. x_w is water mass fraction and q is a variable having a value of either 1 or -1, which will give either the second or the third case, respectively. The equation gives a value of f_{X,k_0} ranging from 0 to 1 depending on the moisture content and the scenario. For Case 1, a constant value of $f_{X,k_0} = 0.5$ is used. The three cases are shown in Fig. 6.3, along with the obtained dC_{wh}/dt at different temperatures.

Process parameters and solid material properties used in the simulations are summarized in Table 6.3. Initial droplet properties (size and solid content) and drying conditions (gas temperature, pulsation frequency, and velocity components) are varied to elucidate how they influence the drying and denaturation process. Pulsation frequency indicates the intensity of pulsation, whereas velocity amplitude determines the strength. A condition in which there is no pulsation ($f = 0$ Hz) is also simulated. For each variable a value is chosen as the main value. Unless the variable values are specified in the results shown later, the main values are used in the simulations. The same protein component composition as given in Table 6.1 is used. Equilibrium moisture content is calculated using Eq. 2.11 with $A = 0.1499$ and $B = 2.306 \times 10^{-3}$. The values are actually for skim milk [232], but used nonetheless due to the close nature of skim milk to that of WPI and the lack of reliable data for WPI.

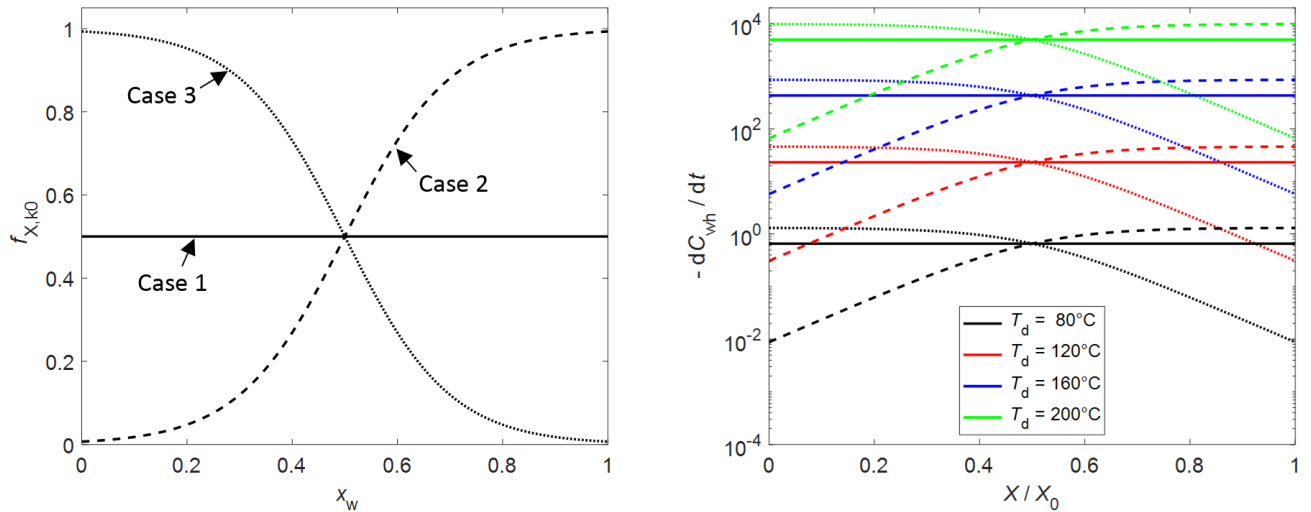


Fig. 6.3. Influence of moisture content on $f_{X,k0}$ (left) and dC_{wh}/dt (right) at different temperatures in three cases of protein denaturation considered: (1) independent of moisture content (solid lines); (2) decreasing at lower moisture content (dashed lines); and (3) increasing at lower moisture content (dotted lines).

Table 6.3. Process parameters and solid material properties used in the simulations.

Variables		Values
<i>General simulation parameters</i>		
No. of discretization elements	N_{el}	50
Average pressure (Pa)	\bar{P}	101325
Initial droplet velocity (m/s)	$u_{d,0}$	40
Initial droplet temperature (°C)	$T_{d,0}$	24
Absolute humidity (kg _{water} /kg _{air})	$Y_{g,\infty}$	0.008
Target moisture content (d.b.)	X_{dry}	8%
Length of drying chamber (m)	L	2
<i>Varied parameters</i>		
Gas temperature (°C)	T_g	80; 100; 120*; 160; 200; 300
Initial droplet size (μm)	$D_{d,0}$	10; 20; 30; 40; 50; 60; 70*; 80; 90; 100; 110; 120; 130
Initial solid mass fraction (-)	$x_{s,0}$	0.05; 0.1*; 0.2; 0.3
Average gas velocity (m/s)	\bar{u}_g	3; 6*; 12
Amplitude of gas velocity (m/s)	$u_{g,amp}$	0; 3; 6*; 12
Pulsation frequency (Hz)	f	0; 40; 80*; 120; 200; 300
<i>Solid properties</i>		
Density (kg/m ³)	ρ_s	1334 [233]
Specific heat capacity (J/(kg.K))	$c_{p,s}$	3170 [234]
Molar mass (g/mol)	M_s	26600 [235]
Thermal conductivity (W/(m.K))	λ_s	0.11 [236]

* the main value

In the simulation droplets are assumed to be sprayed from a two-fluid nozzle with a uniform release velocity approximated at 40 m/s (as in Chapter 3). Additionally, air is used instead of flue gas as the drying medium for simplicity, with moisture content of 8 g/kg air. It is further assumed that the chamber is fully insulated and the spray rate is small, so that heat and mass transfer between droplets and gas has negligible influence on the gas properties.

Two time variables, namely drying time and droplet residence time, are used for result presentation. Drying time is defined as the time required by a droplet to reach a desired final moisture content, below which product deterioration during storage can be minimized. A value of 8% d.b. can be considered acceptable for powder produced from spray dryer [101] and thus is used in this study. Droplet residence time is the time required for the droplet to reach a certain distance in the flow direction, which corresponds to the length of the drying chamber in a real situation with given equipment. Droplets can, then, be fully dried or still wet when they exit the drying chamber, depending on the initial properties and the process conditions. An arbitrary value of 2 m is used as the chamber length here.

A crucial step is to decide how locking point will be determined. The value of critical moisture content used earlier is not directly transferable to different drying temperatures and initial solid contents in the PCD simulations. For colloidal droplets (in Chapter 3) locking point is assumed to be reached when the layer of packed primary particles just below the surface is strong enough to withstand stresses due to surface tension and capillary forces. The key parameter is the strength of particle packing, which is a material dependent property and is strongly related to the ratio of saturated layer thickness to the droplet size at the locking point. The opposite can thus be assumed here: Locking point can be determined from this ratio. The latter increases continuously from zero during the 1st drying stage, and locking point is reached when a critical ratio has been achieved. At predetermined critical ratio value, the moisture content at the locking point will vary depending on the operating conditions. Given an initial droplet size, the ratio will be achieved earlier when the initial solid content is higher. This results in higher critical moisture content and larger locking diameter. The same will happen when drying rate is higher due to higher drying temperature or higher surrounding gas velocity, as faster evaporation means there is less time for the solute to diffuse back from the surface. For the experimental data by Haque et al., at the critical moisture content the saturated layer thickness-droplet radius ratio is 0.06. This value is used as the critical ratio for all simulations from this point onward.

6.4 Results and discussions

Figure 6.4 shows how protein activity, temperatures, and relative velocity of a 70 μm droplet change during drying at the main operating condition. Three protein activity values, which refer to those of liquid core, crust, and the whole droplet, are presented. Similarly, droplet temperatures are also differentiated between the crust and the liquid core for the 2nd drying stage. It can be seen that denaturation becomes noticeable when the crust temperature is

high enough. In the liquid core, denaturation practically does not occur as the temperature remains low. The relative velocity between the droplet and the surrounding gas oscillates following the pulsation. From the number of pulsation cycles it can be expected that the initial period of droplet release from a nozzle has limited influence on the process. The amplitude of relative velocity starts to decrease from the 1st drying stage. This is attributed to the decrease in droplet size, which reduces the drag force working on the droplet. The amplitude decreases further during the 2nd drying stage. Although droplet size remains at locking diameter in this period, droplet mass keeps on decreasing and it becomes easier for the droplet to get dragged away by the gas flow, thus reducing the relative velocity. The relative velocity could in the end be maintained above 2 m/s due to the pulsation.

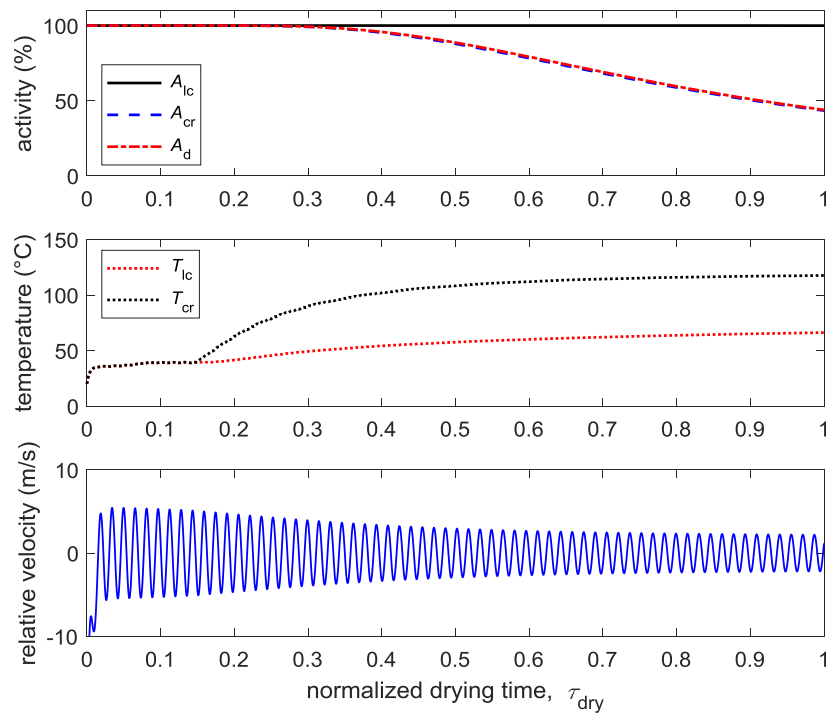


Fig. 6.4. Changes in activity (*top*), temperature (*middle*) and relative velocity (*bottom*) of a whey protein droplet ($D_{d,0} = 70 \mu\text{m}$) at the main operating condition.

6.4.1 Denaturation model behavior

Activities of dried particles obtained at different temperatures, values of kinetic multipliers, and cases of moisture dependence are shown in Fig. 6.5. At higher f_{Ea} protein denaturation is less. Higher activation energy means that it is harder for reactions to start, and as a result the final product activity is higher. Opposite results are obtained for reaction order, as at higher f_n denaturation rate is increased and the final product activity is lower. The same holds for k_0 , straightforwardly from Eqs. 6.1 and 6.2. Final product activity is more sensitive to n and E_a than to k_0 .

6 Drying and denaturation of proteins in PCD

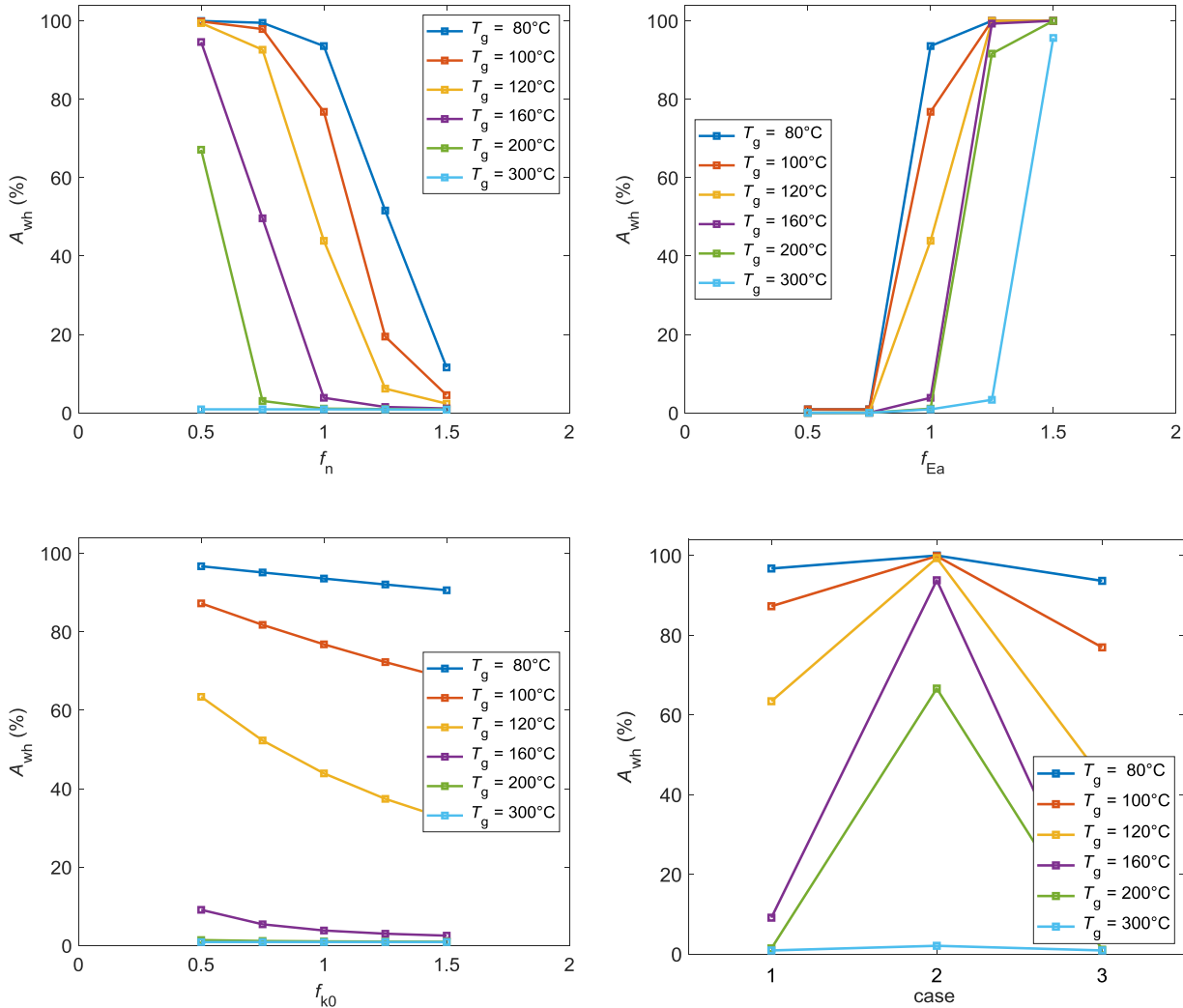


Fig. 6.5. Influences of the multipliers of denaturation kinetic parameters and moisture dependence on activities of dried particles ($X = 8\%$ d.b.) at different process temperatures and $f = 80$ Hz.

In regard to the moisture content dependence, Case 2 leads to less denaturation compared to Case 1. This is because denaturation happens mostly later during the process, that is, when the temperature is high and water content is low. In Case 2 the denaturation kinetics is slow during this period, resulting in higher product activity. Although for Case 3 $f_{X,k0}$ is low at the beginning (Fig. 6.3), less protein activity than in Case 1 is obtained. This shows that denaturation happens mostly in the later stage of drying, i.e., when the moisture content is low and droplet temperature is high. At the beginning the temperature is still not high enough and the denaturation is practically negligible regardless of the $f_{X,k0}$ value. When the gas temperature is low enough or very high, the difference in results between the three cases is small.

Following discussions are focused on how operating conditions and initial droplet properties influence the process and final product properties. The results are obtained with the original

form of the model. The multipliers and the scenarios of moisture content dependence, while affecting the results quantitatively, do not change the trends obtained for each process variable. The points made on the role of process conditions are thus unaffected by the modifications on denaturation kinetics.

6.4.2 *Process time and protein activity of dried particles*

The required drying time varies with process conditions and initial droplet properties. At given process conditions, drying time translates to the required residence time and consequently the length of drying chamber, which is related to initial investment costs. Figure 6.6 shows the required drying time at different process parameters. Higher drying temperature leads to shorter drying time. Drying time is also shorter when the droplets are small, as there is less water to evaporate. Later in Fig. 6.8 it will be shown that at a given chamber length smaller droplets actually stay longer in the chamber. The influence of initial solute content on drying time is not straightforward, despite the fact that higher solid content means less water to evaporate. When solid content is increased from 0.05 to 0.1 and 0.2, drying time initially increases. This is because with more solid the locking point will be achieved earlier, which leads to early reduction in evaporation rate. When solid content is increased further to 0.3 the drying time decreases, as having less available water becomes the dominant factor. The results show that drying can be made faster with gas pulsation. Increasing pulsation frequency or velocity amplitude decreases drying time further, but with weaker effect at higher magnitudes. In general, the influence of other process parameters on drying time weakens at higher temperatures. Average flow velocity is the only variable that has negligible effect on the drying time in the investigated range. With pulsation, the relative velocity between droplets and drying gas is more strongly influenced by the frequency and velocity amplitude for the most part of the process, whereas average velocity only plays a role at the beginning, after the droplets have been sprayed, as discussed in Chapter 3.

Protein activities of the dried particles are given in Fig. 6.7. Big droplets result in particles with lower activity. The larger the droplet size, the longer it takes to evaporate water from the start of crust formation, and thus the crust is exposed to the hot air longer. This, combined with larger surface area and higher relative velocity, results in more severe heating of the crust and, thus more protein denaturation. The trend obtained for protein activity at different initial solid contents is the opposite of the one observed for drying time. At most temperatures it initially decreases and then increases when the solid content is increased. Additionally, the difference is more pronounced at higher temperatures. The opposite trend is due to the fact that longer drying time means longer heat exposure and thus more protein denaturation. Interestingly, for most process parameters (except initial droplet diameter) variations of final protein activity are less pronounced than those of drying time. Gas pulsation results in slightly lower product activity, and further intensification by increasing the velocity amplitude or the pulsation frequency gives negligible difference. Just like observed for drying time, average gas velocity has no influence on the activity.

6 Drying and denaturation of proteins in PCD

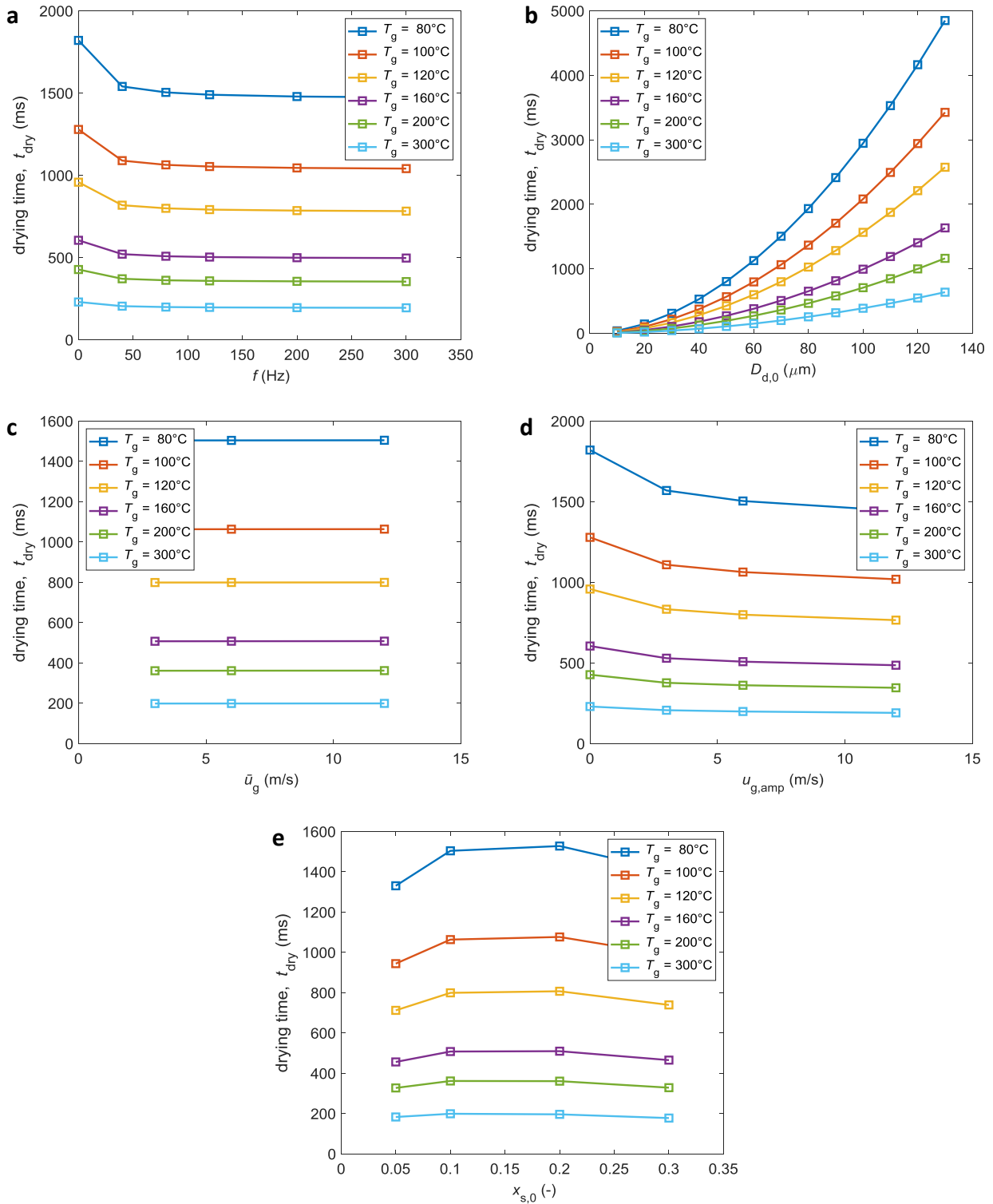


Fig. 6.6. Drying times required by a droplet ($D_{d,0} = 70 \mu\text{m}$) to reach $X = 8\%$ d.b. at different gas temperatures and (a) pulsation frequencies; (b) initial droplet diameters; (c) average gas velocities; (d) gas velocity amplitudes; and (e) initial solid mass fractions.

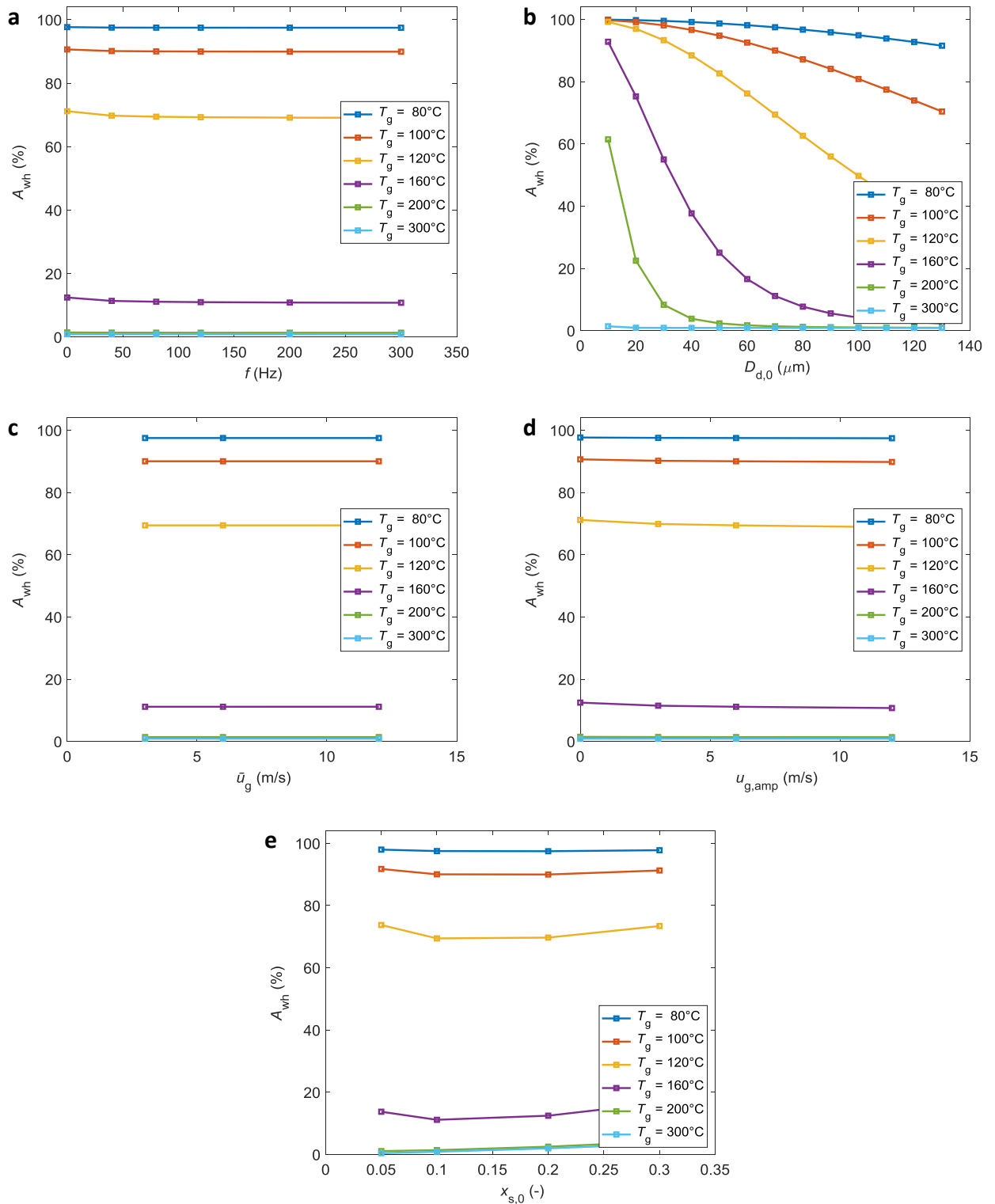


Fig. 6.7. Final protein activities of particles ($X = 8\%$ d.b.) obtained from $70\ \mu\text{m}$ droplets dried at different process temperatures and (a) pulsation frequencies; (b) initial droplet diameters; (c) average gas velocities; (d) gas velocity amplitudes; and (e) initial solid mass fractions.

6.4.3 *In specified drying chamber: Residence time and outlet properties*

In reality, the drying chamber is often given. Then droplet residence time greatly influences the final product properties. Residence time and outlet protein activity of particles obtained at different temperatures, pulsation frequencies, and initial droplet sizes from a 2 m drying chamber are plotted in Fig. 6.8. No protein denaturation occurs when the droplets are dried at 80 and 100 °C. On the other hand, the proteins are completely inactivated at $T_g = 300$ °C. With gas pulsation, residence time becomes lower than when there is no pulsation. The residence time decreases further when the velocity amplitude is increased (results not shown). This indicates that the accelerating effect of the pulsation on the droplet is more dominant than the decelerating effect. When the pulsation is intensified (the frequency is increased), however, the residence time increases again. This is because at higher frequency the velocity vector direction changes more quickly and there is less time for the pulsating gas flow to accelerate and decelerate the droplets. As a result, its influence on droplet velocity weakens. Gas pulsation results in lower residual protein activity. The influence becomes weaker as the pulsation velocity is increased.

Results of further variations are not presented, but just discussed briefly. At higher velocity amplitude, the residence time is shorter. Regarding protein activity, the trend is similar to the one observed for pulsation frequency in Fig. 6.8. Pulsation makes a difference, but its influence weakens as it is further intensified. Influence of average flow velocity on the process is straightforward. When the average flow velocity is increased, droplets have less time in the chamber, and, as a result, residual protein activity and moisture content are higher. Shorter residence time is also obtained with higher initial solid content. Since the solute has higher density than water, the droplet has higher inertia and its velocity is less affected by the flow. The influence of solid content on outlet protein activity, on the other hand, has no particular trend and depends on temperature.

From Fig. 6.8 it can be seen that smaller droplets have longer residence time. This is because small droplets follow the flow and decelerate more easily due to the oscillating gas velocity. Big droplets on the other hand have higher inertia, despite experiencing stronger drag force due to larger cross-sectional area. Contrasting results were reported in a previous numerical investigation [68]. However, it must be mentioned that in the referred study the simulated particles are way bigger (125-500 μm) and the flow is in upward direction. Particle movement is thus more influenced by gravity, which was taken into account in the reference (but not considered here).

For small droplets, locking point and subsequent crust exposure to high temperature come earlier. This, in combination with longer residence time, leads to more severe product deterioration, as shown in the figure. Although protein is conserved better for large particles, the final moisture content is higher. Given that in a real spray the droplet size spans over a distribution, non-uniform final product properties cannot be avoided. It is, then, the population-average product quality that is of interest. The influence of initial droplet size

distribution on final protein activity level and particle moisture content is investigated in the following section.

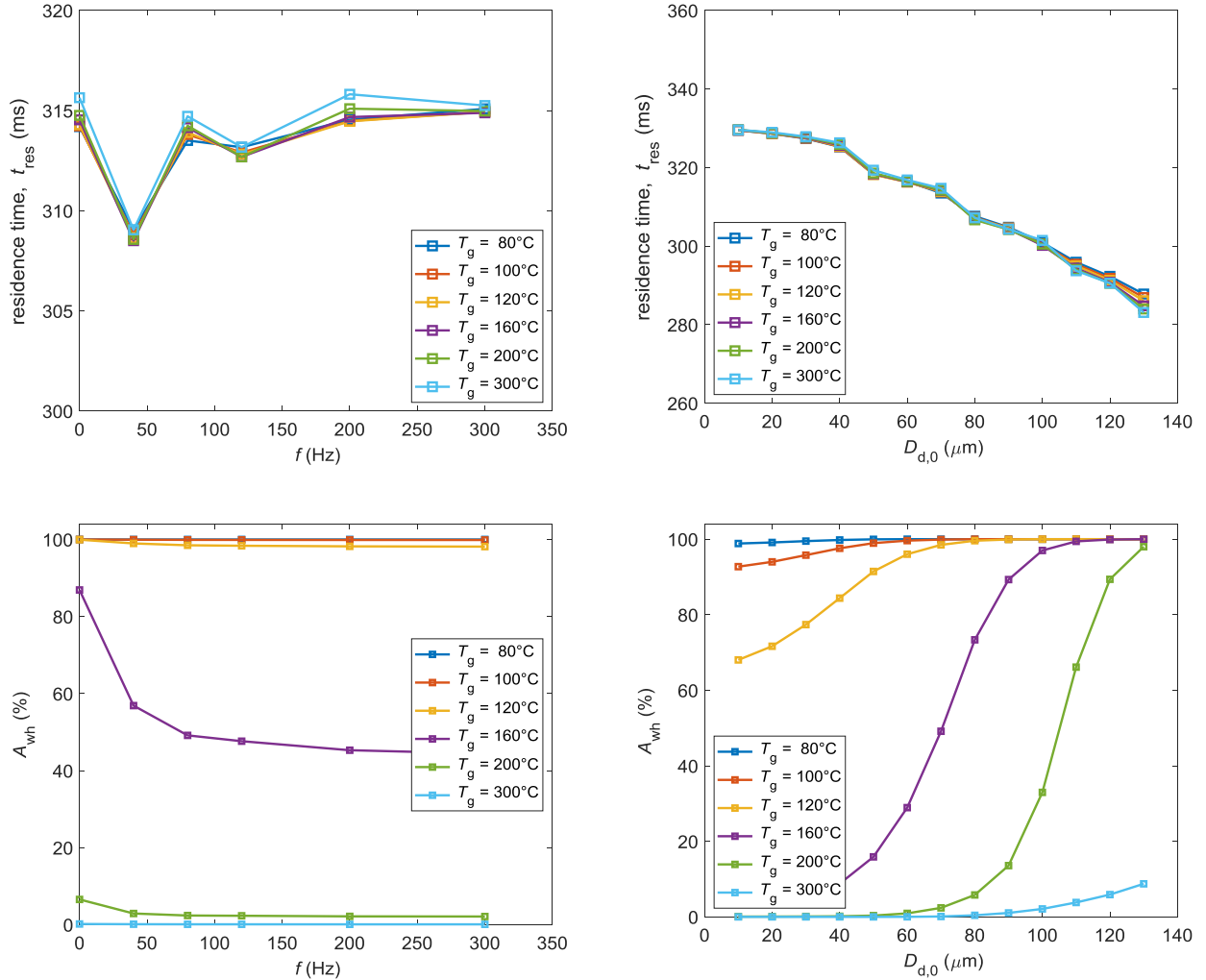


Fig. 6.8. Influences of pulsation frequencies (*left*) and initial droplet diameters (*right*) on residence time (*top*) and product activity (*bottom*) at different process temperatures and $L = 2$ m.

6.4.4 Influence of initial droplet size distributions

As in the previous chapters, initial droplet size distribution is assumed to be log-normal. The two parameters of the log-normal distribution, namely σ_{dist} and μ_{dist} , are related to the mean value \bar{D}_d and standard deviation SD as follows:

$$\sigma_{\text{dist}} = \sqrt{\ln\left(\frac{SD^2}{\bar{D}_d^2} + 1\right)}, \quad (6.11)$$

$$\mu_{\text{dist}} = \ln \left(\frac{\bar{D}_d^2}{\sqrt{SD^2 + \bar{D}_d^2}} \right), \quad (6.12)$$

with the standard deviation calculated as $SD = (D_{d,\text{max}} - D_{d,\text{min}})/6$ [205].

The mean diameter is related to median diameter $D_{d,\text{med}}$ and the standard deviation as

$$\bar{D}_d = \sqrt{\frac{D_{d,\text{med}}^2 + D_{d,\text{med}}^2 \sqrt{1 + 4 \left(\frac{SD}{D_{d,\text{med}}} \right)^2}}{2}}. \quad (6.13)$$

Table 6.4 presents five initial droplet size distributions. Variations are realized by making the distribution wider or narrower, or by shifting it to smaller or bigger size. It is done by changing either the maximum, minimum, or median diameters by 20 μm . It is shown that when the distribution width is changed at the same median diameter, the mean diameter also changes. However, the influence is relatively small compared to when the distribution is shifted (skewed) to one direction. The initial droplet size distributions and their respective final particle distributions (obtained at the main operating conditions) are presented in Fig. 6.9.

Table 6.4. Variations of initial droplet size distribution tested.

Distribution	$D_{d,0}$ (μm)			
	min	median	max	mean*
Main	30	70	110	71.22
Wide	10	70	130	72.61
Narrow	50	70	90	70.31
Skew left	30	50	110	51.64
Skew right	30	90	110	90.96

* calculated using Eq. 6.13

For each initial size distribution three population-average particle properties, namely moisture content (d.b.), activity (%), and energy consumption (J/kg solid), are investigated. They respectively refer to the amounts of remaining moisture and active ingredient in particles, and the total energy consumed during the process per solid mass. They are calculated as follows. From a droplet at given process conditions, entity variables such as particle size, volume, and component masses (total solid, active solid material, and remaining water) are obtained. Since neither droplet breakup nor particle breakage is considered, one droplet will result in one particle. The particles are distributed into bins ranging from 0 to 130 μm with an equal width of 10 μm each. This results in 13 isogradient bins, which is considered large enough to give accurate particle size distributions [237]. Quantity variables of the particles

(number, volume, and masses) and the energies consumed during the process are distributed to the bins according to the final particle size and the initial droplet number distribution. The population-average particle properties are obtained by averaging over all bins.

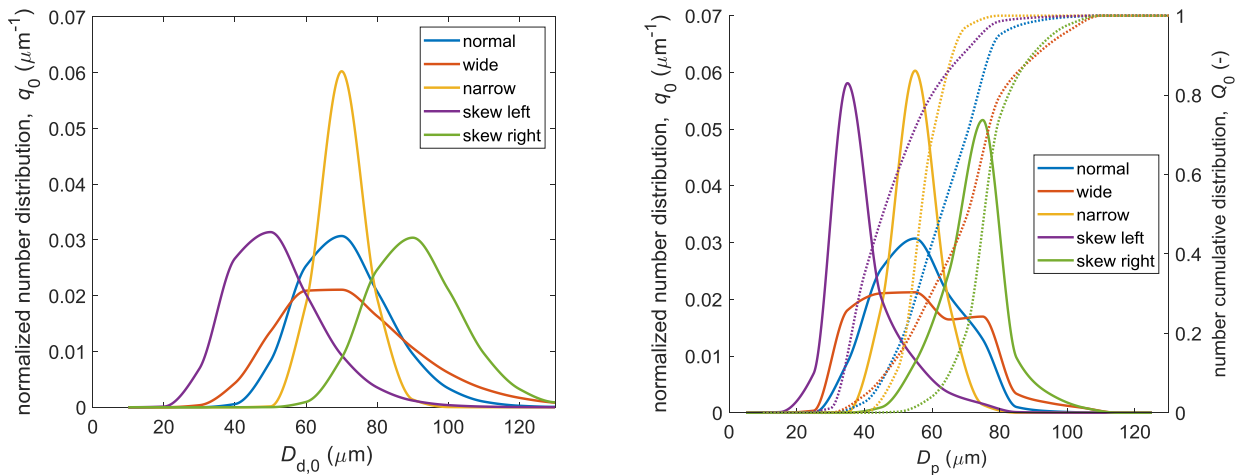


Fig. 6.9. Initial droplet size distributions (*left*) generated with different width (span)-median diameter combinations given in Table 6.4 and their respective final particle size distributions (*right*).

Average final product activities and moisture contents obtained from different initial size distributions at different temperatures and pulsation frequencies are shown in Fig. 6.10. It is shown that same trends are obtained for final product activity and moisture content. The trends obtained when the distribution is moved in horizontal direction are pretty much the same as previously shown for droplet size. Shifting the distribution to the right means larger droplets, giving higher residual protein activity and moisture content. The opposite is obtained when the distribution is shifted to the left. A wider size distribution results in higher residual protein activity and moisture content. Although additional numbers of larger and smaller droplets than in the main distribution are present, the large droplets contribute more to the total product mass and thus the average product activity and moisture content are increased. Average droplet size seems to have a more pronounced effect on final product quality than droplet distribution width.

Figure 6.11 shows how energy use is affected by the initial droplet size distributions at various temperatures, without and with pulsation at $f = 80$ Hz. Two parameters are given here: total heat consumption and fraction of sensible heat. The first refers to the total heat transferred from the gas to the droplets (particles), whereas the latter is the fraction of the absorbed heat that is not used for water evaporation. Opposite trends in total energy consumption and sensible heat fraction are obtained for different initial size distributions. When droplet size distribution is skewed to the right (more large droplets), there are notable decreases in energy consumption but increases in sensible heat fraction. This is because large droplets have lower

residence times, which means there is less time for heat and mass transfer. Thus, this yields higher residual moisture content and protein activity, as shown in Fig. 6.10. Since the objective is to get much drying with less product deterioration, a process is considered more energy efficient when the fraction of energy used for evaporation is higher, i.e., when the sensible heat fraction is lower. Discrepancies in energy use between different initial droplet size distributions are decreased when gas pulsation is employed. Overall energy consumption is higher with pulsation, especially at lower temperatures, indicating intensified heat transfer. Evaporation energy efficiency is higher with pulsation at lower temperatures, as shown by lower sensible heat fractions. However, the opposite effect is obtained at higher temperatures.

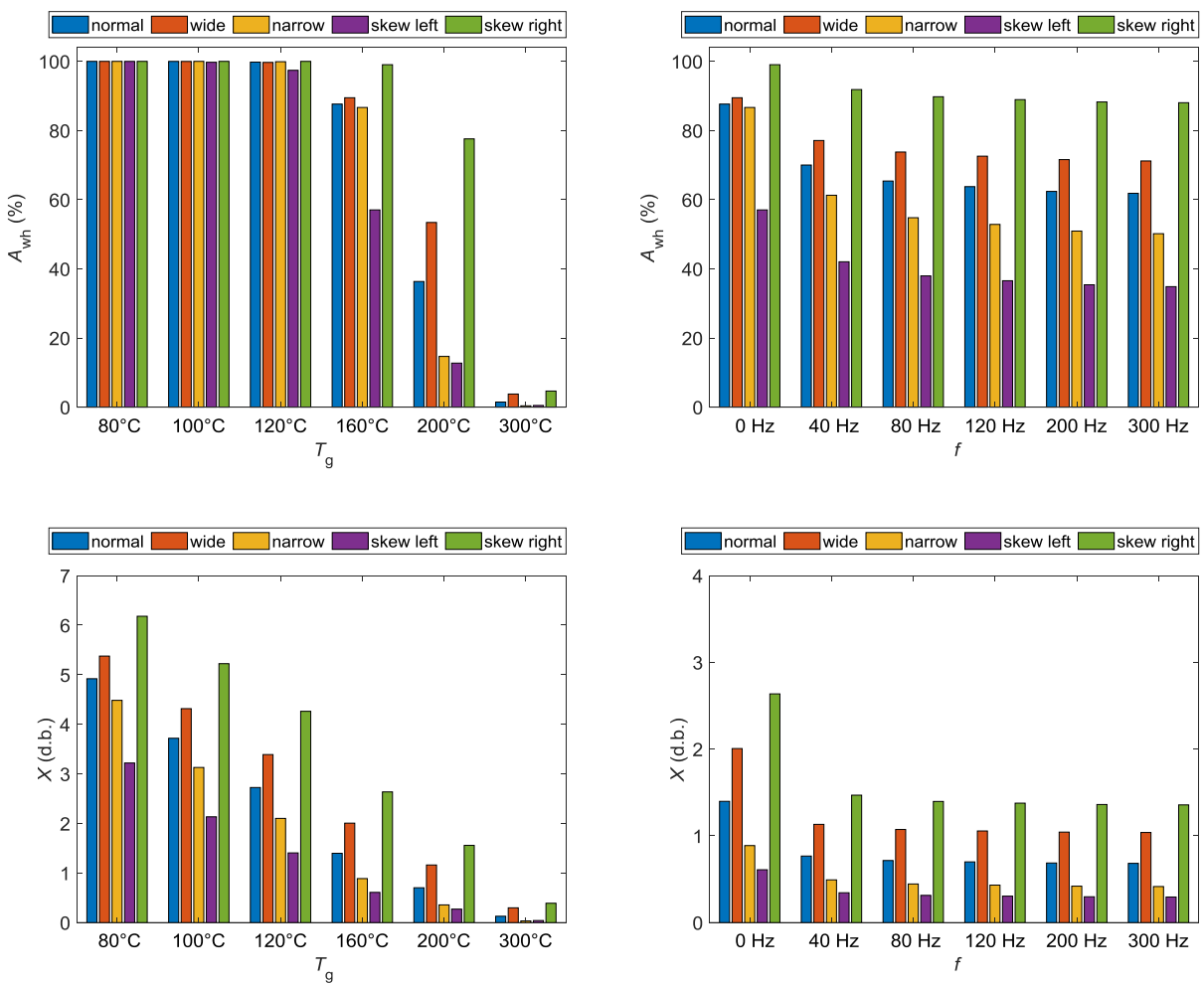


Fig. 6.10. Population-average final particle activity (*top*) and moisture content (*bottom*) obtained at various temperatures without pulsation (*left*) and at various pulsation frequencies and $T_g = 160$ °C (*right*) for different initial droplet size distributions. The length of drying chamber is 2 m.

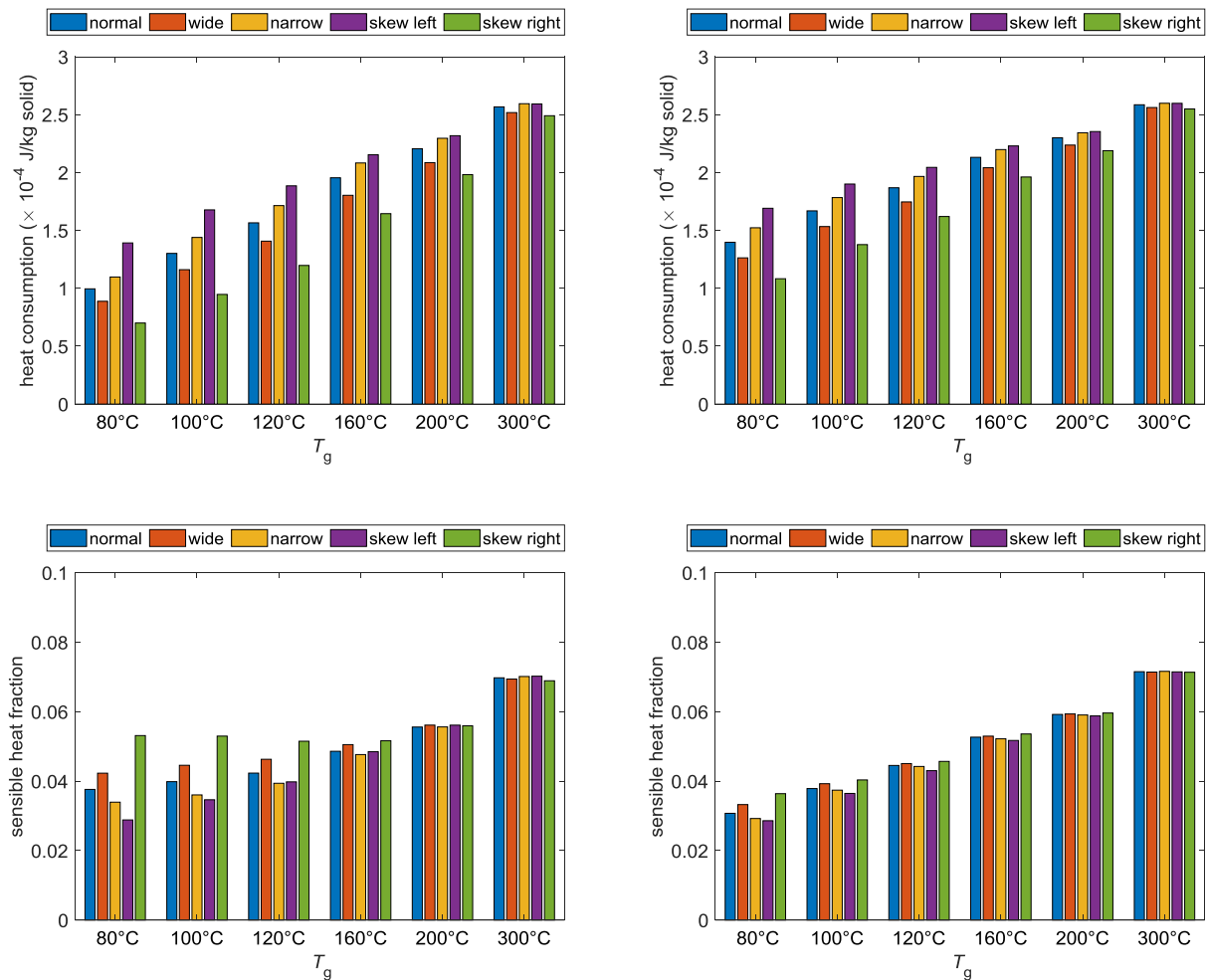


Fig. 6.11. Energy consumption per solid mass (*top*) and the fraction of sensible heat (*bottom*) obtained at various temperatures, without pulsation (*left*) and with pulsation at $f = 80$ Hz (*right*) for different initial droplet size distributions. The length of drying chamber is 2 m.

6.4.5 Increased temperature vs gas pulsation

From the results in Figs. 6.6, 6.7, 6.10 and 6.11, it can be comprehended that at high temperatures it is not possible to get dry enough product without having the protein severely inactivated. In respect to product properties low temperature is better. Low temperature, however, leads to longer process time and drying chamber required. Gas pulsation has been shown to intensify heat and mass transfer, so it may be a solution to this dilemma.

Table 6.5 shows a comparison between the two strategies to achieve the desired moisture content (8% d.b.). Using stationary gas flow at $T_g = 120$ °C as the departing point, the process is intensified either by increasing the gas temperature up to 150 °C or by pulsating the gas flow up to 300 Hz. The relative changes in protein activity, drying time, chamber length, and energy consumption are presented. Using hotter gas at 140 and 150 °C decreases the drying time (and chamber length) more compared to using gas pulsation, but the product quality is

greatly sacrificed. At $T_g = 130$ °C the drying time is still higher than at $T_g = 120$ °C with pulsation, but even with that the protein activity is already lower. To achieve same drying time the temperature must be increased to around 134-137 °C, but then the product quality will be worse. Moreover, the additional energy consumption is slightly higher when the gas temperature is increased than when the gas is pulsed.

Table 6.5. Comparison of drying process intensification by increasing temperature and by gas pulsation.

T_g (°C)	120*	130	140	150	120	120
f (Hz)	0*	0	0	0	80	300
A_{wh} (%)	71.18	55.56 (-21.94%)	38.38 (-46.08%)	23.19 (-67.42%)	69.44 (-2.44%)	69.09 (-2.93%)
t_{dry} (ms)	958	843 (-11.96%)	749 (-21.80%)	670 (-29.98%)	799 (-16.59%)	782 (-18.39%)
L (m)	5.86	5.17 (-11.74%)	4.61 (-21.38%)	4.14 (-29.41%)	4.91 (-16.16%)	4.80 (-18.08%)
Q_{vap} ($\times 10^7$ J/kg)	2.120	2.133 (+0.62%)	2.147 (+1.27%)	2.161 (+1.93%)	2.112 (-0.38%)	2.110 (-0.47%)
Q_{tot} ($\times 10^7$ J/kg)	2.206	2.226 (+0.90%)	2.246 (+1.81%)	2.266 (+2.72%)	2.207 (+0.01%)	2.207 (+0.02%)

* base condition

For the scenarios given in Table 6.5, population-average protein activity and moisture content obtained from a 5 m drying chamber are shown in Fig. 6.12. Similar to the results in Table 6.5, the moisture content can be decreased more with gas pulsation than by using higher temperature. Even by increasing the temperature to 140 °C, the outlet moisture contents are still higher than those obtained with gas pulsation. From these results it can be concluded that intensifying the process by using pulsation is a better strategy than using hotter gas, as the drying process can be made faster with less product deterioration.

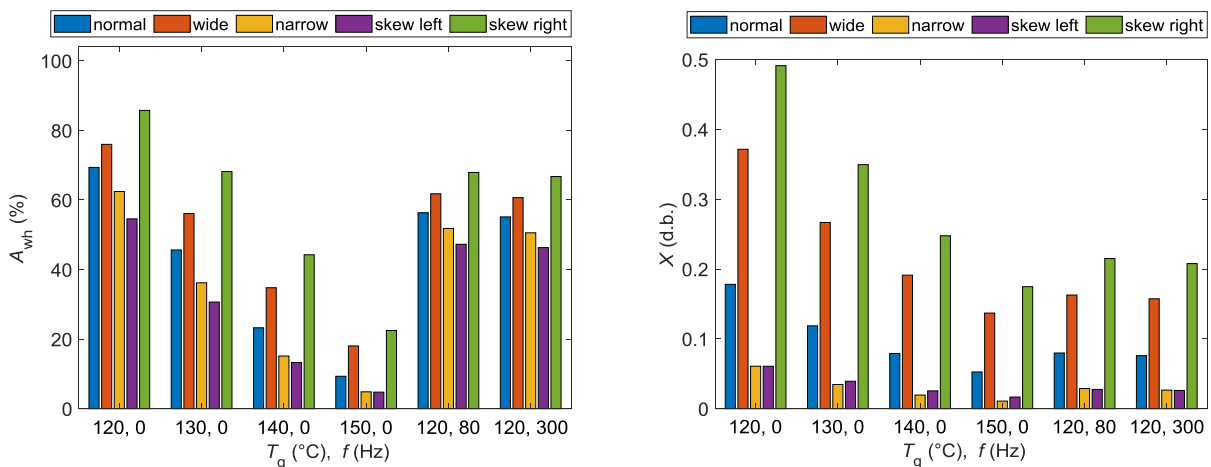


Fig. 6.12. Population-average final protein activity (*left*) and moisture content (*right*) obtained from a 5 m drying chamber at various temperature-frequency combinations and initial droplet size distributions.

6.5 Conclusion

Drying and product inactivation during production of WPI powder from solution using PCD has been investigated in this chapter. This was achieved by combining a validated single droplet drying model with separately derived protein denaturation kinetic model from literature. The sensitivity of denaturation kinetics to model parameters has been discussed. Additionally, by investigating some scenarios of dependence on moisture content, it is found that protein denaturation starts at low overall droplet (particle) moisture content after crust formation. Influences of operating conditions and initial droplet properties on the final product properties and process dynamics have been elucidated. Gas temperature strongly affects drying and denaturation, but has minor influence on droplet residence time. Higher pulsation intensity (i.e., increasing frequency) leads to intensified heat and mass transfer, but the effects get weaker at high frequency. Stronger pulsation (i.e., higher velocity amplitude) also results in faster drying and shorter droplet residence time. The two pulsation related parameters also have an enhancing effect on protein denaturation, although it is less pronounced compared

to that on moisture content. Average flow velocity on the other hand has negligible effect on the properties of dried product, although it strongly determines the droplet residence time. Opposite trends are obtained with variation of initial droplet size, as smaller droplets dry faster but stay longer in the chamber, whereas the large ones exit the chamber earlier despite needing more time to dry. This strongly influences the results obtained with variations in initial droplet size distribution. The influence of initial solid content is less straightforward and depends on the other variables. For heat sensitive materials like WPI it is better to employ low enough temperature and dry slowly. Intensification of the drying process by using pulsating flow has been shown better than by increasing temperature from the perspectives of final product quality and energy consumption.

The present results show that there is no condition that favors drying and activity retention at the same time. In a real situation, optimization would not be easy, as not only the product properties change with process conditions, but also the process parameters are in a complex way intertwined with each other. For instance, in a given drying chamber pulsation frequency changes dynamically with velocity. Resonance frequency, which is the frequency at which pulsation is strongest, thus giving the maximum pulsation effect, is also a function of chamber dimensions and shape. Optimum conditions must thus be determined case by case, depending on available process conditions and product requirements. The key here is to strike the balance between the two opposing quality parameters, namely moisture content and substance activity. Although the model has been applied only to one material here, the same concept can be used for other materials, given the properties and degradation kinetics are known.

7. General conclusion & outlook

PCD is a relatively new technology in the field of spray drying. It utilizes pulsating gas flow, which is the flue gas generated from intermittent combustion occurring in a pulsed combustor, as the medium for drying. Additionally, the flow also helps in disintegrating feed material. In this study, intensified processes, in particular related to fine particle formation and change in product quality, during drying of suspension or solution droplets in PCD have been investigated. Atomization of droplets, i.e., generation of the spray, is out of the scope of this study.

Droplets experience a drag force in the flow, due to their relative velocity to the gas. The drag force dynamically affects droplet velocity, and consequently the relative velocity. Gas pulsation accelerates and decelerates droplets in cyclical manner. It keeps the relative velocity high throughout the drying process. The overall heat and mass transfer coefficients are thus higher than when there is no pulsation.

The drag force does not only influence the droplet movement, but also distorts the shape. The process of droplet distortion has been calculated using the Taylor analogy breakup model. Above a certain value of non-dimensional distortion, a droplet might break. Dynamic interaction between pulsated gas flow and droplets keeps the distortion level higher than when there is no pulsation. As a result, droplets break more easily in pulsed flow. Droplet distortion is also influenced by droplet properties: size, viscosity, and effective surface tension. The latter is governed by interaction forces between primary particles in a colloidal droplet. Surface charge of the primary particles governs the repulsive electrostatic force and subsequently the effective surface tension. Both the viscosity and effective surface tension are functions of the primary particle size and concentration. In general, large initial droplet size, small nanoparticles, high surface charge, high gas temperature, strong gas pulsation, and relatively high frequency are favorable for droplet breakup.

It has been shown that there is a limit of how small a droplet can become prior to reaching a locking point. Morphology and size distribution of particles obtained from a pilot-scale PCD suggests that further deformation and size reduction occurred after the locking point. This happened regardless of gas pulsation in the investigated temperature range. Two possible mechanisms for breakage of droplet crust have been investigated. Stresses due to temperature and pressure gradient, instead of flow induced shear, have been shown as the main possible cause, which explains the limited influence of gas pulsation on this process. Qualitative agreement with experimental data for metal oxides has been found.

Since applications to heat sensitive materials such as food and pharmaceuticals have been reported, a question has been raised on how the intensified heat and mass transfer affects the quality of material being dried. Numerical investigation on whey protein has been carried out, to see how drying and protein denaturation are influenced by process conditions. Droplet residence time is more influenced by flow velocity profile than by temperature. While pulsation leads to faster moisture removal and protein denaturation, the enhancing effect is less pronounced for the latter. Additionally, pulsation reduces discrepancies in energy use and final product quality due to different initial droplet size distributions. As there is no condition that favors drying and activity retention at the same time, optimization is required. It is shown that using pulsating gas flow can be a better strategy than simply increasing the temperature to intensify the drying process without sacrificing product quality and requiring too much additional energy. There is, however, a certain limit of how much the process can be enhanced.

The results obtained in this study have shown that the main feature of PCD in respect to process intensification in droplet drying is the ability to keep the relative velocity between drying gas and droplets high. While more intense pulsation intensifies the process, the enhancing effect weakens as the frequency is further increased, as shown for droplet breakup and drying. Gas pulsation promotes the production of smaller particles by increasing the possibility of droplet breakup. Additionally, for the process conditions investigated here, the intensification by pulsation has been shown to be larger on drying than on heating, which is favorable. The findings here thus confirm the advantages that PCD can offer over conventional spray drying.

In the numerical investigations emphasis has been put on the influence of process variables. It is important to note that the models presented here assume dilute condition in the drying chamber. Possible interactions between droplets are not taken into account. Droplet-to-droplet collision and coalescence are expected in the atomization region [238] and have negative effect on heat and mass transfer coefficients [239]. Moreover, there is also a grouping effect of droplets (or particles) in the flow that is enhanced with stronger pulsation [68]. As a result, object velocity and residence time will be affected by the interactions. The influence of droplet evaporation on the composition of surrounding gas has also been neglected. Micro-environment surrounding each droplet will change dynamically and become different due to different process dynamics, although initially the flow profile in droplet-filled region can be taken as uniform. Droplets of different sizes, for example, will develop different velocity and humidity profiles around them. Droplet breakup and crust breakage are also expected to strongly influence the surrounding flow field. Despite the drawbacks and inaccuracies, the models can nevertheless give clear ideas on the process and the obtained product properties. More advanced calculation tools such as CFD are needed to simulate better the dynamic interaction between gas and droplets, and thus give more detailed and accurate results. The main challenge will be how to incorporate the models into CFD, especially since when accurate calculation of crust formation and properties is required.

Many other aspects of PCD are still there to investigate, especially since the technology is relatively new and the number of studies is still limited. One of known advantages of PCD is simpler atomizer requirement due to pulsating flow. However, thorough investigation on primary atomization in pulsating flow is not available. Additionally, applications for other forms of feed material such as pellets and highly viscous pastes have been reported but the studies are scarce. Another possible investigation topic is how fuel and flue gas composition might influence process dynamics and final product properties, especially related to possible adsorption of gas components. The latter is particularly important for foods and pharmaceuticals. Although PCD has often been claimed safe for such materials, studies were only conducted on the obtained product properties. Further investigations on dynamic interactions between gas compounds and droplets or particles would be interesting and could also open up new process possibilities.

References

- [1] R. Vehring, Pharmaceutical particle engineering via spray drying, *Pharmaceutical Research*. 25 (2008) 999–1022.
- [2] B.R. Bhandari, X.D. Chen, K.C. Patel, Spray drying of food materials: Process and product characteristics, in: X.D. Chen, A.S. Mujumdar (Eds.), *Dry. Technol. Food Process.*, Blackwell Publishing Ltd., Oxford, 2008: pp. 113–159.
- [3] A.B.D. Nandiyanto, K. Okuyama, Progress in developing spray-drying methods for the production of controlled morphology particles: From the nanometer to submicrometer size ranges, *Advanced Powder Technology*. 22 (2011) 1–19.
- [4] R.A. Khaire, P.R. Gogate, Novel approaches based on ultrasound for spray drying of food and bioactive compounds, *Drying Technology*. 39 (2021) 1832–1853.
- [5] K. Samborska, S. Poozesh, A. Barańsk, M. Sobulska, A. Jedlińska, C. Arpagaus, N. Malekjani, M.S. Jafarif, Innovations in spray drying process for food and pharma industries, *Journal of Food Engineering*. 321 (2022) 110960.
- [6] C. Santivarangkna, U. Kulozik, P. Foerst, Alternative drying processes for the industrial preservation of lactic acid starter cultures, *Biotechnology Progress*. 23 (2007) 302–315.
- [7] M.R.I. Shishir, W. Chen, Trends of spray drying: A critical review on drying of fruit and vegetable juices, *Trends in Food Science and Technology*. 65 (2017) 49–67.
- [8] E. Assadpour, S.M. Jafari, Advances in spray-drying encapsulation of food bioactive ingredients: From microcapsules to nanocapsules, *Annual Review of Food Science and Technology*. 10 (2019) 103–131.
- [9] J.T. Pinto, E. Faulhammer, J. Dieplinger, M. Dekner, C. Makert, M. Nieder, A. Paudel, Progress in spray-drying of protein pharmaceuticals: Literature analysis of trends in formulation and process attributes, *Drying Technology*. 39 (2021) 1415–1446.
- [10] X. Meng, W. De Jong, T. Kudra, A state-of-the-art review of pulse combustion: Principles, modeling, applications and R&D issues, *Renewable and Sustainable Energy Reviews*. 55 (2016) 73–114.
- [11] T. Kudra, Pulse-combustion drying: Status and potentials, *Drying Technology*. 26 (2008) 1409–1420.
- [12] Z. Xiao, X. Xie, Y. Yuan, X. Liu, Influence of atomizing parameters on droplet properties in a pulse combustion spray dryer, *Drying Technology*. 26 (2008) 427–432.
- [13] W. Widiyastuti, W.N. Wang, A. Purwanto, I.W. Lenggono, K. Okuyama, A pulse combustion-spray pyrolysis process for the preparation of nano- and submicrometer-sized oxide particles, *Journal of the American Ceramic Society*. 90 (2007) 3779–3785.

- [14] Z. Wu, L. Yue, Z. Li, J. Li, A.S. Mujumdar, J.A. Rehkopf, Pulse combustion spray drying of egg white: Energy efficiency and product quality, *Food and Bioprocess Technology*. 8 (2014) 148–157.
- [15] I. Zbicinski, T. Kudra, X. Liu, Pulse combustion drying, in: E. Tsotsas, A.S. Mujumdar (Eds.), *Mod. Dry. Technol. Vol. 5*, Wiley-VCH, 2014: pp. 27–56.
- [16] I.M. Joni, A. Purwanto, F. Iskandar, M. Hazata, K. Okuyama, Intense UV-light absorption of ZnO nanoparticles prepared using a pulse combustion-spray pyrolysis method, *Chemical Engineering Journal*. 155 (2009) 433–441.
- [17] P. V. Akulich, A. V. Akulich, V.L. Dragun, Wave motion and heat and mass transfer of the disperse phase under the conditions of low-frequency gas pulsations, *International Journal of Heat and Mass Transfer*. 53 (2010) 3213–3221.
- [18] P.S. Kuts, P. V. Akulich, N.N. Grinchik, E.F. Nogotov, C. Strumillo, I. Zbiciński, Modeling of gas dynamics in a pulse combustion chamber to predict initial drying process parameters, *Chemical Engineering Journal*. 86 (2002) 25–31.
- [19] P. V. Akulich, P.S. Kuts, Wave motion of solid particles in a pulsed gas flow, *Journal of Engineering Physics and Thermophysics*. 76 (2003) 788–794.
- [20] I. Zbiciński, C. Strumillo, M. Kwapińska, I. Smucerowicz, Calculations of the pulse combustion drying system, *Energy Conversion and Management*. 42 (2001) 1909–1918.
- [21] D.N. Nguyen, C. Clasen, G. van den Mooter, Pharmaceutical applications of electrospraying, *Journal of Pharmaceutical Sciences*. 105 (2016) 2601–2620.
- [22] I. Gouaou, S. Shamaei, M.S. Koutchoukali, M. Bouhelassa, E. Tsotsas, A. Kharaghani, Impact of operating conditions on a single droplet and spray drying of hydroxypropylated pea starch: Process performance and final powder properties, *Asia-Pacific Journal of Chemical Engineering*. 14 (2019) e2268.
- [23] P. Walzel, Influence of the spray method on product quality and morphology in spray drying, *Chemical Engineering and Technology*. 34 (2011) 1039–1048.
- [24] W. Liu, X.D. Chen, C. Selomulya, On the spray drying of uniform functional microparticles, *Particuology*. 22 (2015) 1–12.
- [25] W.D. Wu, K.C. Patel, S. Rogers, X.D. Chen, Monodisperse droplet generators as potential atomizers for spray drying technology, *Drying Technology*. 25 (2007) 1907–1916.
- [26] M.I.U. Islam, T.A.G. Langrish, The effect of different atomizing gases and drying media on the crystallization behavior of spray-dried powders, *Drying Technology*. 28 (2010) 1035–1043.
- [27] J. Vicente, J. Pinto, J. Menezes, F. Gaspar, Fundamental analysis of particle formation in spray drying, *Powder Technology*. 247 (2013) 1–7.
- [28] J. Elversson, A. Millqvist-Fureby, Particle size and density in spray drying: Effects of carbohydrate properties, *Journal of Pharmaceutical Sciences*. 94 (2005) 2049–2060.

- [29] F. Tatar Turan, A. Cengiz, T. Kahyaoglu, Evaluation of ultrasonic nozzle with spray-drying as a novel method for the microencapsulation of blueberry's bioactive compounds, *Innovative Food Science and Emerging Technologies*. 32 (2015) 136–145.
- [30] S.M. Jafari, C. Arpagaus, M.A. Cerqueira, K. Samborska, Nano spray drying of food ingredients; materials, processing and applications, *Trends in Food Science and Technology*. 109 (2021) 632–646.
- [31] F. Tatar Turan, A. Cengiz, D. Sandıkçı, M. Dervisoglu, T. Kahyaoglu, Influence of an ultrasonic nozzle in spray-drying and storage on the properties of blueberry powder and microcapsules, *Journal of the Science of Food and Agriculture*. 96 (2016) 4062–4076.
- [32] E. Boel, R. Koekoekx, S. Dedroog, I. Babkin, M.R. Vetrano, C. Clasen, G. van den Mooter, Unraveling particle formation: From single droplet drying to spray drying and electrospraying, *Pharmaceutics*. 12 (2020) 625–682.
- [33] T.W. Wong, P. John, Advances in spray drying technology for nanoparticle formation, in: M. Aliofkhae (Ed.), *Handb. Nanoparticles*, Springer International Publishing AG, 2015: pp. 329–346.
- [34] M. Sangkhamanee, S. Tekasakul, P. Tekasakul, Y. Otani, Performance of a combined cyclone-filter aerosol collector, *Particulate Science and Technology*. 29 (2011) 345–355.
- [35] S. Poozesh, S.M. Jafari, N.K. Akafuah, Interrogation of a new inline multi-bin cyclone for sorting of produced powders of a lab-scale spray dryer, *Powder Technology*. 373 (2020) 590–598.
- [36] A.M. Goula, K.G. Adamopoulos, Spray drying of tomato pulp in dehumidified air, Part 2: The effect on powder properties, *Journal of Food Engineering*. 66 (2005) 35–42.
- [37] A. Barańska, A. Jedlińska, K. Samborska, Dehumidified-air-assisted spray drying of buckwheat honey with maltodextrin and skim milk powder as carriers, *Applied Sciences*. 11 (2021) 3150–3169.
- [38] F. de Melo Ramos, V. Silveira Junior, A.S. Prata, Assessing the vacuum spray drying effects on the properties of orange essential oil microparticles, *Food and Bioprocess Technology*. 12 (2019) 1917–1927.
- [39] F. de M. Ramos, C.C.M. de Oliveira, A.S.P. Soares, V. Silveira Junior, Assessment of differences between products obtained in conventional and vacuum spray dryer, *Food Science and Technology*. 36 (2016) 724–729.
- [40] D. Semyonov, O. Ramon, E. Shimoni, Using ultrasonic vacuum spray dryer to produce highly viable dry probiotics, *LWT - Food Science and Technology*. 44 (2011) 1844–1852.
- [41] F.P. Hanrahan, A. Tamsma, K.K. Fox, M.J. Pallansch, Production and properties of spray-dried whole milk foam, *Journal of Dairy Science*. 45 (1962) 27–31.
- [42] D.D. Frey, C.J. King, Experimental and theoretical investigation of foam-spray drying,

- Part 2: Experimental investigation of volatiles loss during foam-spray drying, *Industrial and Engineering Chemistry Fundamentals*. 25 (1986) 730–735.
- [43] L. Gallo, M.A. Serain, C. Renaudo, E. López, V. Bucalá, Influence of microbubbles on the production of spray-dried inhalable particles, *Drying Technology*. (2021) 1–13.
- [44] M. Piatkowski, M. Taradaichenko, I. Zbicinski, Flame spray drying, *Drying Technology*. 32 (2014) 1343–1351.
- [45] M. Sobulska, I. Zbicinski, M. Piatkowski, Mechanism of flame spray drying process: Experimental and CFD analysis, *Drying Technology*. 38 (2020) 80–92.
- [46] M. Piatkowski, M. Taradaichenko, I. Zbicinski, Energy consumption and product quality interactions in flame spray drying, *Drying Technology*. 33 (2015) 1022–1028.
- [47] K. Bürki, I. Jeon, C. Arpagaus, G. Betz, New insights into respirable protein powder preparation using a nano spray dryer, *International Journal of Pharmaceutics*. 408 (2011) 248–256.
- [48] C.G.J. Baker, K.A. McKenzie, Energy consumption of industrial spray dryers, *Drying Technology*. 23 (2005) 365–386.
- [49] I. Zbicinski, Equipment, technology, perspectives and modeling of pulse combustion drying, *Chemical Engineering Journal*. 86 (2002) 33–46.
- [50] G. Križan, J. Križan, I. Bajsić, M. Gaberšček, Control of a pulse combustion reactor with thermoacoustic phenomena, *Instrumentation Science and Technology*. 46 (2018) 43–57.
- [51] G.A. Richards, D.W. Shaw, S.A. Keeley, M.J. Welter, G.J. Morris, Thermal pulse combustion, *Combustion Science and Technology*. 94 (1993) 57–85.
- [52] M. Abu-Qudais, Instantaneous exhaust-gas temperature and velocity for a diesel engine, *Applied Energy*. 56 (1997) 59–70.
- [53] V.S. Arpaci, J.E. Dec, J.O. Keller, Heat transfer in pulse combustor tailpipes, *Combustion Science and Technology*. 94 (1993) 131–146.
- [54] J.E. Dec, J.O. Keller, Pulse combustor tail-pipe heat-transfer dependence on frequency, amplitude, and mean flow rate, *Combustion and Flame*. 77 (1989) 359–374.
- [55] S. Thyageswaran, Numerical modeling of pulse combustor tail pipe heat transfer, *International Journal of Heat and Mass Transfer*. 47 (2004) 2637–2651.
- [56] A. Kilicarslan, A. Arisoy, Acoustic analysis of a liquefied petroleum gas-fired pulse combustor, *Applied Acoustics*. 69 (2008) 770–777.
- [57] A.G. Buchkowski, Pulse combustion dryer development for drying wood waste, in: EXFOR, Montreal, Canada, 1999: pp. 1–4.
- [58] A.G. Buchkowski, J.A. Kitchen, Drying wood waste with a pulse combustion dryer, in: 1st Biomass Conf. Am., Vermont, 1993: pp. 730–735.

- [59] T. Kudra, A.G. Buchkowski, J.A. Kitchen, Pulse-combustion drying of white pine, in: 4th IUFRO Int. Wood Dry. Conf., Rotorua, New Zealand, 1994: pp. 396–403.
- [60] T. Patterson, F. Ahrens, G. Stipp, High performance impingement paper drying using pulse combustion technology, in: TAPPI Spring Tech. Conf. Exhib., Chicago, 2003.
- [61] L. Wang, F. De Cui, H. Sunada, Improvement of the dissolution rate of nitrendipine using a new pulse combustion drying method, *Chemical and Pharmaceutical Bulletin*. 55 (2007) 1119–1125.
- [62] L. Xu, S.M. Li, H. Sunada, Preparation and evaluation of ibuprofen solid dispersion systems with Kollidon particles using a pulse combustion dryer system, *Chemical and Pharmaceutical Bulletin*. 55 (2007) 1545–1550.
- [63] Z. Wu, L. Wu, Z. Li, A.S. Mujumdar, Atomization and drying characteristics of sewage sludge inside a Helmholtz pulse combustor, *Drying Technology*. 30 (2012) 1105–1112.
- [64] D. San Martin, S. Ramos, J. Zufía, Valorisation of food waste to produce new raw materials for animal feed, *Food Chemistry*. 198 (2016) 68–74.
- [65] J. Chowdhury, Pulse combustion lowers drying costs, *Chemical Engineering (New York)*. 91 (1984) 44–45.
- [66] R.W. Ozer, Review of operating data from pilot plant and field pulse combustion drying system, in: *Proc. Powder Bulk Solids Conf.*, Chicago, USA, 1993: pp. 407–419.
- [67] C. Strumillo, I. Zbiciński, I. Smuczerowicz, C. Crowe, An analysis of a pulse combustion drying system, *Chemical Engineering and Processing: Process Intensification*. 38 (1999) 593–600.
- [68] A. Teiwes, M. Dosta, M. Jacob, S. Heinrich, Pulsed multiphase flows: Numerical investigation of particle dynamics in pulsating gas-solid flows at elevated temperatures, *Processes*. 8 (2020) 815.
- [69] D. Pramudita, E. Tsotsas, A model of pulse combustion drying and breakup of colloidal suspension droplets, *Powder Technology*. 355 (2019) 755–769.
- [70] D. Pramudita, A. Teiwes, M. Jacob, E. Tsotsas, Crust breakage in production of fine particles using pulse combustion drying: Experimental and numerical investigations, *Powder Technology*. 393 (2021) 77–98.
- [71] D. Pramudita, S. Humjaa, E. Tsotsas, Droplet drying and whey protein denaturation in pulsed gas flow: A modeling study, *Journal of Food Engineering*. 321 (2022) 110959.
- [72] A. Bück, M. Peglow, M. Naumann, E. Tsotsas, Population balance model for drying of droplets containing aggregating nanoparticles, *AIChE Journal*. 58 (2012) 3318–3328.
- [73] S. Nešić, J. Vodnik, Kinetics of droplet evaporation, *Chemical Engineering Science*. 46 (1991) 527–537.
- [74] T.T.H. Tran, M. Jaskulski, J.G. Avila-Acevedo, E. Tsotsas, Model parameters for single-

- droplet drying of skim milk and its constituents at moderate and elevated temperatures, *Drying Technology*. 35 (2017) 444–464.
- [75] D.H. Charlesworth, W.R. Marshall, Evaporation from drops containing dissolved solids, *AIChE Journal*. 6 (1960) 9–23.
- [76] Y. Sano, R.B. Keey, The drying of a spherical particle containing colloidal material into a hollow sphere, *Chemical Engineering Science*. 37 (1982) 881–889.
- [77] H.W. Cheong, G. V. Jeffreys, C.J. Mumford, A receding interface model for the drying of slurry droplets, *AIChE Journal*. 32 (1986) 1334–1346.
- [78] N. Abuaf, F.W. Staub, Drying of liquid-solid slurry droplets, in: A.S. Mujumdar (Ed.), *Dry. '86*, Hemisphere, Washington DC, 1986: pp. 277–284.
- [79] I. Borde, A. Zlotnitsky, *Drying and combustion of solid-liquid slurry droplets*, 1991.
- [80] D. Levi-Hevroni, A. Levy, I. Borde, Mathematical modeling of drying of liquid/solid slurries in steady state one-dimensional flow, *Drying Technology*. 13 (1995) 1187–1201.
- [81] T. Elperin, B. Krasovitov, Evaporation of liquid droplets containing small solid particles, *International Journal of Heat and Mass Transfer*. 38 (1995) 2259–2267.
- [82] M. Farid, A new approach to modelling of single droplet drying, *Chemical Engineering Science*. 58 (2003) 2985–2993.
- [83] P.S. Kuts, C. Strumiłło, I. Zbiciński, Evaporation kinetics of single droplets containing dissolved biomass, *Drying Technology*. 14 (1996) 2041–2060.
- [84] T. Furuta, H. Hayash, T. Ohash, Some criteria of spray dryer design for food liquid, *Drying Technology*. 12 (1994) 151–177.
- [85] M. Ali, T. Mahmud, P.J. Heggs, M. Ghadiri, D. Djurdjevic, H. Ahmadian, L.M. de Juan, C. Amador, A.E. Bayly, A one-dimensional plug-flow model of a counter-current spray drying tower, *Chemical Engineering Research and Design*. 92 (2014) 826–841.
- [86] C.S. Handscomb, M. Kraft, A.E. Bayly, A new model for the drying of droplets containing suspended solids, *Chemical Engineering Science*. 64 (2009) 628–637.
- [87] C.S. Handscomb, M. Kraft, A.E. Bayly, A new model for the drying of droplets containing suspended solids after shell formation, *Chemical Engineering Science*. 64 (2009) 228–246.
- [88] C.S. Handscomb, M. Kraft, Simulating the structural evolution of droplets following shell formation, *Chemical Engineering Science*. 65 (2010) 713–725.
- [89] M. Mezhericher, A. Levy, I. Borde, Modelling the morphological evolution of nanosuspension droplet in constant-rate drying stage, *Chemical Engineering Science*. 66 (2011) 884–896.
- [90] M.H. Sadafi, I. Jahn, A.B. Stilgoe, K. Hooman, Theoretical and experimental studies on a solid containing water droplet, *International Journal of Heat and Mass Transfer*. 78

- (2014) 25–33.
- [91] U. Maurice, M. Mezhericher, A. Levy, I. Borde, Drying of droplets containing insoluble nanoscale particles: Second drying stage, *Drying Technology*. 33 (2015) 1837–1848.
- [92] M. Mezhericher, M. Naumann, M. Peglow, A. Levy, E. Tsotsas, I. Borde, Continuous species transport and population balance models for first drying stage of nanosuspension droplets, *Chemical Engineering Journal*. 210 (2012) 120–135.
- [93] U. Maurice, M. Mezhericher, A. Levy, I. Borde, Drying of droplet containing insoluble nanoscale particles: Numerical simulations and parametric study, *Drying Technology*. 31 (2013) 1790–1807.
- [94] S. Wang, T.A.G. Langrish, A distributed parameter model for particles in the spray drying process, *Advanced Powder Technology*. 20 (2009) 220–226.
- [95] D. Parienta, L. Morawska, G.R. Johnson, Z.D. Ristovski, M. Hargreaves, K. Mengersen, S. Corbett, C.Y.H. Chao, Y. Li, D. Katoshevski, Theoretical analysis of the motion and evaporation of exhaled respiratory droplets of mixed composition, *Journal of Aerosol Science*. 42 (2011) 1–10.
- [96] J.M. Gac, L. Gradoń, A distributed parameter model for the spray drying of multicomponent droplets with a crust formation, *Advanced Powder Technology*. 24 (2013) 324–330.
- [97] H. Abdullahi, C.L. Burcham, T. Vetter, A mechanistic model to predict droplet drying history and particle shell formation in multicomponent systems, *Chemical Engineering Science*. 224 (2020) 115713.
- [98] D.A. van Meel, Adiabatic convection batch drying with recirculation of air, *Chemical Engineering Science*. 9 (1958) 36–44.
- [99] X.D. Chen, The basics of a reaction engineering approach to modeling air-drying of small droplets or thin-layer materials, *Drying Technology*. 26 (2008) 627–639.
- [100] X.D. Chen, G.Z. Xie, Fingerprints of the drying behaviour of particulate or thin layer food materials established using a reaction engineering model, *Food and Bioproducts Processing: Transactions of the Institution of Chemical Engineers, Part C*. 75 (1997) 213–222.
- [101] T.T.H. Tran, M. Jaskulski, E. Tsotsas, Reduction of a model for single droplet drying and application to CFD of skim milk spray drying, *Drying Technology*. 35 (2017) 1571–1583.
- [102] M.W. Woo, W.R.W. Daud, A.S. Mujumdar, Z.H. Wu, M.Z.M. Talib, S.M. Tasirin, CFD evaluation of droplet drying models in a spray dryer fitted with a rotary atomizer, *Drying Technology*. 26 (2008) 1180–1198.
- [103] I. Schmitz-Schug, U. Kulozik, P. Foerst, Modeling spray drying of dairy products: Impact of drying kinetics, reaction kinetics and spray drying conditions on lysine loss, *Chemical Engineering Science*. 141 (2016) 315–329.

- [104] I. Schmitz-Schug, U. Kulozik, P. Foerst, Reaction kinetics of lysine loss in a model dairy formulation as related to the physical state, *Food and Bioprocess Technology*. 7 (2014) 877–886.
- [105] M. Jaskulski, J.C. Atuonwu, T.T.H. Tran, A.G.F. Stapley, E. Tsotsas, Predictive CFD modeling of whey protein denaturation in skim milk spray drying powder production, *Advanced Powder Technology*. 28 (2017) 3140–3147.
- [106] J.C. Atuonwu, J. Ray, A.G.F. Stapley, A kinetic model for whey protein denaturation at different moisture contents and temperatures, *International Dairy Journal*. 75 (2017) 41–50.
- [107] H. Habtegebriel, D. Edward, O. Motsamai, M. Wawire, E. Seifu, S. Daniel, The potential of computational fluid dynamics simulation to investigate the relation between quality parameters and outlet temperature during spray drying of camel milk, *Drying Technology*. (2021) 1–15.
- [108] A. Putranto, M. Foerster, M.W. Woo, C. Selomulya, X.D. Chen, A continuum-approach modeling of surface composition and ternary component distribution inside low fat milk emulsions during single droplet drying, *AIChE Journal*. 63 (2017) 2535–2545.
- [109] S.E. Papadakis, R.E. Bahu, K.A. McKenzie, I.C. Kemp, Correlations for the equilibrium moisture content of solids, *Drying Technology*. 11 (1993) 543–553.
- [110] C.S. Rao, S. Damodaran, Is surface pressure a measure of interfacial water activity? Evidence from protein adsorption behavior at interfaces, *Langmuir*. 16 (2000) 9468–9477.
- [111] I. V. Nesselova, V.D. Skirda, V.D. Fedotov, Generalized concentration dependence of globular protein self-diffusion coefficients in aqueous solutions, *Biopolymers*. 63 (2002) 132–140.
- [112] M. Rensizbulut, M.C. Yuen, Experimental study of droplet evaporation in a high-temperature air stream, *Journal of Heat Transfer*. 105 (1983) 384.
- [113] D. Megias-Alguacil, L.J. Gauckler, Erratum: Capillary and van der Waals forces between uncharged colloidal particles linked by a liquid bridge, *Colloid and Polymer Science*. 288 (2010) 1501–1502.
- [114] D. Megias-Alguacil, L.J. Gauckler, Capillary and van der Waals forces between uncharged colloidal particles linked by a liquid bridge, *Colloid and Polymer Science*. 288 (2010) 133–139.
- [115] H.C.H. Rumpf, Zur Theorie der Zugfestigkeit von Agglomeraten bei Kraftübertragung an Kontaktpunkten, *Chemie Ingenieur Technik*. 42 (1970) 538–540.
- [116] S.R.L. Werner, R.L. Edmonds, J.R. Jones, J.E. Bronlund, A.H.J. Paterson, Single droplet drying: Transition from the effective diffusion model to a modified receding interface model, *Powder Technology*. 179 (2008) 184–189.

- [117] O. Krischer, *Die wissenschaftlichen Grundlagen der Trocknungstechnik*, 1st ed., Springer, Berlin, 1956.
- [118] T.R. Marrero, E.A. Mason, Gaseous diffusion coefficients, *Journal of Physical and Chemical Reference Data*. 1 (1972) 3–118.
- [119] D. Nicholson, J.H. Petropoulos, Calculation of the “surface flow” of a dilute gas in model pores from first principles, Part 3: Molecular gas flow in single pores and simple model porous media, *Journal of Colloid And Interface Science*. 106 (1985) 538–546.
- [120] D. Kim, H. Choi, H. Choi, Characteristics of laminar flow past a sphere in uniform shear, *Physics of Fluids*. 17 (2005) 103602.
- [121] S. Lyonard, J.R. Bartlett, E. Sizgek, K.S. Finnie, T. Zemb, J.L. Woolfrey, Role of interparticle potential in controlling the morphology of spray-dried powders from aqueous nanoparticle sols, *Langmuir*. 18 (2002) 10386–10397.
- [122] A.J. Webster, M.E. Cates, Stabilization of emulsions by trapped species, *Langmuir*. 14 (1998) 2068–2079.
- [123] B. Derjaguin, L. Landau, Theory of the stability of strongly charged lyophobic sols and of the adhesion of strongly charged particles in solutions of electrolytes, *Progress in Surface Science*. 43 (1993) 30–59.
- [124] E.J.W. Verwey, J.T.G. Overbeek, Theory of the stability of lyophobic colloids, *Journal of Colloid Science*. 10 (1955) 224–225.
- [125] J.N. Israelachvili, *Intermolecular and Surface Forces*, 3rd Ed., Academic Press, San Diego, USA, 2011.
- [126] B. Jiang, Y. Xie, D. Xia, X. Liu, A potential source for PM_{2.5}: Analysis of fine particle generation mechanism in Wet Flue Gas Desulfurization System by modeling drying and breakage of slurry droplet, *Environmental Pollution*. 246 (2019) 249–256.
- [127] R. Clift, J.R. Grace, M.E. Weber, *Bubbles, Drops, and Particles*, Academic Press, New York, USA, 1978.
- [128] B.E. Gelfand, Droplet breakup phenomena in flows with velocity lag, *Progress in Energy and Combustion Science*. 22 (1996) 201–265.
- [129] A.A. Ranger, J.A. Nicnolls, Aerodynamic shattering of liquid drops, *AIAA Journal*. 7 (1969) 285–290.
- [130] D.R. Guildenbecher, C. López-Rivera, P.E. Sojka, Secondary atomization, *Experiments in Fluids*. 46 (2009) 371–402.
- [131] S. Khosla, C. Smith, R.P. Throckmorton, Detailed understanding of drop atomization by gas crossflow using the volume of fluid method, in: *ILASS Am. 19th Annu. Conf. Liq. At. Spray Syst.*, Toronto, 2006: p. 22.
- [132] O. Gobyzov, Y. Lozhkin, M. Ryabov, D. Markovich, Experimental study of submillimeter

- droplets dynamics and breakup in continuous supersonic flow terminated by shock wave, in: EPJ Web Conf., 2016: p. 02031.
- [133] A. Gupta, H.B. Eral, T.A. Hatton, P.S. Doyle, Controlling and predicting droplet size of nanoemulsions: Scaling relations with experimental validation, *Soft Matter*. 12 (2016) 1452–1458.
- [134] P.J. O'Rourke, A.A. Amsden, The TAB method for numerical calculation of spray droplet breakup, in: SAE Tech. Pap. 872089, SAE Internationals, 1987.
- [135] E.A. Ibrahim, H.Q. Yang, A.J. Przekwas, Modeling of spray droplets deformation and breakup, *Journal of Propulsion and Power*. 9 (1993) 651–654.
- [136] Z. Liu, R.D. Reitz, An analysis of the distortion and breakup mechanisms of high speed liquid drops, *International Journal of Multiphase Flow*. 23 (1997) 631–650.
- [137] M. Marek, The double-mass model of drop deformation and secondary breakup, *Applied Mathematical Modelling*. 37 (2013) 7919–7939.
- [138] E. Movahednejad, F. Omimi, S.M. Hosseinalipour, Prediction of droplet size and velocity distribution in droplet formation region of liquid spray, *Entropy*. 12 (2010) 1484–1498.
- [139] M.W. Lee, J.J. Park, M.M. Farid, S.S. Yoon, Comparison and correction of the drop breakup models for stochastic dilute spray flow, *Applied Mathematical Modelling*. 36 (2012) 4512–4520.
- [140] C. Storm, F. Joos, Comparison of secondary breakup models for droplet-laden compressor flows, *International Journal of Multiphase Flow*. (2019).
- [141] D. Stefanitsis, G. Strotos, N. Nikolopoulos, E. Kakaras, M. Gavaises, Improved droplet breakup models for spray applications, *International Journal of Heat and Fluid Flow*. 76 (2019) 274–286.
- [142] J.-K. Yeom, K. Ashida, J. Senda, H. Fujimoto, T. Dan, Analysis of diesel spray structure by using a hybrid model of TAB breakup model and vortex method, in: SAE Tech. Pap. Ser., 2010.
- [143] F.X. Tanner, Liquid jet atomization and droplet breakup modeling of non-evaporating diesel fuel sprays, SAE Technical Papers. 970050 (1997).
- [144] J.H. Park, Y. Yoon, S.S. Hwang, Improved TAB model for prediction of spray droplet deformation and breakup, *Atomization and Sprays*. 12 (2002) 387–401.
- [145] I.M. Krieger, T.J. Dougherty, A mechanism for non-Newtonian flow in suspensions of rigid spheres, *Transactions of the Society of Rheology*. 3 (1959) 137–152.
- [146] W.G. McMillan, J.E. Mayer, The statistical thermodynamics of multicomponent systems, *The Journal of Chemical Physics*. 13 (1945) 276–305.
- [147] K. Janáček, K. Sigler, Osmotic pressure: Thermodynamic basis and units of measurement, *Folia Microbiologica*. 41 (1996) 2–9.

- [148] L.F. Cameretti, Modeling of thermodynamic properties in biological solutions, PhD thesis, TU Dortmund, Germany, 2009.
- [149] C. Huang, C. Li, P.Y.K. Choi, K. Nandakumar, L.W. Kostiuk, Effect of cut-off distance used in molecular dynamics simulations on fluid properties, *Molecular Simulation*. 36 (2010) 856–864.
- [150] A.P. Philipse, B.W.M. Kuipers, Second virial coefficients of dipolar hard spheres, *Journal of Physics Condensed Matter*. 22 (2010) 325104.
- [151] P. Bryk, Effective interactions in colloid-semipermeable membrane systems, *Langmuir*. 22 (2006) 3214–3220.
- [152] American Petroleum Institute, API RP 520: Sizing, Selection, and Installation of Pressure-Relieving Devices in Refineries , 8th Edition, (2008).
- [153] X. Li, L.P. Chin, R.S. Tankin, T. Jackson, J. Stutrud, G. Switzer, Comparison between experiments and predictions based on maximum entropy for sprays from a pressure atomizer, *Combustion and Flame*. 86 (1991) 73–89.
- [154] C.H. Mathewson, Zinc: The science and technology of the metal, its alloys and compounds, Reinhold Pub. Corp, New York, USA, 1959.
- [155] P. Veluswamy, S. Sathiyamoorthy, K.H. Chowdary, O. Muthusamy, K. Krishnamoorthy, T. Takeuchi, H. Ikeda, Morphology dependent thermal conductivity of ZnO nanostructures prepared via a green approach, *Journal of Alloys and Compounds*. 695 (2017) 888–894.
- [156] Y. Yang, W. Guo, X. Wang, Z. Wang, J. Qi, Y. Zhang, Size dependence of dielectric constant in a single pencil-like ZnO nanowire, *Nano Letters*. 12 (2012) 1919–1922.
- [157] I. Bodurov, I. Vlaeva, A. Viraneva, T. Yovcheva, S. Sainov, Modified design of a laser refractometer, *Nanoscience & Nanotechnology*. 16 (2016) 31–33.
- [158] D.E. Kühner, H.W. Blanch, J.M. Prausnitz, Salt-induced protein precipitation: Phase equilibria from an equation of state, *Fluid Phase Equilibria*. 116 (1996) 140–147.
- [159] F. Iskandar, L. Gradon, K. Okuyama, Control of the morphology of nanostructured particles prepared by the spray drying of a nanoparticle sol, *Journal of Colloid and Interface Science*. 265 (2003) 296–303.
- [160] M. Mezhericher, A. Levy, I. Borde, Multi-scale multiphase modeling of transport phenomena in spray-drying processes, *Drying Technology*. 33 (2015) 2–23.
- [161] PROSPECT Global Nanomaterials Safety, Protocol for Nanoparticle Dispersion, 2010.
- [162] J.S. Taurozzi, V.A. Hackley, M.R. Wiesner, Preparation of nanoparticle dispersions from powdered material using ultrasonic disruption, Version 1.1, 2012.
- [163] E. Petrakis, V. Karmali, G. Bartzas, K. Komnitsas, Grinding kinetics of slag and effect of final particle size on the compressive strength of alkali activated materials, *Minerals*. 9

- (2019) 714–735.
- [164] V.A. Kuzmin, I.A. Zagrai, A comprehensive study of combustion products generated from pulverized peat combustion in the furnace of BKZ-210-140F steam boiler, in: *J. Phys. Conf. Ser.*, 2017: p. 012226.
- [165] T.T.H. Tran, J.G. Avila-Acevedo, E. Tsotsas, Enhanced methods for experimental investigation of single droplet drying kinetics and application to lactose/water, *Drying Technology*. 34 (2016) 1185–1195.
- [166] M. Mazumdar, G.A. Irdi, Determination of pyrite particle size distribution in coal by merging analyses of size distributions at different microscopic magnifications: Optimum allocation of number of observations to different size groups, *Fuel*. 68 (1989) 890–894.
- [167] B. Adhikari, T. Howes, B.R. Bhandari, V. Troung, Effect of addition of maltodextrin on drying kinetics and stickiness of sugar and acid-rich foods during convective drying: Experiments and modelling, *Journal of Food Engineering*. 62 (2004) 53–68.
- [168] B. Adhikari, T. Howes, B.R. Bhandari, V. Troung, Surface stickiness of drops of carbohydrate and organic acid solutions during convective drying: Experiments and modeling, *Drying Technology*. 21 (2003) 839–873.
- [169] N. Castro, V. Durrieu, C. Raynaud, A. Rouilly, Influence of DE-value on the physicochemical properties of maltodextrin for melt extrusion processes, *Carbohydrate Polymers*. 144 (2016) 464–473.
- [170] M. Kobayashi, F. Juillerat, P. Galletto, P. Bowen, M. Borkovec, Aggregation and charging of colloidal silica particles: Effect of particle size, *Langmuir*. 21 (2005) 5761–5769.
- [171] K. Ueno, M. Kobayashi, Y. Adachi, T. Kojima, Electric charging and colloid stability of fabricated needle-like TiO₂ nanoparticles, *Communications in Physics*. 24 (2014) 13–21.
- [172] M. Borkovec, S.H. Behrens, Electrostatic double layer forces in the case of extreme charge regulation, *Journal of Physical Chemistry B*. 112 (2008) 10795–10799.
- [173] J. Lyklema, Overcharging, charge reversal: Chemistry or physics?, *Colloids and Surfaces A: Physicochemical and Engineering Aspects*. 291 (2006) 3–12.
- [174] J. Lyklema, Surface charges and electrokinetic charges: Distinctions and juxtapositionings, *Colloids and Surfaces A: Physicochemical and Engineering Aspects*. 376 (2011) 2–8.
- [175] W. Piasecki, W. Rudziński, R. Charmas, 1-pK and 2-pK protonation models in the theoretical description of simple ion adsorption at the oxide/electrolyte interface: A comparative study of the behavior of the surface charge, the individual isotherms of ions, and the accompanying electrokinetic e, *Journal of Physical Chemistry B*. 105 (2001) 9755–9771.
- [176] M. Borkovec, Origin of 1-pK and 2-pK models for ionizable water-solid interfaces,

- Langmuir. 13 (1997) 2608–2613.
- [177] N. Kallay, *Interfacial Dynamics*, CRC Press, Boca Raton, 2000.
- [178] M. Borkovec, B. Jönsson, G.J.M. Koper, Ionization processes and proton binding in polyprotic systems: Small molecules, proteins, interfaces, and polyelectrolytes, in: E. Matijević (Ed.), *Surf. Colloid Sci.*, Springer, Boston, MA, 2001: pp. 99–339.
- [179] T. Hiemstra, J.C.M. De Wit, W.H. van Riemsdijk, Multisite proton adsorption modeling at the solid/solution interface of (hydr)oxides: A new approach, Part 2: Application to various important (hydr)oxides, *Journal of Colloid And Interface Science*. 133 (1989) 105–117.
- [180] T.W. Healy, D.E. Yates, L.R. White, D. Chan, Nernstian and non-Nernstian potential differences at aqueous interfaces, *Journal of Electroanalytical Chemistry*. 80 (1977) 57–66.
- [181] T. Preočanin, N. Kallay, Point of zero charge and surface charge density of TiO₂ in aqueous electrolyte solution as obtained by potentiometric mass titration, *Croatica Chemica Acta*. 79 (2006) 95–106.
- [182] M. Kosmulski, The pH-dependent surface charging and the points of zero charge, *Journal of Colloid and Interface Science*. 253 (2002) 77–87.
- [183] M. Kosmulski, The pH-dependent surface charging and points of zero charge. V. Update, *Journal of Colloid and Interface Science*. 353 (2011) 1–15.
- [184] R.O. James, G.A. Parks, Characterization of aqueous colloids by their electrical double-layer and intrinsic surface chemical properties, in: E. Matijević (Ed.), *Surf. Colloid Sci.*, Springer, Boston, MA, 1982: pp. 119–216.
- [185] S. Al-Hilli, R. Al-Mofrarji, P. Klason, N. Gutman, A. Sa'ar, A. Öst, P. Strålfors, M. Willander, Zinc oxide nanorods as an intracellular pH sensor, in: *ENS*, Paris, 2007: pp. 37–43.
- [186] S.H. Behrens, M. Borkovec, Electrostatic interaction of colloidal surfaces with variable charge, *Journal of Physical Chemistry B*. 103 (1999) 2918–2928.
- [187] F. Smalenburg, N. Boon, M. Kater, M. Dijkstra, R. van Roij, Phase diagrams of colloidal spheres with a constant zeta-potential, *Journal of Chemical Physics*. 134 (2011) 074505.
- [188] M. Schmitt, Synthesis and testing of ZnO nanoparticles for photo-initiation: Experimental observation of two different non-migration initiators for bulk polymerization, *Nanoscale*. 7 (2015) 9532–9544.
- [189] M. Kosmulski, The pH dependent surface charging and points of zero charge. VII. Update, *Advances in Colloid and Interface Science*. 251 (2018) 115–138.
- [190] G.D.M. Madeira, H.J. Hugo, M.C. Faleiros, M. Mulato, Model improvement for super-Nernstian pH sensors: The effect of surface hydration, *Journal of Materials Science*. 56 (2021) 1–10.

- [191] K. Higashitani, K. Iimura, H. Sanda, Simulation of deformation and breakup of large aggregates in flows of viscous fluids, *Chemical Engineering Science*. 56 (2001) 2927–2938.
- [192] M. Renaud, E. Mauret, R.P. Chhabra, Power-law fluid flow over a sphere: Average shear rate and drag coefficient, *Canadian Journal of Chemical Engineering*. 82 (2004) 1066–1070.
- [193] D.L. Feke, Shear-induced dispersion of particle agglomerates, in: A.D. Salman, M.J. Hounslow, J.P.K. Seville (Eds.), *Handb. Powder Technol. Vol. 11 Granulation*, Elsevier Inc., 2007: pp. 815–852.
- [194] M. Mezhericher, A. Levy, I. Borde, Heat and mass transfer and breakage of particles in drying processes, *Drying Technology*. 27 (2009) 870–877.
- [195] S. Timoshenko, J.N. Goodier, *Theory of Elasticity*, 2nd ed., McGraw-Hill, New York, USA, 1951.
- [196] L.J. Gibson, M.F. Ashby, *Cellular Solids: Structure and Properties*, 2nd ed., Cambridge University Press, 1997.
- [197] A. Beskok, G.E. Karniadakis, Report: A model for flows in channels, pipes, and ducts at micro and nano scales, *Microscale Thermophysical Engineering*. 3 (1999) 43–77.
- [198] F. Civan, Effective correlation of apparent gas permeability in tight porous media, *Transport in Porous Media*. 82 (2010) 375–384.
- [199] S.A. Tison, C.R. Tilford, Low density water vapor measurements: The NIST primary standard and instrument response, in: B.A. Moore, J.A. Carpenter Jr. (Eds.), *NIST Intern. Rep. 5241 - Proc. RL/NIST Work. Moisture Meas. Control Microelectron.*, National Institute of Standards and Technology, Gaithersburg, 1993: pp. 19–29.
- [200] F.E. Kruis, B. Scarlett, K.A. Kusters, S.E. Pratsinis, A simple model for the evolution of the characteristics of aggregate particles undergoing coagulation and sintering, *Aerosol Science and Technology*. 19 (1993) 514–526.
- [201] T. Seto, M. Shimada, K. Okuyama, Evaluation of sintering of nanometer-sized titania using aerosol method, *Aerosol Science and Technology*. 23 (1995) 183.
- [202] S.H. Ehrman, S.K. Friedlander, M.R. Zachariah, Characteristics of SiO₂/TiO₂ nanocomposite particles formed in a premixed flat flame, *Journal of Aerosol Science*. 29 (1998) 687–706.
- [203] A. Mansour, N. Chigier, Air-blast atomization of non-Newtonian liquids, *Journal of Non-Newtonian Fluid Mechanics*. 58 (1995) 161–194.
- [204] M. Alderliesten, Mean particle diameters, Part 7: The Rosin-Rammler size distribution: Physical and mathematical properties and relationships to moment-ratio defined mean particle diameters, *Particle and Particle Systems Characterization*. 30 (2013) 244–257.
- [205] S.P. Hozo, B. Djulbegovic, I. Hozo, Estimating the mean and variance from the median,

- range, and the size of a sample, *BMC Medical Research Methodology*. 5 (2005) 13–22.
- [206] AZoM, Silica - Silicon Dioxide (SiO₂), 2001.
- [207] AZoM, Titanium Dioxide - Titania (TiO₂), 2002.
- [208] K. Takamura, A. James, Paving with asphalt emulsions, in: S.-C. Huang, H. Di Benedetto (Eds.), *Adv. Asph. Mater. Road Pavement Constr.*, Woodhead Publishing, Cambridge, 2015: pp. 393–426.
- [209] X. Hou, Y. Zhang, H. Ding, P.K. Chu, Environmentally friendly wollastonite@TiO₂ composite particles prepared by a mechano-chemical method, *Particuology*. 40 (2018) 105–112.
- [210] W. Naffouti, T. Ben Nasr, H. Meradji, N. Kamoun-Turki, First-principles investigation of structural, thermal and transport properties of anatase TiO₂, *Journal of Electronic Materials*. 45 (2016) 5096–5103.
- [211] T. Deschamps, J. Margueritat, C. Martinet, A. Mermet, B. Champagnon, Elastic moduli of permanently densified silica glasses, *Scientific Reports*. 4 (2014) 7193.
- [212] X. Liu, J. Fu, Electronic and elastic properties of the tetragonal anatase TiO₂ structure from first principle calculation, *Optik*. 206 (2020) 164342.
- [213] K. Yang, L. Yang, C.Z. Ai, Z. Wang, S.W. Lin, Elastic properties of anatase titanium dioxide nanotubes: A molecular dynamics study, *Chinese Physics B*. 28 (2019) 103102.
- [214] G.W. Scherer, Bending of gel beams: Method for characterizing elastic properties and permeability, *Journal of Non-Crystalline Solids*. 142 (1992) 18–35.
- [215] X. Yang, J. Lee, D.E. Barker, X. Wang, Y. Zhang, Comparison of six particle size distribution models on the goodness-of-fit to particulate matter sampled from animal buildings, *Journal of the Air and Waste Management Association*. 62 (2012) 725–735.
- [216] J. Li, Assessing the accuracy of predictive models for numerical data: Not r nor r², why not? Then what?, *PLoS ONE*. 12 (2017) e0183250.
- [217] Y.J. Suh, J.W. Lee, H. Chang, H.D. Jang, K. Cho, Non-spherical particle formation induced by repulsive hydration forces during spray drying, *Journal of Nanoparticle Research*. 15 (2013) 1903.
- [218] D.J. Oldfield, Heat-induced whey protein reactions in milk, PhD thesis, Massey University, 1996.
- [219] R.P. Singh, D.R. Heldman, *Introduction to Food Engineering*, 5th ed., Elsevier, 2014.
- [220] Q. Fang, J. Sun, D. Cao, Y. Tuo, S. Jiang, G. Mu, Experimental and modelling study of the denaturation of milk protein by heat treatment, *Korean Journal for Food Science of Animal Resources*. 37 (2017) 44–51.
- [221] H.B. Wijayanti, N. Bansal, H.C. Deeth, Stability of whey proteins during thermal processing: A review, *Comprehensive Reviews in Food Science and Food Safety*. 13

- (2014) 1235–1251.
- [222] T.T.H. Tran, From single droplet to spray tower drying of dairy solutions, PhD thesis, Otto von Guericke University Magdeburg, 2017.
- [223] D.J. Oldfield, H. Singh, M.W. Taylor, Kinetics of heat-induced whey protein denaturation and aggregation in skim milks with adjusted whey protein concentration, *Journal of Dairy Research*. 72 (2005) 369–378.
- [224] M. Khaldi, G. Ronse, C. André, P. Blanpain-Avet, L. Bouvier, T. Six, S. Bornaz, T. Croguennec, R. Jeantet, G. Delaplace, Denaturation kinetics of whey protein isolate solutions and fouling mass distribution in a plate heat exchanger, *International Journal of Chemical Engineering*. (2015) 139638.
- [225] A.E. Mongo, H. Chaveron, A.A. Abena, Whey protein concentrates added in a beverage and their thermal denaturation studied by liquid phase chromatography, *Biotechnology*. 6 (2007) 64–67.
- [226] V.R. Harwalkar, Kinetic study of thermal denaturation of proteins in whey, *Milchwissenschaft*. 41 (1986) 206–209.
- [227] N. Fu, M.W. Woo, X.D. Chen, Colloidal transport phenomena of milk components during convective droplet drying, *Colloids and Surfaces B: Biointerfaces*. 87 (2011) 255–266.
- [228] M.A. Haque, P. Aldred, J. Chen, C.J. Barrow, B. Adhikari, Comparative study of denaturation of whey protein isolate (WPI) in convective air drying and isothermal heat treatment processes, *Food Chemistry*. 141 (2013) 702–711.
- [229] B. Adhikari, T. Howes, B.R. Bhandari, Use of solute fixed coordinate system and method of lines for prediction of drying kinetics and surface stickiness of single droplet during convective drying, *Chemical Engineering and Processing: Process Intensification*. 46 (2007) 405–419.
- [230] J.N. de Wit, G. Klarenbeek, Effects of various heat treatments on structure and solubility of whey proteins, *Journal of Dairy Science*. 67 (1984) 2701–2710.
- [231] J. Sloth, P. Bach, A.D. Jensen, S. Kiil, Evaluation method for the drying performance of enzyme containing formulations, *Biochemical Engineering Journal*. 40 (2008) 121–129.
- [232] T.K. Kockel, S. Allen, C. Hennigs, T.A.G. Langrish, An experimental study of the equilibrium for skim milk powder at elevated temperatures, *Journal of Food Engineering*. 51 (2002) 291–297.
- [233] L.B. de Carvalho-Silva, F.Z. Vissotto, J. Amaya-Farfan, Physico-chemical properties of milk whey protein agglomerates for use in oral nutritional therapy, *Food and Nutrition Sciences*. 4 (2013) 69–78.
- [234] L. Zhao, H. Wang, D. Kong, R. Gao, J. Yang, Research on thermal characteristics of whey powder, milk replacer and lactose, in: *Am. Soc. Agric. Biol. Eng. Annu. Int. Meet. 2013*, ASABE 2013, Kansas City, Missouri, 2013: p. 131622139.

- [235] J.C. Bassan, A.J. Goulart, A.L.M. Nasser, T.M.S. Bezerra, S.S. Garrido, C.B. Rustiguel, L.H.S. Guimarães, R. Monti, Buffalo cheese whey proteins, identification of a 24 kDa protein and characterization of their hydrolysates: In vitro gastrointestinal digestion, *PLoS ONE*. 10 (2015) e0139550.
- [236] J. Chen, K. Pitchai, S. Birla, R. Gonzalez, D. Jones, J. Subbiah, Temperature-dependent dielectric and thermal properties of whey protein gel and mashed potato, *Transactions of the ASABE*. 56 (2013) 1457–1467.
- [237] G. Foret, G. Bergametti, F. Dulac, L. Menut, An optimized particle size bin scheme for modeling mineral dust aerosol, *Journal of Geophysical Research Atmospheres*. 111 (2006) D17310.
- [238] B. Frackowiak, G. Lavergne, C. Tropea, A. Strzelecki, Numerical analysis of the interactions between evaporating droplets in a monodisperse stream, *International Journal of Heat and Mass Transfer*. 53 (2010) 1392–1401.
- [239] H. Li, M. Kuschel, M. Sommerfeld, Experimental investigation and modeling of coalescence and agglomeration for spray drying of solutions, in: U. Fritsching (Ed.), *Process. Funct. Part. Prod. Spray Process.*, Elsevier Inc., Amsterdam, 2016: pp. 205–233.
- [240] TheEngineeringToolBox, Densities and molecular weights of some common gases: Acetylene, air, methane, nitrogen, oxygen and others, (2006).
- [241] Y. Cengel, A. Ghajar, *Heat and Mass Transfer: Fundamentals and Applications*, 5th ed., McGraw-Hill Education, New York, USA, 2015.
- [242] M. Chase, NIST-JANAF Thermochemical Tables, 4th Edition, *Journal of Physical and Chemical Reference Data*, Monograph 9. (1998).
- [243] S.H. Chen, S.C. Saxena, Thermal conductivity of argon in the temperature range 350 to 2500 K, *Molecular Physics*. 29 (1975) 455–466.
- [244] TheEngineeringToolBox, Absolute viscosities of gases, (2014).

Appendices

Appendix A: Material properties

Table A.1. Empirical equations for drying gas properties.

Properties		Equations *	Ref.
Mass density of gas (kg/m ³)	ρ_g	Ar : $7.43985e-12 T_g^4 - 1.53930e-8 T_g^3 + 1.25938e-5 T_g^2 - 5.60971e-3 T_g + 1.74008$	[240]
		N ₂ : $-0.26670 \log(T_g) + 2.12166$	[241]
		O ₂ : $-0.30467 \log(T_g) + 2.42366$	
		CO ₂ : $-0.41899 \log(T_g) + 3.33316$	
		H ₂ O : $-0.17152 \log(T_g) + 1.36447$	
		Air : $7.92982e-18 T_g^6 - 2.78938e-14 T_g^5 + 3.97826e-11 T_g^4 - 3.02685e-8 T_g^3 + 1.40358e-5 T_g^2 - 4.59903e-3 T_g + 1.29071$	[240]
Specific heat capacity of gas (J/(kg.K))	$c_{p,g}$	Ar : 520	[242]
		N ₂ : $3.27304e-10 T_g^4 - 1.05788e-06 T_g^3 + 1.05e-03 T_g^2 - 0.15325 T_g + 1046.76$	[241]
		O ₂ : $1.69489e-10 T_g^4 - 4.46985e-07 T_g^3 + 2.2796e-04 T_g^2 + 0.26456 T_g + 905.811$	
		CO ₂ : $-1.84868e-10 T_g^4 + 7.30578e-07 T_g^3 - 1.18163e-03 T_g^2 + 1.11379 T_g + 814.173$	
		H ₂ O : $3.74801e-10 T_g^4 - 1.28946e-06 T_g^3 + 1.39135e-03 T_g^2 + 0.13158 T_g + 1862.59$	
		Air : $-1.17974e-15 T_g^6 + 3.4101e-12 T_g^5 - 3.256075e-9 T_g^4 + 7.33765e-7 T_g^3 + 4.98e-4 T_g^2 - 2.8951e-2 T_g + 1006.845$	
Thermal conductivity of gas (W/(m.K))	λ_g	Ar : $(0.1599e-8 T_g^3 - 0.1111e-4 T_g^2 + 0.04729 T_g + 5.465) / 1000$	[243]
		N ₂ : $2.22605e-11 T_g^3 - 4.1285e-08 T_g^2 + 7.45742e-05 T_g + 2.38308e-02$	[241]
		O ₂ : $3.45856e-12 T_g^3 - 1.7629e-08 T_g^2 + 8.16264e-05 T_g + 2.45565e-02$	
		CO ₂ : $-4.8367e-12 T_g^3 - 5.51866e-09 T_g^2 + 8.0709e-05 T_g + 1.45575e-2$	
		H ₂ O : $-1.64816e-11 T_g^3 + 6.35663e-08 T_g^2 + 7.28022e-05 T_g + 1.6397e-2$	
		Air : $-2.261297e-8 T_g^2 + 7.527445e-5 T_g + 0.02364315$	
Dynamic viscosity of gas (x 10 ⁻⁵ Pa.s)	μ_g	Ar : $-2.26085e-06 T_g^2 + 6.21082e-03 T_g + 2.11294$	[244]
		N ₂ : $6.76881e-10 T_g^3 - 2.35499e-06 T_g^2 + 4.61454e-03 T_g + 1.65497$	[241]
		O ₂ : $4.99997e-10 T_g^3 - 1.89182e-06 T_g^2 + 5.16751e-03 T_g + 1.95177$	
		CO ₂ : $3.78745e-10 T_g^3 - 1.68524e-06 T_g^2 + 4.82990e-03 T_g + 1.37465$	
		H ₂ O : $-3.22293e-10 T_g^3 + 4.12678e-07 T_g^2 + 3.79167e-03 T_g + 0.882239$	
		Air : $-7.17732e-18 T_g^4 + 2.179924e-14 T_g^3 - 3.151104e-11 T_g^2 + 4.782845e-8 T_g + 1.7311e-5$	

* T_g in °C.

Appendix B: Calculation example for pH-dependent surface charge

This is an example of pH-dependent surface charge calculation for a colloidal silica droplet ($D_{pp} = 12$ nm) with $D_d = 40$ μm , $x_s = 0.1$, and $pH = 9$ at $T_d = 20$ $^\circ\text{C}$.

The initial droplet volume is

$$V_d = \frac{\pi D_d^3}{6} = 3.351 \times 10^{-14} \text{ m}^3. \quad (\text{B.1})$$

With $\rho_w = 998$ kg/m^3 and $\rho_s = 2363.64$ kg/m^3 , the solid and water volumes are thus

$$V_s = \frac{V_d x_s \rho_w}{\rho_s + x_s \rho_w - x_s \rho_s} = 1.5017 \times 10^{-15} \text{ m}^3, \quad (\text{B.2})$$

$$V_w = V_d - V_s = 3.2009 \times 10^{-14} \text{ m}^3. \quad (\text{B.3})$$

The number of primary particles can be calculated as

$$N_{pp} = \frac{6 V_s}{\pi D_{pp}^3} = 1.6579 \times 10^9. \quad (\text{B.4})$$

The closest distance between the surface of two closest particles is calculated according to the method explained in Section 5.1. Volume and diameter of imaginary spheres are respectively

$$V_{is} = \frac{V_d \phi_{\max}}{N_{pp}} = 1.2114 \times 10^{-23} \text{ m}^3, \quad (\text{B.5})$$

$$D_{is} = \sqrt[3]{\left(\frac{6}{\pi} V_{is}\right)} = 2.8494 \times 10^{-8} \text{ m} \approx 28.5 \text{ nm}. \quad (\text{B.6})$$

Thus,

$$\hat{d}_{\min} = D_{is} - D_{pp} = 1.6495 \times 10^{-8} \text{ m} \approx 16.5 \text{ nm}. \quad (\text{B.7})$$

The surface potential is

$$\psi_0 = \alpha_N k_B T_d \frac{\ln 10}{e_0} (pH_{\text{eln}} - pH) = -0.3212 \text{ V}. \quad (\text{B.8})$$

At half dissociation condition ($\theta_d = 0.5$), $pH = pK$. The bulk H^+ ion concentration and the surface potential at this points are, respectively,

$$[H^+]_{pK} = 10^{-pK} = 3.6 \times 10^{-8} \text{ M}, \quad (\text{B.9})$$

$$\psi_{0,pK} = \alpha_N k_B T_d \frac{\ln 10}{e_0} (pH_{\text{eln}} - pK) = -0.2524 \text{ V}. \quad (\text{B.10})$$

The degree of deprotonation in the droplet is thus

$$\theta_d = \frac{[H^+]_{pK} \exp\left(-\frac{e_0 \psi_{0,pK}}{k_B T}\right)}{[H^+]_{pK} \exp\left(-\frac{e_0 \psi_{0,pK}}{k_B T}\right) + [H^+] \exp\left(-\frac{e_0 \psi_0}{k_B T}\right)} = 0.7512. \quad (\text{B.11})$$

Surface charge density at large separation distance (i.e., dilute condition) is

$$q_{A,\infty} = e_0 N_A (-[SiO^-]) = -e_0 N_A N_s \theta_d = -0.3611 \text{ C/m}^2. \quad (\text{B.12})$$

Debye screening length is calculated as

$$\kappa^{-1} = \sqrt{\frac{\varepsilon_{r,l} \varepsilon_0 k_B T_d}{\sum(N_i q_i^2/V_w)}} = \sqrt{\frac{\varepsilon_{r,l} \varepsilon_0 k_B T_d}{e_0^2 N_A 1000 ([H_{H_2O}^+] + [OH_{H_2O}^-] + [H_{pp}^+] + [Na^+] + [OH^-])}}. \quad (\text{B.13})$$

Here, 1000 is a conversion factor to SI, since the concentrations are in M. It follows:

$$\kappa^{-1} = \sqrt{\frac{\varepsilon_{r,l} \varepsilon_0 k_B T_d}{\sum(N_i q_i^2/V_w)}} = 1.4077 \text{ nm}. \quad (\text{B.14})$$

The first two ion species come from water ionization at neutral $pH (= 7)$, thus

$$[H_{H_2O}^+] + [OH_{H_2O}^-] = 2 \times 10^{-7} \text{ M}. \quad (\text{B.15})$$

$[H_{pp}^+]$ denotes the counter ions of the charged surface, which is

$$[H_{pp}^+] = \frac{q_{A,\infty} \pi D_{pp}^2 N_{pp}}{e_0 V_w}. \quad (\text{B.16})$$

The last two species in Eq. B.13 are the ions of pH determining species, which is here assumed to be either HCl or NaOH (a 1:1 electrolyte) depending on the initial droplet pH . The calculated value of Debye screening length is 1.4077 nm.

The regulated surface charge density (with $p = 0$) is

$$q_A(\hat{d}_{\min}) = \frac{q_{A,\infty}}{p + (1-p) \coth(\kappa \hat{d}_{\min}/2)} = -0.3611 \text{ C/m}^2. \quad (\text{B.17})$$

Same values of $q_{A,\infty}$ and $q_A(\hat{d}_{\min})$ indicate that with the current (initial) droplet properties charge regulation effect is non-existent. When the droplet is dried, interparticle distance becomes shorter and the regulated surface charge density deviates from the dilute value at some point, as depicted in Fig. 5.3.

Appendix C: Shell thickness measured from SEM images of SiO₂ and TiO₂ particles

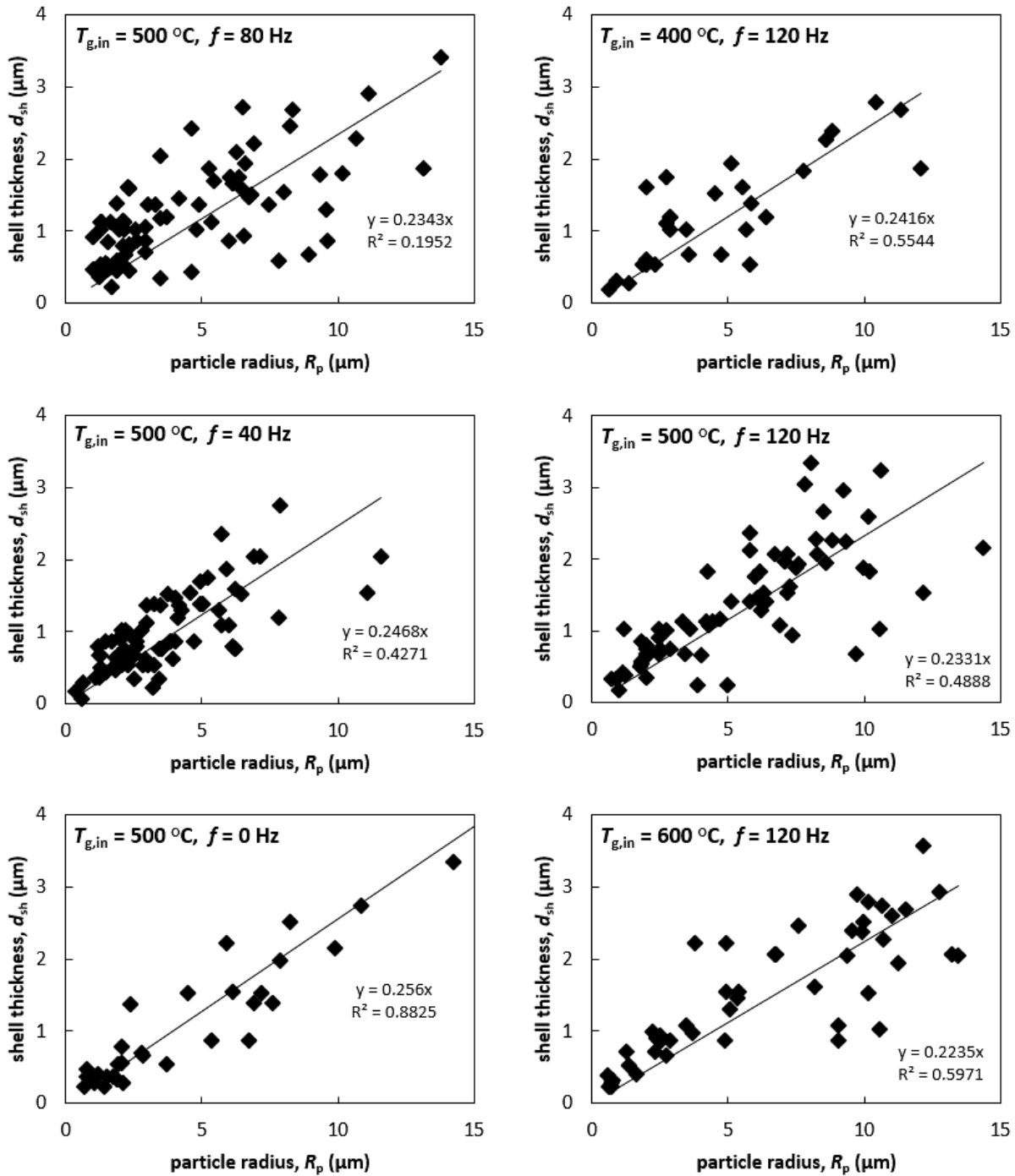


Fig. C1. Plots of shell thickness against radius of SiO₂ particles.

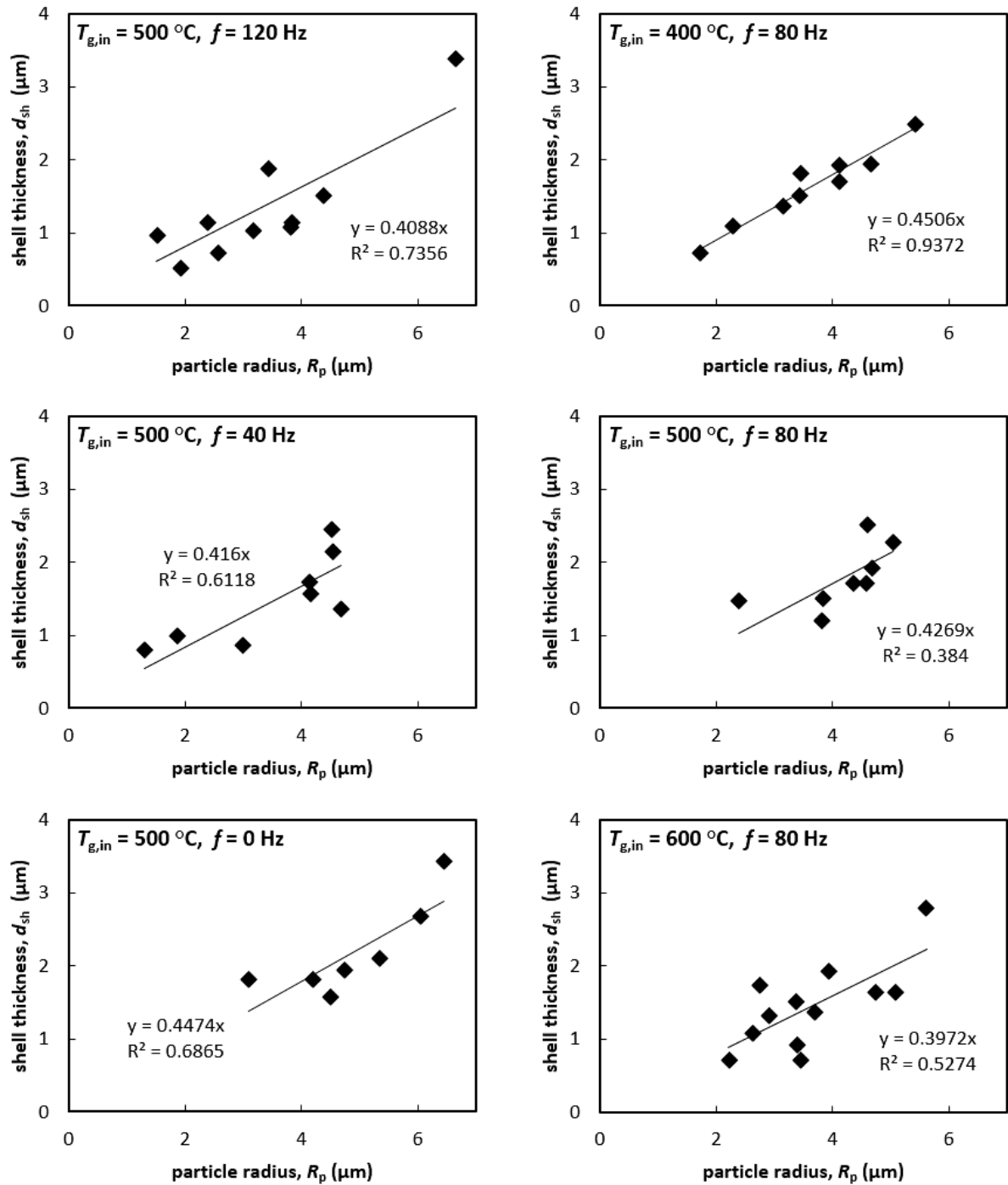


Fig. C2. Plots of shell thickness against radius of TiO₂ particles.

Appendix D: Particle size distribution data from experiments in Chapter 5

Table D.1. Number-based particle size distribution of SiO₂ particles.

Inlet gas temperature, $T_{g,in}$ (°C)				500	500	500	500	600	400
Pulsation frequency, f (Hz)				80	120	40	0	120	120
D_{min} (μm)	D_{mid} (μm)	D_{max} (μm)	\log D_{max}	% - number					
0.017	0.024	0.032	-1.5	61.65	32.82	43.43	37.96	25.85	24.61
0.032	0.042	0.056	-1.25	23.07	41.85	33.66	41.31	47.27	52.40
0.056	0.075	0.100	-1	8.32	10.62	10.86	17.30	14.03	12.70
0.100	0.133	0.178	-0.75	4.90	9.27	6.12	2.79	6.87	7.25
0.178	0.237	0.316	-0.5	1.18	3.75	3.91	0.07	4.28	1.95
0.316	0.422	0.562	-0.25	0.51	0.96	1.30	0.23	1.23	0.54
0.562	0.750	1	0	0.16	0.29	0.29	0.12	0.20	0.22
1	1.334	1.778	0.25	0.06	0.14	0.13	0.06	0.11	0.16
1.778	2.371	3.162	0.5	0.06	0.13	0.11	0.07	0.07	0.08
3.162	4.217	5.623	0.75	0.03	0.09	0.11	0.04	0.04	0.05
5.623	7.500	10	1	0.02	0.03	0.03	0.00	0.01	0.01
10	13.335	17.783	1.25	0.02	0.04	0.03	0.01	0.01	0.01
17.783	23.714	31.623	1.5	0.01	0.02	0.02	0.01	0.02	0.01
31.623	42.170	56.234	1.75	0.00	0.01	0.00	0.00	0.00	0.00
56.234	74.989	100	2	0.00	0.00	0.00	0.00	0.00	0.00

Table D.2. Number-based particle size distribution of TiO₂ particles.

Inlet gas temperature, $T_{g,in}$ (°C)				500	400	600	500	500	500
Pulsation frequency, f (Hz)				80	80	80	120	40	0
D_{min} (μm)	D_{mid} (μm)	D_{max} (μm)	\log D_{max}	% - number					
0.017	0.024	0.032	-1.5	0.00	0.00	0.00	0.00	0.00	0.00
0.032	0.042	0.056	-1.25	0.00	0.00	0.00	0.00	0.00	0.00
0.056	0.075	0.100	-1	3.46	3.03	0.00	0.00	0.00	0.00
0.100	0.133	0.178	-0.75	20.74	3.03	0.00	0.00	0.00	0.00
0.178	0.237	0.316	-0.5	24.20	12.11	0.00	2.57	23.70	9.87
0.316	0.422	0.562	-0.25	6.91	21.19	23.79	20.53	19.75	14.80
0.562	0.750	1	0	3.97	7.54	15.37	15.73	11.35	15.12
1	1.334	1.778	0.25	6.62	14.49	22.21	30.96	18.91	14.17
1.778	2.371	3.162	0.5	13.24	19.13	22.21	16.22	12.86	15.12
3.162	4.217	5.623	0.75	14.56	13.91	11.96	11.30	8.32	25.51
5.623	7.500	10	1	4.59	4.59	3.75	2.43	4.39	4.44
10	13.335	17.783	1.25	1.48	0.95	0.58	0.27	0.71	0.81
17.783	23.714	31.623	1.5	0.23	0.05	0.13	0.00	0.00	0.15
31.623	42.170	56.234	1.75	0.00	0.00	0.00	0.00	0.00	0.00
56.234	74.989	100	2	0.00	0.00	0.00	0.00	0.00	0.00

Table D.3. Volume-based particle size distribution of SiO₂ particles.

Inlet gas temperature, $T_{g,in}$ (°C)				500	500	500	500	600	400
Pulsation frequency, f (Hz)				80	120	40	0	120	120
D_{min} (μm)	D_{mid} (μm)	D_{max} (μm)	\log D_{max}	% - volume					
0.017	0.024	0.032	-1.5	0.000	0.000	0.000	0.000	0.000	0.000
0.032	0.042	0.056	-1.25	0.001	0.000	0.001	0.001	0.001	0.001
0.056	0.075	0.100	-1	0.002	0.000	0.001	0.002	0.001	0.001
0.100	0.133	0.178	-0.75	0.004	0.003	0.003	0.002	0.003	0.004
0.178	0.237	0.316	-0.5	0.007	0.006	0.012	0.000	0.009	0.005
0.316	0.422	0.562	-0.25	0.019	0.010	0.018	0.005	0.012	0.010
0.562	0.750	1	0	0.029	0.016	0.029	0.013	0.013	0.022
1	1.334	1.778	0.25	0.061	0.054	0.066	0.037	0.048	0.072
1.778	2.371	3.162	0.5	0.386	0.199	0.405	0.221	0.205	0.188
3.162	4.217	5.623	0.75	1.272	1.384	2.113	0.982	0.931	0.694
5.623	7.500	10	1	3.987	1.837	2.915	0.536	0.435	1.379
10	13.335	17.783	1.25	22.712	16.016	14.271	11.266	5.744	8.701
17.783	23.714	31.623	1.5	66.179	31.732	47.232	48.231	50.794	30.233
31.623	42.170	56.234	1.75	5.339	48.741	13.057	25.469	41.804	38.259
56.234	74.989	100	2	0.000	0.000	19.880	13.235	0.000	20.431

Table D.4. Volume-based particle size distribution of TiO₂ particles.

Inlet gas temperature, $T_{g,in}$ (°C)				500	400	600	500	500	500
Pulsation frequency, f (Hz)				80	80	80	120	40	0
D_{min} (μm)	D_{mid} (μm)	D_{max} (μm)	\log D_{max}	% - volume					
0.017	0.024	0.032	-1.5	0.000	0.000	0.000	0.000	0.000	0.000
0.032	0.042	0.056	-1.25	0.000	0.000	0.000	0.000	0.000	0.000
0.056	0.075	0.100	-1	0.000	0.000	0.000	0.000	0.000	0.000
0.100	0.133	0.178	-0.75	0.000	0.000	0.000	0.000	0.000	0.000
0.178	0.237	0.316	-0.5	0.002	0.004	0.000	0.002	0.010	0.003
0.316	0.422	0.562	-0.25	0.006	0.030	0.040	0.073	0.029	0.020
0.562	0.750	1	0	0.021	0.070	0.124	0.288	0.155	0.099
1	1.334	1.778	0.25	0.226	0.849	1.086	3.164	1.371	0.585
1.778	2.371	3.162	0.5	2.896	4.935	6.320	9.807	4.518	3.864
3.162	4.217	5.623	0.75	13.594	22.361	16.544	33.760	16.726	29.181
5.623	7.500	10	1	19.819	34.503	27.087	33.091	46.090	28.897
10	13.335	17.783	1.25	34.396	30.929	18.250	19.816	31.101	21.071
17.783	23.714	31.623	1.5	29.040	6.318	30.550	0.000	0.000	16.281
31.623	42.170	56.234	1.75	0.000	0.000	0.000	0.000	0.000	0.000
56.234	74.989	100	2	0.000	0.000	0.000	0.000	0.000	0.000

Table D.5. Volume-based particle size distribution of shriveled maltodextrin particles.

Inlet gas temperature, $T_{g,in}$ (°C)				200	250	300	300	300	400
Pulsation frequency, f (Hz)				80	80	0	80	120	80
D_{min} (μm)	D_{mid} (μm)	D_{max} (μm)	\log D_{max}	% -volume					
0.056	0.075	0.100	-1	0.00	0.00	0.00%	0.00%	0.00%	0.00%
0.100	0.133	0.178	-0.75	0.01	0.00	0.00%	0.00%	0.00%	0.00%
0.178	0.237	0.316	-0.5	0.00	0.00	0.00%	0.00%	0.00%	0.00%
0.316	0.422	0.562	-0.25	0.00	0.00	0.00%	0.00%	0.00%	0.00%
0.562	0.750	1	0	0.00	0.00	0.00%	0.00%	0.00%	0.00%
1	1.334	1.778	0.25	0.07	0.02	0.00%	0.02%	0.00%	0.01%
1.778	2.371	3.162	0.5	0.80	1.99	0.10%	0.07%	0.17%	0.09%
3.162	4.217	5.623	0.75	6.43	1.07	0.93%	1.97%	1.03%	0.48%
5.623	7.500	10	1	21.12	32.66	9.41%	9.62%	4.71%	0.70%
10	13.335	17.783	1.25	26.80	11.22	13.93%	10.17%	3.61%	3.53%
17.783	23.714	31.623	1.5	33.62	0.00	3.42%	18.27%	5.49%	0.00%
31.623	42.170	56.234	1.75	0.00	0.00	0.00%	0.00%	0.00%	0.00%
56.234	74.989	100	2	0.00	0.00	0.00%	0.00%	0.00%	0.00%

Table D.6. Volume-based particle size distribution of spherical maltodextrin particles.

Inlet gas temperature, $T_{g,in}$ (°C)				200	250	300	300	300	400
Pulsation frequency, f (Hz)				80	80	0	80	120	80
D_{min} (μm)	D_{mid} (μm)	D_{max} (μm)	\log D_{max}	% -volume					
0.056	0.075	0.100	-1	0.00	0.00	0.00	0.00	0.00	0.00
0.100	0.133	0.178	-0.75	0.00	0.00	0.00	0.00	0.00	0.00
0.178	0.237	0.316	-0.5	0.00	0.01	0.00	0.00	0.00	0.00
0.316	0.422	0.562	-0.25	0.01	0.01	0.00	0.00	0.00	0.00
0.562	0.750	1	0	0.04	0.03	0.00	0.01	0.00	0.03
1	1.334	1.778	0.25	0.03	0.03	0.04	0.06	0.04	0.03
1.778	2.371	3.162	0.5	0.15	0.07	0.36	0.23	0.37	0.70
3.162	4.217	5.623	0.75	0.30	7.79	0.98	1.05	1.53	5.59
5.623	7.500	10	1	1.53	1.47	7.10	4.40	5.70	12.78
10	13.335	17.783	1.25	9.08	0.90	5.58	5.87	3.71	10.05
17.783	23.714	31.623	1.5	0.00	11.86	0.00	16.67	0.00	0.00
31.623	42.170	56.234	1.75	0.00	30.88	0.00	0.00	0.00	66.00
56.234	74.989	100	2	0.00	0.00	0.00	0.00	0.00	0.00

Table D.7. Volume-based particle size distribution of torn maltodextrin particles.

Inlet gas temperature, $T_{g,in}$ (°C)				200	250	300	300	300	400
Pulsation frequency, f (Hz)				80	80	0	80	120	80
D_{min} (μm)	D_{mid} (μm)	D_{max} (μm)	\log D_{max}	%-volume					
0.056	0.075	0.100	-1	0.00	0.00	0.00	0.00	0.00	0.00
0.100	0.133	0.178	-0.75	0.00	0.00	0.00	0.00	0.00	0.00
0.178	0.237	0.316	-0.5	0.00	0.00	0.00	0.00	0.00	0.00
0.316	0.422	0.562	-0.25	0.00	0.00	0.00	0.00	0.00	0.00
0.562	0.750	1	0	0.00	0.00	0.00	0.00	0.00	0.00
1	1.334	1.778	0.25	0.00	0.00	0.00	0.00	0.00	0.00
1.778	2.371	3.162	0.5	0.00	0.00	0.00	0.00	0.00	0.00
3.162	4.217	5.623	0.75	0.00	0.00	0.00	0.00	0.00	0.00
5.623	7.500	10	1	0.00	0.00	0.00	9.19	0.28	0.00
10	13.335	17.783	1.25	0.00	0.00	0.92	5.34	0.00	0.00
17.783	23.714	31.623	1.5	0.00	0.00	53.21	17.04	23.43	0.00
31.623	42.170	56.234	1.75	0.00	0.00	4.03	0.00	16.76	0.00
56.234	74.989	100	2	0.00	0.00	0.00	0.00	33.17	0.00

Table D.8. Fractions of maltodextrin particles according to their shapes.

Inlet gas temperature, $T_{g,in}$ (°C)		200	250	300	300	300	400
Pulsation frequency, f (Hz)		80	80	0	80	120	80
%-number							
<i>shrivel</i>		9.9	13.4	27.1	20.3	25.2	8.2
<i>sphere</i>		90.1	86.6	69.2	74.8	73.7	91.8
<i>torn</i>		0.0	0.0	3.7	4.9	1.1	0.0
%-volume							
<i>shrivel</i>		88.8	47.0	27.8	40.1	15.0	4.8
<i>sphere</i>		11.2	53.0	14.1	28.3	11.4	95.2
<i>torn</i>		0.0	0.0	58.2	31.6	73.6	0.0

Scientific Contributions

Journal articles

1. D. Pramudita, E. Tsotsas, A model of pulse combustion drying and breakup of colloidal suspension droplets, *Powder Technology*. 355 (2019) 755–769.
2. D. Pramudita, A. Teiwes, M. Jacob, E. Tsotsas, Crust breakage in production of fine particles using pulse combustion drying: Experimental and numerical investigations, *Powder Technology*. 393 (2021) 77–98.
3. D. Pramudita, S. Humjaa, E. Tsotsas, Droplet drying and whey protein denaturation in pulsed gas flow: A modeling study, *Journal of Food Engineering*. 321 (2022) 110959.

Conferences

1. D. Pramudita, M. Jacob, E. Tsotsas, Modeling breakup of a suspension droplet containing nanoparticles during pulse combustion drying, International Congress on Particle Technology (oral presentation), Nuremberg, Germany, 9-11th of April 2019.
2. D. Pramudita, A. Teiwes, A. K. Singh, M. Jacob, E. Tsotsas, Effects of material types and operating conditions on properties of particles produced with pulse combustion drying, 9th International Granulation Workshop, Granulation Conference (poster presentation), Lausanne, Switzerland, 26-28th of June 2019.

Supervised master student thesis

1. S. Humjaa, Modeling of product quality change during powder production by pulse combustion drying (Master Thesis), Otto von Guericke University Magdeburg, Germany, 2020